APPLIED COMPUTATIONAL ELECTROMAGNETICS SOCIETY JOURNAL

April 2018
Vol. 33 No. 4
ISSN 1054-4887

The ACES Journal is abstracted in INSPEC, in Engineering Index, DTIC, Science Citation Index Expanded, the Research Alert, and to Current Contents/Engineering, Computing & Technology.

The illustrations on the front cover have been obtained from the research groups at the Department of Electrical Engineering, The University of Mississippi.

EMERITUS ASSOCIATE EDITORS-IN-CHIEF

EMERITUS EDITORIAL ASSISTANTS

APRIL 2018 REVIEWERS: REGULAR PAPERS

Mohammad Alibakhshikenari
Stamatios Amanatiadis
Zsolt Badics
Subbarao Bandaru
Cemile Bardak
Thomas Bauernfeind
Marek Bleszynski
Bair Budaev
Mohammed Hadi
Zhixiang Huang
Irum Jafri
Mario Jakas
Ulrich Jakobus
Ming Jin
Angelo Liseno
Biswajeet Mukherjee
Sovanlal Mukherjee
Imaculate Rosaline
Esther S.
Christoph Statz
Candace Suriano
Aathmanesan T.
Yuvaraja T.
Qi Wu
Zubiao Xiong
Rengan Xu
Ravindra Yadav
Ferdows Zarrabi

APRIL 2018 REVIEWERS: EXPRESS PAPERS

Robert Burkholder
Fangyuan Chen

THE APPLIED COMPUTATIONAL ELECTROMAGNETICS SOCIETY JOURNAL

Vol. 33 No. 4 April 2018

TABLE OF CONTENTS – REGULAR PAPERS

TABLE OF CONTENTS – EXPRESS PAPERS

Temperature Rise and SAR Distribution at Wide Range of Frequencies in a Human Head due to an Antenna Radiation

Fatih Kaburcuk [1] and Atef Z. Elsherbeni [2]

[1] Electrical and Electronic Engineering Department
Erzurum Technical University, Erzurum, 25700, Turkey
fkaburcu@syr.edu – fatih.kaburcuk@erzurum.edu.tr

[2] Electrical Engineering Department
Colorado School of Mines, Golden, CO, 80401, USA
aelsherb@mines.edu

Abstract ─ Temperature rise and specific absorption rate distribution in a human head due to electromagnetic energy produced by an adjacent antenna are evaluated. An algorithm proposed in this paper provides these distributions at multiple frequencies using a single simulation. The head tissue parameters are used from the available three-term Debye coefficients obtained by the experimental data from 500 MHz to 20 GHz. The proposed algorithm is developed by integrating the Debye model of human head tissues parameters into the finite-difference time-domain method by using the auxiliary differential equation approach along with the use of bioheat equation for specific absorption rate and temperature computations.

Index Terms ─ Dispersive material, FDTD method, Specific Absorption Rate (SAR), temperature rise.

I. INTRODUCTION

Many researchers have studied the temperature rise and specific absorption rate (SAR) distribution in the human head due to electromagnetic (EM) radiation produced by cellular phones with different types of antennas [1–8] using the nondispersive algorithm based on the finite-difference time-domain (FDTD) method. In the previous work [1–8], the SAR computation for a human head was conducted at only one frequency of interest using a single simulation because of the depressiveness properties of the biological tissue. Therefore, the thermal analysis and SAR computation for multiple frequencies was not integrated into the nondispersive algorithm because the EM properties of the biological tissues are dependent on frequency.

In this paper, a dispersive algorithm is developed to obtain SAR and temperature distributions at multiple frequencies of interest from a single FDTD simulation. The dispersive algorithm is based on the integration of Debye tissue model into the FDTD method using the ADE as presented in [9] along with the Pennes bioheat equation from [10]. The dispersive EM properties of the human head tissues for a wide range of frequencies (500 MHz to 20 GHz) used in this investigation are based on the three-term Debye coefficients (the relative permittivity of medium at infinite frequencies, the static relative permittivity, and the relaxation time) calculated and tabulated in [11]. The dispersive algorithm provides the temperature rise and SAR distribution in the head at multiple frequencies of interest in a single FDTD simulation.

The simulation procedure of the dispersive algorithm can be achieved in the following steps: 1) EM simulation of the dispersive head model using the FDTD method due to a multi-frequency source; 2) computation of the steady-state SAR distribution due to the EM simulation at the frequencies of interest; 3) computation of the steady-state temperature distribution using the bioheat equation when SAR=0; and 4) computation of the final temperature distributions at the frequencies of interest by substituting the steady-state SAR distribution in the bioheat equation. Finally, the difference of the final and steady-state temperature distributions in the head gives the temperature rise distribution. As expected, the computed temperature rise and SAR in the head are found to be different for different frequencies because of the frequency dependent of the biological tissues EM parameters. The temperature rise in the head due to the antenna is insufficient to cause a remarkable change on EM parameters of head tissues.

To prove the validity of the developed algorithm, the radiation from an antenna is evaluated in the presence of a heterogeneous head model obtained from [12]. The temperature rise and SAR distributions in the head at multiple frequencies centered around 900 MHz and 1.5 GHz are obtained using multiple simulations using the traditional nondispersive algorithm as well as using a single FDTD simulation based on the developed

Submitted On: October 18, 2017
Accepted On: January 22, 2018

algorithm. Furthermore, in order to show the effect of distance between the head model and the antenna, the maximum temperature rise and SAR in the head are calculated for a set of separation distances. This work will facilitate the future interaction between a human head and EM plane waves produced by 5G base stations.

II. MODEL AND METHODS

A. Human head model

The realistic and heterogeneous head model used in this work has been constructed from a ZUBAL MRI head phantom [12]. MATLAB is used to read and resampled the head data which consists of 8 tissues, including skin, muscle, bone, blood, fat, lens, and white and grey matter. The head model consists of 86(width)×110(depth)×120(height) cubic cells. In order to ensure the numerical stability in the FDTD method, a cell dimension should be less than $\lambda_{\min}/10$, where $\lambda_{\min}$ is the wavelength of the highest frequency in free space. The cell size used here is 2 mm in the three Cartesian directions. The time step is restricted by the Courant stability criterion.

B. Dispersive head tissues

The head model used in this paper consists of eight dispersive tissues. A numerical procedure developed in [11] provides two-term and three-term Debye coefficients to accurately fit the experimental data from [13] for the head tissues for the frequency range 500 MHz to 20 GHz. The three-term Debye coefficients of the head tissues used in this work are given in Table 1. The complex relative permittivity $\left(\varepsilon_r^*(\omega)\right)$ for three-term Debye coefficients is given [11] as:

$$\varepsilon_r^*(\omega) = \varepsilon_\infty + \sum_{k=1}^{3} \frac{\Delta\varepsilon_k}{1 + j\omega\tau_k}, \tag{1}$$

where ε_∞ is the relative permittivity at infinite frequencies, ε_k and τ_k are the static relative permittivity and the relaxation time of the kth term, respectively.

Table 1: Three-term Debye parameters of head tissues for the frequency range 500 MHz to 20 GHz

Tissue	ε_∞	$\Delta\varepsilon_1$	$\Delta\varepsilon_2$	$\Delta\varepsilon_3$	τ_1[ps]	τ_2[ps]	τ_3[ps]
Skin	4.136	32.51	2.499	125.6	7.248	527.2	1.380
Fat	2.994	2.467	6.066	31.39	3.970	7904	3.739
Bone	3.532	4.992	12.47	34.85	5.811	133.5	1.172
Blood	5.939	46.72	8.064	693.1	7.203	125.2	4.387
Muscle	5.896	45.70	2.956	324.1	6.474	139.0	3.443
Lens	5.415	32.56	8.388	304.1	6.719	106.3	3.909
W. Matter	5.338	30.04	2.090	70.50	7.181	225.7	1.156
G. Matter	5.380	42.16	2.754	137.1	7.187	224.6	1.399

C. FDTD method and antenna

The proposed dispersive algorithm and the nondispersive algorithm are used to analyze the interactions between the human head model and an antenna as a wave source. The antenna is placed 24 mm away from the right ear of the head model and excited by a voltage source with a Gaussian waveform containing the frequencies of interest. The width and time delay of the Gaussian waveform are set to T=50 ps and 4.5T, respectively [9]. In this work, CPML [14] absorbing boundaries are applied at the borders to truncate the problem domain.

D. SAR calculation in the head

The FDTD method is used for the computation of the SAR which is used in the temperature rise calculation. The average electric (E) field components at the center of each cell for all frequencies of interest are determined by using the discrete Fourier transform during the FDTD time-marching loop. Once the FDTD time-marching loop is completed, the amplitudes of the E field components are used for the calculation of the steady-state SAR distribution at each frequency of interest. The calculated steady-state SAR at each frequency of interest is considered the EM heat source and is used in the temperature rise calculation of the head. The SAR is defined at a given location as:

$$SAR(i,j,k) = \frac{\sigma(i,j,k)}{2\rho(i,j,k)}\left(\left|E_x(i,j,k)\right|^2 + \left|E_y(i,j,k)\right|^2 + \left|E_z(i,j,k)\right|^2\right), \tag{2}$$

where $\sigma(i,j,k)$ and $\rho(i,j,k)$ are the electric conductivity and mass density [kg/m^3] of the tissue at a given location, respectively. In Equation (2), an averaging of E_x, E_y, and E_z is performed to obtain the corresponding values at the exact location of interest. The computed SAR distribution is normalized to the antenna output power. For calculating the peak SAR over 1 gram of tissue in the head, the IEEE standard C95.3-2002 is considered [15].

E. Temperature rise calculation in the head

When the steady-state SAR distribution in the head is computed, the thermal simulation is performed by solving the bioheat equation [10] which consists of two simulations: In the first simulation, the temperature distribution in the head is calculated by using the bioheat equation without EM power (i.e., SAR=0) during the thermal time-marching loop. This calculation is carried out until the convergence is reached. The calculated temperature distribution is considered as the steady-state temperature distribution in the head. In the second simulation, the final temperature distribution is calculated by substituting the obtained steady-state SAR distribution into the bioheat equation. The temperature rise distribution is achieved by taking the difference between final and steady-state temperature distributions.

The bioheat equation is given by:

$$\rho \cdot C \cdot \frac{\partial T}{\partial t} = K \cdot \nabla^2 T + \rho \cdot SAR - B \cdot \left(T - T_b\right), \tag{3}$$

where T is the temperature of the tissue at time t, ρ is the mass density of the tissue [kg/m^3], C is the heat capacity

of the tissue [J/(kg·°C)], K is the thermal conductivity of a tissue [J/(m·°C)], B is the blood perfusion rate [W/(m^3.°C)], and T_b is the blood temperature.

Heat exchange [1] between the skin surface and air is modeled by imposing the continuity of the heat flow perpendicular to skin surface as a boundary condition. The boundary condition applied to skin surface and also internal cavity surface of the head is expressed as:

$$K \cdot \frac{\partial T}{\partial n} = -h \cdot \left(T - T_a\right), \tag{4}$$

where T_a is the air temperature, n is the unit normal vector to the skin surface or internal cavity, and h is the convection heat transfer coefficient [W/(m^2·°C)].

During each thermal time-step, the bioheat equation in (3) is applied to all tissues in the head and then the boundary condition in (4) is applied to the skin surface and internal cavity surface of the head. The temperature is computed at the center of each cell with a spatial step d equal to that used in the FDTD simulation and a thermal time-step equal to Δt. The discretized form of the bioheat equation in (3) and the boundary condition in (4) at mth thermal time-step with a cell indexed as (i, j, k) can be written, respectively in (5) and (6) as:

$$T^{m+1}(i,j,k) = \left(\begin{array}{c} T^m(i,j,k) + \frac{\Delta t}{C(i,j,k)} \cdot SAR(i,j,k) \\ - \frac{\Delta t}{\rho(i,j,k) \cdot C(i,j,k)} \cdot B(i,j,k) \cdot \left[T^m(i,j,k) - T_b \right] \\ + \frac{\Delta t}{\rho(i,j,k) \cdot C(i,j,k) \cdot d^2} \cdot K(i,j,k) \cdot \\ \left[\begin{array}{c} T^m(i+1,j,k) + T^m(i,j+1,k) \\ + T^m(i,j,k+1) + T^m(i-1,j,k) \\ + T^m(i,j-1,k) + T^m(i,j,k-1) - 6T^m(i,j,k) \end{array} \right] \end{array} \right), \tag{5}$$

$$T^{m+1}\left(i,j,k_{\min}\right) = \frac{K \cdot T^m\left(i,j,k_{\min}+1\right)}{K + h \cdot d} + \frac{T_a \cdot h \cdot d}{K + h \cdot d}. \tag{6}$$

The finite-difference approximation of the boundary condition in (6) computed at the skin/air interface is given only for the z-direction, which is normal to the skin surface of the head. Similarly, this approximation can be applied to x- and y-directions which are normal to the skin surface of the head. The convection heat transfer coefficients (h) is set to 10.5 [W/(m^2·°C)] from the skin surface to air and 50 [W/(m^2·°C)] from the internal surface to the internal cavity [1]. Table 2 gives the mass density (ρ) and thermal parameters (C, K, B) of the head tissues [2, 5, 7]. The air temperature (T_a) and initial head temperature (T_b) in the simulations were set to 20 °C and 37 °C, respectively. In order to avoid the numerical instability, the thermal time-step (Δt) is chosen to satisfy the following criterion [1]:

$$\Delta t \le \frac{2\rho C d^2}{12K + Bd^2}. \tag{7}$$

III. NUMERICAL RESULTS

In the first part of this section, the temperature rise and SAR distributions are obtained using the proposed dispersive algorithm at all frequencies of interest in a single simulation. In the second part, these distributions are obtained using the nondispersive algorithm by performing multiple simulations, each at a single frequency. These two approaches were conducted to compare results and to show the performance and efficiency of the developed dispersive algorithm. Finally, in the last part of this section, the performance of the developed algorithm and the effect of distance from the head model to the antenna on the SAR and temperature rise are presented. In all simulations, the output power of the antenna was set to 0.6 W for 900 MHz and 0.27 W for 1.5 GHz as in [1].

Table 2: Mass density and thermal parameters of the head tissues

Type of Tissue	ρ [kg/m^3]	C [J/(kg.°C)]	K [W/(m.°C)]	B [W/(m^3.°C)]
Skin	1125	3600	0.42	9100
Fat	916	3000	0.25	1700
Bone	1810	1300	0.40	1000
Blood	1058	3900	0.56	0
Muscle	1047	3800	0.50	2700
Lens	1100	3000	0.40	0
W. Matter	1038	3500	0.50	40000
G. Matter	1038	3800	0.57	40000
Air (internal)	1.2	1000	0.03	0

A. Temperature rise and SAR distributions in the head using the proposed dispersive algorithm

In order to provide solutions at multiple frequencies, an antenna with at least two frequency bands is required to radiate towards the head. Thus, a modified dipole antenna of 156 mm length and 0.74 mm diameter is modified by adding two passive wires replaced at a distance of 4 mm at the two sides of a dipole antenna as shown in Fig. 1. The diameter and length of the passive wires are 1.56 mm and 88 mm, respectively. The center operating frequencies of this loaded dipole antenna are 900 MHz and 1.5 GHz. The input reflection coefficient (S_{11}) and directivity pattern in the xy plane cut at 900 MHz and 1.5 GHz are shown in Fig. 2.

The temperature rise and SAR distributions of the head due to the antenna are calculated at three frequencies centered at 900 MHz and at three other frequencies centered at 1.5 GHz using a single simulation. The maximum 1 gram averaged SAR value in the head is 1.628 Watt/kg at 900 MHz and 1.068 Watt/kg at 1.5 GHz. The SAR values calculated in this work are found to be exactly the same as those values reported in [1]. Figure 3 shows the 1 gram averaged SAR distribution at 900 MHz and 1.5 GHz in the x-y cross section of the head model. Figure 4 shows the resulting temperature rise distribution at 900 MHz and 1.5 GHz in the x-y cross section of the head model. The maximum temperature rise in the head is 0.281 °C at 900 MHz and 0.149 °C at

1.5 GHz. The maximum temperature rise calculated in [1] is 0.18 ºC at 900 MHz and 0.15 ºC at 1.5 GHz. There is some small difference between our results and those published in [1], mainly due to the fact that the head model used in this paper is different and the head phone set as a source in [1] is different from the dipole antenna used in this paper. The maximum temperature variation in the head as a function of time is shown in Fig. 7 at 870, 900, 930 MHz and 1.46, 1.50, 1.54 GHz. It can be seen from Fig. 5 that the temperature increases rapidly over the first 10 minutes, then temperature increase slows down, and the maximum (steady-state) temperature is reached after 32 minutes of exposure.

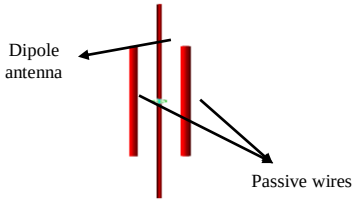

Fig. 1. The dipole antenna loaded with two passive wires.

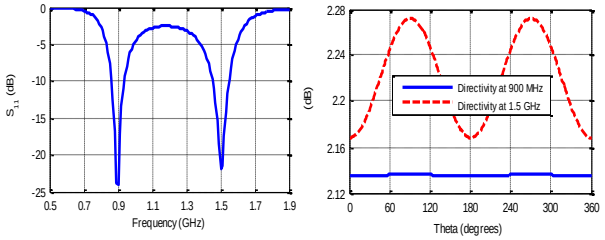

Fig. 2. S_{11} and directivity pattern in the *xy* plane cut.

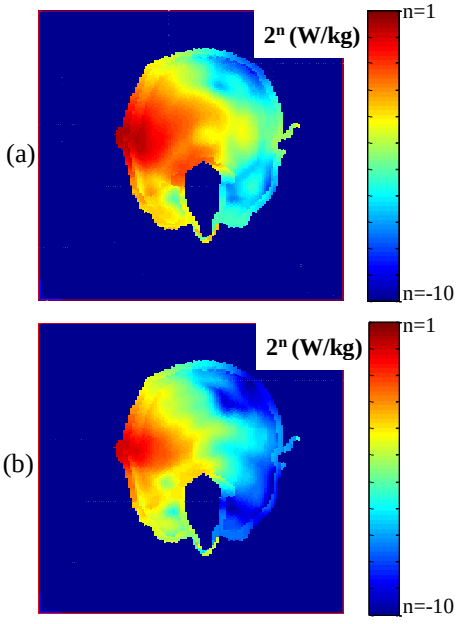

Fig. 3. 1 gram averaged SAR distribution in the head at (a) 900 MHz and (b) 1.5 GHz.

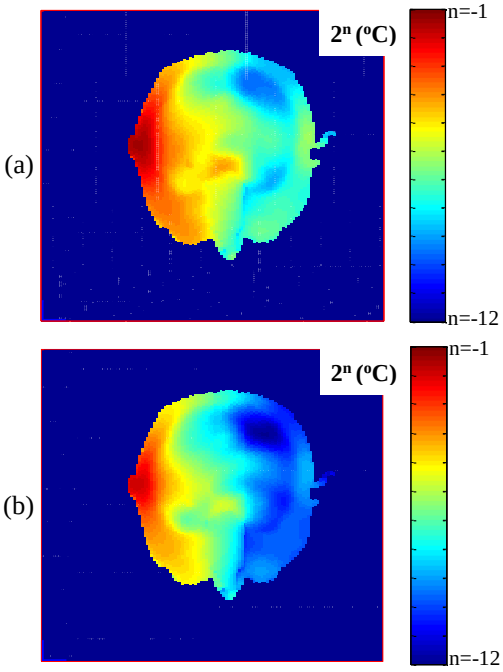

Fig. 4. Temperature rise distribution in the head at (a) 900 MHz and (b) 1.5 GHz.

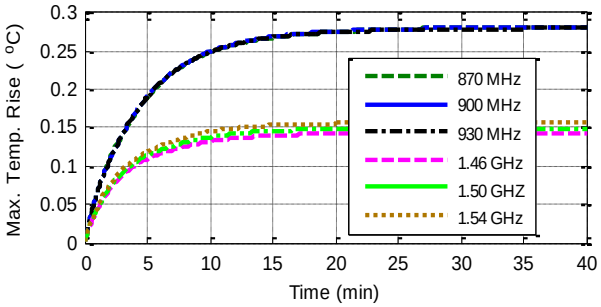

Fig. 5. Maximum temperature rise in the head vs. time at 870, 900, 930 MHz and 1.46, 1.50, 1.54 GHz.

B. Temperature rise and SAR distributions in the head using the nondispersive algorithm

In order to prove the validity of the proposed dispersive algorithm, the temperature rise and SAR distributions in the head are calculated at the same frequencies listed in the above section, but using multiple simulations using the nondispersive algorithm. The SAR and temperature rise distributions obtained from these simulations agree very well with the results obtained from the single simulation shown in previous section. The 1 gram averaged SAR and temperature rise distributions are shown in Fig. 6 and Fig. 7, respectively. The maximum 1 gram averaged SAR value in the head is 1.628 Watt/kg at 900 MHz and 1.068 Watt/kg at 1.5 GHz. The maximum temperature rise in the head is 0.281 ºC at 900 MHz and 0.149 ºC at 1.5 GHz.

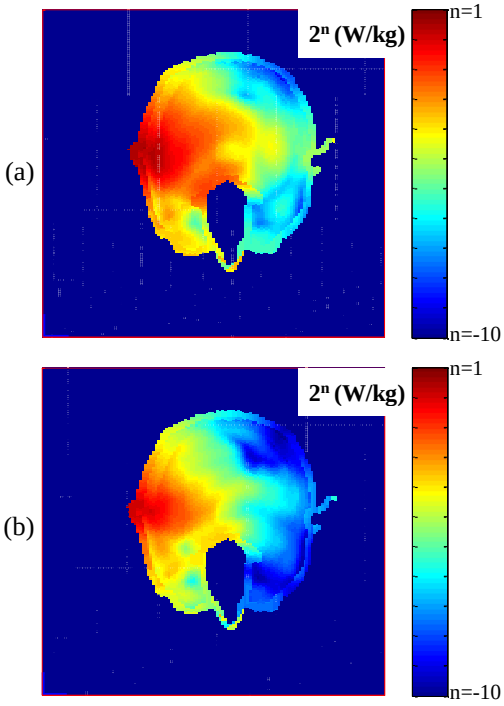

Fig. 6. 1 gram averaged SAR distribution in the head at (a) 900 MHz and (b) 1.5 GHz.

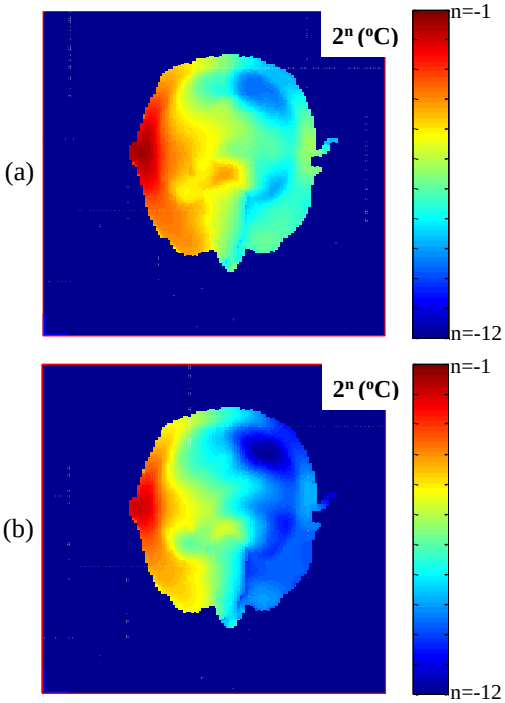

Fig. 7. Temperature rise distribution in the head at (a) 900 MHz and (b) 1.5 GHz.

C. Performance of the dispersive algorithm

For practical applications, it is always necessary to expect results at multiple frequencies. The formulation of the dispersive algorithm [9] is more complicated than that of the nondispersive algorithm. However, the dispersive algorithm can provide solutions at multiple frequencies using a single simulation, whereas the nondispersive algorithm can also provide solutions at multiple frequencies but using multiple simulations. To show the efficiency of the proposed dispersive algorithm, the computation time of both algorithms is recorded for results at six frequencies and are shown in Fig. 8. As shown, when the number of frequencies of interest is increased the dispersive algorithm is more efficient than the nondispersive algorithm while producing exactly the same results. The effect of distance between the human head and the antenna on the SAR and the temperature rise is also investigated. The maximum 1 gram SAR and temperature rise at 900 MHz and 1.5 GHz are given in Table 3 when the distance between the human head and the antenna is changed.

Table 3: Distance effect on SAR and temperature rise

Distance	Max. Temp. Rise [°C]		Max. SAR_{1g} [Watt/kg]	
	900 MHz	1.5 GHz	900 MHz	1.5 GHz
28 mm	0.239	0.120	1.364	0.851
36 mm	0.174	0.080	0.965	0.568
44 mm	0.129	0.058	0.698	0.407

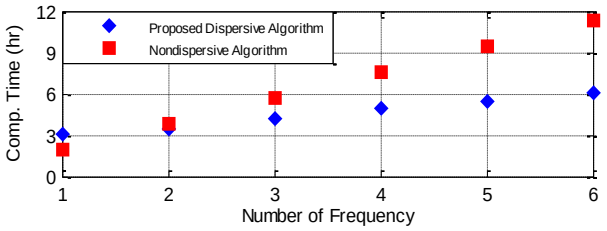

Fig. 8. Comparison of the computation time performed by both algorithms vs. number of frequency.

IV. CONCLUSION

An efficient algorithm is developed for the computation of the temperature rise and SAR distributions in a head model due to the radiation from a nearby antenna operating at 900 MHz and 1.5 GHz. The maximum temperature rise is 0.281 °C at 900 MHz and 0.149 °C at 1.5 GHz with antenna output powers of 0.6 W at 900 MHz and 0.27 W at 1.5 GHz, respectively. The key contribution here is the computation of the temperature rise and SAR distributions at multiple frequencies in a single FDTD simulation. Remarkable saving in computation time is achieved when the analysis is performed at more than one frequency.

REFERENCES

[1] J. Wang and O. Fujiwara, "FDTD computation of temperature rise in the human head for portable

telephones," *IEEE Trans. Microwave Theory Tech.*, vol. 47, pp. 1528-1534, Aug. 1999.

[2] P. Bernardi, M. Cavagnaro, S. Pisa, and E. Piuzzi, "Specific absorption rate and temperature increases in the head of a cellular-phone user," *IEEE Trans. Microwave Theory Tech.*, vol. 48, pp. 1118-1126, July 2000.

[3] P. Bernardi, M. Cavagnaro, S. Pisa, and E. Piuzzi, "Power absorption and temperature elevations induced in the human head by a dual-band monopole-helix antenna phone," *IEEE Trans. Microwave Theory Tech.*, vol. 49, no. 12, pp. 2539-2546, Dec. 2001.

[4] A. Hirata, M. Morita, and T. Shiozawa, "Temperature increase in the human head due to a dipole antenna at microwave frequencies," *IEEE Trans. Electromag. Compat*., vol. 45, no. 1, pp. 109-116, Feb. 2003.

[5] A. Hirata, and T. Shiozawa, "Correlation of maximum temperature increase and peak SAR in the human head due to handset antennas," *IEEE Trans. Microw. Theory Tech*., vol. 51, no. 7, pp. 1834-1841, July 2003.

[6] M. Fujimoto, A. Hirata, J. Q. Wang, O. Fujiwara, and T. Shiozawa, "FDTD-derived correlation of maximum temperature increase and peak SAR in child and adult head models due to dipole antenna," *IEEE Trans. Electromagn. Compat.*, vol. 48, no. 1, pp. 240-247, Feb. 2006.

[7] A. Hirata, K. Shirai, and O. Fujiwara, "On averaging mass of SAR correlating with temperature elevation due to a dipole antenna," *Progress In Electromagnetics Research*, vol. 84, pp. 221-237, 2008.

[8] M. R. Islam and M. Ali, "Temperature rise induced by wire and planar antennas in a high-resolution human head model," *IEEE Trans. Electromagn. Compat*., vol. 55, no. 2, pp. 288-298, Apr. 2013.

[9] A. Z. Elsherbeni and V. Demir, *The Finite-Difference Time-Domain Method for Electromagnetics with MATLAB Simulations*. second edition, ACES Series on Computational Electromagnetics and Engineering, SciTech Publishing, an Imprint of IET, Edison, NJ, 2016.

[10] H. H. Pennes, "Analysis of tissue and arterial blood temperature in resting forearm," *J. Appl. Physiol*., vol. 1, pp. 93-122, 1948.

[11] M. A. Eleiwa and A. Z. Elsherbeni, "Debye constants for biological tissues from 30 Hz to 20 GHz," *ACES Journal*, vol. 16, no. 3, Nov. 2001.

[12] http://noodle.med.yale.edu/zubal/ [Online website 2017].

[13] S. Gabriel, R. W. Lau, and C. Gabriel, "The dielectric properties of biological tissues: III. Parametric models for the dielectric spectrum of tissues," *Phys. Med. Biol*., 41, pp. 2271-2293, 1996.

[14] J. Roden and S. Gedney, ''Convolution PML (CPML): An efficient FDTD implementation of the CFS-PML for arbitrary media," *Microwave and Optical Technology Letters*, vol. 27, no. 5, pp. 334-339, 2000.

[15] *IEEE Recommended Practice for Measurements and Computations of Radio Frequency Electromagnetic Fields With Respect to Human Exposure to Such Fields, 100 kHz-300 GHz*, IEEE Standard C95.3-2002, Annex E, 2002.

Fatih Kaburcuk received both the M.Sc. and Ph.D. degrees from Syracuse University, Syracuse, New York in 2011 and 2014, respectively, all in Electrical Engineering. Kaburcuk is an Assistant Professor at Erzurum Technical University, Turkey.

Atef Z. Elsherbeni received his Ph.D. degree in Electrical Engineering from Manitoba University, Winnipeg, Manitoba, Canada, in 1987. Elsherbeni was with the University of Mississippi from 1987 to 2013. He was a Finland Distinguished Professor from 2009 to 2011. He joined the Electrical Engineering and Computer Science Department at Colorado School of Mines in August 2013 as the Dobelman Distinguished Chair Professor. Currently he is the Head of the Electrical Engineering Department. His research interest includes the scattering and diffraction of EM waves, finite-difference time-domain analysis of antennas and microwave devices, field visualization and software development for EM education, interactions of electromagnetic waves with the human body, RFID and sensor integrated FRID systems, reflector and printed antennas and antenna arrays, and measurement of antenna characteristics and material properties. His academic achievements include: Funded Research Grants with a total amount of $11,413,903, 13 books, 29 book chapters, 171 journal publications, 15 developed software packages, 56 (35 MS and 21 PhD) graduate students advised, 40 invited presentations, 221 proceedings publications, 174 conference abstracts, 74 technical reports, 35 short courses offered, 43 invited talks. Elsherbeni is a Fellow Member of IEEE and ACES. He is the Editor-in-Chief for ACES Journal. He was the general Chair for the 2014 APS-URSI Symposium and was the president of ACES Society from 2013 to 2015.

Modulation of the Antenna-Head Interaction inside a Closed Environment Using MOM-GEC Method

Hafawa Messaoudi and Taoufik Aguili

Republic of Tunisia Ministry of Higher Education and Scientific Research University of Tunis El Manar
National Engineering School of Tunis Communications Systems Laboratory, Tunis Tunisia
hafewa@yahoo.fr

Abstract ─ The interaction between human head and GSM antenna evaluations are usually conducted in free-space situations but wireless communication devices are frequently used in enclosed environments, such as vehicle, that consist of metallic boundaries. In such fully enclosed or semi-enclosed spaces, human exposure in terms of SAR is closely related to the EM field, which is multiplied, reflected and scattered by the metallic walls of the enclosure. This could lead to complicated resonance effects and affections in the antenna performances. This possible argument of an EM field inside an enclosure has raised serious concerns among the general public. This paper will therefore focus on the impact of dipole antenna modeling the handsets on the SAR distribution inside a cavity modeling the vehicle. Theoretical formulation and simulations are used to study this phenomenon but there is a lot of limitations. Despite, modulation using numerical method are used. A MoM-GEC modeling approach is applied to study the behavior of a dipole antenna resonating at 1.8 GHz. First of all, we are interested in studying the convergence of the input impedance. The current and the electric field distribution are simulated. The specific absorption rate (SAR) is examined for several different tissues.

Index Terms ─ Cavity, dipole antenna, human head, MOM-GEC, SAR.

I. INTRODUCTION

With the recent explosive increase of the use of mobile communication handsets, there has been a growing concern about possible hazard to a human body, especially head part. The influence of these devices on the environment and in particular their interaction with biological tissue must be investigated. Whether or not the presence of the human head affects the antenna performances in a partially closed environment which could be, the interior of a car, a condition of exposure that is largely diffused nowadays. Certainly, the presence of the handset user's influence on the antenna parameters (gain, radiation pattern and input impedance) is an issue which deserves a detailed investigation. Furthermore, growing concerns over the health effects of tissue exposed to electromagnetic energy motivates an effort to understand the power absorption distribution in the tissue when a GSM antenna is used inside a car.

These constraints must be modeled very precisely. Current efforts using numerical methods are aimed to define human head models, phone models, and environment that allow the comparison between numerical and experimental procedures [1], [2] involve practical details like rotating the head model to maintain the cell phone model oriented along the computation axis, to be able to obtain meaningful results.

However, actual exposure in real life is not always produced in a free-space like in our case.

Partially closed environments, like vehicle, are especially rough scenarios for many reasons, the structure is large compared to the wavelength, the metallic structures produce large reflections and the near field effects must be considered. This case of exposition could be characterized by measurements, but the procedure can be very complex. Numerical computation methods constitute an attractive alternative way for those scenarios. Popular numerical techniques currently used for electromagnetic interaction computations are the finite difference time domain (FDTD) method [3-5], the method of moment (MoM) [6] and the finite element method (FEM).

The most popular technique is the FDTD method because of its computational flexibility in modeling complex antenna geometries and the nearby biological tissues. However, it requires significant computer sources for thin layer and at high frequencies. Using the MoM method only the structure in question, not free space as is the case for FDTD is discretized, and boundary conditions do not have to be set. However, method of moments (MoM) cannot be used alone to calculate fields and currents inside lossy dielectrics such as people or phantoms, due to the memory requirements scale in proportion to the size of the problem in question and the required frequency.

These limitations can be offset by parallelization and by hybridization techniques. Approaches in which

Submitted On: June 17, 2017
Accepted On: August 12, 2017

MoM method is hybridized with other methods such as finite difference time domain (FDTD) [6-8] or finite elements method (FEM) [9-10] are attractive for dosimetry problems such as exposure from base station antennae since the need to discretize the free space region between antenna and the exposed dielectric body is avoided.

Actually, few studies to evaluate the effects on SAR arising from reflecting walls located near to a head model have been made [11]. The influence of the metallic structures of a car body frame on the SAR produced by a cell phone when a complete human body model is placed at different locations inside the vehicle was analyzed in [12].

In [13], the scenarios of passengers using different wireless communication devices inside a vehicle was studied. Also, the effects of the devices with different operational frequencies 900 MHz/1.8 GHz/2.4 GHz, and different seating locations on the SARs were investigated. All those studies are based on a simulation using FDTD method.

This paper tries to investigate the EM interaction of a handset antenna and user's head inside a car using the MoM-GEC method. This can be achieved by evaluating the handset antenna performance affection and the amount of the SAR induced in the user's head. The methods and results we present in this paper are the first step in such a process and provide some insight into the expected changes on power deposition for a particular environment that will help in directing subsequent approximation steps.

II. DESIGN MODELS

A simple metal frame was used to simulate the vehicle. A block model for the head were used. The generic phone was used in a vertical position and placed in close vicinity to head (d=1 cm). In our study the user head is reperesnted as a heterogenous and lossy dielectric with rectangular side walls aligned with the cavity walls, this choice of geometry is mainly for sake of simplicity in data management. We trait a case of a head model consisting of four layers modeling, whose macroscopic electrical properties are described in Table 1.

Table 1: Dielectric properties of the head tissue used in our study for f=1.8 GHz

	Permittivity ε_r	Conductivity σ (S/m)	Mass Density ρ (Kg/m^3)	Thickness δ (mm)
Skin	41.36	1.21	1010	2.5
Fat	5.35	0.078	920	5
Skull	16.4	0.45	1810	5
Brain	43.22	1.29	1040	80.5

III. NUMERICAL MODULING

To model the interaction phenomena, there is a set of methods that solves a number of problems. The integral ones are the most suitable to achieve an electromagnetic study of microwave structures.

The integral method used in our study is the method of moment (MOM) combined to the equivalent circuit method (GEC) [14-15]. The concept of generalized equivalent circuit is based on the representation of integral equations by an equivalent circuit in order to alleviate the resolution of Maxwell's equations, which presents a true electric image of the studied structures for describing the discontinuity and its environment [16-19].

In Fig. 1 we represented the advantage of our method which consists of modelling all the problem (structure) using the same formulation which is detailed in Section 5.

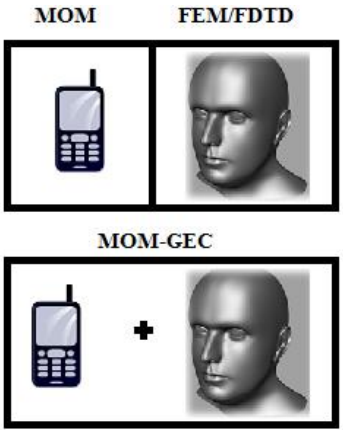

Fig. 1. Advantage of the MoM-GEC method.

IV. PROBLEM FORMULARTION

In this section, we are going to present our formulation to modulate our structure Fig. 2.

Considering the circuit example shown in Fig. 3. We can determine the current density lying in the metal part including the source domain and its associated field to verify the boundary conditions. Next, the integral equation is solved by applying the MOM method using Galerkin procedure.

The cavity used is a waveguide section closed by electrical walls (Fig. 2).

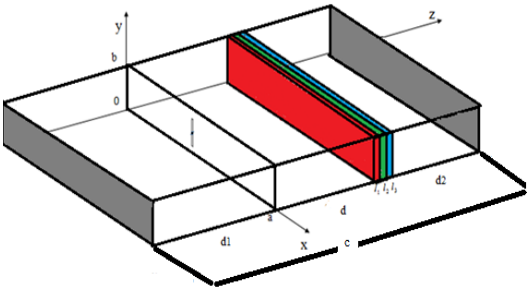

Fig. 2. Dipole antenna in presence of multilayered model inside a cavity.

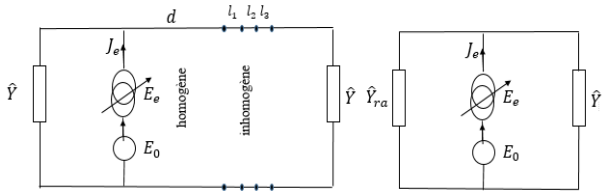

Fig. 3. Representation of dipole antenna in presence of dielectric model with finite thickness using an equivalent circuit.

A particular choice of the trial functions which describe the unknowen current density is defined on the metallic part of the dipole antenna:

$$g_p = \cos(\frac{(2p-1)}{l}\pi(y-\frac{b}{2}). \quad (1)$$

Let $f_{mn}(m\in\{0,1,2,...,M\}$ be the local modal basis corresponding the waveguide with electric walls [10]:

$$f_{mn}^{TE,TM} = \begin{cases} N_x^{TE,TM}\cos(\frac{m\pi x}{a})\sin(\frac{n\pi y}{b}) \\ N_y^{TE,TM}\sin(\frac{m\pi x}{a})\cos(\frac{n\pi y}{b}) \end{cases}. \quad (2)$$

Two sources, a virtual and a real one being involved in the formulation process. We trait the case where the virtual source is of current type and the real one is of electric field type.

The real source $E_0 = V_0 F_0$ represents the excitation term associated to feeding element. The function F_0 acts as the shape function, which ensures reliable expression for the voltage and current case of rectangular source $F_0 = \frac{1}{\delta}$.

J_e is the virtual source defined on the metallic domain of the discontinuity surface and it is the problem unknown.

It is expressed as a series of known test functions g_p weighted by unknown coefficients x_p:

$$J_e = \sum_{p=1}^{N_p} x_p g_p . \quad (3)$$

Then the equivalent circuit of the studied structure is completed by addition the terminating operator. The admittance operator $\hat{Y}^{cav}_{\{even\}\{odd\}}$ is given by:

$$\hat{Y}^{cav}_{\{even\}\{odd\}} = \sum_{\substack{m=0,n=0 \\ \alpha=TE,TM}}^{\infty} \left| f_{mn}^{cav} \right\rangle y_{mn}^{cav} \left\langle f_{mn}^{cav} \right|, \quad (4)$$

where

$$y_{mn}^{cav} = \frac{\gamma_{mn}^{cav}}{j\omega\mu_0}\coth(\gamma_{mn}^{cav}c),$$

and

$$(\gamma_{mn}^{cav})^2 = \left(\frac{m\pi}{a}\right)^2 + \left(\frac{n\pi}{b}\right)^2 - k_0^2).$$

We modulate the human head as a dielectric multilayered model. Every layer will be considered us a transmission line section with γ_{mn} is the propagation constant for the i^{th} transmission line section, l_i the length of each section.

The admittance operator for the reduced admittance $\hat{Y}_{ra}$ of the inhomogeneous line sections representing the head model is defined by:

$$\hat{Y}_{ra} = \sum \left| f_{mn} \right\rangle Y_{ra}^{\alpha} \left\langle f_{mn} \right|, \quad (5)$$

$$Y_{i+1}^{\alpha} = Y_{\varepsilon i}^{\alpha}\frac{Y_i^{\alpha} + Y_{\varepsilon i}^{\alpha}\coth(\gamma_i l_i)}{Y_{\varepsilon i}^{\alpha} + Y_i^{\alpha}\coth(\gamma_i l_i)}, \quad (6)$$

$$Y_{i=4}^{\alpha} = \begin{cases} Y_4^{TE} = \frac{\gamma_{mn}}{j\omega\mu_0} \\ Y_4^{TM} = \frac{j\omega\varepsilon_0\varepsilon_r}{\gamma_{mn}} \end{cases}, \quad (7)$$

$$Y_{\varepsilon i}^{\alpha} = \begin{cases} Y_{\varepsilon i}^{TE} = \frac{\gamma_{mn}}{j\omega\mu_0} \\ Y_{\varepsilon i}^{TM} = \frac{j\omega\varepsilon_0\varepsilon_{r(i)}}{\gamma_{mn}} \end{cases}. \quad (8)$$

In the dielectric domain, the generalized Ohm and Kirchhoff lows applied to the GEC depicted Fig. 3 lead to the equations system:

$$\begin{cases} J_e = J \\ E_e = (\hat{Y} + \hat{Y}_{ra})^{-1} J_e - E_0 \end{cases}. \quad (9)$$

The current J is expressed in modal basis functions $f_{mn}(m\in\{0,1,2,...,M\}$ weighted by unknown coefficients I_m:

$$J = \sum_{m=0}^{M} I_m f_m . \quad (10)$$

Therefore, the application of the Galerkin's method and Kirchhoff's theorem leads to obtain the simplified matrix representation as follows:

$$\begin{pmatrix} I_0 \\ 0 \end{pmatrix} = \begin{pmatrix} 0 & [A] \\ -[A]^t & [B] \end{pmatrix}\begin{pmatrix} V_0 \\ X \end{pmatrix}. \quad (11)$$

Thus, from equation (11), we obtain the equation system:

$$\begin{cases} I_0 = [A][X] \\ 0 = [X][B] - V_0[A]^t \end{cases}. \quad (12)$$

A formal relation between sources (real and virtual) and their dual is then deduced:

$$[A] = \begin{pmatrix} < F_0, g_1 > \\ < F_0, g_1 > \\ \vdots \\ < F_0, g_p > \end{pmatrix}, \quad (13)$$

$$[B]=\begin{bmatrix} \langle g_1,(\hat{Y}+\hat{Y}_{ra})^{-1}g_1\rangle & \langle g_1,(\hat{Y}+\hat{Y}_{ra})^{-1}g_2\rangle & \cdots & \langle g_1,(\hat{Y}+\hat{Y}_{ra})^{-1}g_{N_e}\rangle \\ \langle g_2,(\hat{Y}+\hat{Y}_{ra})^{-1}g_1\rangle & \langle g_2,(\hat{Y}+\hat{Y}_{ra})^{-1}g_2\rangle & \cdots & \langle g_2,(\hat{Y}+\hat{Y}_{ra})^{-1}g_{N_e}\rangle \\ \vdots & \vdots & & \vdots \\ \langle g_{N_e},(\hat{Y}+\hat{Y}_{ra})^{-1}g_1\rangle & \langle g_{N_e},(\hat{Y}+\hat{Y}_{ra})^{-1}g_2\rangle & \cdots & \langle g_{N_e},(\hat{Y}+\hat{Y}_{ra})^{-1}g_{N_e}\rangle \end{bmatrix}. \quad (14)$$

The resolution of the equation system (14) leads to calculate the structure input admittance:

$$Y_{in}=[A]^t[B]^{-1}[A]. \quad (15)$$

V. NUMERICAL RESULTS

The electromagnetic interaction was presented by two mutual effects, one is the induced specific absorption rate level inside the head tissues and the second on the handset performance.

In this section, we present a quantitative discussion about obtained numerical results, while the convergence study is firstly achieved. Figure 4 presents the input impedance variation as a function of the mode number for different used basis function number. In the next, we use a test functions number $N_e=10$ and $N_b=200\times200$ mode number to ensure the convergence.

Figure 5 illustrates the electric field and current density evaluated by the MOM-GEC at f=1.8 GHz. It shows that the boundary conditions are verified.

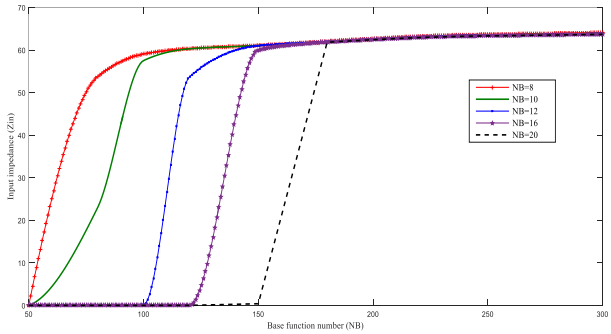

Fig. 4. Variation of the input impedance as a function of the guide modes number for different test functions number at f=1.8 GHz.

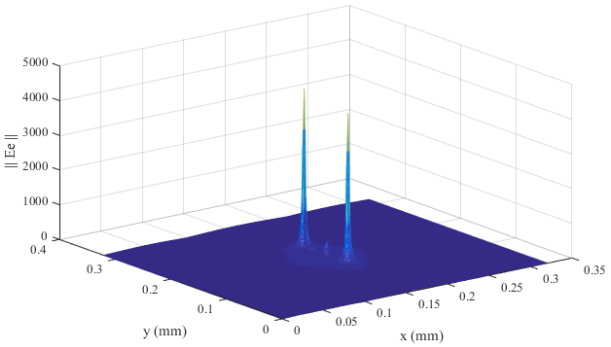

(a)

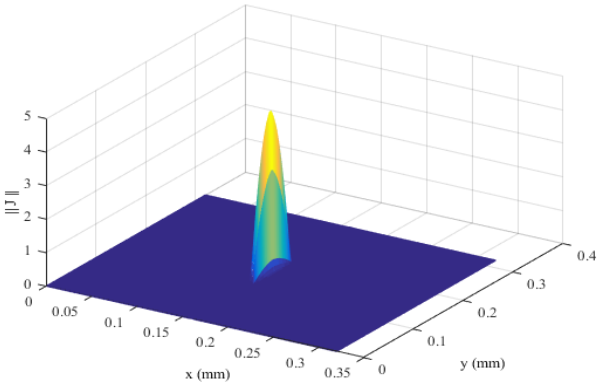

(b)

Fig. 5. (a) 2D representation of the diffracted electric field, and (b) 2D representation of the current density (A.m^{-1}).

A. Modification of the antenna performance

The S parameters has been calculated after convergence from the simulations. The return loss (S_{11}) of the antenna due to a single dipole antenna operated at GSM1, 8 GHz and in presence of the head model are presented in Fig. 6. It was found that the antenna is operating within this semi-enclosed environment with the multilayered head model loadings, the return loss of the antenna is affected, and there is a little shift in the resonant frequency and the shape of the curve in red is also affected by the presence of head model.

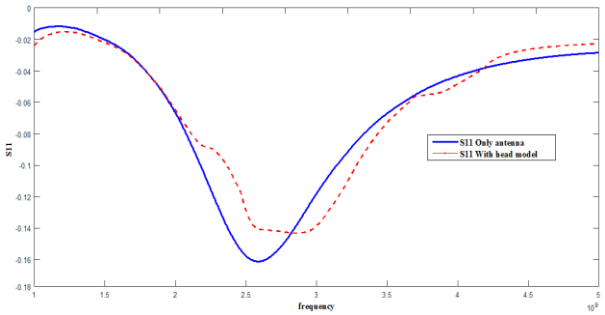

Fig. 6. Current distribution for a dipole antenna in the presence of a layered model inside an infinite waveguide and cavity.

Also, to explain the perturbation of the antenna performance in presence of the head, Fig. 7 shows the current density for a dipole antenna in the presence of a layered model inside a cavity. For a comparison purpose, the response of a single antenna is presented. We conclude that the level of the density of current increased inside a cavity.

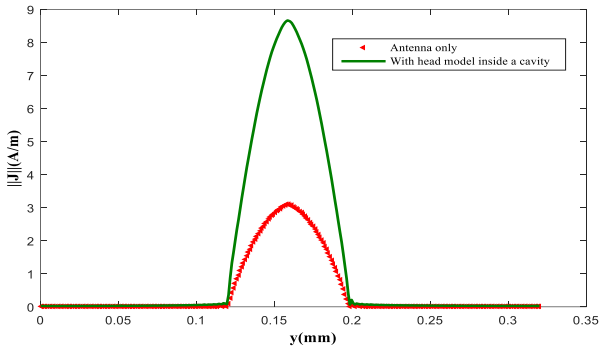

Fig. 7. Current distribution for a dipole antenna in the presence of a layered model.

B. SAR distribution inside several tissues

Inside a cavity (modelling a car), where multipath propagation, reflections and scattering must be accounted for, the SAR distribution undergoes large changes. However, the value of SAR is quite high compared to those in international limiting human exposure [20]. There is a large difference found between free-space and being inside a vehicle.

The SAR value decreases by penetrating into layers. The maximum SAR value is generated at the skin layer. Figure 8 represents the variation in model with four layers. The presence of the "fat" layer reduces the SAR value which increases again in layers of "skull" and "brain", this is due to the low conductivity of the tissue ($\sigma_{Fat} = 0{,}45 S/m$). We can also say that "fat" layer acts as a barrier against penetration of waves.

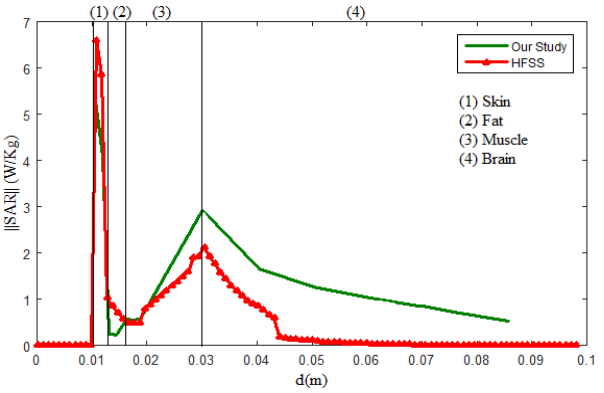

Fig. 8. Specific absorption rate SAR variation inside a four-layered model.

The validation of the SAR calculation was performed by comparison with Simulation using the Ansoft HFSS simulator. Because we are most interested in assessing changes in the SAR distribution rather than in obtaining a figure comparable with the standards.

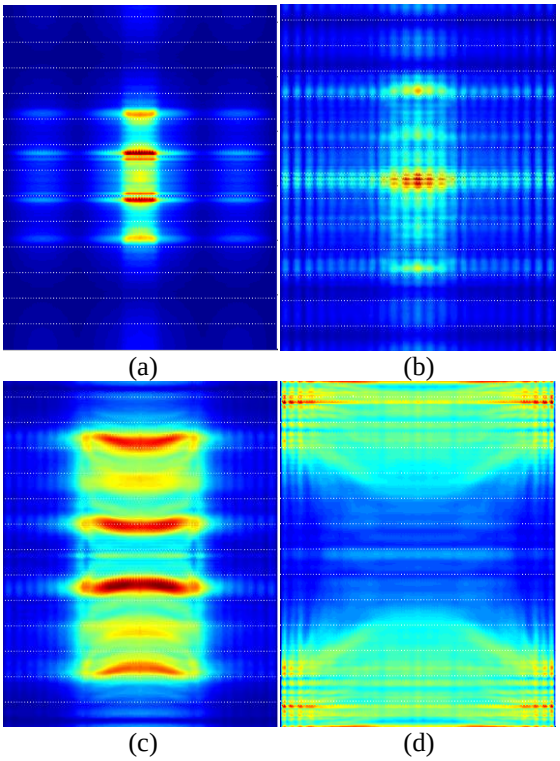

Fig. 9. Specific absorption rate SAR distribution in a four-layered model: (a) skin, (b) fat, (c) skull, and (d) brain inside a car.

The skin (the peripheral layer which is very thin) has a relatively high dielectric permittivity and concentrates the absorbed power (SAR) at the surface of the head. This peripheral layer presents screening effect for the electric component of the incident field. Fat and skull with its lower permittivity act like a barrier for the power penetration.

However, SAR distribution is highly focused in the area proximal to the antenna, and decreases rapidly inside the body, as the penetration depth and SAR distribution shown in Fig. 9 for a four-layered head model inside a cavity.

Table 2: SAR value inside a cavity (four layered head model)

	SAR (W/Kg)
ANSI limit	1,6
Free space	2
Cavity (MOM-GEC)	5.2
Cavity (HFSS)	6.57

As shown in Table 2, exposition inside a partially closed environment will certainly increase the induced SAR in head model. The numerical computations showed a 54% increase of the SAR induced in the tissues while

exposed to a dipole antenna inside a cavity, as compared with the obtained in free space. In other words, the exposition inside a car is more hazardous than in free space and the SAR induced in the tissues may cross the ANSI standard limit.

Most of the coupling is in the near field and the most relevant parameters are the distance from the dipole to the head. Table 3 shows that the SAR level decreases with increasing distance from the excitation source. The SAR level is more intense when in an electrical environment.

Table 3: SAR value for different distance inside a cavity

Distance (cm)	SAR (W/Kg)
0,5	8,89
1	5.2
2	3,64
3	1.2

VI. CONCLUSION

The introduction of a realistic partially closed environment would have produced a set of results difficult to interpret. We have taken some decisions about models, complexity results presented, etc. that certainly have some impact on the interpretation of the results.

Instead, for the sake of simplicity we have used a dipole antenna some differences in SAR disposition will arise from that fact. More research and a better understanding of the behavior of actual phones is needed to address this point.

Our results are of comparative nature and are valuable as indicators of the changes expected between the free space widely studied situation and other more realistic exposure conditions, but cannot be directly used for compliance assessment.

The results obtained can also be used to gain knowledge about the influence of user head over the specific absorption rate distribution inside a car, which is of great interest on other research areas, such as electromagnetic compatibility, since the use of electromagnetic sources inside a vehicle is an interesting situation.

We show the feasibility of investigating and obtaining results for the specific absorption rate (SAR) within a complex and large structure (compared to the wavelength) such as a user car. A formulation with the combination between MoM method and GEC method is developed and results compared with those obtained in other works and simulations.

The proposed method can be efficiently used for investigating the effect of the variation of distance on the power absorption by the head as well as the antenna performance. The penetration depth and the specific absorption rate are also computed.

REFERENCES

[1] J. Wang and O. Fujiwara, "Comparison and evaluation of electromagnetic absorption characteristics in realistic human head models of adult and children for 900-MHz mobile telephones," *IEEE Transactions on Microwave Theory and Techniques*, pp. 966-971, 2003.

[2] W. Kainz, A. Christ, T. Kellom, S. Seidman, N. Nikoloski, B. Beard, and N. Custer, "Dosimetric comparison of the specific anthropomorphic mannequin (SAM) to 14 anatomical head models using a novel definition for the mobile phone positioning," *Phys. Med. Biol.*, vol. 50, pp. 3423-3445, July 2005.

[3] G. Lazzi and O. P. Gandhi, "On modeling and personal dosimetry of cellular telephone helical antennas with the FDTD code," *IEEE Trans. Antennas Propagat*., vol. 46, pp. 525-530, Apr. 1998.

[4] G. Lazzi, Q. S. Yu, and O. P. Gandi, "Extension and validation of the equivalent sources helical antenna modeling with the FDTD code," in *Proc. IEEE Antennas and Propagation Society Int. Symp*., vol. 2, pp. 1054-1057, July 1999.

[5] T. S. C. Hagness, *Computational Electrodynamics: The Finite-Difference Time-Domain Method*. 2nd ed., Norwood, MA: Artech House, 2000.

[6] A. R. Bretones, R. Mittra, and G. Martin, "Hybrid technique combining the MoM in the time domain and FDTD," *IEEE Microwave Guided Wave Lett*., vol. 8, pp. 281-283, Aug. 1998.

[7] G. Cerri, P. Russo, et al., "MoM-FDTD hybrid technique for analyzing scattering problems," *Electron. Lett*., vol. 34, pp. 433-440, 1998.

[8] E. A. Forgy, W. C. Chew, and J. M. Jin, "A hybrid MoM/FDTD technique for studying human head/ antenna interactions," *IEEE-APS Conference on Antennas and Propagation for Wireless Communications*, pp. 81-84, 1998.

[9] U. Pekel, R. Mittra, E. Ngai, T. Wells, and A. Cohen, "A hybrid FEM/MoM approach for analyzing inhomogeneous structures with fine features," *Antennas and Propagation Society International Symposium*, 1995.

[10] U. Jakobus, F. J. C. Meyer, M. Bingle, and D. B. Davidson, "Combination of MoM and FEM for the solution of bioelectromagnetic problems," *International ITG-Conference on Antennas*, Berlin, Germany, pp. 241-244, Sep. 2003.

[11] G. Anzaldi, F. Silva, M. Fernandez, M. Quilez, and P. Riu, "Initial analysis of SAR from a cell phone inside a vehicle by numerical computation," *IEEE Transactions on Biomedical Engineering*, vol. 54, no. 5, pp. 921-930, 2007.

[12] Y. Diao, W. Sun, K. Hung Chan, S. Leung, and Y.

Siu Y, "SAR evaluation for multiple wireless communication devices inside a vehicle," *URSI International Symposium on Electromagnetic Theory (EMTS)*, p. 626, 2013.

[13] S. Al-Mously and M. Abousetta, "Anticipated Impact of hand-hold position on the electromagnetic interaction of different antenna types/ positions and a human in cellular communications," *International Journal of Antennas and Propagation (IJAP)*, 22 pages, 2008.

[14] H. Baudrand, "Representation by equivalent circuit of the integral methods in microwave passive elements," *European Microwave Conference*, Budapest, Hungary, vol. 2, pp. 1359-1364, Sep. 10-13, 1990.

[15] H. Baudrand and D. Bajon, "Equivalent circuit representation for integral formulations of electromagnetic problems," *International Journal of Numerical Modelling-Electronic Networks Devices and Fields*, vol. 15, pp. 23-57, Jan. 2002.

[16] T. Aguili, "Modélisation des Composantes SFH Planaires par la Methode des Circuits Equivalents Généralisées," *Thesis Manuscript, National Engineering School of Tunis*, Tunisia, 2000.

[17] N. Raveu and O. Pigaglio, *Résolution de Problèmes Hautes Fréquences par les Schémas Équivalents*. Editions Cépaduès, May 2012.

[18] H. Baudrand, *Circuits Passifs en Hyperfréquences*. Editions Cépaduès, Jan. 2001.

[19] S. Mili, "Approach of Multi Scale Generalized Equivalent Circuits Combined to the Renormalization Group Theory for Electromagnetic Modeling of Passive and Active Fractal Structures," *Ph.D. Thesis, Tunis: National Engineering School of Tunis ENIT*, 2011.

[20] ICNIRP, "Guidelines for limiting exposure to time-varying electric, magnetic and electromagnetic fields (up to 300 GHz)," *Health Phys*., vol. 74, no. 4, pp. 494-522, 1998.

Hafawa Messaoudi received the Master degree in Electronics from the Faculty of Science Bizerte. In 2017, she received the Ph.D. degree in Telecommunications at the National Engineering School of Tunis. Her research interest is in the electromagnetic modeling of the interaction phenomena of electromagnetic waves especially GSM.

Taoufik Aguiliis currently a Professor in the National Engineering School of Tunis (ENIT), Tunis El Manar University. He is also the Director of Communications Systems Laboratory (Syscom) and he is responsible of the Research and the Master Degree in the Communications and Information's Technology Department. His research interests include modeling of microwave systems and nano-devices, numerical methods in electromagnetic wave phenomena in layered media, integrated transmission lines, waveguides and antennas, and leaky wave phenomena.

Design and Measurements of Rectangular Dielectric Resonator Antenna Linear Arrays

Feras Z. Abushakra [1], Asem S. Al-Zoubi [1], and Derar F. Hawatmeh [2]

[1] Department of Telecommunications Engineering
Yarmouk University, Irbid, Jordan
feras_abushakrah@yahoo.com, asem@yu.edu.jo

[2] Department of Electrical Engineering
University of South Florida, Tampa, FL, USA
dfh_ee@hotmail.com

Abstract ─ In this paper, two, four, eight and sixteen-element Rectangular Dielectric Resonator Antenna (RDRA) linear arrays fed by microstrip line have been designed and simulated. The DRA is excited by a vertical strip placed on the middle of the DRA wide side wall through a coaxial probe attached to the microstrip line on the other side of the substrate. The ground plane is sitting directly underneath the RDRA while the microstrip line feeder is at the opposite side of the substrate to avoid the unwanted radiation from the feeder. The simulated and measured 10 dB return loss bandwidth of the antenna arrays are 67.8%, 75%, 73.5%, and 76% for the two, four, eight and sixteen-element arrays respectively. The simulated gain of the single element antenna is about 6 dBi, while it reaches to about 17 dBi for the 16-element array.

Index Terms ─ Avoidance of spurious radiation dielectric resonator antennas, linear array, low cross polarization level, low side lobe level.

I. INTRODUCTION

Dielectric resonator antenna (DRA) is fabricated from a high-relative permittivity (from about 6 to 100) low loss dielectric material [1]. The dielectric resonator antennas DRAs have several advantages which make them a good choice for the new wireless communication systems, especially if small size antenna is required. There are some features of the DRA that give it an advantage compared to the microstrip antennas such as wider impedance bandwidth, high gain, avoidance of surface waves and high radiation efficiency [2]. In new wireless communication systems the high gain and wide bandwidth are essential demands. Sometimes, it is difficult to obtain the desired gain value for certain application when single element is used. Arrays with different number of elements could be used to achieve the wanted radiation parameter for the new communication systems. The most common type of arrays is the linear array. The linear array is set with different number of elements with fixed spacing between them. The elements are positioned in a straight line along one of the axes [3]. It has several properties that make it a good choice for many applications, such as, narrow main beam. The main beam becomes narrower as the number of elements in the array increases [4]. Recently, many researches focused on the design of DRA arrays. This is because they could offer high gain value which is hard to achieve when using other types of antennas. In [5], a dual segment two-element cylindrical DRA array was designed. This array covered a frequency band of (3.85-6.2) GHz and the gain varied between (4-6) dBi. In [6], two-element RDRA linear array was designed. The proposed array covered the frequency band from (3.15-3.83) GHz, with gain value of 6.4 dBi. In [7], a linear array of RDRA with dielectric image guide (DIG) feeder was designed. By adding a narrow metal strip around the DRA, the cross polarization level decreased by 20 dB. In [8], a back reflector was used with a linear array with (DIG) feeder; a reflecting PEC was inserted above the (DIG) to decrease the back lobe radiation. Four-element RDRA with high relative permittivity of (ϵ_r=35.9) was designed in [9]. The RDRA has dimensions of (18×18×8.9) mm. The elements were fed by aperture of window shape, the designed array covered frequency band from (1.5-3.2) GHz, the gain reached to 14 dBi. However, the distance between the adjacent elements was (66.6) mm. In [10], a linear DRA polarized array fed by radial line waveguide was designed. This array had 180 elements with 223 mm diameter. The gain reached 26.7 dBi. In [11], a series DRA array was designed. The array was fed by substrate integrated waveguide (SIW). The 4×1 array achieved 11.7 dBi gain, with 4.7% impedance bandwidth. In [12], eight-element RDRA series fed array reached more than 14 dBi gain value. A slot windows and reflector were used to improve the performance for this array. In this

Submitted On: July 20, 2017
Accepted On: April 21, 2018

paper up to sixteen elements RDRA linear arrays will be designed, simulated and measured. A microstrip line feeder with multi-section will be used to feed the RDRA's and to enhance the bandwidth [13]. The feeder will be at the bottom side of the substrate while the ground plane is at the top side of the substrate. A coaxial probe is attached between the microstrip line and a center strip mounted on the side of the DRA. By using this feeding method the spurious radiation from the feeder will be isolated.

II. SINGLE ELEMENT RDRA

Several methods for the mathematical calculation of the resonant frequency of the RDRA have been reported. These methods include the dielectric waveguide model (DWM) [14] and applying the perturbation theory to the (DWM) to determine the accurate resonant frequency of the RDRA [15]. However, the focus in this paper will be on the design of the arrays with wide band by simulation and measurement. Figure 1 presents the single element RDRA geometry. The RDRA material is Rogers RO 3010 with relative permittivity of (ϵ_r=10.2) and dielectric loss tangent of (tanδ=0.0035). The dimensions of the RDRA are (a×b×d) which corresponds to (15.7×14.3×11) mm, respectively. The substrate is Rogers RO 4350 with relative permittivity of (ϵ_r=3.66) and dielectric loss tangent of (tanδ=0.004), the dimensions of the substrate are (50×40×1.524) mm. The materials of the RDRA and substrate for the single RDRA element will be used in all designs in this paper.

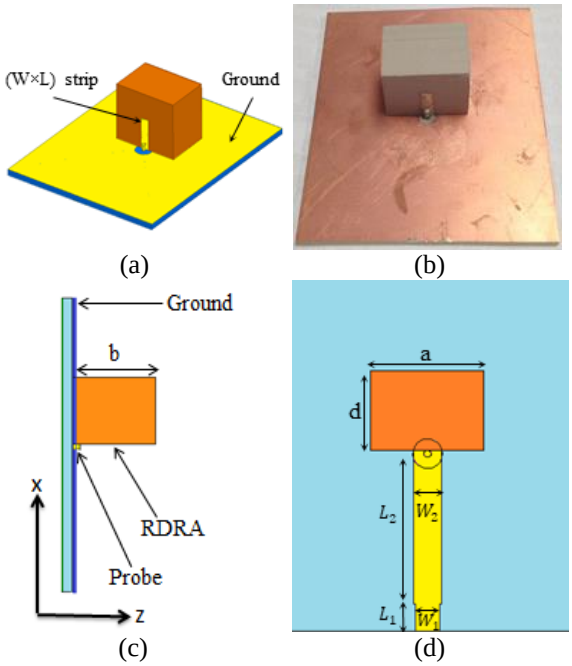

Fig. 1. Geometry of the single RDRA: (a) 3D view, (b) fabrication, (c) side view, and (d) top view.

In the single element RDRA design the ground plane is at the top side of the substrate. The microstrip line feeder is at the bottom side of the substrate as shown in Fig. 1. By sitting the RDRA directly on the ground plane the spurious radiation from the feeder will be isolated and the cross polarization level will be reduced [16-18]. A probe is attached to microstrip line and pass through a circular aperture that is created in the ground plane with 2.05 mm radius. The probe then is attached to a rectangular strip mounted on the DRA side surface with (W×L) dimensions. The dimensions of single element RDRA are mentioned in Table 1.

Table 1: Dimensions of the single RDRA in (mm)

Parameter	Value	Parameter	Value
L	7.76	W	2
L_1	3.72	W_1	3.36
L_2	21.27	W_2	3.84

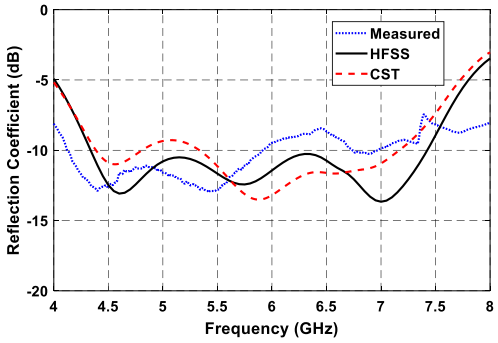

Fig. 2. The reflection coefficient for the single RDRA.

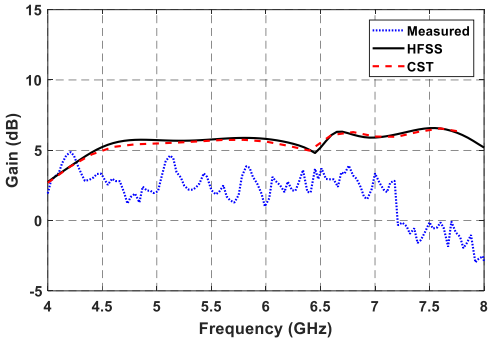

Fig. 3. The peak gain for the single RDRA.

The simulation results of both software, HFSS [19] and CST MWS [20], are in good agreement. The HFSS works based on the finite element method (FEM) while the CST uses the finite integration technique (FIT) which is relevant to finite domain time difference (FDTD) [21]. The -10 dB reflection coefficient for the single RDRA is achieved in a frequency band of 4.3-7.4 GHz (53%), as shown in Fig. 2. The simulated peak realized gain for the

single RDRA is between (5-6.5) dBi, as shown in Fig. 3. The difference between the measured and the simulated results is due to the fabrication tolerances, gluing in the RDRA's since we used four layers of substrate materials to fabricate each RDRA, surface roughness of the ground plane and the effect of the connector. However, the results still close to each other.

III. MUTUAL COUPLING

Mutual coupling is described as the amount of energy that absorbed by the neighbor element. It is an important parameter when array design is considered. The higher mutual coupling level will decrease the gain of the array and decrease the radiation efficiency for the main beam [22]. The distance between center to center of two elements should be theoretically between λ/2 and λ. The chosen distance will be within the theoretical range. However, the exact value for the distance which is 23.8 mm is chosen based on a parametric study to reach the best matching and radiation pattern for the designs. This distance represent 0.76 λ at *f*=5 GHz. In Fig. 4, two elements RDRA are placed beside each other to determine the mutual coupling between them.

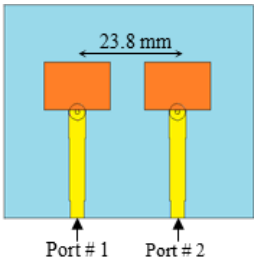

Fig. 4. Geometry of two single RDRA.

The parameter $|S_{21}|$, which represents the mutual coupling between the two RDRA is plotted in Fig. 5, which indicates that the mutual coupling is less than -13 dB in the operating band which considered low value for the mutual coupling.

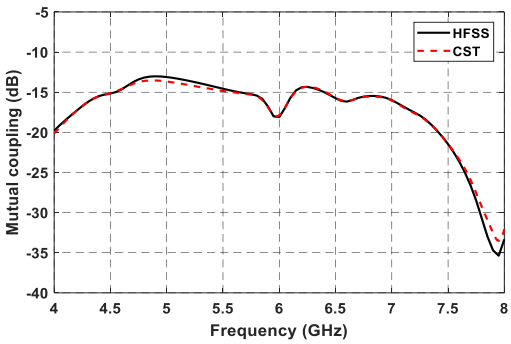

Fig. 5. The simulated mutual coupling.

IV. TWO-ELEMENT RDRA

Two-element RDRA linear array is designed and simulated. Figure 6 shows the geometry of the two-element linear array. Same feeding method and materials for the single RDRA is used here. The feeder is at the bottom side of the substrate. The dimensions of the two-element linear array are shown in Fig. 6 (b) and mentioned in Table 2. The same RDRA dimensions and slot aperture radius in the single element will be used here. The rectangular strip dimensions are adjusted to (3×7.5) mm. These dimensions will be used in all arrays in this paper.

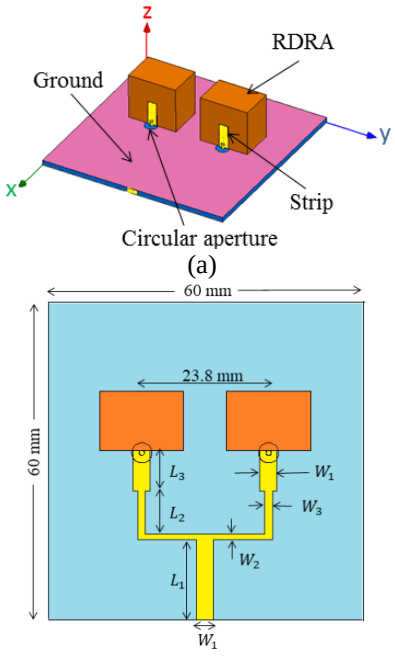

Fig. 6. (a) Geometry of two-element RDRA linear array, and (b) two-element DRA feeder.

Table 2: Dimensions of the two-element RDRA linear array in (mm)

Parameter	Value	Parameter	Value
L_1	15	W_1	3.2
L_2	8	W_2	1.2
L_3	7.7	W_3	1.4

Figure 7 shows the simulated reflection coefficient for the two-element RDRA linear array. The -10 dB reflection coefficient is achieved in the frequency range 3.9-7.9 GHz (67.8%). The simulated peak realized gain for the two-element RDRA linear array varying between (6.5-10) dBi, as shown in Fig. 8. The gain increases at the end of the band, which is expected since the distance between the elements exceeds λ.

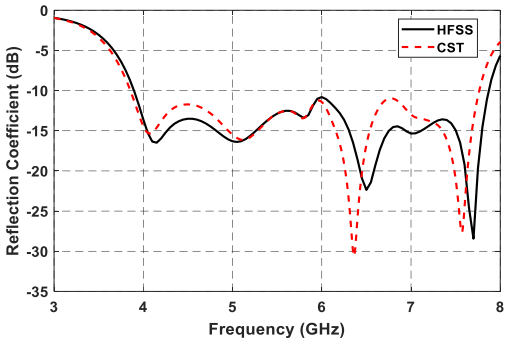

Fig. 7. The simulated reflection coefficient for the two-element linear array.

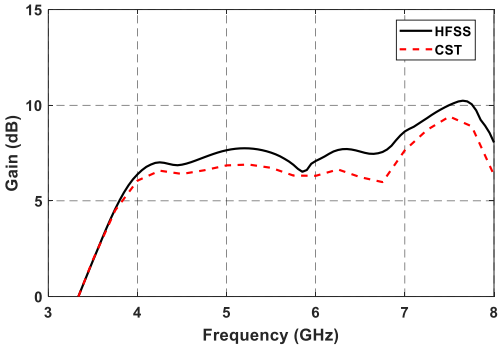

Fig. 8. The simulated peak gain for the two-element linear array.

V. FOUR-ELEMENT RDRA

The Geometry for the four-element RDRA linear array is shown in Fig. 9. The dimensions are mentioned in Table 3. It could be seen that the array substrate has dimensions of (70×100) mm only, which is considered small array size for this number of elements. The dimensions which were mentioned in the two-element array are used here. So, it will not be repeated. Also, same direction for the feeder as in Fig. 6 (a) will be used here.

The simulated reflection coefficient for the four-element RDRA linear array is shown in Fig. 10. The operating frequency is from 3.57-7.85 GHz (75%). The simulated peak gain has a stable value between (8-10) dBi within the operating band and reaches 12 dBi at *f*=7.7 GHz as shown in Fig. 11. A good agreement between both software is achieved in the simulated results.

Table 3: Dimensions of the four-element RDRA linear array in (mm)

Parameter	Value	Parameter	Value
L_4	14	W_1	3.2
L_5	46.4	W_4	1
L_6	4.5	W_5	1.2

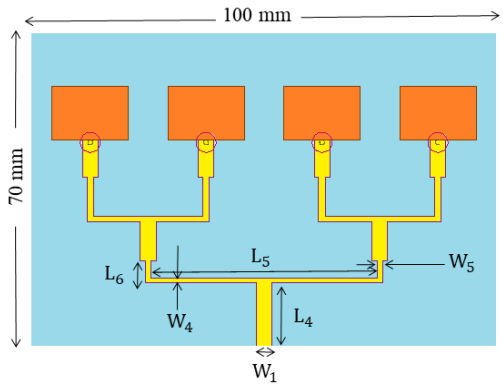

Fig. 9. Geometry of four-element RDRA linear array.

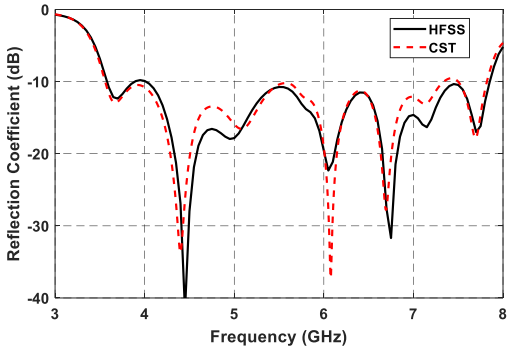

Fig. 10. The simulated reflection coefficient for the four-element linear array.

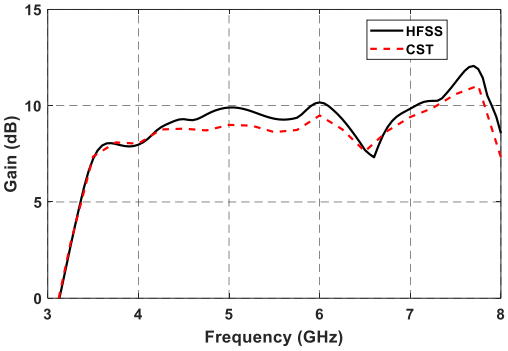

Fig. 11. The simulated peak gain for the four-element linear array.

VI. EIGHT-ELEMENT RDRA

The eight-element linear array is designed, simulated and fabricated, as shown in Fig. 12. In Fig. 12 (a) the fabricated array from the top view is presented. As mentioned in the previous arrays, the DRAs are sitting directly on the ground plane. The feeder is at the back side as shown in Fig. 12 (b). The dimensions for this array are plotted in Fig. 12 (c) and mentioned at Table 4 in (mm).

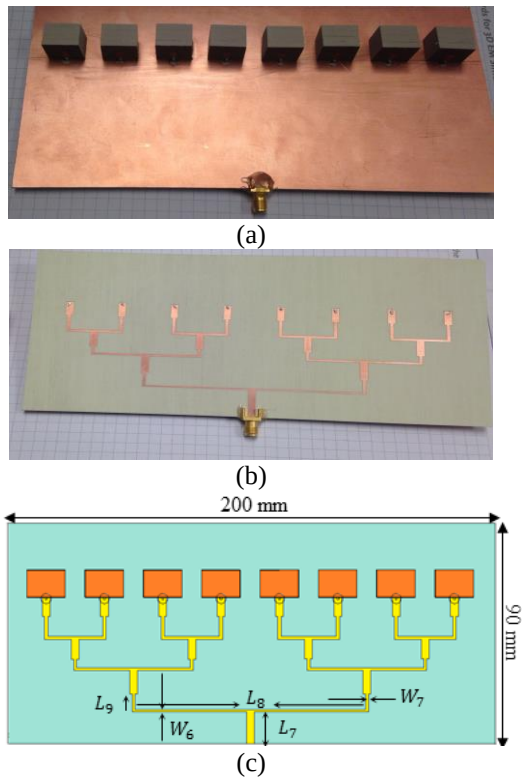

Fig. 12. Eight-element array: (a) fabricated 3D view, (b) fabricated bottom view, and (c) feeder dimensions.

Table 4: Dimensions of the eight-element RDRA linear array in (mm)

Parameter	Value	Parameter	Value
L_7	14.5	W_6	0.8
L_8	93.95	W_7	1.25
L_9	7.2	----	----

The measured and simulated reflection coefficients for the eight-element RDRA linear array are plotted in Fig. 13. A good agreement between HFSS, CST MWS and the measured results could be noticed in this figure. The -10 dB reflection coefficient is achieved in the frequency range (3.7-8) GHz, which is equivalent to 73.5% impedance bandwidth for the simulated results while the measured result shows a little difference compared to the simulated results only at the beginning of the band. However, the results still close to each other.

Figure 14 shows the measured and simulated peak realized gain. The gain has stable value which is above 12 dBi through most of the band according to both HFSS and CST MWS, while it reaches 14 dBi at the end of the band. A good agreement is noticed between simulated and measured gain values for this array, except at the end of the band where the difference between the simulated and measured results is noticed, which is due to the previously mentioned reasons in Section II in the fabrication process of the RDRA.

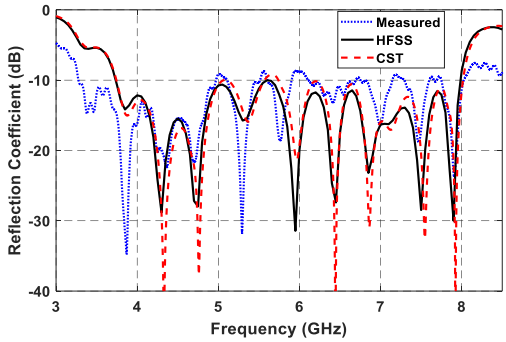

Fig. 13. The reflection coefficient for the eight-element linear array.

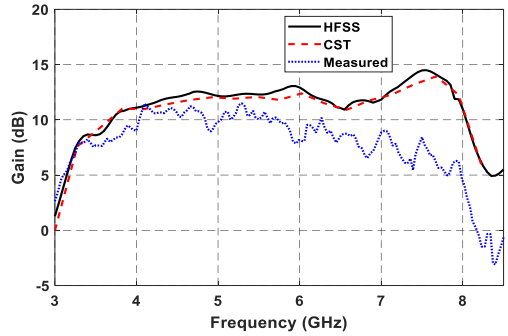

Fig. 14. The peak gain for the eight-element linear array.

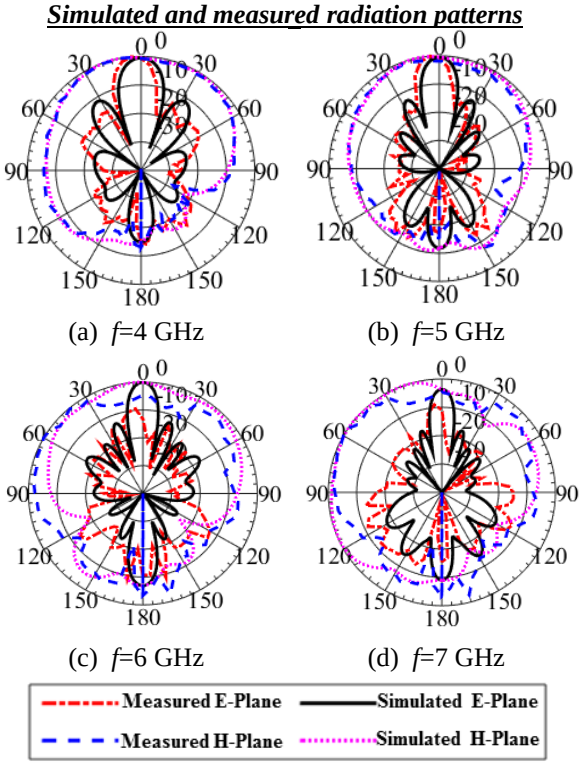

Fig. 15. The normalized radiation patterns of the eight-element linear array at different frequencies.

The measured and simulated radiation patterns are plotted in Fig. 15. The co-polarized E-Plane and H-Plane are plotted. The radiation patterns show a 10-dB front to back ratio through the band. The side lobe level (SLL) is around (-15) dB in the band. The simulated and measured cross polarization level was found less than -10 dB within the band. The simulated results for the radiation pattern will be presented using one software only which is HFSS, since both software give the same results and this would be easier to read.

VII. SIXTEEN-ELEMENT RDRA

Finally, sixteen-element RDRA linear array is simulated. The substrate size for this design is (390×110) mm, as shown in Fig. 16. The dimensions are mentioned in Table 5.

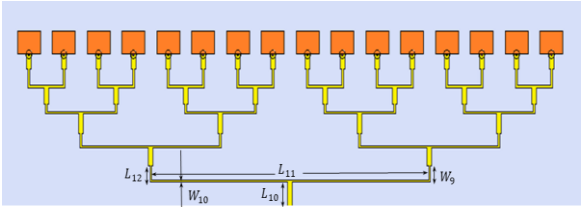

Fig. 16. Geometry of the sixteen-element linear array.

Table 5: Dimensions of the sixteen-element RDRA linear array in (mm)

Parameter	Value	Parameter	Value
L_{10}	12.9	W_8	0.62
L_{11}	189.3	W_9	1
L_{12}	6.4	-----	-----

The operating frequency range is from (3.57-7.95) GHz, as shown in Fig. 17, which is about 76% impedance bandwidth. The simulated peak realized gain for the sixteen-element linar array is stable between 14-17 dBi as shown in Fig. 18. It could be seen that the theoretical 3 dBi gain increment when doubling the elements number in the linear arrays didn't achieved, since the presences of the losses in the substrate, feeder and the RDRA itself [23].

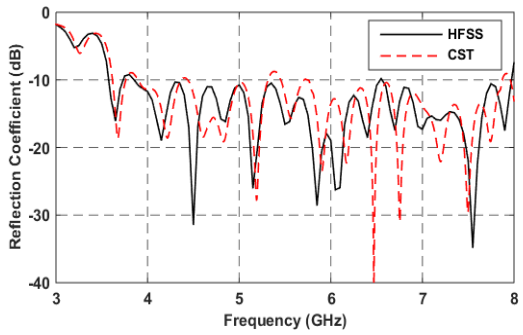

Fig. 17. The simulated reflection coefficient for the sixteen-element linear array.

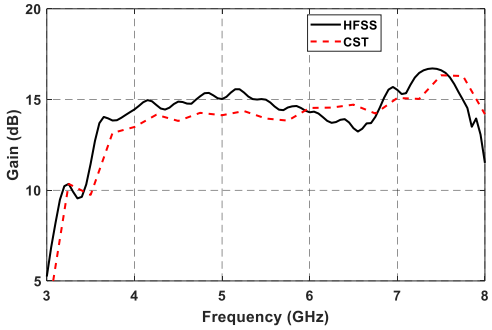

Fig. 18. The simulated peak gain for the sixteen-element linear array.

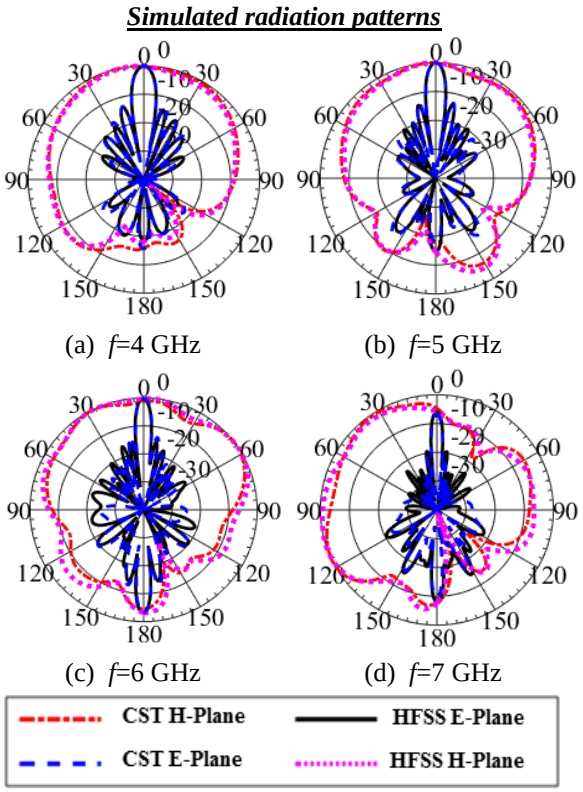

Fig. 19. The simulated normalized radiation patterns of the sixteen-element linear array at different frequencies.

The simulated radiation patterns for the sixteen-element RDRA linear array are plotted in Fig. 19. The co-polarized E-plane and H-plane are plotted using both HFSS and CST MWS. It could be seen that both software give almost the same results. The radiation patterns show a 10-dB front to back ratio through most of the band. The side lobe level (SLL) is between (-12 to -15) dB in the band. It could be seen from the radiation patterns that the beam width decreased as the frequency increased within the band at both the eight-element and sixteen-element array which is due to distance increase in wavelength [24]. The HPBW is varied between 10° at f=4 GHz while

reached 6° at *f*=7 GHz. The simulated cross polarization level was found less than -10 dB within the band according to both softwares. Table 6 shows the summery for the RDRA linear array designs for different elements number in this paper.

Table 6: Summary for the RDRA linear arrays

No. of Elements	Frequency Range (GHz)	BW %	Gain (dBi)	Antenna Size (mm)
1	4.3-7.4	53	5-6.5	40×50
2	3.9-7.9	67.8	8-10	60×60
4	3.57-7.85	75	10-12	70×100
8	3.7-8	73.5	12-14	90×200
16	3.57-7.95	76	14-17	110×390

Table 7 shows the HPBW value for both eight-element and sixteen-element RDRA linear array at different frequencies, while Table 8 shows some recent papers results obtained for the dielectric resonator antenna linear array with different element numbers.

Table 7: HPBW (E-plane) for the RDRA linear arrays

No. of Elements	*f*=4 GHz	*f*=5 GHz	*f*=6 GHz	*f*=7 GHz
2	68.9°	64.6°	46.8°	46.3°
4	42.2°	31.2°	24.2°	23.8°
8	18.8°	15.6°	12.7°	11.9°
16	9.7°	8°	6.5°	6°

Table 8: Recent papers results for linear array

No. of Elements	Ref #	Frequency Range (GHz)	Gain (dBi)	Antenna Size (mm)
2	5	3.85-6.2	4-6	74 × 52.7
4	9	1.5-3.2	10-12	66.6 mm (between elements)
8	12	6.57-9.08	15.7	250 × 41.4
15	7	8-12.5	10-12	23.5 mm (between elements)

VIII. CONCLUSIONS

Rectangular dielectric resonator antenna (RDRA) linear arrays were designed, simulated and fabricated in this paper. The arrays with different element numbers, from two up to sixteen-element, were introduced. In order to isolate the spurious radiation from the feeder, the ground plane was placed on the top side of the substrate and directly underneath the RDRAs. Multi section feeder was used to enhance the bandwidth which was varies from 67% to 76%. A peak gain between 8 to 17 dBi were achieved for the different number of elements. Also, low side lobe level (SLL) were obtained in these designs, which was between (-10 to -18) dB for most of the arrays. Narrower beamwidth was obtained with 6° HPBW for the sixteen-element linear array. Good agreement between HFSS and CST MWS simulated results and the measured results. The overall size for all designs is relatively small compare to other designs with the same element number.

REFERENCES

[1] D. Soren, R. Ghatak, R. K. Mishra, and D. R. Poddar, "Dielectric resonator antennas designs and advances," *Electromagnetics Research*, vol. 60, pp. 195-213, 2014.

[2] R. S. Yaduvanshi and H. Parthasarathy, *Rectangular Dielectric Resonator Antennas*. Springer India, 2016.

[3] W. H. Kummer, "Basic array theory," *Proceeding of the IEEE*, vol. 80, no. 1, pp. 127-140, 1992.

[4] C. A. Balanis, *Antenna Theory Analysis and Design*. John Wiley & Sons, 2005.

[5] G. Das, A. Sharma, and R. K. Gangwar, "Two elements dual segment cylindrical dielectric resonator antenna array with annular shaped microstrip feed," *2016 Twenty Second National Conference on Communication (NCC)*, pp. 1-6, 2016.

[6] A. Gupta and R. K. Gangwar, "Design, fabrication, and measurement of dual-segment rectangular dielectric resonator antenna array excited with conformal strip for S-band application," *Electromagnetics*, vol. 36, no. 4, pp. 236-248, 2016.

[7] A. S. Al-Zoubi, A. A. Kishk, and A. W. Glisson, "A linear rectangular dielectric resonator antenna array fed by dielectric image guide with low cross polarization," *IEEE Transactions on Antenna and Propagation*, vol. 58, pp. 697-705, 2010.

[8] A. S. Al-Zoubi, A. A. Kishk, and A. W. Glisson, "Aperture coupled rectangular dielectric resonator antenna array fed by dielectric image guide," *IEEE Transactions on Antennas and Propagation*, vol. 57, no. 8, pp. 2252-2259, 2009.

[9] M. R. Nikkhah, A. A. Kishk, and J. Rashed-Mohassel, "Wideband DRA array placed on array of slot windows," *IEEE Transactions on Antenna and Propagation*, vol. 63, pp. 5382-5390, 2015.

[10] M. Su, L. Yuan, and Y. Liu, "A linearly polarized radial line dielectric resonator antenna array," *IEEE Antennas and Wireless Propagation Letters*, vol. PP, no. 99, pp. 1-1, 2016.

[11] W. M. Abdel-Wahab, D. Busuioc, and S. Safavi-Naeini, "Millimeter-wave high radiation efficiency planar waveguide series-fed dielectric resonator antenna (DRA) array: Analysis, design, and measurements," *IEEE Transactions on Antennas and Propagation*, vol. 59, no. 8, pp. 2834-2843, 2011.

[12] J. Lin, W. Shen, and K. Yang, "A low sidelobe and wideband series fed linear dielectric resonator antenna array," *IEEE Antennas and Wireless Propagation Letters*, vol. PP, no. 99, pp. 1-1, Doi: 10.1109/LAWP.2016.2586579, 2016.

[13] R. Khare and R. Nema, "Review of impedance

matching networks for bandwidth enhancement," *International Journal of Emerging Technology and Advanced Engineering*, vol. 2, iss. 1, pp. 92-96, 2012.

[14] R. K. Mongia, "Theoretical and experimental resonant frequencies of rectangular dielectric resonators," *IEE Proc.-H*, vol. 139, pp. 98-104, 1992.

[15] S. Fakhte and H. Oraizi, "Derivation of the resonant frequency of rectangular dielectric resonator antenna by the perturbation theory," *ACES Journal*, vol. 31, no. 8, 2016.

[16] A. S. Al-Zoubi, "Enhanced radiation patterns of a wide-band strip-fed dielectric resonator antenna," *Jordanian Journal of Computers and Information Technology*, Dec. 2015.

[17] A. Al-Zoubi and A. Kishk, "Wide band strip-fed rectangular dielectric resonator antenna," *3rd European Conference on Antennas and Propagation*, Berlin, Germany, 23-27 Mar. 2009.

[18] F. Abushakrah and A. Al-Zoubi, "Wideband vertical T-shaped dielectric resonator antennas fed by coaxial probe," *Jordan Journal of Electrical Engineering (JJEE)*, vol. 3, no. 4, pp. 250-258, 2017.

[19] HFSS: High Frequency Structure Simulator Based on the Finite Element Method, version 11.1, ANSYS Corporation 2008.

[20] CST STUDIO SUITE-3D EM Simulation Software by CST, version 11.0.

[21] A. Vasylchenko, Y. Schols, W. Raedt, and G. Vandenbosch, "Quality assessment of computational techniques and software tools for planar antenna analysis," *IEEE Antennas Propagations Magazine*, vol. 51, no. 1, pp. 23-38, 2009.

[22] I. Gupta and A. Ksienski, "Effect of mutual coupling on the performance of adaptive arrays," in *IEEE Transactions on Antennas and Propagation*, vol. 31, no. 5, pp. 785-791, 1983.

[23] J. R. Baker-Jarvis, M. D. Janezic, B. F. Riddle, C. L. Holloway, N. G. Paulter, Jr., J. Blendell, *Dielectric and Conductor-Loss Characterization and Measurements on Electronic Packaging Materials*, National Institute of Standards and Technology, July 2001.

[24] S. F. Maharimi, M. F. Abdul Malek, M. F. Jamlos, S. C. Neoh, and M. Jusoh, "Impact of spacing and number of elements on array factor," *PIERS Proceedings*, Kuala Lumpur, Malaysia, 2012.

Feras Z. Abushakra received the B.Sc. degree in Communications and Electronics Engineering from the Jordan University of Science and Technology (JUST), Irbid, Jordan, in 2011. From 2014 to 2016, he joined the master program of the Communication Engineer Department at Al-Yarmouk University, Jordan, majoring in Wireless Communications. His researches focus on Ultra-wideband antennas and dielectric resonator antenna with different shapes and different feeding methods.

Asem S. Al-Zoubi received his B.Sc. degree of Electrical Engineering from Eastern Mediterranean University, Cyprus in 1993, the M.Sc. degree in Electrical Engineering from Jordan University of Science and Technology, Jordan in 1998, and the Ph.D. degree in Electrical Engineering from the University of Mississippi, USA, in 2008. Currently, he is an Associate Professor with the Department of Telecommunications Engineering in Yarmouk University, Jordan. His current research interests include dielectric resonator antennas and microstrip antennas. Al-Zoubi is a Member of the IEEE.

Derar F. Hawatmeh received the B.Sc. degree in Communications and Electronics Engineering from the Jordan University of Science and Technology (JUST), Jordan, in 2010. In 2010, he joined the master program of the Electrical Engineering Department in JUST. From 2012 to 2013, he was a Researcher with the R&D Department, Waseela-Integrated Telecommunication Solutions. He was an Instructor with the Network and Communications Engineering Department, Al Ain University of Science and Technology, Al Ain, UAE, from 2013 to 2014. In 2014, he joined the Center for Wireless and Microwave Information Systems, University of South Florida, Tampa, FL, USA, as a Graduate Research Assistant. His current research interests include the analysis and the design of planar antennas, 3-D antennas compact, planar, passive, and multi-frequency and ultra-wideband microwave components.

Design, Fabrication, and Measurements of Extended L-Shaped Multiband Antenna for Wireless Applications

Ashfaq Ahmad [1], Farzana Arshad [1], Syeda I. Naqvi [1], Yasar Amin [1,2], and Hannu Tenhunen [2,3]

[1] ACTSENA Research Group
University of Engineering and Technology (UET), Taxila, 47050, Pakistan
Ashfaquetb11@gmail.com, farzana.arshad@uettaxila.edu.pk, iffat.naqvi@uettaxila.edu.pk

[2] iPack VINN Excellence Center
Royal Institute of Technology (KTH), Isafjordsgatn 39, Stockholm, SE-16440, Sweden
yasar.amin@uettaxila.edu.pk

[3] TUCS, Department of Information Technology
University of Turku, Turku-20520, Finland
hannu@kth.se

Abstract ─ This article expounds a multi-band compact shaped antenna, which is based on CPW ground plane. FR-4 with a thickness of 1.6 mm is used as a substrate for the proposed antenna. The proposed antenna is capable of operating at 1.56 GHz for (Global Positioning System), 2.45 GHz (Wireless Local Area Network) and 4.49 GHz (Aeronautical Mobile Telemetry (AMT) fixed services). The efficiency at 1.56, 2.45, and 4.49 GHz is 79.7, 76.9 and 76.7%, respectively. The VSWR of the presented antenna is less than 1.5 at all the desired resonance modes, which confirms its good impedance matching. The performance of the proposed antenna is evaluated in terms of VSWR, return loss, radiation pattern and efficiency. CST®MWS® software is used for simulations. In order to validate the simulation results, a prototype of the designed antenna is fabricated and a good agreement is found between the simulated and measured results.

Index Terms ─ AMT Fixed Services, GPS, multiband antenna, Wi-Fi.

I. INTRODUCTION

With the rapid development of communication technology, researchers have paid huge attention towards multiband antennas. Portable devices demand multi-band antennas for their operation at different standards, like Wi-Fi, WiMAX, GSM, GPS [1] and many more. Due to the restriction of size selection, ease of fabrication and provision of connection to feed network, multi-band antennas offer edge over single band antennas. Multiband functionality can be achieved by introducing slots or cuts of different sizes in conventional microstrip antennas. Currently, some approaches for the design of multiband antennas, like the integration of a metamaterial inspired split ring resonator [2], and insertion of slots [3] within the radiating elements have been proposed. Defective ground planes [4] are also proposed to get multiple frequency bands. Similarly, different shapes of radiating elements [5-6] have been used to modify the microstrip antennas for achieving multi resonances. Despite all the latest advancements in microstrip antenna, they inherently exhibit narrow bandwidth. Monopole antenna is another attractive option for researcher due to their light weight, outstanding efficiencies, wide bandwidth, simple geometry and ease of fabrication. These antennas can be integrated with various portable devices for the efficient transmission and reception of data [7]. In order to incorporate these requirements, various types of multiband antennas have been designed recently [8]-[10].

In [11], a dual-band B-shaped antenna is (operating on 2.45 and 5.8 GHz) is proposed; however, it exhibits perturbed radiation patterns, E-shaped dual band antenna for WLAN application is designed in [12], but its efficiency is low (59%). Similarly, an H-shaped antenna for GPS and Wi-Fi applications is proposed in [13], but the antenna is bulky and its efficiency at the desired bands is 49-78%. Moreover, four sub-patches were employed to accomplish multi-band functionality in [14], but it increases the overall size (50×50 mm^2) of the proposed antenna which ultimately limits its integration with future wireless communication systems. In this context antenna structure needs careful optimization. Although, up to four operating bands were achieved in [15], this antenna is suitable for limited applications, due to complexity in shape. A monopole tri-band antenna is expounded in [16]. It is small in size, having three stage microstrip feed line possess distorted radiation pattern

Submitted On: October 12, 2017
Accepted On: April 1, 2018

and negative gain at 2 GHz band. In [17] triple-band microstrip antenna having complex geometry is presented for WLAN/WiMAX applications.

Similarly, CPW fed antennas are good candidates for achieving multi resonances. These antennas can be preferred due to the fact that they offer less coupling and easier integration with microwave circuits. A tri-band CPW (Coplanar waveguide) fed antenna is designed in [18]. The proposed antenna shows good performance, but it is difficult to fabricate due to its complex geometry. A CPW fed antenna having dimensions of 180x80 mm^2 is presented in [19].

This paper presents an efficient and compact multiband CPW fed antenna. The suggested antenna offers potential to replace multiple single band antennas in various applications. The proposed antenna is capable of operating at GPS (1.567 GHz), WLAN (2.45 GHz) and AMT Fixed services (4.49 GHz) with efficiency greater than 76%. The extended L-Shaped antenna is designed to operate on two lower frequency bands; moreover, this antenna is extended to acquire the higher resonance mode.

This paper is arranged as follows. Section II covers design methodology and underlying theory. Results are discussed in Section III. Section IV comprises the conclusion of this work.

II. ANTENNA GEOMETRY AND THEORY

This section depicts the basic geometry and theoretical aspect/detail of the proposed antenna. For multiple resonances two antenna designs are investigated, Extended L-shaped Ant-1 and Extended L-shaped with a crescent, that is Ant-2. CPW-fed technique is used for incorporating different radiation features; the antennas have non-complex structure of the single metallic layer and are easy to integrate with other systems [6].

A. Antenna Geometry

The geometry of proposed antennas, Ant-1 and Ant-2 is shown in Figs. 1 (a) and (b) respectively. The proposed antennas are implemented on Flame Retardant 4 (FR-4) with thickness of 1.6 mm, relative permittivity 4.3 and loss tangent of 0.025, while copper having a thickness of 0.035 mm is used as a radiating element. Ant-1 is responsible for antenna's operation on two lower frequencies (1.565 GHz and 2.415 GHz), while the crescent shape takes care of antenna's working on higher frequency (i.e., 4.5 GHz). For excitation of antenna, a 50Ω transmission line with a width of 2.3 mm is used. Table 1 elaborates physical characteristics of the antenna.

B. Theory

According to transmission line theory model [20] the effective resonance length can be computed using the following mathematical equations.

The resonance length L and guided wavelength are related as follows:

$$L_{1.565} = \lambda_{1.565}/4, \quad (1)$$

$$L_{2.41} = \lambda_{2.41}/4, \quad (2)$$

$$L_{4.5} = \lambda_{4.5}/4. \quad (3)$$

Where the guided wavelength can be calculated as:

$$\lambda_{fr} = \frac{c}{fr\sqrt{\varepsilon e}}. \quad (4)$$

c in the above equation refers to speed of light, f_r is resonance frequency and ε_e is effective permittivity:

$$\varepsilon_e = \frac{\varepsilon r+1}{2} + \frac{\varepsilon r-1}{2}(1+12h/w)^{-1/2}, \quad (5)$$

h, w and ε_r are the thickness of substrate, width of the radiating elements and relative permittivity respectively in equation (5).

The proposed antenna is optimized for best radiation efficiency η_{rad}. Radiation efficiency can be defined as the ratio of radiated power (P_{rad}) of the antenna to its input power (P_{in}):

$$\eta_{rad} = \frac{Prad}{Pin}. \quad (6)$$

The higher efficiency can be achieved by feeding the antenna properly, which results in minimum return loss (Γ). Factor Γ is the ratio of reflected electric field to the incident electric fields. Mathematically,

$$[\Gamma] = \frac{Zant-Zc}{Zant+Zc}, \quad (7)$$

where Z_{ant} is driving point impedance of antennas and Z_c is the characteristic impedance of the antenna. The proposed design has a characteristic impedance of nearly 50 Ω at all three resonances/resonating frequencies. For small return loss (Γ), the Voltage Standing Wave Ratio (VSWR) approaches unity.

The directivity and gain are related by efficiency. The gain is expressed in decibel (dB) and is given below:

$$G\,(dB) = 10\times\log(\eta_{rad}.D). \quad (8)$$

The equations presented above are applicable for the rectangular microstrip patch antenna; however, dimensions of proposed antenna are optimized after carrying out various simulations.

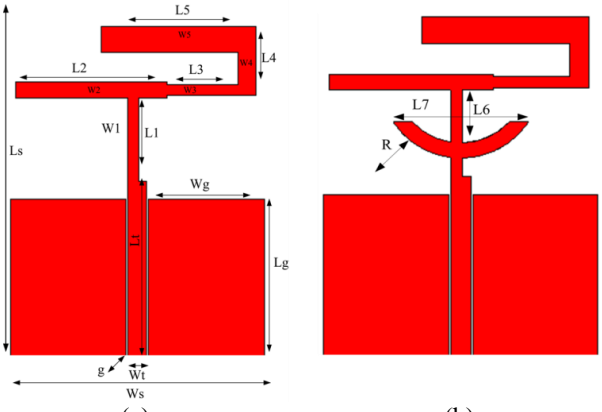

Fig. 1. Geometry of the proposed antennas. (a) Ant-1 and (b) Ant-2.

Table 1: Dimension of Extended L-Shaped antenna

Parameter	Size (mm)	Parameter	Size (mm)
Ls	40	L5	16
Ws	38	L6	5.8
Lg	18	L7	15
Wg	13.85	W1	1.3
R	7.49	W2	1.8
G	0.15	W3	1.3
L1	9	W4	2.1
L2	18	W5	3
L3	8.5	Lt	20
L4	3.6	Wt	2.3

III. RESULTS

To analyze the performance of the proposed antennas, CST® Micro Wave Studio environment is used. Both antennas are then fabricated and measured as shown in Fig. 2. Both computed and simulated results show close resemblance in terms of return loss and radiation pattern. Fabrication errors attribute to the minor discrepancy emerged in frequency shifts.

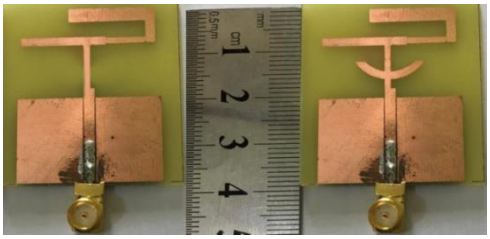

(a) (b)

Fig. 2. Fabricated design: (a) Ant-1 and (b) Ant-2.

A. Reflection coefficient

The proposed antenna is capable to work on 1.567 GHz (GPS), 2.41 GHz (WLAN) and 4.49 GHz (AMT fixed service). Figure 3 shows the reflection coefficient of Ant-1 and Ant-2. Both antennas are then fabricated and measured. The results reveal that close agreements between measured and simulated results has been achieved.

B. Voltage standing wave ratio (VSWR)

The simulated voltage standing wave ratio for the proposed designs is presented in Fig. 4. The VSWR of the Ant-1 is 1.06 and 1.5 at 1.56 GHz and 2.41 GHz respectively; while for Ant-2, VSWR is 1.24 at 4.5 GHz. This shows that designs are perfectly matched at desired frequencies.

C. Radiation patterns

The gain pattern and radiation pattern of the proposed antennas is presented in this section. Figure 5 illustrates the gain patterns. The far-field 3D patterns are presented in Fig. 6. The gain of the proposed antennas is 1.03, 1.33 and 1.84 dB at 1.565, 2.415 and 4.49 GHz, respectively. It is noticed that the designed antennas radiate omni-directional in H-plane for two lower frequency bands, while distinct behavior is observed for higher frequency. E-plane polar plots are depicted in figure of 8 having a null at $\theta = 90^0$ for 1.56 and 2.45 GHz as shown in the figure below. For 4.49 GHz, the position of nulls is shifted to $\theta = 70^0$ for E-plane pattern and is nearly omnidirectional except in null position. Both measured and simulated results are in good agreement.

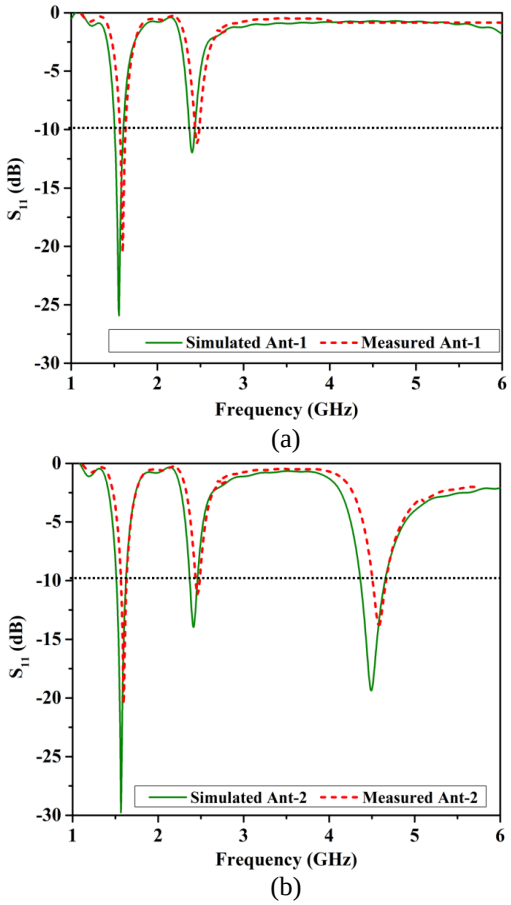

Fig. 3. S parameter: (a) Ant-1 and (b) Ant-2.

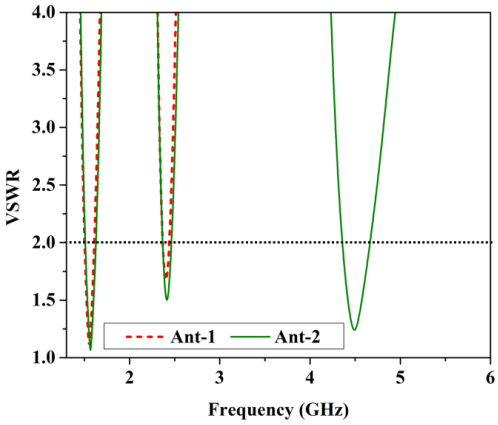

Fig. 4. Voltage Standing Wave Ratio.

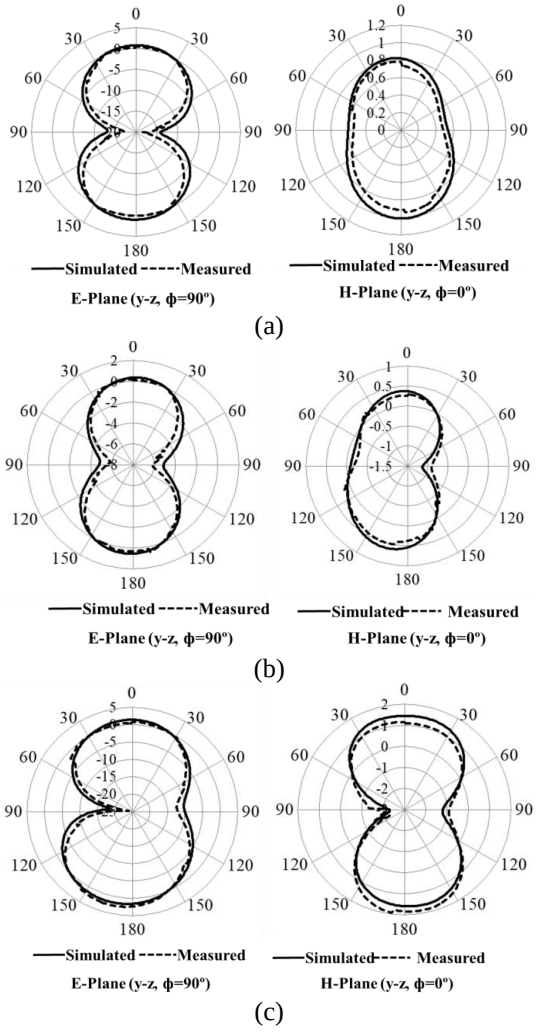

Fig. 5. Simulated and measured gain patterns: (a) 1.567 GHz, (b) 2.415 GHz, and (c) 4.5 GHz.

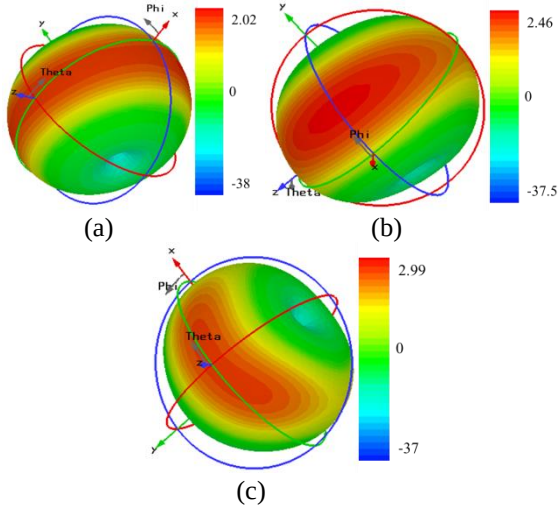

Fig. 6. 3D Radiation patterns: (a) 1.565 GHz, (b) 2.415 GHz, and (c) 4.49 GHz.

D. Surface current

Figure 7 depicts the simulated surface current distribution at different resonance frequencies. Figure 7 (a) suggests that the current distribution is maximum along the feedline and upper half part of the radiator which generates the lower frequency band (1.5 GHz). Figure 7 (b) shows the strong current intensity in the radiator as well as along the feed line which resonates at 2.45 GHz band. In part (c) maximum current density is observed in crescent shape and in the feedline. In this case, current follows the smaller path; hence, antenna resonates at large frequency of 4.49 GHz.

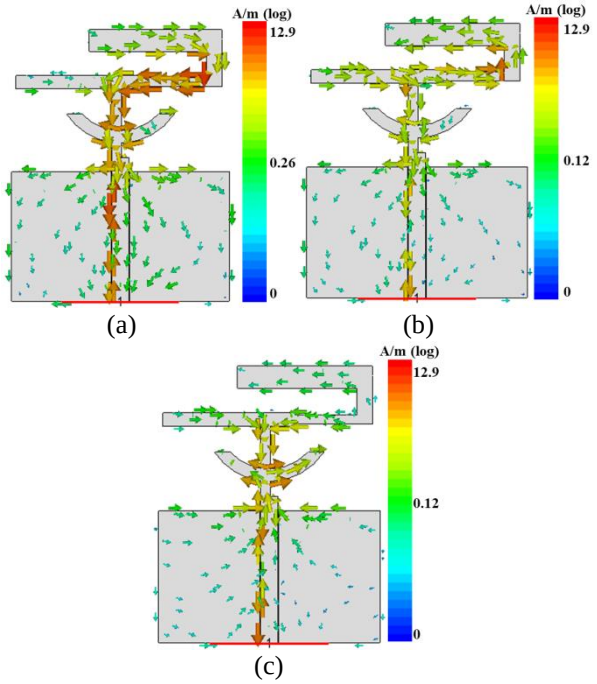

Fig. 7. Surface current distribution: (a) 1.56 GHz, (b) 2.41 GHz, and (c) 4.49 GHz.

Table 2: Comparison table

Characteristic	[12]	[8]	[9]	[10]	[6]	[7]	This Work
Area (mm^2)	1200	5625	3905	8496	3600	4500	1520
Height (mm)	0.4	4.8	1.6	1.6	0.4	1	1.6
Substrate	FR-4	FR-4	FR-4	FR-4	FR-4	FR-4	FR-4
No of resonance	2	2	3	2	3	3	3
Bandwidth (MHz)	130, 355	----	100, 110, 300	120, 750	22, 300, 9600	84, 200’ 100	109, 86, 284
Efficiency (%)	57, 58	85, 77		----	56, 70, 52	97, 95, 95	78, 77, 77

The proposed design is compared with some work published recently. Comparison in terms of various parameters is presented in Table 2. In [12] miniaturize

design is presented, but only two resonances with minimum efficiency (even less than <58% are achieved). While [6], [9], and [10] are successful in attaining high bandwidth, but at the cost of size and number of resonances. Tri-band antennas proposed in [6], [7], & [9] cannot be easily integrated with most of the applications due to their bulky size. Moreover, [6] present-tri-band antenna with high bandwidth but low efficiency. It can be concluded that the proposed design is miniaturized and show better performance in terms of bandwidth, efficiency and radiation patterns. Table 3, summarizes overall performance of the proposed antenna at three different frequencies.

Table 3: Summarized results

Parameters	Frequency 1	Frequency 2	Frequency 3
Frequency (GHz)	1.565	2.415	4.49
Return loss (dB)	-29.76	-13.95	-19.375
Directivity (dB)	2.02	2.46	2.99
Gain (dBi)	1.03	1.33	1.84
Bandwidth (MHz)	109.5	86.8	283.9
Efficiency (%)	79.7	76.9	76.7
VSWR	1.067	1.501	1.24

IV. CONCLUSION

In this paper, coplanar waveguide (CPW) multiband antennas are designed and analyzed. The proposed antennas operate at three different frequencies, i.e., GPS (1.565 GHz), WLAN (2.45 GHz) and AMT fixed services (4.49 GHz). Radiating element consists of two parts, an extended L-shaped, while the other is an extended L-shaped with a crescent. Extended L-Shaped design is responsible for operation at two lower frequencies (1.565 GHz and 2.415 GHz), while the Ant-2 is responsible for the higher frequency (4.5 GHz). The proposed antennas are compact, lightweight and efficient (<76%) and can be used for different wireless applications. Prototype of the proposed designs is fabricated and measured. Both computed and simulated results are compared in term of return loss and gain pattern. The measured results show good agreement.

ACKNOWLEDGMENT

This work was financially supported by Vinnova (The Swedish Governmental Agency for Innovation Systems) and University of Engineering and Technology Taxila, Pakistan through the Vinn Excellence Centers program and ACTSENA research group funding, respectively.

REFERENCES

[1] A. Ramadan, M. Al-Husseini, K. Y. Kabalan, and A. EI-Hajj, "Fractal-shaped reconfigurable antennas," *INTECH Open Access Publisher*, vol. 1, pp. 237-250, 2011.

[2] V. Rajeshkumar and S. Raghavan, "A compact metamaterial inspired triple band antenna for reconfigurable WLAN/WiMAX applications," *AEU-Int. J. Electron. Commun.*, vol. 69, pp. 274-80, 2015.

[3] W. C. Liu, C. M. Wu, and N. C. Chu, "A compact low-profile dual-band antenna for WLAN and WAVE applications," *AEU-Int. J. Electron. Commun*., vol. 66, pp. 467-71, 2012.

[4] A. K. Gautam, A. Bisht, and B. K. Kanaujia, "A wideband antenna with defected ground plane for WLAN/WiMAX applications," *AEU-Int. J. Electron. Commun*., vol. 70, pp. 70, 2016.

[5] L. Bing, J. S. Hong, and B. Z. Wang, "A novel circular disc monopole antenna for dual-band WLAN applications," *Applied Computational Electromagnetics Society (ACES) Journal*, vol. 27, pp. 41-448, 2012.

[6] T.-H. Chang and J.-F. Kiang, "Compact multi-band H-shaped slot antenna," *IEEE Transactions on Antennas and Propagation*, vol. 61, pp. 4345-4349, 2013.

[7] H. Wang, and M. Zheng, "An internal triple-band WLAN antenna," *IEEE Antennas and Wireless Propagation Letters*, vol 10, pp. 569-572, 2013.

[8] M. F. Karim and A. Alphones, "A low-profile dual-band circularly polarized GPS antenna," *In Microwave Conference (APMC) Asia-Pacific*, pp. 1-4, 2016.

[9] C.-X. Mao, S. Gao, Y. Wang, and B. Sanz-Izquierdo, "A novel multiband directional antenna for wireless communications," *IEEE Antennas and Wireless Propagation Letters*, vol. 16, pp. 1217-1220, 2017.

[10] X. He, S. Hong, H. Xiong, Q. Zhang, and E. M. Tentzeris, "Design of a novel high-gain dual-band antenna for WLAN applications," *IEEE Antennas and Wireless Propagation Letters*, vol. 8, pp. 798-801, 2009.

[11] H. U. Iddi, M. R. Kamarudin, T. A. Rahman, and R. Dewan, "Design of dual-band B-shaped monopole antenna for MIMO application," *In Antennas and Propagation Society International Symposium (APSURSI), IEEE*, pp. 1-2, 2012.

[12] S. D. Sairam and S. A. Arunmozhi, "A novel dual-band E and T-shaped planar inverted antenna for WLAN applications," *In Communications and Signal Processing (ICCSP)*, pp. 1922-1926, 2014.

[13] T.-H. Chang and J.-F. Kiang, "Compact multi-band H-shaped slot antenna," *IEEE Transactions on Antennas and Propagation*, 61, no. 8, pp. 4345-4349, 2013.

[14] H. F. AbuTarboush, R. Nilavalan, S. W. Cheung, and K. M. Nasr, "Compact printed multiband antenna with independent setting suitable for fixed and reconfigurable wireless communication systems," *IEEE Trans. Antennas Propag*., vol. 60, pp. 3867-3874, 2012.

[15] A. Khan, S. I. Naqvi, F. Arshad, Y. Amin, and H. Tenhunen, "A compact quad-band CPW-fed planar resonator for multiple wireless communication applications," *Applied Computational Electromagnetics Society Journal*, vol. 32, pp. 11, 2017.

[16] S. C. Basaran, U. Olgun, and K. Sertel, "Multiband monopole antenna with complementary split-ring resonators for WLAN and WiMAX applications," *Electronics Letters*, vol. 49, pp. 636-638, 2013.

[17] A. K. Gautam, L. Kumar, B. K. Kanaujia, and K. Rambabu, "Design of compact F-shaped slot triple-band antenna for WLAN/WiMAX applications," *IEEE Transactions on Antennas and Propagation*, vol. 64, pp. 1101-1105, 2016.

[18] R. Z. Wu, P. Wang, Q. Zheng, and R. P. Li, "Compact CPW-fed triple-band antenna for diversity applications," *Electronics Letters*, vol. 51, pp. 735-736, 2015.

[19] S. W. Chen, D. Y. Wang, and W. H. Tu, "Dual-band/tri-band/broadband CPW-fed stepped-impedance slot dipole antennas," *IEEE Transactions on Antennas and Propagation*, vol. 62, pp. 485-49, 2014.

[20] C. A. Balanis, *Antenna Theory, Analysis and Design*. 2nd ed., New York: J. Wiley & Sons, pp. 14, 68 and 817-820, 1997.

Ashfaq Ahmad received his B.Sc. degree in Telecommunication Engineering from UET Peshawar in 2016. He is doing his M.Sc. in Telecommunication Engineering from UET Taxila. Currently, he is doing research on reconfigurable antennas. His research interests include planar antenna, millimeter wave antennas, multi band antennas, implanted antennas, Specific Absorption Rate analysis and EBGs.

Farzana Arshad received her B.Sc. and M.Sc. degree in Software Engineering and Telecommunication Engineering from UET Taxila, Pakistan in the year 2006 and 2010, respectively. Currently, she is working towards her Ph.D. degree in Telecommunication Engineering from UET Taxila. She is also a Member of ACTSENA, Research Group. Her current research interests include Low profile Multiband and reconfigurable antenna design.

Syeda Iffat Naqvi received her B.Sc. and M.Sc. degree in Computer Engineering and Telecommunication Engineering from UET Taxila, Pakistan in the year 2006 and 2011, respectively. Currently, she is pursuing her degree of Ph.D. in Telecommunication Engineering from (UET) Taxila. She is also a Member of ACTSENA, Research Group. Her current research interests include RF and microwave antenna designing for cutting edge wireless technologies. Naqvi is a Member of IEEE and ACES.

Yasar Amin is Chairman and Associate Professor of Telecommunication Engineering Department, University of Engineering and Technology Taxila, Pakistan. He is Founder of ACTSENA, Research Group at UET Taxila, Pakistan. He has done his B.Sc. in Electrical Engineering in 2001 with specialization in Telecommunication and M.Sc. in Electrical Engineering in 2003 with specialization in System-on Chip Design from Royal Institute of Technology (KTH), Sweden. His Ph.D. is in Electronic and Computer Systems from Royal Institute of Technology (KTH), Sweden, with research focus on printable green RFID antennas for embedded sensors, while has MBA in Innovation and Growth from Turku School of Economics, University of Turku, Finland.

Hannu Tenhunen is Chair Professor of Electronic Systems at Royal Institute of Technology (KTH), Stockholm, Sweden. Tenhunen has held Professor positions as Full Professor, Invited Professor or Visiting Honorary Professor in Finland (TUT, UTU), Sweden (KTH), USA (Cornel U), France (INPG), China (Fudan and Beijing Jiatong Universities), and Hong Kong (Chinese University of Hong Kong), and has an Honorary Doctorate from Tallinn Technical University. He has been Director of multiple national large scale research programs or being an Initiator and Director of national or European graduate schools. He as actively contributed on VLSI and SoC design in Finland and Sweden via creating new educational programs and research directions, most lately at European level as being the EU-level Education Director of the new European flagship initiative European Institute of Technology and Innovations (EIT), and its Knowledge and Innovation Community EIT ICT Labs.

A Novel Dielectric Loaded Vivaldi Antenna with Improved Radiation Characteristics for UWB Application

Hua Zhu [1,2], Xiuping Li [1,2], Li Yao [1,2], and Jun Xiao [1,2]

[1] School of Electronic Engineering
Beijing University of Posts and Telecommunications, Beijing, 100876, China
judy-cool@163.com, xpli@bupt.edu.cn, 951684999@qq.com, xiaojun19861986@163.com

[2] Beijing Key Laboratory of Work Safety Intelligent Monitoring
Beijing, 100876, China

Abstract ─In this paper, a compact ($40\times50\times0.8mm^3$) Vivaldi antenna with trapezoidal corrugation and a triangular director element is proposed for high gain performance. The exponential slot with diamond slot stub is designed to broaden the bandwidth. The measured bandwidth is 11.3 GHz from 2.9 to 14.2 GHz under the condition of Voltage Standing Wave Ratio (VSWR) less than 2. The simulated gain is 5.5-9 dBi at the full bandwidth. The measured gain is 5-7.6 dBi from 3 to 5.8 GHz. In addition, the measured group delay of the proposed antenna is around 2±0.8 ns. The simulated and measured results agree well.

Index Terms ─ Diamond cavity, dielectric loaded, gain enhancement, Vivaldi antenna.

I. INTRODUCTION

Since the Federal Communications Commission (FCC) declaration of the frequency band 3.1 to 10.6 GHz for commercial communication applications in 2002, inexpensive realization of ultra-wideband (UWB) systems have become one of the key topics in the industry worldwide [1]. Vivaldi antenna has been designed and researched due to its natural wide impedance bandwidth, low cross polarization and end-fire radiation characteristic [2-4]. However, Vivaldi antenna is facing many challenges including miniaturization, good radiation performance, high gain and stable group delay through the entire band.

Facing the above challenges, there have been quite a few reported methods. In [5], two pairs of eye-shaped slots at outer edges is used to concentrate the current along the inner edges to improve the performance. In [6, 7], dielectric is loaded to enhance the gain and improve the radiation performance. In [8], the artificial material with lower effective refractive index acts as a regular lens in beam focusing. In [9], six periodic metallic strips in middle of tapered slot are added to improve gain. In [10], resistive loading Vivaldi antenna is designed to enhance bandwidth by the high chip resistor and short pin. In [11], a hybrid loaded with patches, resistors and the split-ring resonator (SRR) structure is used to extend the low-end bandwidth limitation. The resistor loaded method can effectively broaden the bandwidth but reduce the gain.

In this paper, a compact and high gain Vivaldi antenna is proposed for UWB application. The four kinds of Vivaldi antennas are designed and compared in this paper. Antenna B is obtained by loading trapezoidal corrugation at outer edges of original antenna (antenna A). Antenna C is achieved by extending the substrate of antenna B and adding a triangular metallic element as director to enhance the gain. Finally, antenna D is proposed by designing a diamond slot stub instead of circular one to broaden the impedance matching at low-end frequency band. The measured bandwidth of proposed antenna is 2.9 GHz to 14.5 GHz under the condition $S_{11} < -10$ dB. The simulated gain of antenna D has been increased by 2-4 dB over full UWB compared with original antenna.

II. DIELECTRIC LOADED ANTENNA DESIGN AND SIMULATION

A. Dielectric loaded Vivaldi antenna

The configurations of three types of Vivaldi antennas are shown in Figs. 1 (a)-(d). The original antenna (antenna A) consists of exponential slot, microstrip feeding line, and the microstrip line to slotline transition, as shown in Figs. 1 (a)-(b). In Fig. 1 (c), symmetrical trapezoid-shaped slots are etched on the outer edges, which formed antenna B to concentrate the current along inner edge. In Fig. 1 (d), the dielectric substrate is extended 10 mm and the triangular metallic element is added in the middle of radiating slot as a director to enhance the gain in antenna C.

Submitted On: December 25, 2017
Accepted On: April 21, 2018

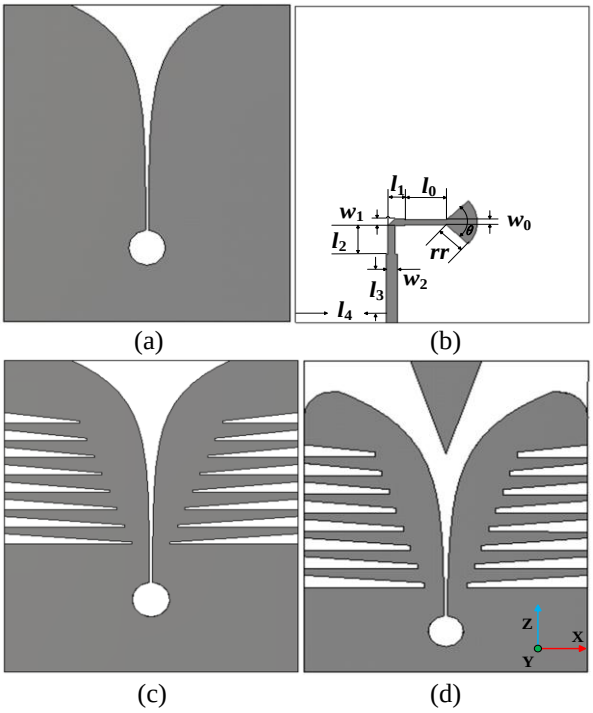

Fig. 1. Geometry of the Vivaldi antenna: (a) bottom view of antenna A, (b) top view of antenna A, (c) tottom view of antenna B, and (d) bottom view of antenna C.

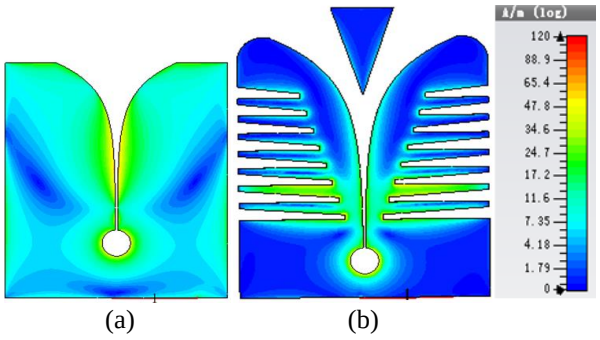

Fig. 2. Simulated surface current distribution at 3.5 GHz of (a) antenna A and (b) proposed antenna.

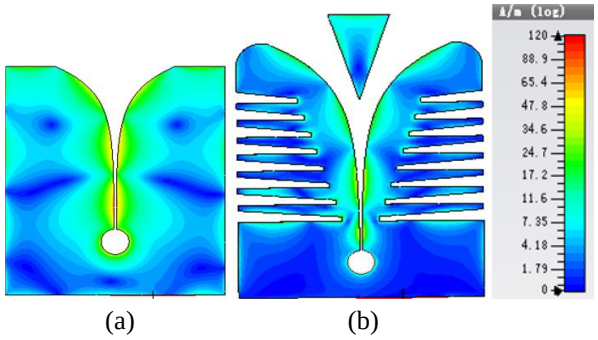

Fig. 3. Simulated surface current distribution at 10 GHz of (a) antenna A and (b) antenna C.

The performance of the designed antenna is simulated using the simulation tool HFSS v16. In order to further understand the operating characteristic of the antenna C at the low frequencies, surface current distribution of both the original (antenna A) and antenna C at 3.5 GHz and 10 GHz are given in Figs. 2-3, respectively. We can see that the surface current concentrated along the inner edges of exponential slots and the trapezoid-shaped slots. However, for the antenna A, the current is mostly distributed around the exponential slots. This phenomenon indicates that lower frequency resonance is formed because of the trap ezoid-shaped slots. In Fig. 3 (b), the surface current distribution is stronger at the triangular metallic element, which acts as director at high-end frequency to improve the gain.

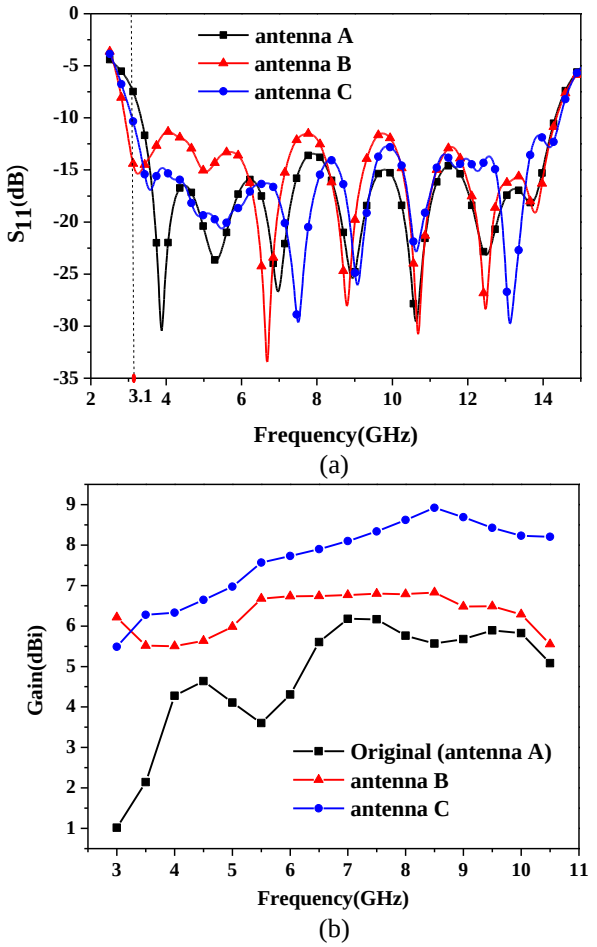

Fig. 4. The simulated performance of three Vivaldi antennas: (a) simulation of peak realized gain versus frequency, and (b) simulation of S_{11} versus frequency.

Figure 4 (a) illustrates the S_{11} variation of the antenna A, antenna B, and antenna C. As shown in the figure, the lower end S_{11} < -10 dB limitation of antenna A is 3.5 GHz, while the antenna B is to 2.9 GHz. It means that the antenna B is able to miniaturize the size of Vivaldi

antenna by lower frequency. In Fig. 4 (b), then we can see that the simulated gain of antenna C has been enhanced by 1-3 dB compared with antenna B and has been enhanced by 2-4 dB compared with antenna A. That caused by extending the substrate which acts as a regular lens in beam focusing. The triangular metallic element is effectively concentrated the currents to improve gain at high-end frequency. But extending the dimension of the substrate deteriorates the bandwidth at low-end frequency band. Compared to antenna B, the low-end frequency band of antenna C is shifted from 2.9 to 3.1 GHz.

B. Dielectric loaded Vivaldi antenna with the diamond cavity

The gradient slot line can achieve a wide impedance bandwidth characteristics. So the microstrip line to slotline transition is the main limit of impedance bandwidth in Vivaldi antenna. Aiming for broaden the impedance matching bandwidth at low-end frequency, the diamond slot stub is designed to replace circular one in transition structure, as shown in Fig. 5 (the blue dashed rectangle). And its equivalent circuit of microstrip line to slotline transition is shown in Fig. 4. In Fig. 6 (a), Z_{om} and Z_{os} are the characteristic impedance of microstrip line and slotline, respectively. C_{oc} represents the equivalent capacitor of the microstrip open end and L_{os} represents inductance of the slot line short end. θ_m and θ_s are the electrical length of extension of the opened microstrip and shorted slotline at central frequency, respectively. The open-circuit microstrip stub and the short-circuit slotline are represented as:

$$X_m^{in} = jX_m = Z_{om}\frac{1/\ jw\cdot C_{os} + jZ_{om}\tan\theta_m}{Z_{om} + \tan\theta_m / wC_{oc}}, \quad (1)$$

$$X_s^{in} = jX_s = Z_{os}\frac{jL_{os} + jZ_{os}\tan\theta_s}{Z_{os} - L_{os}\tan\theta_s}. \quad (2)$$

When $3.8 \le \varepsilon_r \le 9.8$, $0.006 \le d/\lambda_0 \le 0.06$, and $0.0015 \le ll/\lambda_0 \le 0.075$, the characteristic impedance of the slotline is [12]:

$$\begin{aligned} Z_{os} &= 73.6 - 2.15\varepsilon_r + (638.9 - 31.37\varepsilon_r)(ll/\lambda_0)^{0.6} \\ &+ (36.23\sqrt{\varepsilon_r^2 + 41} - 255)\frac{ll/h}{(ll/h + 0.876\varepsilon_r - 2)} \\ &+ 0.51(\varepsilon_r + 2.12)(ll/h)\ln(100h/\lambda_0) \\ &- 0.753\varepsilon_r (h/\lambda_0)/\sqrt{ll/\lambda_0}, \end{aligned} \quad (3)$$

ll and λ_0 is the width of the slot, substrate height and free space wavelength.

The simplified equivalent transmission line model of transition structure is shown in Fig. 6 (b), where,

$$R = n^2 Z_{os} X_s^2 / (Z_{os}^2 + X_s^2), \quad (4)$$

$$X = n^2 Z_{os}^2 X_s / (Z_{os}^2 + X_s^2). \quad (5)$$

Γ of the antenna can be expressed as:

$$\Gamma = \frac{R - Z_{om} + j(X_m + X)}{R + Z_{om} + j(X_m + X)}. \quad (6)$$

In Equation (6), the value of X_m and X_s affects the antenna bandwidth, and X_m is close to zero. If we increase the value of X_s, both the value of X and Γ will be reduced. The antenna bandwidth will be improved. From Fig. 7 we can see that X_s of diamond slot stub is larger than the circular one. In this paper the circular slot stub is replaced by diamond slot stub to enhance the low-end frequency bandwidth. The final optimized dimensions of the proposed antenna are given in Table 1.

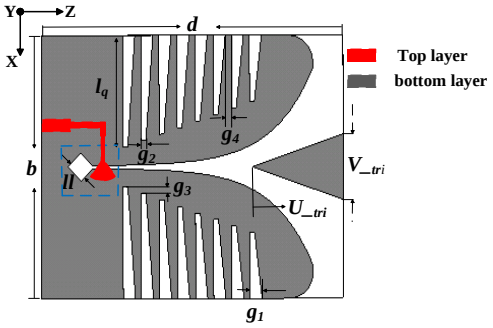

Fig. 5. Bottom view of the proposed antenna.

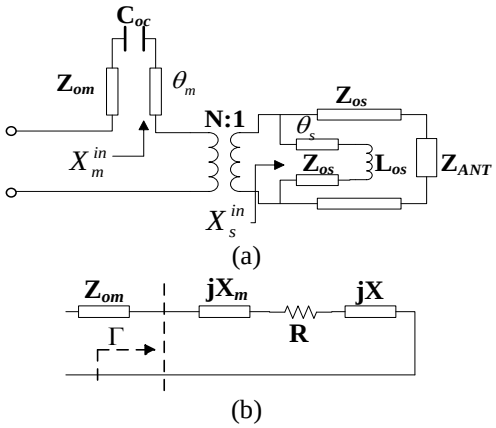

Fig. 6. Equivalent circuit of the microstrip line to slotline transition: (a) equivalent circuit, and (b) simply circuit.

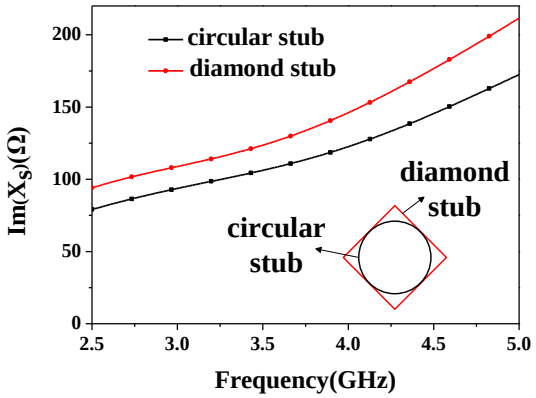

Fig. 7. Simulated Im (X_s) of the diamond and circular slot stub.

Table 1: The optimal dimensions of the proposed antenna (Unit: mm)

Parameters	Value	Parameters	Value
b	40	d	50
W_0	0.8	W_1	1
W_2	1.5	W_3	0.4
rr	4.5	ll	3
L_q	17	L_0	5.6
L_1	1.2	L_2	4
L_3	3.8	L_4	12.6
g_1	1.5	g_2	0.8
g_3	1	g_4	1
U_tri	15	V_tri	10
θ	86°		

III. RESULTS AND DISCUSSIONS

The proposed coplanar fed broadband antenna has been prototyped for the verification and measured using Keysight PNA-X network analyzer. The fabricated prototype of the proposed antenna is shown in Fig. 8. The simulated reflection coefficients for the antenna C and the proposed antenna are compared in Fig. 9. It can be seen that the simulated impedance bandwidth of proposed antenna and antenna C are 11.6 GHz (2.9-14.5 GHz) and 11.4 GHz (3.1-14.5 GHz), respectively. The measured impedance bandwidth is 11.4 GHz (2.8-14.2 GHz). The simulated and measured results agree well. From Fig. 10, it can be seen that the simulated gain of proposed antenna stably varies from 5.5 to 8.9 dBi, which has been increased by 2-4 dB compared with original (antenna A). Due to the test frequency limitation of the anechoic chamber, the gain is measured only in 3-5.8 GHz. It is observed that the measured gain is 5-7.6 dBi and the simulation and measurement results agree well.

The group delay is measured by using two proposed antennas placed in end-to-end orientation in far field at a distance of 40 cm, as shown in Fig. 11. It is observed that the group delay of the proposed antenna is about 2±0.8 ns in the operating UWB frequency band, as shown in Fig. 12. The simulation and measurement results agree well. The proposed antenna have good end-fire radiation at 3 GHz and 5 GHz.

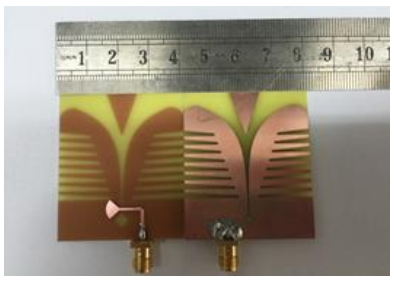

Fig. 8. Photographs of the fabricated proposed antenna.

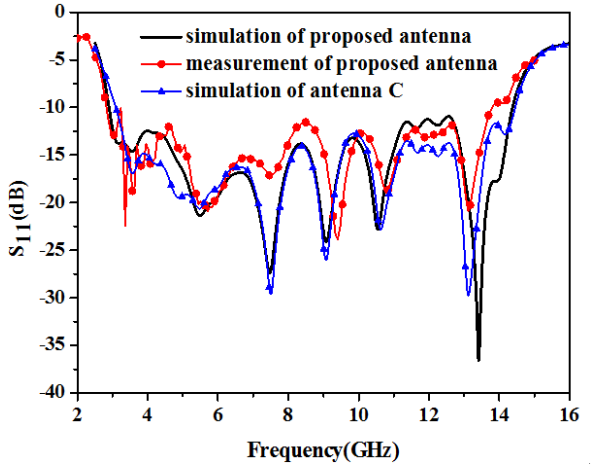

Fig. 9. S_{11} results of proposed antenna and antenna C.

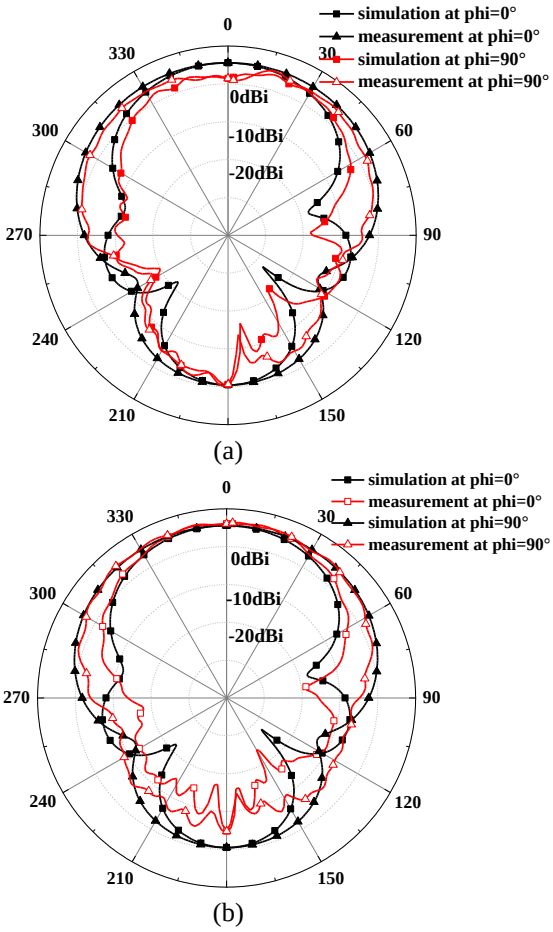

Fig. 10. The simulation and measurement of the radiation pattern: (a) 3 GHz and (b) 5 GHz.

From Table 2, it's demonstrated that the proposed antenna provides compact size and good radiation performance.

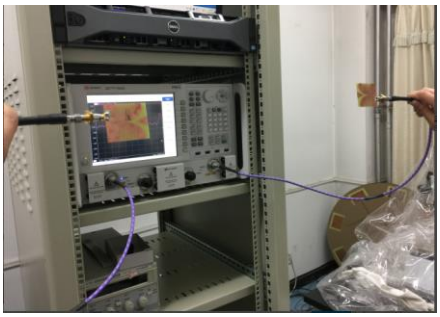

Fig. 11. The group delay measured environment.

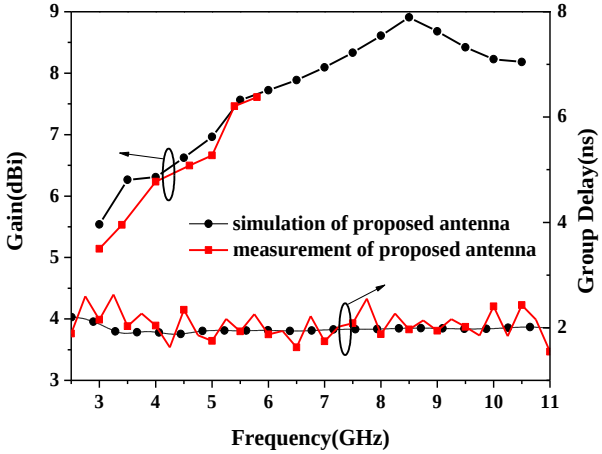

Fig. 12. Measured and simulated results of peak realized gain and group delay for proposed antenna.

Table 2: Performance comparison of the proposed antenna with references

Reference		Dimensions (mm^3)	Bandwidth (GHz)	Gain (dBi)
[5]		36×36×0.8	3-12.5	4-8
[6]		42×77×1	6-19	7.2-12
[7]		40×90×0.508	3.4-40	6-14
[8]		62×70×0.5	1-20	0.9-7.8
[9]		40×82×1	0.58-6.72	-
This work	Antenna A	40×40×0.8	3.5-14.2	1-5.2
	Antenna B	40×40×0.8	2.9-14.5	5-5.5
	Antenna C	40×40×0.8	3.1-14.2	5.5-9
	Proposed antenna	40×50×0.8	2.8-14.2	5.5-9

VI. CONCLUSION

A compact UWB antenna is proposed by loading dielectric and triangular metallic element, etching trapezoidal corrugations to enhance the gain. The low-end frequency band is improved by replacing circular slot stub with diamond one. The proposed antenna yields an impedance bandwidth of 11.4 GHz (2.8-14.2 GHz) under the condition of S_{11} less than -10 dB. The simulated peak gain varies from 5.5 to 9 dBi from 3-10.6 GHz. The measured peak gain varies from 5 to 7.6 dBi from 3-5.8 GHz. The measured group delay of the proposed antenna is around 2±0.8 ns. Both the simulated and measured results agree well. The proposed antenna has good potential for UWB communication applications.

ACKNOWLEDGMENT

This work is supported by the project 61601050 from the National Natural Science Foundation of China (NSFC), the project of 6140135010116DZ08001 and 6140518040116DZ02001.

REFERENCES

[1] Z. N. Low, J. H. Cheong, and C. L. Law, "Low-cost PCB antenna for UWB applications," *IEEE Antennas and Wireless Propagation Letters*, vol. 4, pp. 237-239, 2005.

[2] X. Li, H. Zhou, Z. Gao, H. Wang, and G. Lv, "Metamaterial slabs covered UWB antipodal Vivaldi antenna," *IEEE Antennas and Wireless Propagation Letters*, vol. 16, pp. 2943-2946, 2017.

[3] D. Yang, S. Liu, and D. Geng, "A miniaturized ultra-wideband Vivaldi antenna with low cross polarization," *IEEE Access*, vol. 5, pp. 23352-23357, 2017.

[4] M. Amiri, F. Tofigh, A. Ghafoorzadeh-Yazdi, and M. Abolhasan, "Exponential antipodal Vivaldi antenna with exponential dielectric lens," *IEEE Antennas and Wireless Propagation Letters*, vol. 16, pp. 1792-1795, 2017.

[5] K. Ma, Z. Q. Zhao, J. N. Wu, M. S. Ellis, and Z. P. Nie, "A printed Vivaldi antenna with improved radiation patterns by using two pairs of eye-shaped slots for UWB applications," *Progress In Electromagnetics Research*, vol. 148, pp. 63-71, 2014.

[6] J. Puskely, J. Lacik, Z. Raida, and H. Arthaber, "High gain dielectric-loaded Vivaldi antenna for Ka-band applications," *IEEE Antennas and Wireless Propagation Letters*, vol. 15, pp. 2004-2007, 2016.

[7] M. Moosazadeh and S. Kharkovsky, "A compact high-gain and front-to-back ratio elliptically tapered antipodal Vivaldi antenna with trapezoid-shaped dielectric lens," *IEEE Antennas and Wireless Propagation Letters*, vol. 15, pp. 552-555, 2016.

[8] L. Chen, Z. Lei, R. Yang, J. Fan, and X. Shi, "A broadband artificial material for gain enhancement of antipodal tapered slot antenna," *IEEE Transactions on Antennas and Propagation*, vol. 63, no. 1, pp. 395-400, 2015.

[9] G. K. Pandey and M. K. Mesgram, "A printed high gain UWB Vivaldi antenna design using tapered corrugation and grating elements," *International Journal of RF and Microwave Computer-Aided Engineering*, vol. 25, no. 7, pp. 610-618, 2015.

[10] C. Deng and Y. J. Xie, "Design of resistive loading Vivaldi antenna," *IEEE Antennas and Wireless Propagation Letters*, vol. 8, pp. 240-243, 2009.
[11] D.-W. Wu, X.-M. Wang, Y.-J. Xie, and L.-Q. Niu, "A novel hybrid loaded Vivaldi antenna with broadened relative bandwidth," *Microwave Optical Technology Letter*, vol. 58, pp. 2037-2041, 2016.
[12] R. Janaswamy and D. H. Schaubert, "Characteristic impedance of a wide slotline on low-permittivity substrates (Short Paper)," *IEEE Transactions on Microwave Theory and Techniques*, vol. 34, no. 8, pp. 900-902, Aug. 1986.

Hua Zhu received the M.S. degree from Guilin University of Electronic Technology, P. R. China, in 2010, and the Ph.D. degree from Beijing Institute of Technology, Beijing, P.R. China, in 2015. She has been a Postdoc at Beijing University of Posts and Telecommunications, P.R. China.

Her research interests include UHF RFID beam scanning antenna array design in complex environment and millimeter wave/Terahertz antenna design.

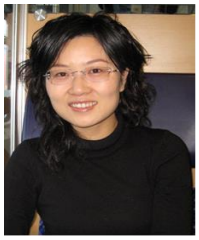

Xiuping Li received the B.S. degree from Shandong University, Jinan, Shandong, P. R. China, in 1996, and the Ph.D. degree from Beijing Institute of Technology, Beijing, P.R. China, in 2001. She has been a Professor at Beijing University of Posts and Telecommunications, P.R. China.

Her research interests include microwave devices for communications, antennas, and microwave circuit design for millimeter wave/Terahertz applications.

Li Yao received the B.S. degree from Chongqing University of Posts and Telecommunications, P.R. China, in 2013, and the M.S. degree from Beijing University of Posts and Telecommunications, P.R. China, in 2016.

His research interests include UWB antenna design and impedance bandwidth enhancement techniques.

Jun Xiao received the B.S. degree from Harbin Institute of Technology, P.R. China, in 2008, and the M.S. degree from Beijing University of Posts and Telecommunications, P.R. China, in 2011.

His research interests include UWB antenna design and millimeter wave/Terahertz antenna design.

A New Compact Planar Antenna for Switching between UWB, Narrow Band and UWB with Tunable-notch Behaviors for UWB and WLAN Applications

Mansour NejatiJahromi [1,4], Mahdi NagshvarianJahromi [2], and MuhibUr Rahman [3]

[1] Department of Electrical Engineering, Islamic Azad University, South Tehran Branch, Tehran, Iran
m_nejati@azad.ac.ir

[2] Department of Electrical and Computer Engineering, McMaster University, Hamilton ON, L8S 4L8, Canada
naghshvm@mcmaster.ca

[3] Division of Electronics and Electrical Engineering, Dongguk University, Seoul, 04620, Republic of Korea
muhib@dongguk.edu, muhib95@gmail.com

[4] Electrical and Electronic Engineering Department, Shahid sattari Aeronautical University of Science, Tehran, Iran
m_nejati@azad.ac.ir

Abstract ─ This paper presents continuously switchable behavior between narrowband (5.5 GHz WLAN), wideband (3-11 GHz UWB), and band-notched UWB using a miniaturized novel resonator. Three essential responses can be achieved from the same resonator by adequately utilizing the two capacitors. The first essential narrowband behavior is obtained from the resonator at 0.1pF is WLAN (5.5 GHz) operating frequency band. The second wideband behavior is achieved from the resonator to work between 3-11 GHz UWB frequency band. This behavior is achieved by changing the value of capacitors from 0.1 pF to 0.8pF. Finally, band-notched UWB response has been achieved by adjusting the position of capacitors, and this band-notch behavior can also be tuned continuously between WLAN and WiMAX frequency band. The antenna designed for these objectives have a compact size of 24×30.5 mm^2 including the particular ground plane. The clean and consistent radiation pattern of the antenna is observed because of the placement of the resonators in the partial ground plane. The antenna is also fabricated, and its response to three behaviors is measured for validation.

Index Terms ─ Band-notched UWB behavior, continuously switchable behavior, narrow-band behavior, tunable band-notched response, wide-band behavior.

I. INTRODUCTION

The wireless communication systems are highly developed in recent years, and the spectrum congestion has been highly increased. Narrow-band to wide-band switchable antennas is one of the best solutions to utilize the spectrum properly. These antennas will properly sense the environment in the particular state and will occupy the existing frequency band instantaneously using the dynamic spectrum allocations. Secondly, the antennas and filters should be integrated so that it can reduce the overall size of the transceiver and improve the capability of antennas as an antenna filter. In this context, a new concept termed as filtering antenna that can realize the filtering functionality and radiation characteristics simultaneously is presented in past years [1-2]. This technique avoids the designing of bandpass filter and antenna separately, and thus a more compact structure can be developed which in turn profoundly improves the performance of RF front-end. By combining the benefits of above two techniques, (switchable antennas and filtering antennas), a narrowband-to-wideband continuously switchable filtering antenna could be developed.

In last decades, many research papers have been published on reconfigurable antennas and narrowband reconfigurable antennas [3-6]. A frequency tunable antenna has been proposed in [7]. The tunability in narrow frequency band has been achieved by utilizing a reconfigurable filter, while PIN diode is used to switch the behavior of antenna between wideband and narrowband. A switchable bowtie dipole antenna between narrowband and wideband response is realized in [8], by controlling the PIN diodes states. Similarly, in [9-11] different MEMS switches, varactor diodes, and PIN diodes have been implemented to achieve the switching functionality between the narrowband and wideband behavior.

Another critical and critical concern of wireless communication appliances is the miniaturization and integration methods that can reduce the overall size of

Submitted On: December 16, 2017
Accepted On: April 21, 2018

the transceiver. In this regard, several techniques of the filters and antennas integration have been proposed in the literature [12-13]. A novel antenna is achieved in [14] with filtering behavior and dual-band response while in [15] a reconfigurable slot has been used to place filtering behavior in the antenna.

Based on the research work discussed above, switchable behavior between narrowband and wideband is achieved with straightforward structure and novel resonator. This manuscript is novel in the following aspects.

(1) For wireless communication devices such as smartphones and handset mobile internet devices to access the wireless spectrum of UWB and WLAN, a continuously switchable antenna is developed as it can instantaneously occupy the available range.

(2) The UWB response is also made band-notched in the WLAN frequency band due to unavoidable electromagnetic interferences.

(3) The band-notched response is also made continuously switchable and can be shifted to WiMAX frequency band depending on the desired application.

(4) Three different behaviors are achieved from the same resonator based on capacitors placement.

(5) The designed filtering antenna is not only valid to the narrow and wideband operation but can also accomplish miniaturization in RF front-end.

In this paper, we have presented a continuously switchable behavior between narrowband (5.5 GHz WLAN), wideband (3-11 GHz UWB), and band-notched UWB using a miniaturized novel resonator. Three essential behaviors are achieved from a single antenna by adequately utilizing the two capacitors. The first important behavior is achieved from the antenna at 0.1pF is WLAN (5.5 GHz) operating frequency band. The second behavior is developed by changing the value of both capacitors to 0.8pF to operate at wideband (UWB). Finally, band-notched UWB response is achieved by further adjusting the capacitor value, and this band-notch is also made continuously tunable between WLAN and WiMAX frequency band. The antenna has a compact size, and its dimensions are 24×30.5 mm^2. The clean and consistent radiation pattern of the antenna is also observed because of the placement of the resonators in the partial ground plane. The antenna is also fabricated, and its three behaviors response is measured.

The arrangement of the paper is carried out in the following manner. Section II contains discussion on simulation and measurement of three essential behaviors that have been achieved from the designed antenna. Section III dealt with the analysis of the resonator implemented and showed how these three behaviors could be achieved from a single resonator. Section IV deals with measurement discrepancies which are followed by conclusion in Section V.

II. DISCUSSION ON SIMULATION AND MEASUREMENTS FOR ACHIEVING THREE IMPORTANT BEHAVIORS FROM RESONATOR

A. Narrowband behavior antenna

The configuration and geometry of the narrowband antenna are shown in Fig. 1. This antenna is fabricated on Rogers RO4003 substrate with a thickness of 1.5 mm and the relative dielectric constant of ε_r=3.38 which has a dimension of 24×30.5 mm^2 (i.e., $W_{sub}\times L_{sub}$). The parameters of the proposed antenna are mentioned in Table 1. Two symmetrical capacitors are placed at the junction of the feedline and proposed resonators to control the response of the antenna. At 0.1pF the antenna is the good narrowband radiator and operate at 5.5 GHz WLAN frequency band.

The behavior of the antenna has been studied and simulated in Ansoft HFSS while it has been validated in CST Microwave studio suite. When the value of both capacitors are 0.1pF, then the resonator is coupled to the feedline and generates a narrowband behavior as shown in Fig. 3. The antenna is also fabricated as shown in Fig. 2 and its response at 0.1pF is correlated with the simulated one in Fig. 3.

Table 1: Dimensions (in millimeters) of the proposed antenna

Parameters	L_{sub}	W_{sub}	L_1	L_2	L_3	L_4
Value (mm)	30.5	24	13	5	1.7	1.2
Parameters	L_5	W_1	W_2	W_3	W_4	W_5
Value (mm)	0.96	22	10.6	5	2.3	0.2
Parameters	G_1	G_2	G_3	T	H	R
Value (mm)	0.2	0.25	0.2	0.017	1.5	11

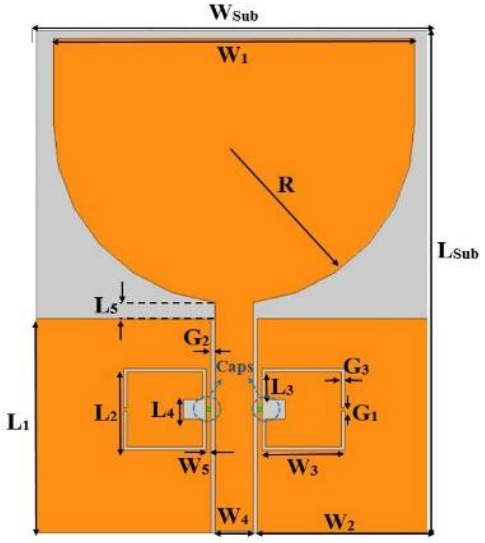

Fig. 1. Geometrical parameters of the narrowband-to-wideband antenna.

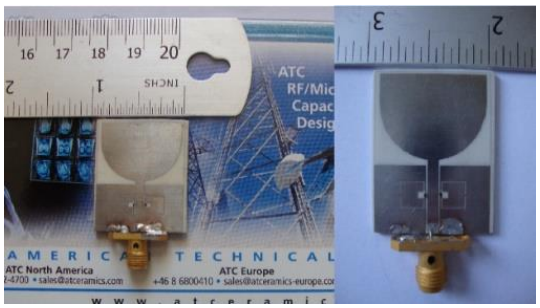

Fig. 2. Fabricated picture of the narrowband antenna.

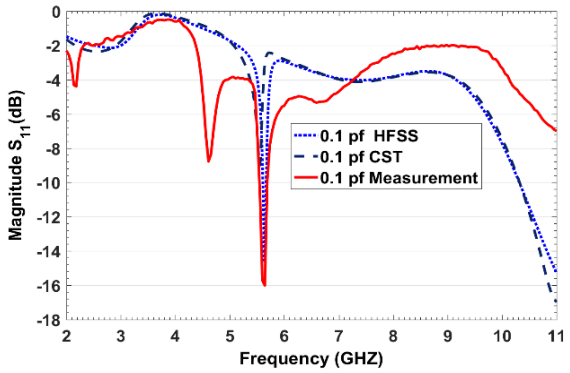

Fig. 3. Simulated and measured narrowband behavior of the antenna.

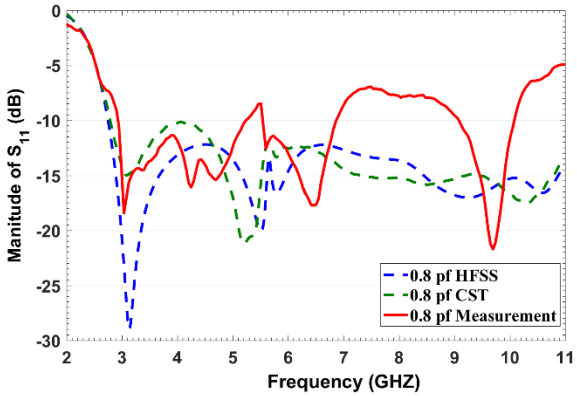

Fig. 4. Simulated and measured the wideband behavior of the antenna.

B. Wideband behavior antenna

The antenna response has been switched to wideband by changing the value of both capacitors. At 0.8pF the antenna is a good UWB radiator and operate within 3-11 GHz. The antenna at 0.8pF is also simulated and measured, and the response has been shown in Fig. 4. Also, the measurement results in comparison to numerical simulation results are shown in Fig. 5 for 0.1 PF and 0.8 PF. When the value of both capacitors are 0.8pF, then all the electromagnetic energy is transformed to the patch radiator, and it acts as a wideband UWB antenna. This behavior can be more clearly studied in Fig. 6 where the parametric analysis has been performed, and it is shown that by increasing the capacitor value, the response has been shifting from narrowband-to-wideband. The measured switching behavior is also more clearly elaborated in Fig. 6. In this way, we can switch the antenna behavior between narrowband-to-wideband behaviors with straightforward structure and analysis.

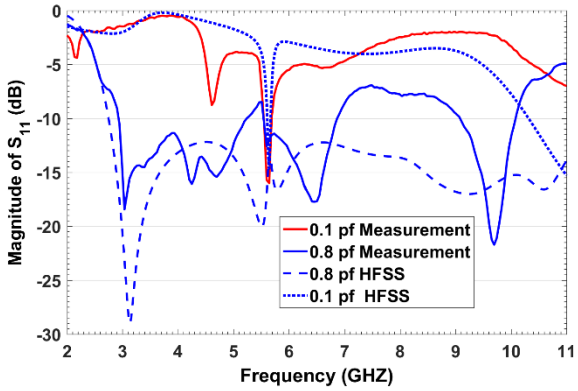

Fig. 5. The transformation from narrowband-to-wideband behavior.

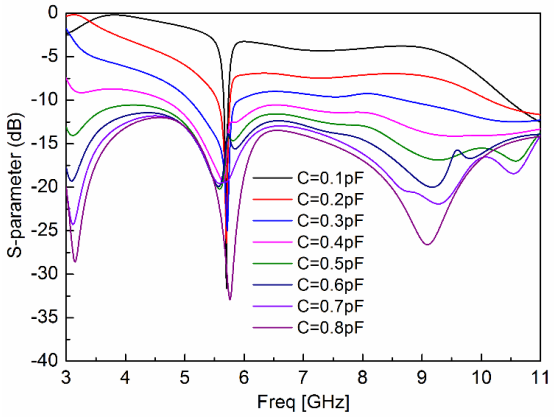

Fig. 6. Parametric analysis between narrowband and wideband behavior by varying capacitor.

C. Continuously tunable band-notched behavior antenna

By shifting both capacitors from the resonator-feed line junction to resonator internally, there is no more narrowband behavior as all electromagnetic energy will be radiated from the patch. Both capacitors have been shifted to the resonator internally as shown in Fig. 7. Now this resonator will act as a filter resonator and can be controlled by using the value of both capacitors. The overall response of the antenna will be wideband having continuously switchable notched band between WLAN

and WiMAX which causes unavoidable interference within UWB frequency band. In this way, we have achieved three important behaviors from the single resonator, which make it advantageous over other reported resonators and antennas.

It can be seen from Fig. 8 that WLAN band-notched UWB antenna response is achieved at 0.1pF while WiMAX band-notched UWB antenna is developed utilizing 0.6pF capacitor. In this way, the response can be made continuously switchable between the two interfering bands depending upon the application. It is due to the reason that the effective resonator length corresponds to the fundamental resonance frequency of 5.3 GHz. This resonance frequency can be further changed by varying the capacitors.

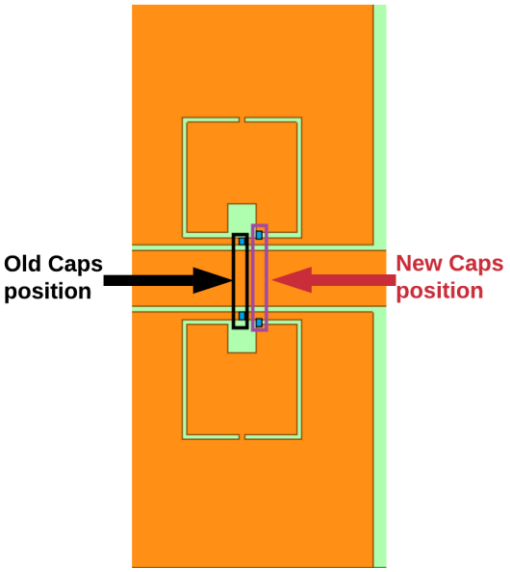

Fig. 7. Changing the position of capacitors for achieving continuously switchable band-notched UWB behavior.

The measurement of the band-notched UWB antenna developed are also carried out at 0.1pF and 0.5pF, and it is seen that the notch band is switching continuously. Figure 9 shows that there is band notch at 5.1 GHz due to the resonance of the resonator. This notched band has been made switchable, and at 0.5pF it is shifted towards 3.5 GHz WiMAX frequency band. The comparison between simulated and measured response at 0.5pf is shown in Fig. 10. The discrepancy between the simulated and measured responses is because of nonperfect cutting of the substrate edges while soldering the SMA connector.

The normalized radiation pattern of wide-band UWB antenna at 0.8pf is also shown in Fig. 11. Because of placing resonators at the ground plane, consistent radiation patterns are obtained for the antenna. The antenna worked in UWB mode and the radiation pattern display dipole type radiation. The primary purpose the radiation pattern is to demonstrate that the antenna radiates over the full frequency bandwidth. The peak antenna gain (dB) in CST and HFSS for the wide-band antenna has been shown in Fig. 12. The gain is very stable in the overall frequency band of 3-11 GHz.

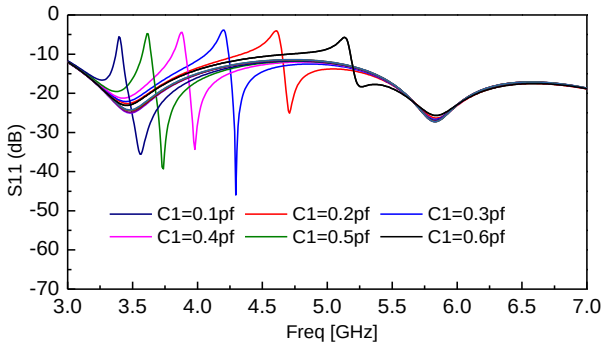

Fig. 8. Switching of notched-band between WLAN and WiMAX frequency band by changing capacitors value.

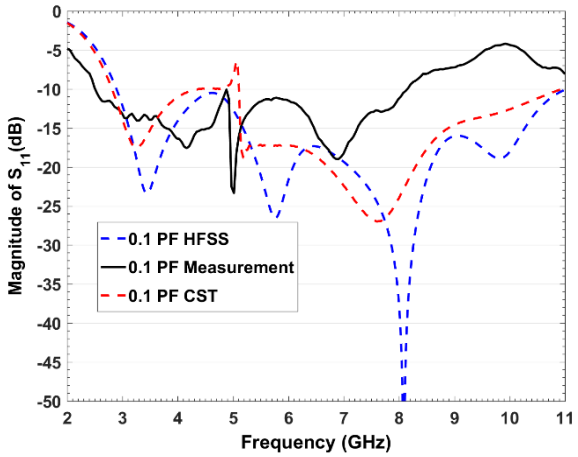

Fig. 9. Simulation and measurement of switchable band-notched UWB antenna at 0.1pF.

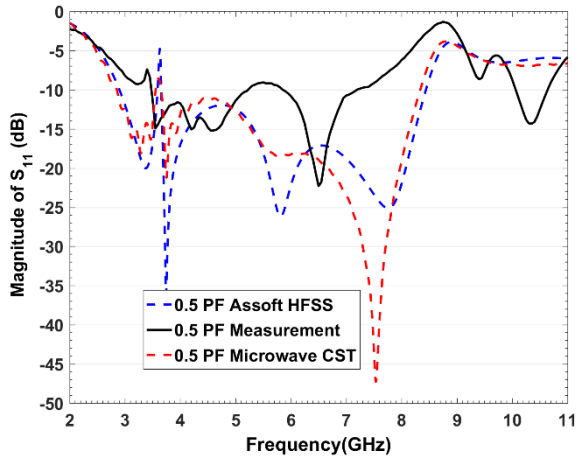

Fig. 10. Simulation and measurement of switchable band-notched UWB antenna at 0.8pF.

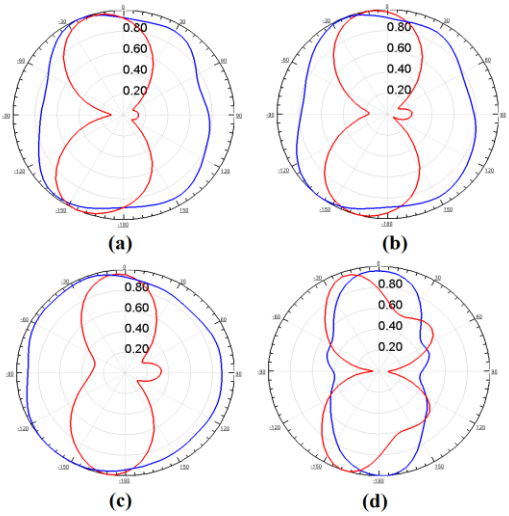

Fig. 11. Radiation patterns of switchable wide-band UWB antenna at 0.8pF: (a) 3.4 GHz, (b) 4.8 GHz, (c) 5.9 GHz, (d) 8.2 GHz. Red lines (E-plane) and blue lines (H-plane).

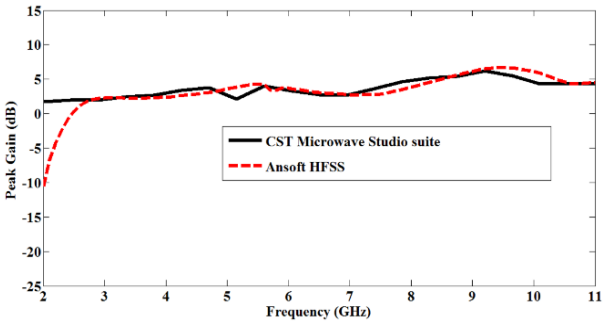

Fig. 12. Peak antenna gain for the wideband antenna in dB having capacitor value = 0.8pF.

III. DISCUSSION AND ANALYSIS ON SQUARE SEMI COMPLEMENTARY SPLIT RING RESONATOR (S-SCSRR)

The proposed miniaturized resonator is shown in Fig. 13 while its dimensions are listed in Table 1. The analysis of the resonator and its corresponding start and stop frequencies are calculated which validates our experimental results. It is proved that the homogeneous media with effective permeability (μ_{eff}) and effective permittivity (ε_{eff}) can replace the effective medium theory of inhomogeneous left-handed media. In such case, it should be noted that the wavelength is large enough in comparison with the basic scattering element dimensions. In such scenario, properties of non-homogeneous media become equivalent to that of homogeneous media. Thus, the condition developed that the average cell size must be less than a quarter wavelength, $l = \lambda g/4$, and this condition guarantees that the wave will propagate inside a metamaterial media and the unit cell will act as a lumped portion of a circuit.

The μ_{eff} and ε_{eff} can be calculated from the following equations [16-19]:

$$\Gamma = k \pm \sqrt{K^2 - 1}. \quad (1)$$

Where, the sign of $\pm$ is determined from the condition of $|G| \leq 1$:

$$k = \frac{S_{11}^{\ 2} - S_{21}^{\ 2} + 1}{2S_{11}}$$

$$Z_{eff} = \sqrt{\frac{\mu_{eff}}{\varepsilon_{eff}}} = \left(\frac{1+\Gamma}{1-\Gamma}\right)\frac{Z^{TL}}{Z_a^{TL}}, \quad (2)$$

$$n = n' - jn'' = \sqrt{\varepsilon_{eff}\mu_{eff}}$$

$$= \pm \frac{c}{j\omega l}\cosh^{-1}\left(\frac{1 - S_{11}^{\ 2} - S_{21}^{\ 2}}{2S_{21}}\right), \quad (3)$$

$$\varepsilon_{eff} = \varepsilon_{eff}' - j\varepsilon_{eff}'' = \frac{n}{Z_{eff}}, \quad (4)$$

$$\mu_{eff} = \mu_{eff}' - j\mu_{eff}'' = n.Z_{eff}, \quad (5)$$

Where, Z^{TL} and Z_a^{TL} are the characteristics impedance. The former one is in the case of reference transmission line while the later one is the transmission line having air-filled and *n* represents the effective refractive index.

An S-SCSRR can engrave as a square ring in the ground plane. It is noteworthy that the proposed S-CSRR is not the dual of conventional SRR, which can be analyzed using babinet principle. Also, the effective length of the LRs is designed at $\lambda g/4$ at the center frequency of the selected band that is 5.5 GHz in our analysis. These LRs dramatically reduces the size of the resonator as it is inserted in the main transmission line and thus we call it miniaturized S-SCSRR. At our desired frequency these lines couple magnetically to the S-SCSRR and thus create resonance. This resonance is advantageously used as narrow-passband in narrowband antenna while narrow-stopband in band-notched UWB antenna. The overall length of the S-SCSRR is almost $\lambda g/2$ while the turn ratio (coupling coefficient can be calculated as $n = \sqrt{\frac{Z_{(cpw)}}{Z_{os}}}$, where Z_{os} is the slot line characteristics impedance, and $Z_{(cpw)}$ is the CPW line characteristics impedance. The reflection (S_{11}) and transmission coefficient (S_{21}) in the analysis is determined by investigating the resonator as two port matched filter [20]. It is noteworthy that when capacitors are 0.1pF to work as an open circuit, then there is a strong coupling between two slots, which generates a narrowband response in the center frequency of 5.52 GHz calculated from Equation (7). When the capacitors values are increased to 0.7pF or 0.8pF, then the resonance frequency is dependent on the coupling between CPW and resonator. The start, center, and stop frequencies are calculated in this case using Equations (6-8), having values of 3.12 GHz, 5.52 GHz, and 9.23 GHz, respectively.

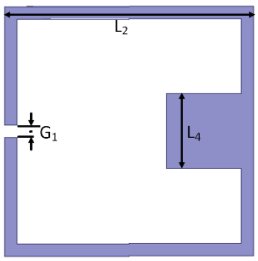

Fig. 13. Structure of the proposed novel miniaturized resonator.

The start, stop, and center frequencies of the resonator can be calculated using the following equations developed from the analysis. It is calculated from the analysis that the center frequency of the resonator lies at 5.5 GHz and so the resonator is responsible in case of narrowband behavior as well as band-notching behavior in the last scenario. In this way, the center frequency is utilized to develop narrow-band behavior as well as band-notched wide-band behavior:

$$f_{start} = \frac{\lambda g}{4} = \frac{300}{4(3L_2 + 3L_4 - G_1)\sqrt{\varepsilon_{eff(CPW)}}}, \quad (6)$$

$$= 3.12GHz$$

$$f_{center} = \frac{\lambda g}{2} = \frac{300}{2(3L_2 + 3L_4 - G_1)\sqrt{\varepsilon_{eff(CPW)}}} \sqrt{\frac{Z_{(cpw)}}{Z_{os(\,fstart)}}}, \quad (7)$$

$$= 5.52GHz$$

$$f_{stop} = \lambda g = \frac{300}{(3L_2 + 3L_4 - G_1)\sqrt{\varepsilon_{eff(CPW)}}} \sqrt{\frac{Z_{(cpw)}}{Z_{os(\,fstop)}}}. \quad (8)$$

$$= 9.23GHz$$

IV. MEASUREMENT DISCREPANCIES

The measurement discrepancies have been analyzed, and it is found that it is because of non-perfect cutting of the substrate edges while soldering the SMA connector. Due to non-perfect cutting, there arises a gap between SMA and ground plane that has been highlighted in Fig. 14. This measurement discrepancy can be depicted from Fig. 9 and Fig. 10 where the measurement has been performed for achieving band-notched wideband behavior.

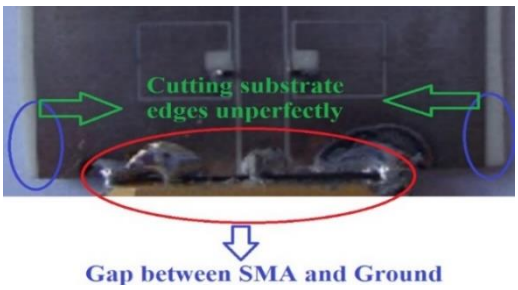

Fig. 14. Non-perfect cutting of substrate edges while soldering connector.

V. CONCLUSION

This paper presented continuously switchable behavior between narrowband (5.5 GHz WLAN), wideband (3-11 GHz UWB), and band-notched UWB using a miniaturized novel resonator. Three essential behaviors are achieved from the same resonator by adequately adjusting two capacitors. The first significant behavior produced by the antenna at 0.1pF is WLAN (5.5 GHz) operating frequency band. The second behavior from the antenna to work between 3-11 GHz UWB frequency band is achieved by changing the value of both capacitors to 0.8pF. Finally, band-notched UWB response is achieved by adjusting the position of the capacitor, and this band-notch behavior can also be tuned continuously between WLAN and WiMAX frequency band. The antenna is designed and fabricated for these behaviors and measured. Consistent radiation pattern and approximately flat antenna gain are observed because of the placement of the resonators in the partial ground plane. The antenna is also fabricated, and three different behaviors are measured using the proposed antenna for validation.

ACKNOWLEDGMENT

The authors would like to thank Islamic Azad University, South Tehran branch for their help & support sincerely.

REFERENCES

[1] H. M. Hizan, I. C. Hunter, and A. I. Abunjaileh, "Integrated dual-band radiating bandpass filter using dual-mode circular cavities," *IEEE Microw. Wireless Compon. Lett.*, vol. 21, no. 5, pp. 246-248, May 2011.

[2] Y. Yusuf, H. Cheng, and X. Gong, "A seamless integration of 3-D vertical filters with highly efficient slot antennas," *IEEE Trans. Antennas Propag.*, vol. 59, no. 11, pp. 4016-4022, Nov. 2011.

[3] X. L. Yang, J. C. Lin, G. Chen, and F. L. Kong, "Frequency reconfigurable antenna for wireless communications using GaAs FET switch," *IEEE Antennas Wireless Propag. Lett.*, vol. 14, pp. 807-810, Dec. 2015.

[4] M. Konca and P. A. Warr, "A frequency-reconfigurable antenna architecture using dielectric fluids," *IEEE Trans. Antennas Propag.*, vol. 63, no. 12, pp. 5280-5286, Dec. 2015.

[5] S. Danesh, S. K. A. Rahim, M. Abedian, and M. R. Hamid, "A compact frequency-reconfigurable dielectric resonator antenna for LTE/WWAN and WLAN applications," *IEEE Antennas Wireless Propag. Lett.*, vol. 14, pp. 486-489, 2014.

[6] M. Rahman "CPW fed miniaturized UWB tri-notch antenna with bandwidth enhancement," *Advances in Electrical Engineering.*, vol. 2016, pp. 1-5, 2016.

[7] P. Y. Qin, F. Wei, and Y. J. Guo, "A wideband-to-narrowband tunable antenna using a reconfigurable filter," *IEEE Trans. Antennas Propag.*, vol. 63, no. 5, pp. 2282-2285, May 2015.

[8] L. Ge and K.-M. Luk, "A band-reconfigurable antenna based on directed dipole," *IEEE Trans. Antennas Propag.*, vol. 62, no. 1, pp. 64-71, Jan. 2014.

[9] A. K. Horestani, Z. Shaterian, J. Naqui, F. Martín, and C. Fumeaux, "Reconfigurable and tunable S-shaped split-ring resonators and application in band-notched UWB antennas," *IEEE Trans. Antennas Propag.*, vol. 64, no. 9, pp. 3766-3776, Sep. 2016.

[10] H. Rajagopalan, J. M. Kovitz, and Y. Rahmat-Samii, "MEMS reconfigurable optimized E-shaped patch antenna design for cognitive radio," *IEEE Trans. Antennas Propag.*, vol. 62, no. 3, pp. 1056-1064, Mar. 2014.

[11] T. Li, H. Zhai, L. Li, and C. Liang, "Frequency-reconfigurable bow-tie antenna with a wide tuning range," *IEEE Antennas Wireless Propag. Lett.*, vol. 13, pp. 1549-1552, Aug. 2014.

[12] J. Shi, et al., "A compact differential filtering quasi-Yagi antenna with high-frequency selectivity and low cross-polarization levels," *IEEE Antennas Wireless Propag. Lett.*, vol. 14, pp. 1573-1576, 2015.

[13] G.-H. Sun, S.-W. Wong, L. Zhu, and Q.-X. Chu, "A compact printed filtering antenna with good suppression of upper harmonic band," *IEEE Antennas Wireless Propag. Lett.*, vol. 15, pp. 1349-1352, Apr. 2016.

[14] C. X. Mao, et al., "Dual-band patch antenna with filtering performance and harmonic suppression," *IEEE Trans. Antennas Propag.*, vol. 64, no. 9, pp. 4074-4077, Sep. 2016.

[15] M. M. Fakharian, P. Rezaei, A. A. Orouji, and M. Soltanpur, "A wideband and reconfigurable filtering slot antenna," *IEEE Antennas Wireless Propag. Lett.*, vol. 15, pp. 1610-1613, 2016.

[16] S.-G. Mao, S.-L. Chen, and C.-W. Huang, "Effective electromagnetic parameters of novel distributed left-handed microstrip lines," *IEEE Trans. Microw. Theory Tech.*, vol. 53, no. 4, pp. 1515-1521, 2005.

[17] A. M. Nicholson and G. F. Ross, "Measurements of the intrinsic properties of materials by time-domain techniques," *IEEE Trans. Instrum. Meas.*, vol. 19, no. 4, pp. 377-382, 1970.

[18] W. B. Weir, "Automatic measurements of complex dielectric constant and permeability at microwave frequencies," *Proc. IEEE*, vol. 62, no. 1, pp. 33-36, 1974.

[19] M. NaghshvarianJahromi and M. Tayarani, "Defected ground structure band-stop filter by semi-complementary split ring resonators," *IET Microwaves, Antennas & Propagation*, vol. 5, no. 11, pp. 1386-1391, Aug. 19, 2011.

[20] M. NaghshvarianJahromi and A. Ghorbani, "On the behavior of compact ultrawideband tunable bandwidth semi-complementary split ring resonator bandpass filter," *Microwave and Optical Technology Letters*, vol. 57, no. 1, pp. 256-263, 2015.

Mansour NejatiJahromi was born in 1970 in Jahrom. He received the B.S. degree in Electronic Engineering from SSA University of Science and Technology, Tehran, Iran, in 1993. He also obtained the M.S. degree in Communication from K. N. Toosi University of Technology, Tehran, Iran, in 1999, and the Ph.D. degree in Communications from Amirkabir University of Technology (AUT), Tehran, Iran, in 2008. He is an Assistant Professor in the Department of Electronic and Electrical Engineering, SSA University & Islamic Azad University, Tehran South Branch.

Mahdi Naghshvarianjahromi received M.S. degree in Communications engineering from Amirkabir University of Technology (AUT) in 2014. He is currently a Ph.D. student in Electrical and Computer Engineering at McMaster University. His current research interests are antennas, arrays, all devices throughout whole RF spectrum, fiber optic communications system and nonlinear impairment mitigation, smart home and automatic disease diagnosis, computer sciences, statistical processing and brain-like intelligence.

MuhibUr Rahman received the M.S. degree in Electrical (Telecommunication) Engineering from Military College of Signals, National University of Sciences and Technology, (NUST) Islamabad, Pakistan, in March 2016. Currently, he is a graduate Research Assistant in Electronics and Electrical Engineering at Dongguk University, Seoul, Republic of Korea. His current research interests include Narrow and Wide-band antennas, UWB band-notched antennas, MIMO UWB antennas, Microstrip bandpass and bandstop filters and metamaterial inspired structures. Rahman has published several research papers, and he is the Reviewer of PIER series, Sensors, Applied Sciences, IJMWT, MOTL, and AEU.

High-Resolution Ultra-Wideband Material Penetrating Radar (UWB-MPR) using Modified Configuration of Receiver Antennas

Mohammad Ojaroudi [1] and Hashem Jahed [2]

[1] Islamic Azad University, Ardabil Branch, Ardabil, Iran
m.ojaroudi@iauardabil.ac.ir

[2] Islamic Azad University, Mahshahr Branch, Mahshahr, Iran
hashem_jahed@yahoo.com

***Abstract*—** In this paper, in order to implement the see through the wall and ground penetrating radars using vector network analyzer at the first step we present a modified UWB Tapered Slot Antenna (TSA) and Wilkinson power combiner. In the following the main purpose of this paper is employing a new technique using modified UWB antennas and power combiner to improve the reflected signal of localizing underground metal for 1D visualization of material penetrating radar results. In the last section two scenarios of GPR profiles with a single receiver antenna and dual receiver antennas over ground surface with buried metal target are presented to validate the accuracy of the proposed approach. This signal collecting technique collect more energy form reflected signals in contrast with conventional MPR. Hence, stronger reflection is available to achieve higher chance for target localization.

***Index Terms*—** Material Penetrating Radar (MPR), See through the Wall, Tapered Slot Antenna (TSA), Wilkinson Power Combiner.

I. INTRODUCTION

Material penetrating radar (MPR) is a nondestructive testing (NDT) technique which uses electromagnetic waves to investigate the composition of non-conducting materials either when searching for buried objects or when measuring their internal structure. Information that can be obtained from GPR includes the depth, orientation, size and shape of buried objects, and the density and water content of soils [1]. The GPR performance is associated with the electrical and magnetic properties of local soil and buried targets. The choice of the central frequency and the bandwidth of the GPR are the key factors in the GPR system design. Although the higher frequencies are needed for better resolution and detailed echo to determine small size objects, the lower frequencies are preferred to detect something buried too deep because of the dramatically increased attenuation of the soil with increasing frequency. Thus, the pulsed GPR is used in order to benefit from both low and high frequencies [2-3]. The pulsed GPR systems acquire pulse response in time domain directly. It is the simplest and understandable method that allows getting unique operation flexibility of the GPR system. Tapered slot antennas/arrays are good candidate for UWB radar system because of their wideband performance and directional radiation characteristic. But the phase center variation with frequency may bring few mm errors in target localization [4-5].

In this paper, we explore the advantages of generating a novel collecting reflected signal technique, similar to the ordinary receiver but instead of single receiver antenna, two modified antennas will be employed. The advantage conferred by "dual-antenna GPR" is that more energy is available at reflected signal than with conventional GPR, subsequently a relatively higher resolution in identifying the reflected signal is achieved. Measured results using vector network analyzer are presented to validate the effectiveness of the proposed method for precisely calculating the time-dependent location of underground targets.

II. MODIFIED UWB TAPERED SLOT ANTENNA AND WILKINSON POWER COMBINER DESIGN

One of key issues in ultra-wideband (UWB) imaging systems is the design of a compact antenna while providing wideband radiation characteristics over the whole operating band. It is a well-known fact that printed TSA antennas present really appealing physical features, such as simple structure, small size and high gain [6]. The configuration of the two-element TSA array is depicted in Fig. 1. A Rogers RT5880 substrate was used, with a relative permittivity of 2.2 and a thickness of 31 mils [7]. The proposed structure is designed based on the antenna presented in Ref. [8]. In this type of antennas, phase center location is shifted by changing frequency. Therefore, one of the advantageous of our proposed structure is solving this phase center

Submitted On: April 18, 2016
Accepted On: October 25, 2016

shifting problem in based on using exponential tapered curve instead of elliptical curve [9]. In addition, the proposed antenna has 16% size reduction in comparison of the antenna in reference [8].

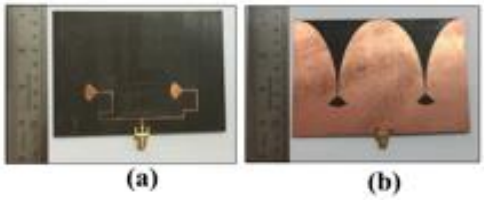

Fig. 1. Photograph the realized tapered slot antenna: (a) top view and (b) bottom view.

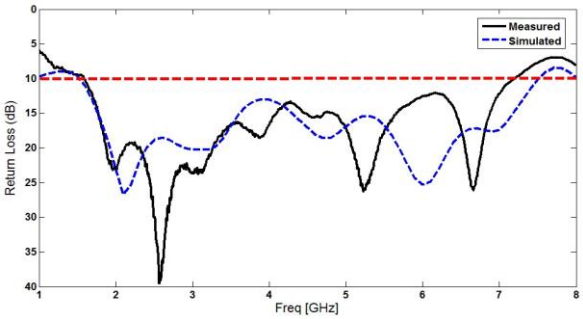

Fig. 2. Measured and simulated return loss results for the proposed antenna.

Figure 2 shows the measured and simulated return loss characteristics of the proposed antenna. The fabricated antenna has the frequency band of 1.57 to over 7.0.4 GHz. As shown in Fig. 2, there exists a discrepancy between measured data and the simulated results. This discrepancy is mostly due to a number of parameters such as the fabricated antenna dimensions as well as the thickness and dielectric constant of the substrate on which the antenna is fabricated, the wide range of simulation frequencies. Figure 3 shows return loss measurement setup for the Wilkinson power combiner. Two 50Ω terminations at output ports; input port connected to an Agilent network analyzer. Also, measured return and insertion losses for the proposed power combiner are shown if Fig. 4.

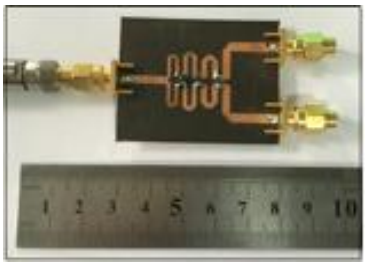

Fig. 3. Return loss measurement setup for the Wilkinson power combiner.

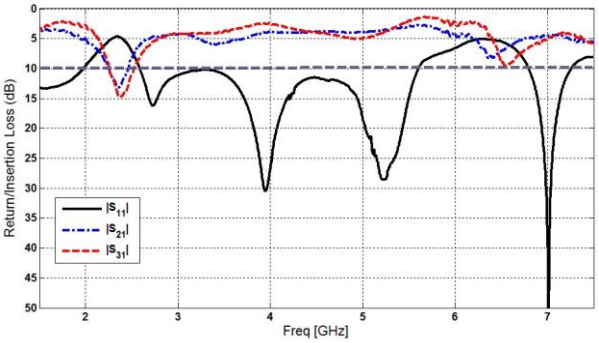

Fig. 4. Measured return and insertion losses for the proposed power combiner.

III. THEATRICAL BACKGROUND OF MATERIAL PENETRATING RADAR

The MPR schematic for the proposed wooden wall surface with metal plate target is shown in Fig. 5. Typically, for ideal impulse excitation we can calculate exactly the amount of reflected energy at an interface as follow:

$$\Gamma_{i,i+1} = \frac{\sqrt{\varepsilon_{r(i+1)}} - \sqrt{\varepsilon_{r(i)}}}{\sqrt{\varepsilon_{r(i+1)}} + \sqrt{\varepsilon_{r(i)}}}, \quad (1)$$

where Γ is the reflection coefficient and $\varepsilon_{r(i)}$ and $\varepsilon_{r(i+1)}$ are the dielectric constants. Similarly, for ideal impulse excitation signal we can calculate precisely the thickness of a layer as follow:

$$d_i = \frac{C.t_i}{\left(2\sqrt{\varepsilon_{r,i}}\right)}, \quad (2)$$

where d_i is the thickness of layer i, t_i the total travel time through that layer, C is the speed of light and $\varepsilon_{r,i}$ the dielectric constant of the medium.

In the ground penetrating radar's scenario, the penetration depth of GPR waves (in a low-loss medium) can be approximated as:

$$\delta(m) = 25\lambda = 25\frac{c}{f\sqrt{\varepsilon_r}}. \quad (3)$$

The vertical resolution (in a low-loss medium) is around 0.01δ [3].

For ideal impulse as excitation signal we can calculate exactly locations of discontinuities as follows: but in practice one can see that the waveform is distorted after the reflection and propagation. Because GPR receives signals already reflected from some distance, the time needed for passing the way back to the object and forth is longer than in a case when the antenna is situated slightly above the examined object. Because of this the cross-section of a pipe will be presented in the reading as a hyperbole [9].

The first step in design material penetrating radar is selecting the operation frequency. High frequency leads to high azimuth resolution, while relatively low frequency

allows penetrating through walls. 2-6 GHz is regarded as the optimal frequency band for seeing through high-loss materials, such as brick-wall and concrete wall.

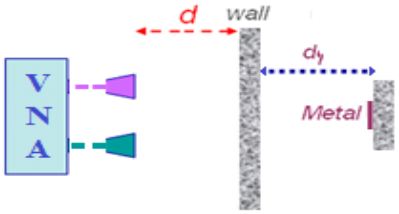

Fig. 5. The MPR schematic for the proposed wooden wall surface with metal plate target.

IV. EXPERIMENTAL RESULTS AND DISCUSSIONS

A. See through the wall radar prototype

Experiments have been carried out to measure the radar prototype using vector network analyzer as a frequency modulated continues wave transceiver. The first experiment was performed by using a metal plate target, as the floor plan of the experimental setup presented in Fig. 6. The VNA was placed in the Antenna Laboratory as shown in Fig. 6 (b), with the transmitting and receiving TSA facing the same direction. The spacing between the transmitting antenna and the receiving antenna is 10 cm. The metal plate's size is 10×8 cm^2 and it is put at 25 cm standoff distance to wooden wall. The wooden wall is put at 15 cm standoff distance to the radar system to acquire the radar response.

(a)

(b)

Fig. 6. Experimental setup of the down range resolution measurement using dihedral as radar object: (a) antennas, wooden wall and metal target, and (b) VNA using as a FMCW transceiver.

Most of the UWB imaging algorithms reported in literature have used the time-domain signals [4]. This approach requires transforming of the earlier acquired frequency-domain reflection coefficient data. Therefore, a short and efficient CAD procedure for the design is performed. This is done using an inverse Fourier transform (IFT) from the impulse response. The CAD procedure has mainly two steps. The first step is a frequency to time domain transformation. The inverse discreet Fourier transform program is used for matching between time steps and frequency steps [10]. The second step is to implement a sampling Hamming window so as to get a smooth time response. Using the [S] parameters of the environment and by getting from Agilent Vector Network Analyzer (VNA), the design of the material transceiver is performed using our full-scale computer simulation program.

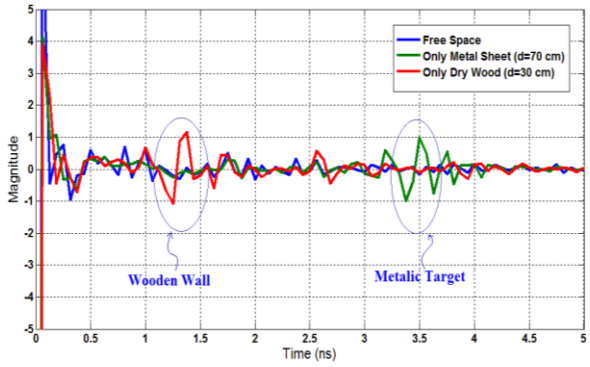

(a)

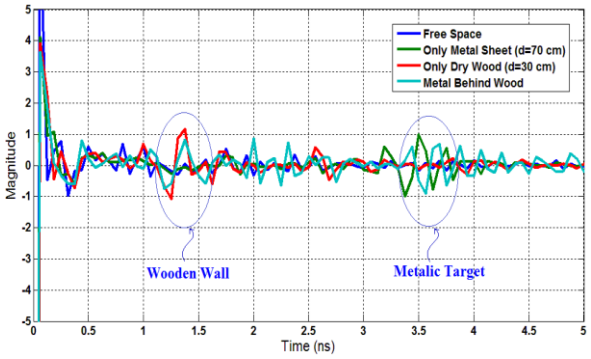

(b)

Fig. 7. Measured reflected signal from see through the wall experimental setup: (a) detection of the wooden wall and the metal target separately, and (b) detection metal target behind the wooden wall.

Figure 7 shows measured reflected signal from see through the wall experimental setup. The measured results in Fig. 7 (a) predict the outline of the wooden block target, as well as its location. In order to illustrate the proposed method performance Fig. 7 (b) describes the reflected voltages of wooden wall, metal targets using the proposed experiments setup and makes a

comparison among them. Figure 7 (b) introduces the recovered signal of the metal plate when it was placed at a distance of 75 cm in the back of the wooden wall. The acquired radar signal indicates a down range resolution of approximately 2 cm, validating the theoretical analysis result. It is worth mentioning that the recovered signal also predicts the locations of the wooden wall, in addition to the metal target. The experiment is performed in a low-contrast condition to emulate the true situation that most of the metal plates.

B. Ordinary ground penetrating radar

The schematic and realized configurations of the UWB ground penetrating radar, which is investigated here, is illustrated in Fig. 8. In the GPR radar experimental setup, we have collected the signals at two scenarios: the first from background only using single-receiver antenna, and the second using with dual-receivers' antenna. The ordinary GPR test field with metal plate located underground is shown in Fig. 8. Figure 9 present the scan A which represents the passing over a zone in which measured GPR was buried in vertically position. Figure 9 shows the original signal, before using the dual-receiver antennas technique. It can be observed that in the case of real measurements, the reflected signal is very noisy, containing, in addition, clutters. The stronger lines are from the strong direct wave form soil surface and background reflection. As shown in Fig. 9, in the ordinary GPR case the metal object isn't clearly distinguished.

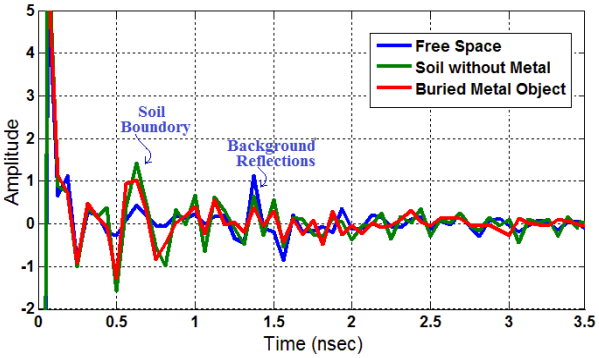

Fig. 9. Measured reflected signal from ordinary GPR setup in the first scenario.

C. Modified GPR configuration

To improve the resolution of the GPR results and extract the target reflection, the received signals are collected using the proposed reflected signal collecting method using dual-receiver antennas as shown in Fig. 10. By subtracting the two signals with and without the target, the newly acquired signals are used in the signal recovery process to remove the clutters. In order to show the effects of on this new method improvement, Figure 11 shows the measured reflection waveform with different scenarios. In other hand after an initial guess of the target location, it is found out from Fig. 11 that the desired signal is totally immersed in the noise signals due to the low-contrast problem.

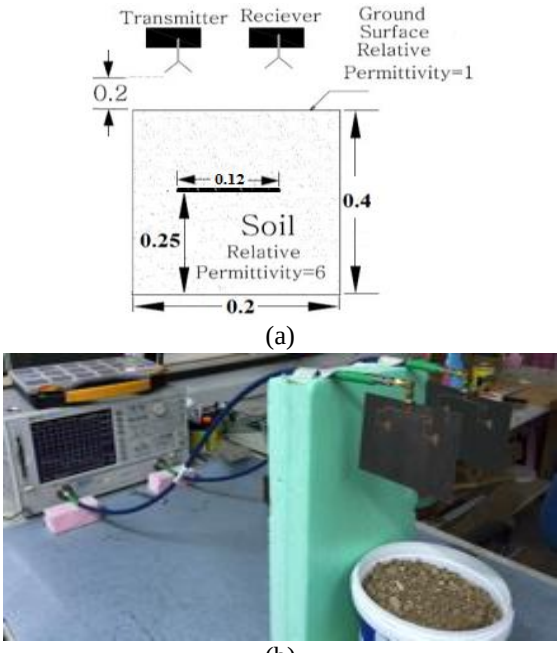

Fig. 8. Experimental setup of the ground penetrating radar with single receiver antenna: (a) schematic and (b) realized.

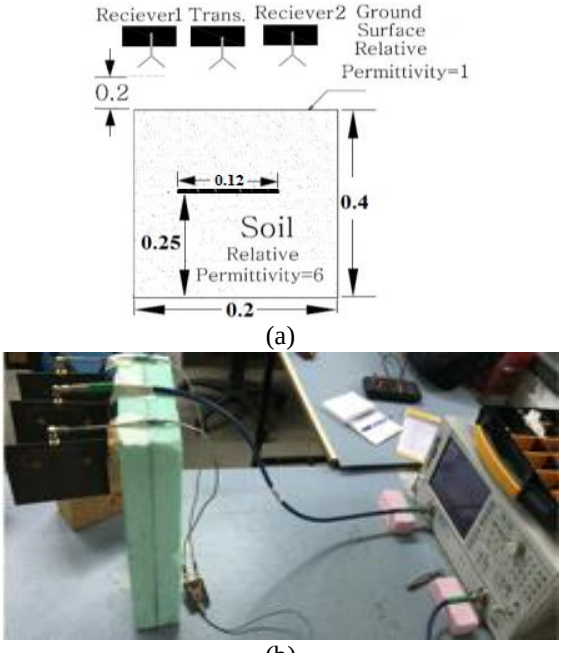

Fig. 10. Experimental setup of the ground penetrating radar with dual receiver antennas: (a) schematic and (b) realized.

As shown in Fig. 11, measured results of the proposed method are compared by free space reflection, ones with only soil without target and the ordinary GPR. It is clearly shown to that GPR results with this proposed collecting reflected signal have very good localization resolution and the peak amount errors at the center of target locations from ideal GPR results are small in this case in our measurement [11]-[12]. It is apparent from this figure, that the energy in the modified GPR reflection exceeds the energy in the ordinary GPR reflection. Therefore, the modified GPR results follow the target more closely than does the ordinary GPR results. Also several small scatters were founded. According to the resolution, the depth resolution in the vertical plane and the distance resolution between two objects can be considered. The depth resolution of the ten of centimeters is obtained. The reason of higher depth resolution is that the lower frequency range is used.

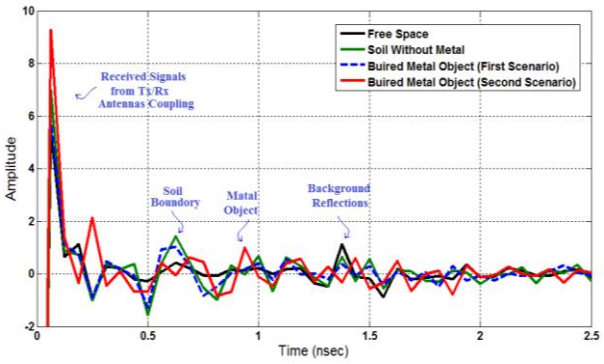

Fig. 11. Measured signal returns after using the proposed reflected signal collecting method.

V. CONCLUSION

This paper has presented UWB microwave imaging system to detect and locate small targets in a see through the wall and ground penetrating radar setups using the frequency-domain data acquired by a VNA and TSA. Additionally, a novel approach for high resolution GPR system using a modified receiver antenna configuration to improve the reflected signal of localizing underground metal target is presented. The validity of the presented system and its target detection algorithm has been verified via experiments in examples. Results obtained by our GPR system prove that our system has a good ability to finding buried targets. The proposed modified GPR is very practical as it is based on more realistic reflected signals from various angles rather than assuming single reflected signal. The measurements show that the developed UWB-GPR system has a good ability in detecting buried metal object, even small targets of several centimeters.

REFERENCES

[1] I. Giannakis, A. Giannopoulos, and C. Warren, "A realistic FDTD numerical modeling framework of ground penetrating radar for landmine detection," in *IEEE Journal of Selected Topics in Applied Earth Observations and Remote Sensing*, vol. 9, no. 1, pp. 37-51, Jan. 2016.

[2] Z. Lin and W. Jiang, "Ground penetrating radar B-scan data modeling and clutter suppression," *2015 Fifth International Conference on Instrumentation and Measurement, Computer, Communication and Control (IMCCC)*, Qinhuangdao, pp. 397-402, 2015.

[3] S. Tan, H. Zhou, and L. Xiang, "An automatic framework using space-time processing and TR-MUSIC for subsurface imaging," *Ground Penetrating Radar (GPR), 14th International Conference on*, Shanghai, 2012, pp. 286-290, 2012.

[4] C. Warren, A. Giannopoulos, and I. Giannakis, "An advanced GPR modelling framework: The next generation of gprmax," *Advanced Ground Penetrating Radar (IWAGPR), 8th International Workshop on*, Florence, 2015, pp. 1-4, 2015.

[5] M. Ojaroudi, S. Bila, and F. Torres, "A new approach of multi-parameter UWB antenna modeling based on knowledge-based artificial neural network," *12th European Conference on Antennas and Propagation (EUCAP)*, London, 9-13 Apr. 2018.

[6] Q. Liu, Y. Wang, and A. E. Fathy, "A compact integrated 100 GS/s sampling module for UWB see through wall radar with fast refresh rate for dynamic real time imaging," *Radio and Wireless Symposium (RWS), 2012 IEEE*, Santa Clara, CA, pp. 59-62, 2012.

[7] RT/duroid® 5880 Laminates, Rogers Corporation. www.rogerscorp.com

[8] Y. Wang, M. Kuhn, and A. E. Fathy, "Advanced system level simulation of UWB three-dimensional imaging radar for performance limitation prediction," in *Proc. IEEE MTT-S Int. Microw. Symp. Dig.*, Anaheim, CA, pp. 165-168, May 2010.

[9] M Ojaroudi, E. Mehrshahi, and A. Fathy, "A novel approach for the design of modified excitation signal using a narrow pulse generator for high-resolution time domain reflectometry applications," *Microwave and Optical Technology Letters*, vol. 56, no. 12, pp. 2987-2990, 2014.

[10] H. Ebrahimian, M. Ojaroudi, and S. Ojaroudi, "Novel approach of high resolution imaging using modified excitation signal for ground penetration radar (GPR) applications," ACES Journal, vol. 31, no. 8, pp. 914-918, Aug. 2016.

[11] A. Giannopoulous, "Modelling ground penetrating

radar by GprMax," *Science Direct*, pp. 755-762, 2 Aug. 2005.

[12] M. Ojaroudi, H. Ojaroudi, and M. Salimi, "Towards super-resolution impulse-radar based on time-space scanning using reconfigurable beamforming and waveform-diversity," *11th European Conference on Antennas and Propagation (EUCAP)*, Paris, pp. 1261-126, 2017.

Dual Layer Convoluted Frequency Selective Surface Design in the 2.4 GHz and 5.8 GHz ISM Bands

Bora Döken and Mesut Kartal

Department of Electronics and Communications Engineering
Istanbul Technical University, Maslak 34469, Istanbul, Turkey
dokenb@itu.edu.tr, kartalme@itu.edu.tr

Abstract ─ Indoor wireless devices operating in 2.4 GHz and 5.8 GHz ISM bands have a wide range of usage area. However, mutual interference in neighboring networks degrades the system performance. It can also cause significant problems in secure personal communications on such wireless networks. Covering building walls with a band stop frequency selective surface (FSS) can be an efficient solution for such problems. Many available FSS structures are designed to have a single stop band. They are also subject to narrow incidence angle range and sensitive to the polarization of the wave. On the other hand, in some studies, FSSs with double stop band are designed such that the second stop band is to be the harmonic frequency of the first band. In this study, a dual layer frequency selective surface element geometry is introduced. This geometry is capable of at least 20 dB attenuation of incoming signals within the incident angle range from 0 to 60 degrees and for all polarizations. Another important contribution is that a periodic cell size of approximately one-tenth of the wavelength corresponding to 2.4 GHz is obtained. Besides, a new design methodology that enables almost independent optimization of each layer at its resonance frequency is also introduced.

Index Terms ─ Frequency selective surface, FSS, indoor propagation, interference, periodic structures, wireless communication, Wireless Local Area Network (WLAN).

I. INTRODUCTION

The utilization of wireless networks within buildings in ISM (The industrial, Scientific and Medical) frequency bands has been grown rapidly in recent years. But, the resulting mutual interferences among the adjacent networks degrades the system performances. Another important problem is the security risks of personal communication on such wireless networks. Some advanced signal processing methods, specific antenna designs and encryption techniques have been recommended to solve these problems in [1, 2]. An efficient solution for interference and security risks encountered within the wireless networks is to affix a frequency selective surface (FSS) onto subsisting prevalent construction materials considering the filtering properties of FSSs at desired resonance frequencies [3, 4, 5, 6, 7, 8].

Periodic conducting structures, known as frequency selective surfaces, have filter characteristics depending upon their geometries when interacting with electromagnetic waves [9]. They have been utilized in many applications and systems such as antennas, radomes, wireless local area networks (WLAN) [9].

The isolation capabilities of band stop FSSs have been investigated by different researchers for WLAN security and interference mitigation in indoor environments [4, 5, 6, 7]. According to the given results, FSSs are capable of providing minimum 10 dB isolation between two adjacent rooms in ISM bands [6]. These researches also showed that wireless signals in an indoor environment have a wide range of incidence angles. Although 2.45 GHz and 5.8 GHz ISM bands have been investigated individually for FSS designs, there is a gap in the literature for double band design, which stops both ISM bands within a single FSS structure [10].

In this study, 20 dB attenuation on the transmission (S_{21}) parameter is desired for ISM bands of interest while providing maximum transmission in other frequency bands for a wide range of oblique incidence angles and for all polarizations. To this end, two different convoluted FSS geometries are designed in a dual layer structure. Such a structure can attain frequency stability for oblique incidence angles and shifts grating lobes to higher frequencies. Multiple layer FSS structures are also considered to achieve maximum attenuation levels for all ISM frequency bands. However, mutual effect between each layer is an important problem for the optimization process of multi-layer structures. Inspection of the transmission curves clearly shows that cascaded periodic structures (double layer), compared to a single layer structure, have almost same frequency characteristic with an observing shift at the resonance frequency [9]. Therefore, identical geometries on each layer is considered to optimize each layer independently.

Equivalent circuit (EC) model is applied to

Submitted On: December 29, 2016
Accepted On: April 21, 2018

understand the influence of geometrical parameters of the FSS geometries on their frequency responses. EC model and a finite element method solver for electromagnetic structures (Ansoft HFSS v.15 software) are performed together to analyze and optimize the proposed FSS structure rapidly. HFSS simulates a unit cell in an infinite periodic structure by using periodic boundaries with Floquet ports. When a Floquet port is defined, a set of modes known as Floquet modes represent the fields on the port boundary. The Floquet modes are plane waves with propagation direction set by the frequency, phasing and geometry of the periodic structure.

The periodic cell size of $0.1\lambda_{2.4GHz}$ is achieved by meandering the conducting geometries of FSS. Besides having 90% of miniaturizing, proposed FSS element geometry has frequency stability at all polarizations with a minimum 20 dB of attenuation for incident angles varies from 0^0 to 60^0.

The paper is organized as follows: Section II explains FSS theory and FSS analysis methods. Multilayer FSS design process, simulation and measurement results are presented in Section III, and the results are discussed in Section IV.

II. FSS THEORY

Frequency selective surfaces are periodic structures that filter certain frequency bands depending on their geometries during interaction with electromagnetic waves. Numerical methods are mostly employed to analyze the frequency characteristics of FSS geometries [11, 12]. Despite their accuracy in analysis, these techniques do not provide information into the physics behind the structures. On the contrary, EC models are helpful for determining the effect of the geometrical parameters on the frequency characteristics of the FSSs [13]. FSS geometry can be represented in the EC model by a single series LC circuit shunted to a transmission line of free space characteristic impedance (Z_o), which is seen in Fig. 1. The width of the gap (s) and the gap (g) between periodic element geometries primarily determine the equivalent capacitance ($C \propto \frac{s}{g}$). The length (d) and the width (w) of the current path primarily determine the equivalent inductance ($L \propto \frac{d}{w}$) of periodic element geometries.

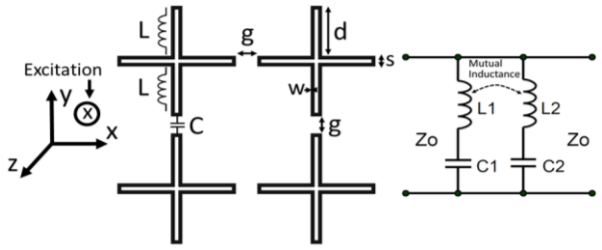

Fig. 1. FSS and its equivalent circuit.

Equivalent impedance (Z) and the resonance frequency (f_0) of such an FSS structure are derived from the EC model described here and can be expressed as in Eq. (1). It can be concluded that the impedance of FSS has one zero at a certain frequency and therefore, the wave is unable to transmit through the surface at that frequency:

$$Z = jwL + \frac{1}{jwC} = j\left(wL - \frac{1}{wC}\right),\ f_0 = \frac{1}{2\pi\sqrt{LC}}. \quad (1)$$

From the expressions in Eq.1 and EC model in Fig. 1, it is obvious that the relationship between the geometrical parameters and the frequency characteristic of the FSS can be determined by using the EC model. Therefore, EC models and numerical analysis techniques can also be performed together to achieve the desired frequency characteristics rapidly [14]. It is important that the periodic cell size should be smaller enough than the resonance wavelength to reduce the sensitivity of the first resonant frequency to the angle of incident wave [9]. Obtaining smaller cell sizes is generally achieved by increasing the effective electrical length of the metallic patch [15]. This method is done either by using lumped elements in every cell of the FSS or meandering the excited metal patch. Using lumped elements in every FSS cell is an effective way to reduce unit cell sizes. However, their costs are high and their electrical properties depend on temperature, moisture etc. Therefore, meandering of the conducting paths of FSS geometries is considered to reduce unit cell size in this study as in [16].

Several methods are defined in the literature in order to achieve multiple stop band FSS behavior [17]. Hybrid geometries are used in one unit cell to achieve multiple stop band behavior [9]. In this method, the distance between the same resonant parts of the two adjacent unit cells cannot be shortened sufficiently in order to have a good frequency stability. As another method, multi-layer FSS structures are used to achieve multiple stop bands. In this study, two different convoluted FSS geometries are used in a dual layer structure to achieve frequency stability for oblique incidence angles. However, an important problem in the optimization process is the undesirable consequences of the mutual effect between each layer. Fortunately, using similar unit cell geometries in each layer enables us to optimize each layer independently and consequently, this approach is proposed in this paper to overcome such mutual effect problems.

III. DESIGN & MEASUREMENT

A band stop FSS design with a good attenuation performance in both 2.45 GHz and 5.8 GHz ISM bands for oblique incidence angles ranging from 0 to 60 degrees is aimed in this study. In order to achieve maximum attenuation and stable frequency characteristics, a novel dual layer convoluted FSS structure is considered. An EC model of a general dual layer FSS structure having different periodic element geometries on each layer is

shown in Fig. 2. Each layer of the structure acts as a reflector for the desired WLAN frequency bands and can be modeled by a serial LC circuit. The coupling effect between two layers of the FSS is represented by a mutual inductance. Similar to the basic structure described in Section 2, the capacitance and inductance values of the equivalent LC circuits of the dual layer structure can be determined by using the periodic element geometries of each layer for the desired resonance frequencies.

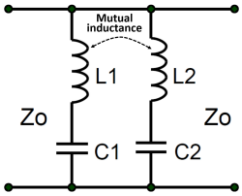

Fig. 2. EC model of a dual layer FSS structure.

Equivalent impedance of the dual layer FSS can be derived from the circuit model given in Fig. 2 as:

$$Z = \frac{(1 - w^2 L_1' C_1)(1 - w^2 L_2' C_2)}{\mathrm{jw}(C_1 + C_2 - w^2 C_1 C_2 (L_1' + L_2'))} \quad (2)$$

$$L_1' = L_1 - M,\ L_2' = L_2 + M.$$

It is obvious that FSS behaves as a metal wall when the impedance Z approaches to zero and as a result, the resonance frequencies of the FSS are derived as:

$$f_{2.45GHz} = \frac{1}{2\pi\sqrt{L_1' C_1}},\ f_{5.8GHz} = \frac{1}{2\pi\sqrt{L_2' C_2}}. \quad (3)$$

As mentioned in Section 2, the desired frequency response can be obtained by changing the element dimensions of the periodic structure considering the relationships between the equivalent capacitance and inductance values and element geometry. It is well known that frequency characteristic of a single layer FSS is the same with a multilayer FSS structure having the same FSS geometries on each layer [10]. Therefore, using identical geometries on each layer allows us to reduce the mutual effect between the layers and thus to optimize each layer individually.

In the first design stage, "Square Loop" element (Fig. 3 (a)) geometry, which is suitable for meandering, is selected. The optimization process starts with the initial selection of the FSS geometry's dimensions in accordance with the desired resonance frequency. However, since the additive higher frequency stop band (5.8 GHz) mostly pushes the first stop band to lower frequencies [9], this geometry is convoluted and optimized to achieve a stop band with a slightly higher frequency than the lowest (first) ISM band (2.4 GHz). The analysis for the observed frequency shifts in the frequency response obtained from HFSS simulations is done. Then, these analysis results are used to predict new dimensions of the FSS elements according to relationships given in Section 2: ($C \propto \frac{s}{g}$, $L \propto \frac{d}{w}$). Subsequently, these new dimensions are optimized by using parametric analysis feature of HFSS software. Thus, the optimization process is shortened by utilizing EC model.

EC model is only valid for the fundamental Floquet modes. In this work, only fundamental modes propagate in the intended frequency band due to having miniaturized structure. However, HFSS simulations are executed for 10 Floquet modes, due to the proposed work is double-layered.

Dimensions and the layout of the proposed FSS geometry are depicted in Fig. 3 (b). At the end of the optimization process, the following dimensions are obtained: h=1.6 mm (thickness of the FR4 substrate), g=1.06674 mm (gap between the periodic elements), w1=0.5288, p=13.5474, b1=1.3221, b2=1.3221, e=0.6346, a1=1.5865, a2=1.6923 and a3=1.6923.

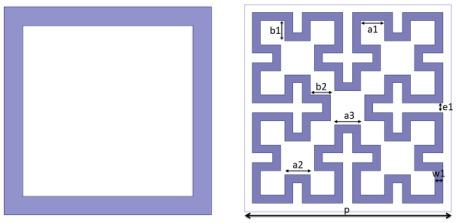

(a) (b)

Fig. 3. FSS geometries: (a) "Square Loop" and (b) "Convoluted Square Loop".

Figure 4 shows the obtained results at incidence angle of 45^0 for both TE and TM polarizations, respectively. According to the obtained results, minimum 20 dB attenuation is achieved at 2.4 GHz ISM band for oblique incidence angles from normal to 60^0 for all polarizations.

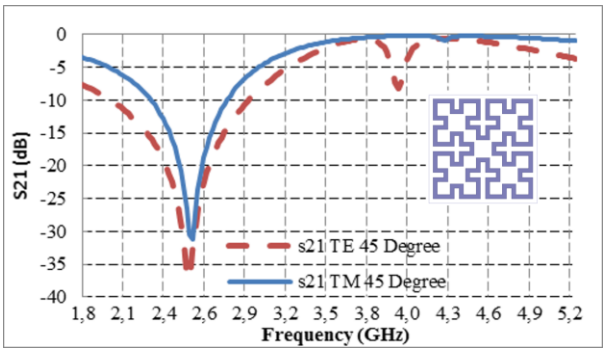

Fig. 4. S_{21} frequency curves for "Convoluted Square Loop" geometry, TE and TM polarization ($\theta=45^0$).

In the second stage of the double layer FSS design, in order to observe the coupling effect between the layers, "Convoluted Square Loop" periodic element

geometry (Fig. 5) is used on each layer of the FSS with the same parameter values.

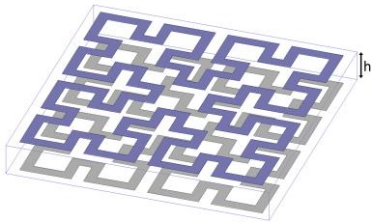

Fig. 5. Double layer periodic element structure.

Simulations are performed by HFSS software. Same frequency behavior (Fig. 6) is obtained with a shift in the resonance frequency as expected [8]. A slight increase over the bandwidth is also observed for the dual layer FSS.

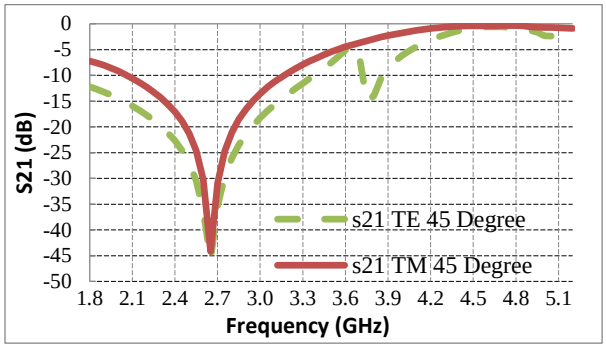

Fig. 6. S_{21} frequency curves for dual layer "Convoluted Square" geometry for TE and TM polarization ($\theta=45^0$).

According to EC model, the resonance frequency of the FSS is inversely proportional to the equivalent inductance values ($L\propto\frac{d}{w}$) which are mainly determined by the length and the width of the current path of the FSS. In order to obtain the second resonance frequency at 5.8 GHz, effective electrical length of the conducting patch is shortened on the top layer as shown in Fig. 7 with different design phases.

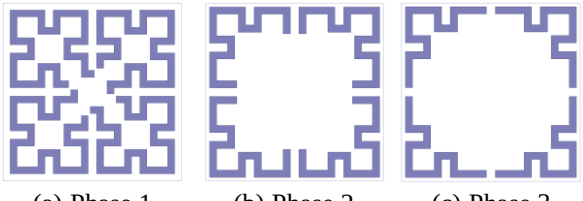

(a) Phase 1 (b) Phase 2 (c) Phase 3

Fig. 7. Design phases of the FSS geometry on the top layer.

Obtained results show that the use of identical geometries on each layer enables us to optimize the resonance frequencies independently (Fig. 8). It is observed that any change of the effective current path length on the top layer has a minor effect on the resonance frequency of the bottom layer (2.45 GHz). On the other hand, effective electrical length of the conducting patch on the top layer affects the second resonance frequency (5.8 GHz) directly.

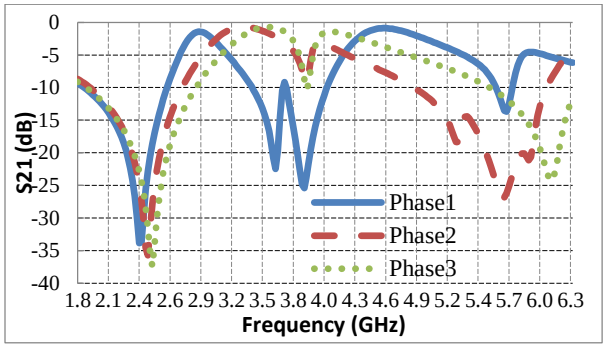

Fig. 8. S_{21} frequency curves for TE polarization for $\theta=45^0$ (Phase 1, Phase 2, Phase 3).

As a result, "Phase 3" FSS geometry is selected as the final geometry of the top layer in the last design stage. In order to shift the second resonance frequency to 5.8 GHz and to narrow its bandwidth, top layer geometry is slightly scaled up. The dimensions and the layout of the final FSS structure are depicted in Fig. 9. The thickness (h) of the FR4 substrate (relative dielectric permittivity 4.54, loss tangent 0.027) is 1.6 mm, the gaps between the periodic elements are 0.36 mm (g1), 0.48 (g2) for the top and bottom layers, respectively. The other parameter values (in mm) are w1=0.52, w2=0.56, p=13.54, b1=1.32, b2=1.32, b3=1.55, e1=0.63, e2=0.67, a1=1.58, a2=1.69, a3=1.69, a4=2.23, a5=1.67 and a6=1.78. According to the obtained simulation results (Figs. 10-11), at least 20 dB attenuation is achieved at oblique incidence angles from normal to 60^0 for all polarizations. A periodic cell size (p=13.54 mm) which is less than one-tenth of the first resonance wavelength is obtained in the design which leads frequency stability within a wide range of incidence angles.

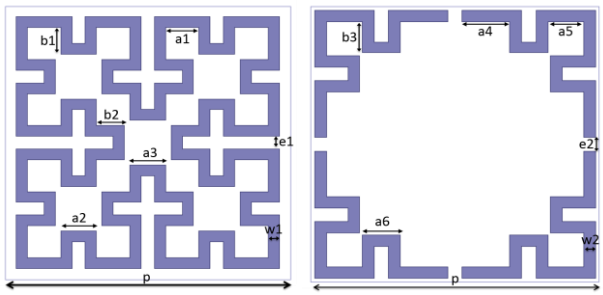

(a) Bottom layer (b) Top layer

Fig. 9. "Updated Phase 3" dual layer FSS geometry.

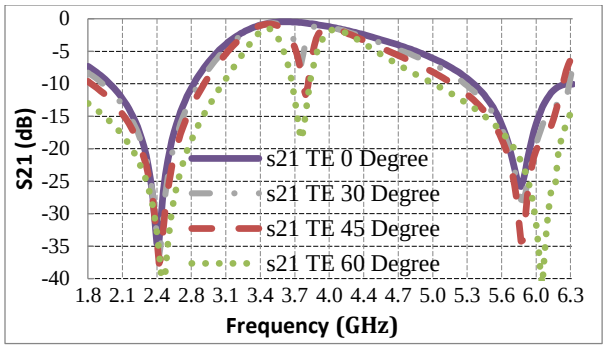

Fig. 10. S_{21} frequency curves for "Updated Phase 3" dual layer FSS geometry for TE polarization ($\theta=0^0$, $\theta=30^0$, $\theta=45^0$, $\theta=60^0$).

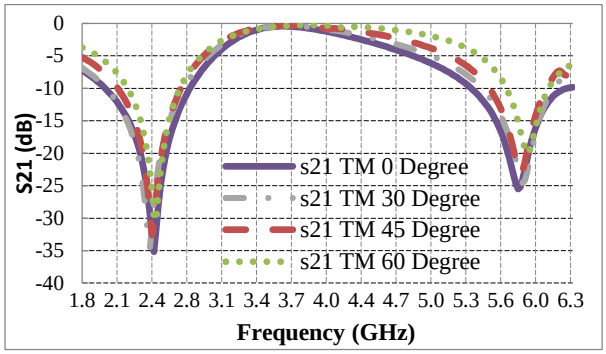

Fig. 11. S_{21} frequency curves for "Updated Phase 3" dual layer geometry for TM polarization ($\theta=0^0$, $\theta=30^0$, $\theta=45^0$, $\theta=60^0$).

As shown in Figs. 12 and 13, the measured results of the manufactured prototype satisfy at least 20 dB attenuation for the desired frequency bands and there is a good agreement between measurement and simulation results.

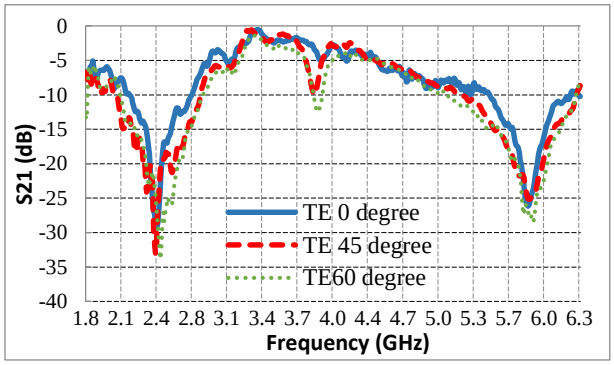

Fig. 12. Measured S_{21} frequency curves for TE polarization ($\theta=0^0$, $\theta=45^0$, $\theta=60^0$).

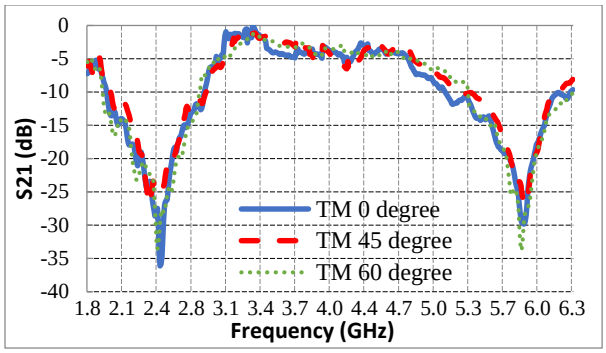

Fig. 13. Measured S_{21} frequency curves for TM polarization ($\theta=0^0$, $\theta=45^0$, $\theta=60^0$).

IV. CONCLUSION

A new dual layer band stop FSS structure is designed for mitigating both interference and WLAN security risks within the buildings in the unlicensed 2.4 GHz and 5.4 GHz ISM bands. The new element geometry is capable of achieving a stable frequency response for a wide range of oblique incidence angles. This is due to a periodic cell size, which is almost one-tenth of the corresponding wavelength of 2.4 GHz obtained in the proposed design. Achieved attenuation levels are around 20 dB for TE and TM polarizations at all incidence angles. Besides, the use of identical geometries on each layer enables the structure to be optimized at 2.4 GHz and 5.8 GHz resonance frequencies independently due to reduced mutual inductance between the layers. The obtained thickness of the structure is only 1.6 mm, which also gives the possibility of using this design as a structural surface material for blocking the ISM signals.

ACKNOWLEDGMENT

We would like to thank TUBITAK (Project No: 115E225).

REFERENCES

[1] R. Ma, Q. Guo, C. Hu, and J. Xue, "An improved WiFi indoor positioning algorithm by weighted fusion," *Sensors*, vol. 15, 2015.

[2] C. H. See, R. Abd-Alhameed, Z. Z. Abidin, and N. McEwan, "Wideband printed MIMO/diversity monopole antenna for WiFi/WIMAX applications," *IEEE Transactions on Antennas and Propagation*, vol. 60, no. 4, pp. 2028-2035, 2012.

[3] M. Raspopoulos and S. Stavrou, "Frequency selective buildings through frequency selective surfaces," *IEEE Transactions on Antennas and Propagation*, vol. 59, no. 8, pp. 2998-3005, 2011.

[4] G. H. Sung, K. W. Sowerby, and A. G. Williamson,

"Modeling a low-cost frequency selective wall for wireless-friendly indoor environments," *IEEE Antennas and Wireless Propagation Letters*, vol. 5, no. 1, pp. 311-314, 2006.

[5] G. H. Sung, K. W. Sowerby, and A. G. Williamson, "A frequency-selective wall for interference reduction in wireless indoor environments," *Antennas and Propagation Magazine, IEEE*, vol. 48, no. 5, pp. 29-37, 2006.

[6] L. Derek and K. Sowerby, "Shielding strategies for interference mitigation in indoor wireless communications with frequency selective surfaces," *In Proceedings of Antennas and Propagation Society International Symposium, 2005 IEEE*, Washington D.C., pp. 260-263, 2005.

[7] M. Raspopoulos, "Radio propagation in frequency selective buildings," *European Transactions on Telecommunications*, vol. 17, no. 3, pp. 407-413, 2006.

[8] J. Roberts, K. L. Ford, and M. R. Jonathan, "Secure electromagnetic buildings using slow phase-switching frequency-selective surfaces," *IEEE Transactions on Antennas and Propagation*, vol. 64, pp. 251-261, 2016.

[9] B. A. Munk, *Frequency Selective Surfaces - Theory and Design*. John Wiley and Sons. Inc., New York, 2000.

[10] R. Natarajan, M. Kanagasabai, S. Bais, S. Palaniswamy, and J. Kizhekke Pak, "A compact frequency selective surface with stable response for WLAN applications," *Antennas and Wireless Propagation Letters*, vol. 12, pp. 718-720, 2013.

[11] R. Mittra, C. H. Chan, and T. Cwik, "Techniques for analyzing frequency selective surfaces a review," *Proceedings of the IEEE*, vol. 76, no. 12, pp. 1593-1615, 1988.

[12] I. Bardi, R. Remski, and Z. Cendes, "Plane wave scattering from frequency-selective surfaces by the finite-element method," *IEEE Transactions on Magnetics*, vol. 38, no. 2, pp. 641-644, 2002.

[13] F. Costa, "An equivalent circuit model of frequency selective surfaces embedded within dielectric layers," *In Proceedings of Antennas and Propagation Society International Symposium, APSURSI '09. IEEE*, Charleston, pp. 1-4, 2009.

[14] F. E. Kent, B. Doken, and M. Kartal, "A new equivalent circuit based FSS design method by using genetic algorithm," *In Proceedings of 2nd International Conference on Engineering Optimization*, pp. 1-4, Portugal, 2010.

[15] A. Ray, M. Kahar, S. Biswas, D. Sarkar, and P. P. Sarkar, "A dual tuned complementary structure frequency selective surface for WLAN applications," *Microwaves, Optoelectronics and Electromagnetic Applications*, vol. 11, no. 1, pp. 144-153, 2012.

[16] R. R. Xu, Z. Y. Zong, and W. Wu, "Low-frequency miniaturized dual-band frequency selective surfaces with close band spacing," *Microwave Optical Technology Letters*, vol. 51, no. 5, pp. 1238-1240, 2009.

[17] B. Rahmati and H. Hassani, "Multiband metallic frequency selective surface with wide range of band ratio," *IEEE Transactions on Antennas and Propagation*, vol. 63, no. 8, pp. 3747-3753, 2015.

Bora Döken received his Ph.D. degree in 2018. He works as an Instructor at the Istanbul Technical University. He is currently involved in the areas of FSSs, periodic structures, antennas, and metamaterials.

Mesut Kartal (M'91) received his Ph.D. degree in 2000. Currently, he is a Professor in the Istanbul Technical University, Department of Electronics and Communication Engineering.

His research interests include remote sensing, inverse problems, RF and microwave design engineering, as well as modelling, design, simulations and analysis, and CAD techniques in high frequency region.

Near to Far-Field Plane-Polar Transformation from Probe Positioning Error Affected Data

F. D'Agostino, F. Ferrara, C. Gennarelli, R. Guerriero, and M. Migliozzi

Department of Industrial Engineering
University of Salerno, via Giovanni Paolo II, 132 - 84084 Fisciano, Italy
fdagostino@unisa.it, flferrara@unisa.it, cgennarelli@unisa.it, rguerriero@unisa.it, mmigliozzi@unisa.it

Abstract ─ In this article, two efficient approaches for the correction of known positioning errors of the measurement probe in a plane-polar near to far-field (NTFF) transformation, requiring a minimum number of NF data in the case of quasi-planar antennas, are presented and experimentally assessed. Such a NTFF transformation benefits from a non-redundant sampling representation of the voltage detected by the probe got by modeling an antenna with a quasi-planar geometry through a double bowl, a surface consisting of two circular bowls with the same aperture radius, but with lateral bends which may differ to better fit the antenna shape. The uniform samples, i.e., those at the points set by the representation, are accurately retrieved from the collected not regularly distributed ones either by applying a singular value decomposition based approach or an iterative scheme. Then, the input NF data necessary for the classical plane-rectangular NTFF transformation are evaluated from the so retrieved non-redundant uniform samples through a 2-D optimal sampling interpolation formula.

Index Terms ─ Antenna measurements, non-redundant representations of electromagnetic fields, plane-polar near to far-field transformation, positioning errors correction.

I. INTRODUCTION

The near to far-field (NTFF) transformation techniques [1-5] are well-assessed and commonly employed tools for the precise evaluation of the radiation pattern of antennas having large dimensions in terms of wavelengths from NF measurements made in an anechoic chamber, which suitably reproduces the free-space propagation conditions by suppressing almost completely the reflections from its walls. Among these transformations, the traditional plane-rectangular one [6, 7] is especially suitable when dealing with high gain antennas which radiate pencil beam patterns. For these antennas, an even more convenient transformation is the one using the plane-polar scan [8-14], which offers the following advantages compared to the plane-rectangular one: i) a simpler mechanical realization, since it can be achieved via a linear movement of the measuring probe and a rotary motion of the antenna under test (AUT); ii) a larger scanning zone for the same dimensions of the anechoic chamber; iii) a more precise measurement of the radiation patterns of gravitationally sensitive spaceborne AUTs when the scanning is accomplished in a horizontal plane. In order to make the number of the required NF data and corresponding measurement time remarkably smaller than those in [8-10], the non-redundant sampling representations of electromagnetic (EM) fields [15] have been suitably applied in [11, 12] to the voltage detected by a non-directive probe, thus developing 2-D optimal sampling interpolation (OSI) formulas, which allow one to accurately recover the NF data necessary for the traditional plane-rectangular NTFF transformation [6, 7] from a minimum number of plane-polar ones. In particular, the AUTs have been considered as contained inside a surface formed by two circular bowls having the same aperture and possibly different lateral surfaces (double bowl) in [11], whereas an oblate ellipsoidal surface has been employed to model them in [12]. The experimental assessments of the non-redundant plane-polar NTFF transformations [11] and [12] have been then provided in [13] and [14], respectively.

It must be noticed that, as a consequence of a not accurate control of the positioners and/or of their limited resolution, it could not be possible to acquire the NF data at the points prescribed by the non-redundant sampling representation, even if their actual positions can be precisely revealed through laser interferometric techniques. Hence, the fulfillment of an efficient and robust procedure, that enables a possibly precise retrieval of the NF data to be employed in the traditional plane-rectangular NTFF transformation from the positioning errors affected (non-uniform) plane-polar ones, appears of fundamental importance. To this purpose, a procedure relying on the conjugate gradient iterative technique and adopting the fast Fourier transform (FFT) for non-equispaced data [16] has been applied for correcting known position errors in the traditional NTFF transformations adopting the planar [17] and spherical [18] scans. However, this procedure is not appropriate for the non-redundant plane-polar NTFF

Submitted On: March 30, 2017
Accepted On: October 24, 2017

transformations [11, 12], wherein efficient OSI expansions are applied to precisely evaluate the NF data necessary for the traditional plane-rectangular NTFF transformation from the collected non-redundant plane-polar samples. As underlined in [19, 20], where a more complete discussion on the non-uniform sampling can be found, the formulas which allow the direct retrieval of the needed data from the non-uniform samples are not stable and easy to use, and are valid only for specific samples grids. A convenient and feasible policy [19] is to retrieve the regularly distributed (uniform) samples from the non-uniform ones and then reconstruct the required NF data by using a precise and stable OSI formula. To reach this goal, two distinct procedures have been proposed. The former adopts an iterative technique, converging only if it is possible to set up a bijective relation linking every uniform sampling point to the nearest non-uniform one, and has been used to reconstruct the uniform samples in a plane-rectangular grid [19]. The latter utilizes the singular value decomposition (SVD) method, does not show the above shortcoming, allows one to benefit from the redundancy of the data to increase the algorithm robustness as regards errors corrupting them, and has been exploited to develop non-redundant NTFF transformations from positioning errors affected samples adopting the plane-polar [21], bi-polar [22], and cylindrical [23] scans. In any case, the SVD based approach can be gainfully employed if the starting 2-D problem of the regularly spaced samples retrieval can be subdivided in two independent 1-D problems; if this is not the case, the dimensions of the related matrices remarkably increase, so that a massive computing effort is needed. Both the procedures have been compared through simulations and experimentally assessed with reference to the cylindrical [24] and spherical [20, 25-27] scans, whereas their effectiveness in the plane-polar NTFF transformation when using an oblate ellipsoidal AUT modeling has been experimentally demonstrated in [28].

The aim of the article is to suitably extend the application of these techniques to the correction of known positioning errors in the non-redundant NTFF transformation with plane-polar scan [11, 13], which adopts a double bowl to shape a quasi-planar antenna (Fig. 1), and to experimentally demonstrate their effectiveness through a measurement campaign executed at the Antenna Characterization Lab of the UNIversity of SAlerno (UNISA).

II. NON-REDUNDANT REPRESENTATION OF THE PROBE VOLTAGE ON A PLANE FROM NON-UNIFORM SAMPLES

A. Uniform samples representation

The non-redundant sampling representation of the voltage detected by a not directive probe, which scans a plane at distance *d* from the aperture of a quasi-planar AUT via a plane-polar NF system, and the corresponding OSI expansion are briefly recalled in this subsection for the case wherein a double bowl model is adopted [11, 13]. The spherical coordinate system (r, ϑ, φ) is used for denoting the observation point, while the plane-polar coordinates (ρ, φ) are also used to identify a point P on the plane (Fig. 1). A double bowl is a surface Σ obtained by joining together two circular bowls having the same aperture radius a, but possibly not equal bending radii h and h' of the upper and lower arcs to allow a better fitting of the actual antenna geometry (see Figs. 1 and 2). As mentioned in the Introduction, the non-redundant sampling representations [15] can be advantageously exploited to represent the voltage detected by a not directive probe, because its spatial bandwidth practically coincides with that of the antenna radiated field [29]. According to these representations, an optimal parameter η must be adopted for describing any of the curves Γ (diameters and rings) representing the plane in a plane-polar frame, and a suitable phase factor $e^{-j\psi(\eta)}$ has to be singled out from the voltage V_φ or V_ρ detected by the scanning probe in its two orientations (probe/rotated probe). The so introduced "reduced voltage":

$$\tilde{V}(\eta) = V(\eta)\, e^{j\psi(\eta)}, \tag{1}$$

is spatially almost bandlimited and not strictly bandlimited, so that an error arises when it is approximated by means of a bandlimited function. In any case, this bandlimitation error can be made reasonably small as the band-width is larger than a critical value W_η [15] and effectively reduced by considering an increased bandwidth $\chi' W_\eta$, χ' being an enlargement bandwidth factor a bit larger than one for AUTs having electrical large sizes [15].

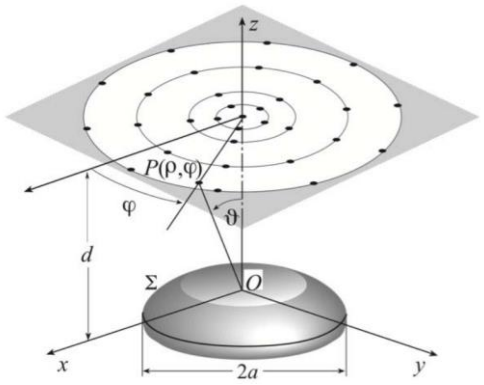

Fig. 1. Plane-polar scanning for a quasi-planar antenna.

If Γ is a diameter, by choosing $W_\eta = \beta \ell'/2\pi$ it results [11, 13]:

$$\psi = (\beta/2)\left[R_1 + R_2 + s_1' - s_2'\right], \tag{2}$$

$$\eta = (\pi/\ell')\left[R_1 - R_2 + s_1' + s_2'\right], \tag{3}$$

wherein $\ell' = 4a + (h+h')(\pi - 2)$ is the length of the

intersection curve C' between the meridian plane passing through the observation point P and the double bowl Σ, β is the wavenumber, $R_{1,2}$ are the distances from P to the two tangency points $P_{1,2}$ between C' and the cone with the vertex at P, and $s'_{1,2}$ their curvilinear abscissas (see Fig. 2). The values of $s'_{1,2}$ and $R_{1,2}$ change depending on the radial distance $\rho(\eta)$. It can be easily verified that, when $\rho < a$, the tangency points $P_{1,2}$ are situated on the upper bowl, whereas, when $\rho > a$, P_1 is still on the upper bowl and P_2 is located on the lower one. The corresponding expressions of $s'_{1,2}$ and $R_{1,2}$ can be evaluated in a straightforward manner and are explicitly reported in [11, 13].

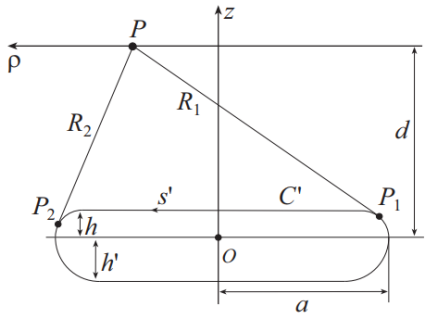

Fig. 2. Relevant to the double bowl modeling.

If Γ is a ring, ψ results to be constant and the angle φ can be conveniently used as optimal parameter. The corresponding bandwidth W_φ is [11, 13]:

$$W_\varphi = \frac{\beta}{2}\max_{z'}(R^+ - R^-) = \frac{\beta}{2}\max_{z'}\left(\sqrt{(\rho+\rho'(z'))^2+(d-z')^2} - \sqrt{(\rho-\rho'(z'))^2+(d-z')^2}\right), \quad (4)$$

where $\rho'(z')$ is the equation of the surface Σ and R^+, R^- are the maximum and minimum distances from Γ to the circumference of Σ at z'. The explicit evaluation of such a maximum is detailed in [11, 13].

At each point $P(\rho, \varphi)$ on the plane, the voltage can be efficiently evaluated through the following OSI expansion [11, 13]:

$$V(\eta(\rho),\varphi) = \mathrm{e}^{-\mathrm{j}\psi(\eta)}\sum_{n=n_0-q+1}^{n_0+q}\tilde{V}(\eta_n,\varphi)\,A(\eta,\eta_n,\bar{\eta},N,N''), \quad (5)$$

wherein $n_0 = n_0(\eta) = \mathrm{Int}(\eta/\Delta\eta)$, $2q$ is the number of the considered nearest intermediate samples $\tilde{V}(\eta_n,\varphi)$, namely, the reduced voltages at the intersections between the diameter through P and the sampling rings,

$$A(\eta,\eta_n,\bar{\eta},N,N'') = \Omega_N(\eta-\eta_n,\bar{\eta})D_{N''}(\eta-\eta_n), \quad (6)$$

is the OSI interpolation function,

$$\eta_n = n\Delta\eta = 2\pi n/(2N''+1);\quad N'' = \mathrm{Int}(\chi N')+1, \quad (7)$$

$$N' = \mathrm{Int}(\chi' W_\eta)+1;\quad N = N''-N';\quad \bar{\eta} = q\Delta\bar{\eta}. \quad (8)$$

Int(x) denotes the greatest integer less than or equal to x, and χ is the oversampling factor needed to control the truncation error [15]. In (6),

$$\Omega_N(\eta,\bar{\eta}) = \frac{T_N\left[2\cos^2(\eta/2)/\cos^2(\bar{\eta}/2)-1\right]}{T_N\left[2/\cos^2(\bar{\eta}/2)-1\right]}, \quad (9)$$

and

$$D_{N''}(\eta) = \frac{\sin\left[(2N''+1)\eta/2\right]}{(2N''+1)\sin(\eta/2)}, \quad (10)$$

are the Tschebyscheff and Dirichlet sampling functions [15], $T_N(\eta)$ being the Tschebyscheff polynomial of degree N.

The intermediate samples can be determined by interpolating the samples on the rings through the OSI formula [11, 13]:

$$\tilde{V}(\eta_n,\varphi) = \sum_{m=m_0-p+1}^{m_0+p}\tilde{V}(\eta_n,\varphi_{m,n})A(\varphi,\varphi_{m,n},\bar{\varphi}_n,M_n,M_n''), \quad (11)$$

wherein $m_0 = m_0(\varphi) = \mathrm{Int}(\varphi/\Delta\varphi_n)$, $2p$ is the number of the considered nearest samples on the ring specified by η_n, and

$$\varphi_{m,n} = m\Delta\varphi_n = 2\pi m/(2M_n''+1);\quad M_n'' = \mathrm{Int}(\chi M_n')+1, \quad (12)$$

$$M_n' = \mathrm{Int}\left[\chi^* W_\varphi(\eta_n)\right]+1;\quad M_n = M_n''-M_n', \quad (13)$$

$$\chi^* = 1+(\chi'-1)\left[\sin\vartheta(\eta_n)\right]^{-2/3};\quad \bar{\varphi}_n = p\Delta\varphi_n. \quad (14)$$

The 2-D OSI expansion, which allows the accurate reconstruction of V_φ and V_ρ at any point in the measurement circle, is easily attained by properly matching the 1-D expansions (5) and (11). It can be exploited to reconstruct in a fast and accurate way these voltages at the points necessary for the plane-rectangular NTFF transformation [6, 7]. However, the probe corrected formulas in [7] (whose expressions in the here used reference system are shown in [13, 30]) are valid only when the probe keeps its orientation with respect to the AUT and this requires its co-rotation with it. In order to avoid this co-rotation, a probe with a far field having a first-order φ-dependence must be utilized. In this case, the voltages V_V and V_H (acquired with co-rotation by the probe and rotated probe) are related to V_φ and V_ρ by:

$$V_V = V_\varphi\cos\varphi - V_\rho\sin\varphi;\quad V_H = V_\varphi\sin\varphi + V_\rho\cos\varphi, \quad (15)$$

thus enabling a "software co-rotation". To this end, an open-ended rectangular waveguide can be conveniently used as scanning probe. In fact, the far field radiated in the forward hemisphere by it, when excited by a TE_{10} mode, has in a practically good approximation a first-order azimuthal dependence [31].

B. Uniform samples recovery

In this subsection, two effective techniques for

correcting NF data affected by known positioning errors in the described non-redundant plane-polar NTFF transformation are presented by pointing out their benefits and shortcomings.

The former technique relies on the SVD method. In such a case, it is supposed that, save for the sample at $\rho = 0$, all the other are not regularly spaced on rings not uniformly distributed on the scanning plane. This hypothesis is indeed realistic if the plane-polar NF data are collected by performing the scan along the rings as needed to benefit from the reduction of the number of NF data on the most inner rings, obtainable when exploiting the previous non-redundant sampling representation. In this case, the problem of the uniform samples retrieval can be subdivided in two independent 1-D problems.

The uniform $2M_k'' + 1$ samples on a non-uniform ring at $\rho(\xi_k)$ are recovered as follows. By considering a set of $J_k \geq 2M_k'' + 1$ non-uniform sampling points (ξ_k, ϕ_j) on this ring and expressing the corresponding reduced voltages $\tilde{V}(\xi_k, \phi_j)$ in terms of the unknown ones at the uniform sampling points $(\xi_k, \varphi_{m,k})$, the linear system:

$$\underline{\underline{C}}\,\underline{X} = \underline{B}, \tag{16}$$

is attained, wherein $\underline{B}$ is the known non-uniform samples vector, $\underline{X}$ is that of the unknown uniform ones $\tilde{V}(\xi_k, \varphi_{m,k})$, and $\underline{\underline{C}}$ is a $J_k \times (2M_k'' + 1)$ sized matrix. The element of the matrix $\underline{\underline{C}}$ are:

$$c_{jm} = A\left(\phi_j, \varphi_{m,k}, \bar{\varphi}_k, M_k, M_k''\right), \tag{17}$$

wherein $\varphi_{m,k} = m\Delta\varphi_k = 2m\pi/(2M_k'' + 1)$ and $\bar{\varphi}_k = p\Delta\varphi_k$. It is worthy to observe that, for a given row j, the elements c_{jm} are zero when the index m is outside the range $[m_0(\phi_j) - p + 1,\ m_0(\phi_j) + p]$. The SVD is then applied to get the best least square approximated solution of (16). After such a step, the intermediate samples $\tilde{V}(\xi_k, \varphi)$ in correspondence of the intersections between the non-uniform rings and the diameter passing through P are recovered via the OSI expansion (11), wherein the samples $\tilde{V}(\xi_k, \varphi_{m,k})$ take the place of the $\tilde{V}(\eta_n, \varphi_{m,n})$ ones. Since these intermediate samples are not regularly distributed, the voltage at P can be reconstructed by first recovering the regularly distributed intermediate samples $\tilde{V}(\eta_n, \varphi)$ again by applying the SVD method and subsequently interpolating them through the OSI expansion (5).

It must be stressed that either the distances from each non-uniform ring to the corresponding uniform one and the ones between the non-uniform sampling points and the associated uniform ones on the non-uniform rings have been supposed less than one half of the related uniform spacing for avoiding a severe ill-conditioning of the correlated linear system. In addition, in order to minimize the computational effort, an equal number N_φ of uniform samples, coincident with that corresponding to the outer uniform ring, has been reconstructed on each non-uniform ring. In this way, the samples are aligned along the diameters and, therefore, the number of systems to be solved is minimum.

At last, V_φ and V_ρ at the points necessary for the traditional plane-rectangular NTFF transformation [6, 7] are efficiently reconstructed via the OSI expansions (5) and (11), this latter appropriately adapted to account for the redundancy in φ.

The latter technique adopts an iterative scheme, converging only if it is possible to set up a bijective relation linking each uniform sampling point to the nearest non-uniform one. In this case, the number Q of the non-uniform samples must be the same as that of the uniform ones. Moreover, it is now supposed that, except the sample at $\rho = 0$, all the other are not regularly spaced on the scanning plane, do no longer lie on rings, but must satisfy the above bijective correspondence. By applying the OSI expansions (5) and (11), it is possible to express the reduced voltages at each non-uniform sampling point $(\xi_k, \phi_{j,k})$ in terms of those unknown at the nearest uniform sampling points $(\eta_n, \varphi_{m,n})$, thus getting the linear system:

$$\tilde{V}(\xi_k, \phi_{j,k}) = \sum_{n=n_0-q+1}^{n_0+q} \left\{ A(\xi_k, \eta_n, \bar{\eta}, N, N'') \cdot \sum_{m=m_0-p+1}^{m_0+p} \tilde{V}(\eta_n, \varphi_{m,n})\, A(\phi_{j,k}, \varphi_{m,n}, \bar{\varphi}_n, M_n, M_n'') \right\}, \tag{18}$$

which can be again recast in the matrix form (16), wherein $\underline{\underline{C}}$ is now a $Q \times Q$ sized matrix. Such a linear system could be solved via the SVD method, but a huge computational effort would be required. On the contrary, it can be efficiently solved by applying an iterative algorithm, which is derived as described in the following. In the first step, the matrix $\underline{\underline{C}}$ is subdivided in its diagonal part $\underline{\underline{C}}_D$ and non-diagonal part $\underline{\underline{\Delta}}$, subsequently, both the sides of the relation $\underline{\underline{C}}\,\underline{X} = \underline{B}$ are multiplied by $\underline{\underline{C}}_D^{-1}$, and, finally, its terms are rearranged thus obtaining the iterative scheme:

$$\underline{X}^{(\nu)} = \underline{\underline{C}}_D^{-1}\underline{B} - \underline{\underline{C}}_D^{-1}\underline{\underline{\Delta}}\,\underline{X}^{(\nu-1)} = \underline{X}^{(0)} - \underline{\underline{C}}_D^{-1}\underline{\underline{\Delta}}\,\underline{X}^{(\nu-1)}, \tag{19}$$

with $\underline{X}^{(\nu)}$ being the uniform samples vector obtained at the νth iteration.

To guarantee the convergence of such an iterative scheme, it is necessary but not sufficient, as stressed in [19], that the amplitude of every element belonging to the main diagonal of the matrix $\underline{\underline{C}}$ be different from zero and larger than the amplitudes of the other elements which lie on the same column or row. It can be easily verified that the assumed hypothesis of bijective relation between each uniform sampling point and the "nearest" non-uniform one ensures the fulfillment of these conditions. By putting relation (19) in explicit form, it results:

$$\tilde{V}^{(\nu)}(\eta_n, \varphi_{m,n}) =$$

$$= \frac{1}{A(\xi_n, \eta_n, \bar{\eta}, N, N'')\, A(\phi_{m,n}, \varphi_{m,n}, \bar{\varphi}_n, M_n, M_n'')} \cdot$$

$$\left\{ \tilde{V}(\xi_n, \phi_{m,n}) - \sum_{s=s_0-q+1}^{s_0+q} \sum_{\substack{i=i_0-p+1 \\ (s \neq n) \wedge (i \neq m)}}^{i_0+p} A(\xi_n, \eta_s, \bar{\eta}, N, N'') \cdot \right.$$

$$\left. \cdot A(\phi_{m,n}, \varphi_{i,s}, \bar{\varphi}_s, M_s, M_s'')\, \tilde{V}^{(\nu-1)}(\eta_s, \varphi_{i,s}) \right\}, \quad (20)$$

where

$$s_0 = \begin{cases} n & \text{if } \xi_n \geq \eta_n \\ n-1 & \text{if } \xi_n < \eta_n \end{cases} ; \quad i_0 = \begin{cases} m & \text{if } \phi_{m,n} \geq \varphi_{m,s} \\ m-1 & \text{if } \phi_{m,n} < \varphi_{m,s} \end{cases} . \quad (21)$$

III. EXPERIMENTAL ASSESSMENT

Some results of laboratory tests performed in the anechoic chamber of the UNISA Antenna Characterization Lab are shown in this section to give the experimental assessment of the two described techniques for compensating the probe positioning errors. The chamber is $8\text{m} \times 5\text{m} \times 4\text{m}$ sized and is provided with a plane-polar NF scanning system, besides the cylindrical and spherical ones. The pyramidal absorbers, covering the chamber walls, assure a reflection level lesser than – 40 dB. A vector network analyzer is utilized to accomplish the measurements of the amplitude and phase of the voltage detected by the adopted probe, an open-ended WR-90 rectangular waveguide. The plane-polar scan is attained by attaching the probe to a linear vertical positioner and putting the AUT on a rotating table, whose rotary axis is normal to the linear positioner. A further rotating table has been recently integrated in the NF scanning system. It has been placed between the linear positioner and the probe and allows to perform a plane-polar scan, wherein the probe axes keep their orientation with respect to AUT ones (hardware co-rotation), as well as to measure the NF data which would be collected by a plane-rectangular NF facility. The considered AUT is a dual pyramidal horn antenna with vertical polarization, positioned on the plane $z = 0$ of the adopted reference system (Fig. 1) and working at 10 GHz. The horns aperture has sizes $8.9\text{cm} \times 6.8\text{cm}$ and the distance between the apertures centers is 26.5 cm. This AUT has been modeled by a double bowl with a = 18.0 cm and $h = h'$ = 3.0 cm. The non-uniform, as well as the uniform, NF plane-polar samples considered in the shown results have been acquired on a circle having radius 110 cm on a plane at distance d = 16.5 cm from the AUT.

In Figs. 3 and 4, the E- and H-planes FF patterns reconstructed from the non-redundant plane-polar NF samples acquired with the hardware co-rotation are compared with those got from the plane-rectangular NF data directly measured, at the sample spacing of 0.45λ, on the $140\text{cm} \times 140\text{cm}$ inscribed square. As can be seen, a very good agreement is found in both the planes. The corresponding recoveries, obtained from the non-redundant plane-polar NF samples acquired when using the software co-rotation, are shown in Figs. 5 and 6. In such a case, especially in the H-plane, a less accurate reconstruction results. This is due to the fact that the far field radiated by an open-ended rectangular waveguide excited by a TE_{10} mode has only approximately a first-order azimuthal dependence [31].

Let us now turn to the case of irregularly spaced samples. The first set of figures (Figs. 7 - 11) refers to the case of not uniformly distributed sampling points which lie on rings. The NF data have been acquired in such a way that the distances from every non-uniform ring to the corresponding uniform one, and those between the non-uniform sampling points and the related uniform ones on the rings are random variables with uniform distributions in $(-\Delta\eta/2, \Delta\eta/2)$ and $(-\Delta\varphi_k/2, \Delta\varphi_k/2)$, respectively.

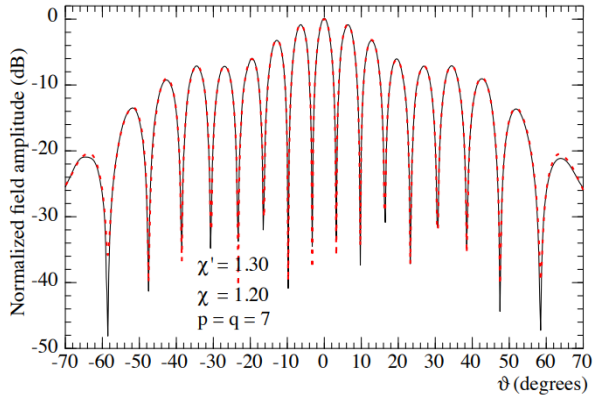

Fig. 3. E-plane pattern. ——— reconstructed from plane-rectangular NF data. – – – – reconstructed from the non-redundant plane-polar NF samples with hardware co-rotation.

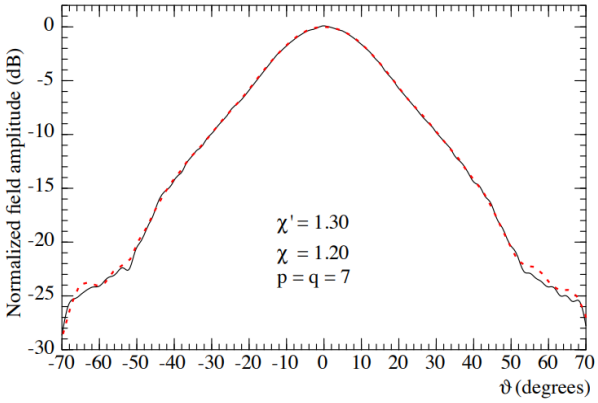

Fig. 4. H-plane pattern. ——— reconstructed from plane-rectangular NF data. – – – – reconstructed from the non-redundant plane-polar NF samples with hardware co-rotation.

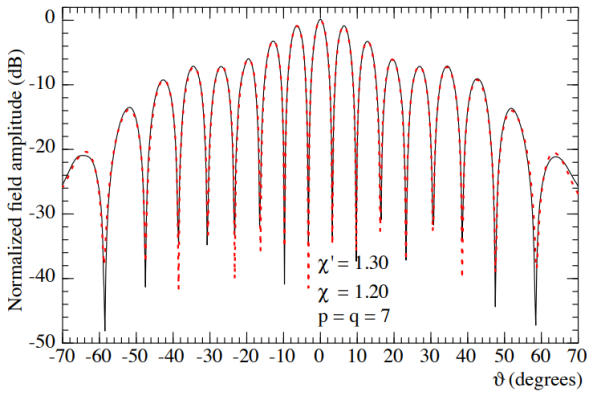

Fig. 5. E-plane pattern. ——— reconstructed from plane-rectangular NF data. – – – – reconstructed from the non-redundant plane-polar NF samples with software co-rotation.

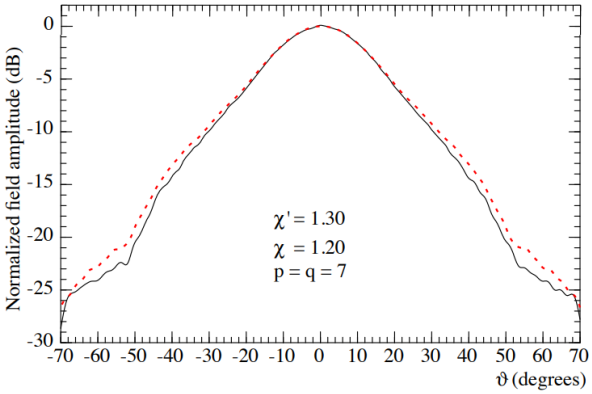

Fig. 6. H-plane pattern. ——— reconstructed from plane-rectangular NF data. – – – – reconstructed from the non-redundant plane-polar NF samples with software co-rotation.

The amplitude and phase of V_ρ on the diameter at $\varphi = 90°$, retrieved via the SVD procedure, are compared in Figs. 7 and 8 with the ones directly measured on the same line. The comparison between the recovered amplitude of V_φ on the diameter at $\varphi = 0°$ and that directly measured is also reported in Fig. 9. As can be clearly observed, notwithstanding the imposed severe values of the positioning errors, all recoveries are very accurate except for the zones where the voltage level is very low.

To put in evidence only the error related to the retrieval of the uniform samples from the acquired non-uniform ones and not just that imputable to the software co-rotation, the overall efficacy of the SVD based technique is validated by comparing the FF patterns in the principal planes E and H (Figs. 10 and 11) recovered from the non-uniform NF data with the ones reconstructed from the non-redundant, uniform, plane-polar NF samples with software co-rotation (reference). The reconstructed FF patterns obtained from the non-uniform plane-polar NF data without using the SVD technique are shown in the same figures for sake of comparison. These last reconstructions appear remarkably worsened with respect to the ones obtained when applying the SVD based procedure, thus further assessing its effectiveness for compensating known position errors. Since the considered set of non-uniform samples satisfies also the applicability conditions for the iterative procedure, this last has been applied too by obtaining quite analogous results, as can be seen from Figs. 12 and 13.

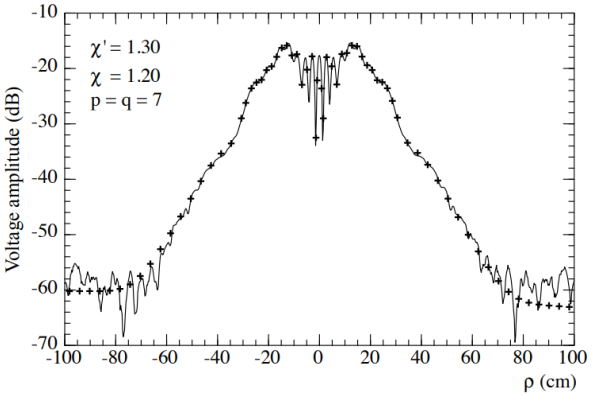

Fig. 7. V_ρ amplitude on the diameter at $\varphi = 90°$. ——— measured. ++++ retrieved from the non-uniform NF samples via the SVD procedure.

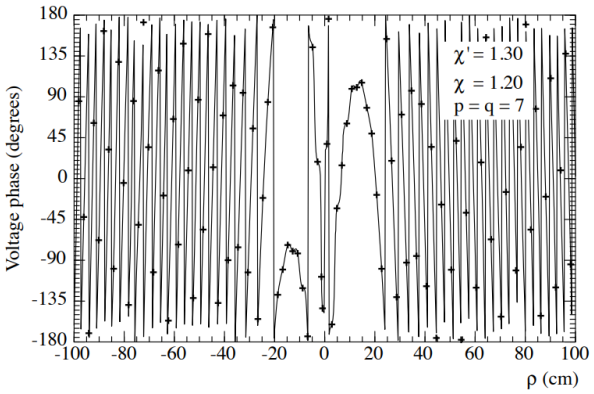

Fig. 8. V_ρ phase on the diameter at $\varphi = 90°$. ——— measured. ++++ retrieved from the non-uniform NF samples via the SVD procedure.

The second set of figures (from Fig. 14 to Fig. 18) refers to the case of non-uniform sampling points which do not lie on rings and, therefore, the iterative technique has been adopted. In this case, the not regularly spaced samples have been collected in such a way that the random shifts in η and φ between the positions of the non-uniform samples

and the related uniform ones are uniformly distributed in $(-\Delta\eta/3, \Delta\eta/3)$ and $(-\Delta\varphi_n/3, \Delta\varphi_n/3)$. Figures 14 and 15 show the comparison between the amplitudes of V_ρ and V_φ on the diameter at $\varphi = 30°$ recovered from the non-uniform samples by applying the iterative procedure and the directly acquired ones on the line. The reconstruction of the phase of the most significant of them is shown in Fig. 16 for completeness. Also in such a case, the reconstructions are very accurate. It should be noticed that the above results have been got by using only 10 iterations, since, as shown in [25], such a number of iterations guarantees that the iterative scheme converges with very low errors. At last, the overall efficacy of the iterative technique for correcting known probe positioning errors is confirmed by the E-plane and H-plane pattern reconstructions reported in Figs. 17 and 18. As a matter of fact, the reconstructions obtained without using the iterative approach, reported in the same figures, appear severely compromised.

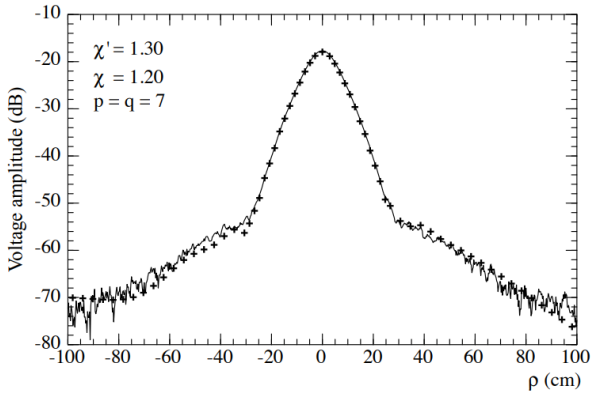

Fig. 9. V_φ amplitude on the diameter at $\varphi = 0°$. ——— measured. ++++ retrieved from the non-uniform NF samples via the SVD procedure.

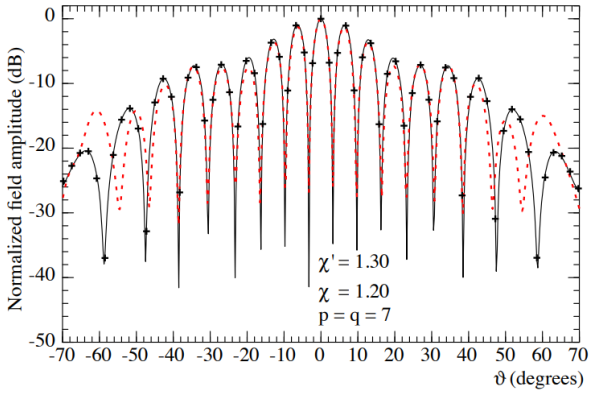

Fig. 10. E-plane pattern. ——— reference. ++++ recovered from the non-uniform NF samples via the SVD procedure. – – – – recovered without using the SVD procedure.

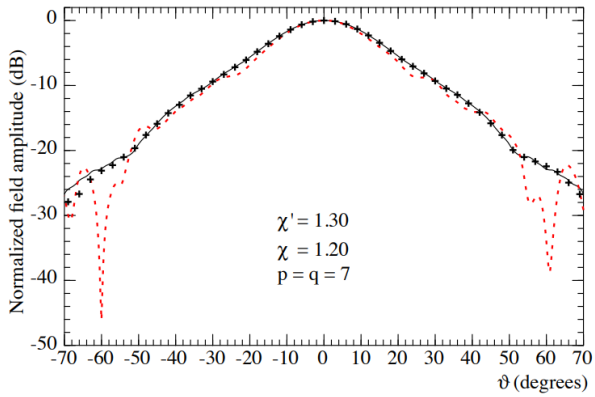

Fig. 11. H-plane pattern. ——— reference. ++++ recovered from the non-uniform NF samples via the SVD procedure. – – – – recovered without using the SVD procedure.

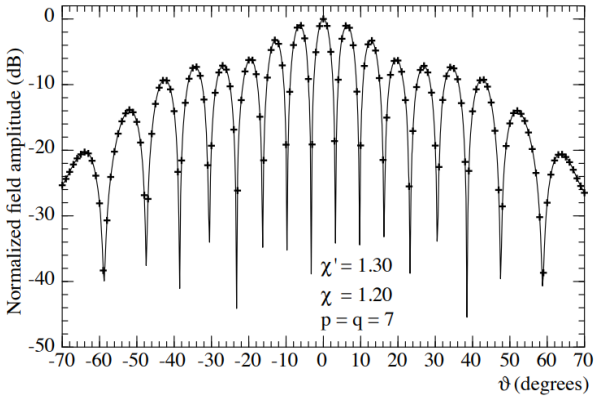

Fig. 12. E-plane pattern. ——— recovered from the non-uniform NF samples via the SVD procedure. ++++ recovered from the non-uniform NF samples via the iterative procedure.

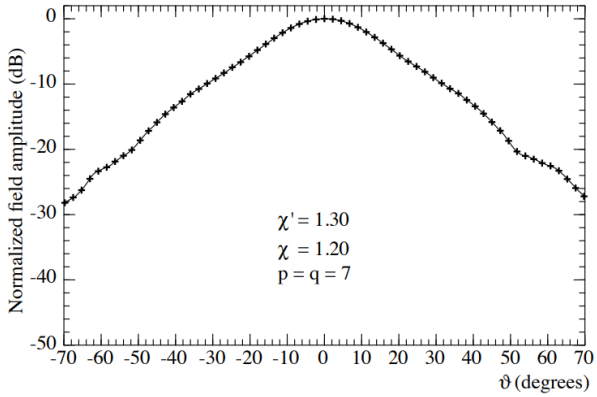

Fig. 13. H-plane pattern. ——— recovered from the non-uniform NF samples via the SVD procedure. ++++ recovered from the non-uniform NF samples via the iterative procedure.

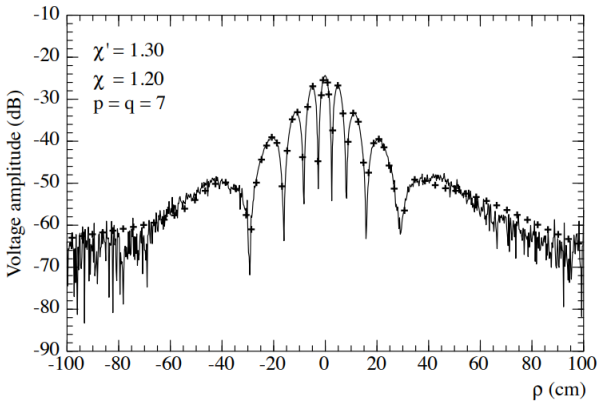

Fig. 14. V_ρ amplitude on the diameter at $\varphi = 30°$. ——— measured. + + + + retrieved from the non-uniform NF samples via the iterative procedure.

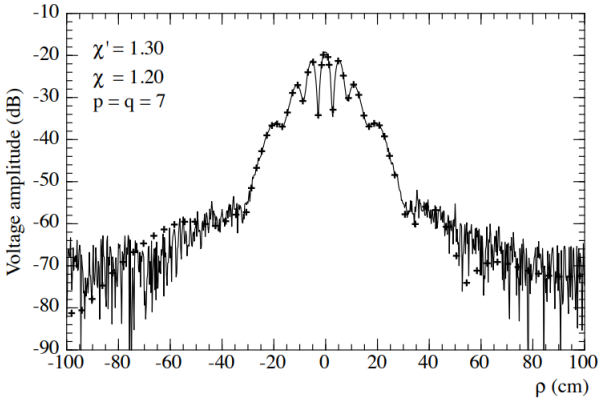

Fig. 15. V_φ amplitude on the diameter at $\varphi = 30°$. ——— measured. + + + + retrieved from the non-uniform NF samples via the iterative procedure.

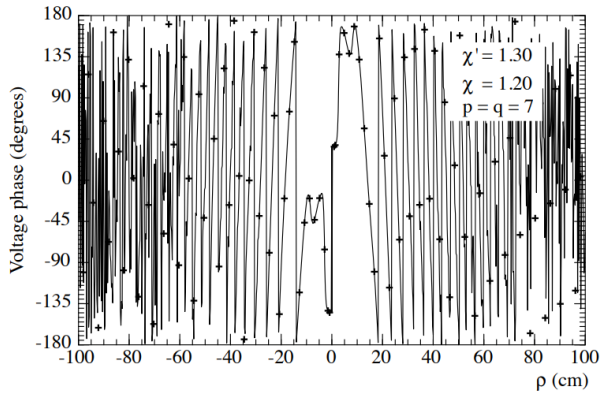

Fig. 16. V_φ phase on the diameter at $\varphi = 30°$. ——— measured. + + + + retrieved from the non-uniform NF samples via the iterative procedure.

It is worthy to point out that the number of the collected not regularly spaced plane-polar NF samples is 1 476 in both the cases and, accordingly, remarkably less than that (33 581) required by the plane-polar scanning techniques [8, 9] to cover the same measurement area.

Another set of experimental results, validating the effectiveness of the two developed techniques and relevant to a different antenna, can be found in [32].

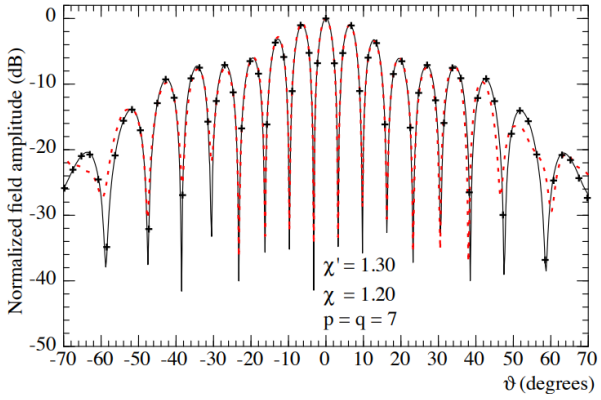

Fig. 17. E-plane pattern. ——— reference. + + + + recovered from the non-uniform NF samples via the iterative procedure. – – – – recovered without using the iterative procedure.

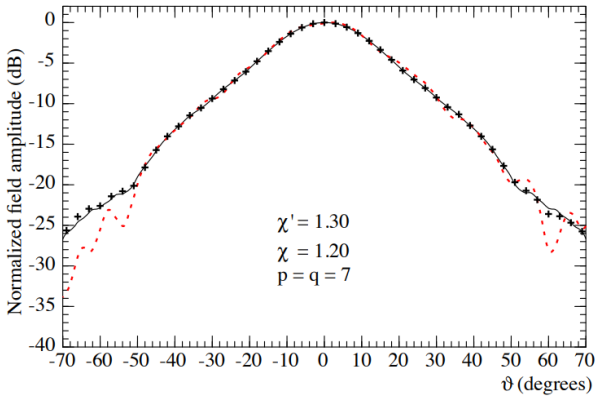

Fig. 18. H-plane pattern. ——— reference. + + + + recovered from the non-uniform NF samples via the iterative procedure. – – – – recovered without using the iterative procedure.

IV. CONCLUSION

In this paper, two effective procedures, which allow the correction of known positioning errors in the plane-polar NTFF transformation based on the double bowl AUT model, have been proposed. The very good NF and FF reconstructions attained when applying them in presence of large and pessimistic positioning errors, as compared with the worsened ones obtained when these procedures are not employed, validate experimentally their

effectiveness.

REFERENCES

[1] A. D. Yaghjian, "An overview of near-field antenna measurements," *IEEE Trans. Antennas Prop*., vol. AP-34, pp. 30-45, Jan. 1986.

[2] E. S. Gillespie, Ed., "Special issue on near-field canning techniques," *IEEE Trans. Antennas Prop*., vol. 36, pp. 727-901, June 1988.

[3] M. H. Francis and R. W. Wittmann, "Near-field scanning measurements: Theory and practice," in *Modern Antenna Handbook*, C.A. Balanis, Ed., chapter 19, John Wiley & Sons, Hoboken, NJ, USA, 2008.

[4] M. H. Francis, Ed., *IEEE Recommended Practice for Near-Field Antenna Measurements*, IEEE Standard 1720-2012, 2012.

[5] C. Gennarelli, A. Capozzoli, L. Foged, J. Fordham, and D. J. van Rensburg, Eds., "Recent advances in near-field to far-field transformation techniques," *Int. Jour. Antennas Prop*., vol. 2012, ID 243203, 2012.

[6] D. T. Paris, W. M. Leach, Jr., and E. B. Joy, "Basic theory of probe-compensated near-field measurements," *IEEE Trans. Antennas Prop*., vol. AP-26, pp. 373-379, May 1978.

[7] E. B. Joy, W. M. Leach, Jr., G. P. Rodrigue, and D. T. Paris, "Application of probe-compensated near-field measurements," *IEEE Trans. Antennas Prop*., vol. AP-26, pp. 379-389, May 1978.

[8] Y. Rahmat-Samii, V. Galindo Israel, and R. Mittra, "A plane-polar approach for far-field construction from near-field measurements," *IEEE Trans. Antennas Prop*., vol. AP-28, pp. 216-230, Mar. 1980.

[9] M. S. Gatti and Y. Rahmat-Samii, "FFT applications to plane-polar near-field antenna measurements," *IEEE Trans. Antennas Prop*., vol. 36, pp. 781-791, June 1988.

[10] A. D. Yaghjian, "Antenna coupling and near-field sampling in plane-polar coordinates," *IEEE Trans. Antennas Prop.*, vol. 40, pp. 304-312, Mar. 1992.

[11] O. M. Bucci, C. Gennarelli, G. Riccio, and C. Savarese, "Near–field – far–field transformation from nonredundant plane-polar data: Effective modellings of the source," *IEE Proc. Microw., Antennas Prop.*, vol. 145, pp. 33-38, Feb. 1998.

[12] O. M. Bucci, F. D'Agostino, C. Gennarelli, G. Riccio, and C. Savarese, "NF–FF transformation with plane-polar scanning: Ellipsoidal modelling of the antenna," *Automatika*, vol. 41, pp. 159-164, 2000.

[13] F. D'Agostino, F. Ferrara, C. Gennarelli, R. Guerriero, and M. Migliozzi, "Reconstruction of the antenna far-field pattern through a fast plane-polar scanning," *Appl. Comp. Electromagn. Soc. Jour.*, vol. 31, pp. 1362-1369, Dec. 2016.

[14] F. D'Agostino, F. Ferrara, C. Gennarelli, R. Guerriero, and M. Migliozzi, "Far-field pattern reconstruction from a nonredundant plane-polar near-field sampling arrangement: Experimental testing," *IEEE Antennas Wireless Prop. Lett.*, vol. 15, pp. 1345-1348, 2016.

[15] O. M. Bucci, C. Gennarelli, and C. Savarese, "Representation of electromagnetic fields over arbitrary surfaces by a finite and nonredundant number of samples," *IEEE Trans. Antennas Prop*., vol. 46, pp. 351-359, Mar. 1998.

[16] A. Dutt and V. Rohklin, "Fast Fourier transforms for nonequispaced data," *Proc. SIAM Jour. Scie. Comput*., vol. 14, pp. 1369-1393, Nov. 1993.

[17] R. C. Wittmann, B. K. Alpert, and M. H. Francis, "Near-field antenna measurements using nonideal measurement locations," *IEEE Trans. Antennas Prop*., vol. 46, pp. 716-722, May 1998.

[18] R. C. Wittmann, B. K. Alpert, and M. H. Francis, "Near-field, spherical-scanning antenna measurements with nonideal probe locations," *IEEE Trans. Antennas Prop*., vol. 52, pp. 2184-2186, Aug. 2004.

[19] O. M. Bucci, C. Gennarelli, and C. Savarese, "Interpolation of electromagnetic radiated fields over a plane from nonuniform samples," *IEEE Trans. Antennas Prop*., vol. 41, pp. 1501-1508, Nov. 1993.

[20] F. D'Agostino, F. Ferrara, C. Gennarelli, R. Guerriero, and M. Migliozzi, "Two effective approaches to correct the positioning errors in a spherical near-field-far-field transformation," *Electromagnetics*, vol. 36, pp. 78-93, 2016.

[21] F. Ferrara, C. Gennarelli, G. Riccio, and C. Savarese, "Far field reconstruction from nonuniform plane-polar data: A SVD based approach," *Electromagnetics*, vol. 23, pp. 417-429, 2003.

[22] F. Ferrara, C. Gennarelli, M. Iacone, G. Riccio, and C. Savarese, "NF–FF transformation with bi-polar scanning from nonuniformly spaced data," *Appl. Comp. Electromagn. Soc. Jour.*, vol. 20, pp. 35-42, Mar. 2005.

[23] F. Ferrara, C. Gennarelli, G. Riccio, and C. Savarese, "NF–FF transformation with cylindrical scanning from nonuniformly distributed data," *Microw. Optical Technol. Lett*., vol. 39, pp. 4-8, Oct. 2003.

[24] F. D'Agostino, F. Ferrara, C. Gennarelli, R. Guerriero, and M. Migliozzi, "On the compensation of probe positioning errors when using a nonredundant cylindrical NF–FF transformation," *Prog. Electromagn. Res. B*, vol. 20, pp. 321-335, 2010.

[25] F. D'Agostino, F. Ferrara, C. Gennarelli, R. Guerriero, and M. Migliozzi, "Two techniques for compensating the probe positioning errors in the spherical NF–FF transformation for elongated antennas," *The Open Electr. & Electron. Eng. Jour.*, vol. 5, pp. 29-36, 2011.

[26] F. D'Agostino, F. Ferrara, C. Gennarelli, R. Guerriero, and M. Migliozzi, "Probe position errors corrected near-field-far-field transformation with

spherical scanning," *Appl. Comp. Electromagn. Soc. Jour.*, vol. 31, pp. 106-117, Feb. 2016.
[27] F. D'Agostino, F. Ferrara, C. Gennarelli, R. Guerriero, and M. Migliozzi, "Far-field pattern evaluation from data acquired on a spherical surface by an inaccurately positioned probe," *IEEE Antennas Wireless Prop. Lett.*, vol. 15, pp. 402-405, 2016.
[28] F. D'Agostino, F. Ferrara, C. Gennarelli, R. Guerriero, and M. Migliozzi, "Two efficient procedures to correct the positioning errors in the plane-polar scanning", *IET Microw., Antennas & Prop.*, vol. 10, no. 13, pp. 1453-1458, 2016.
[29] O. M. Bucci, G. D'Elia, and M. D. Migliore, "Advanced field interpolation from plane-polar samples: Experimental verification," *IEEE Trans. Antennas Prop.*, vol. 46, pp. 204-210, Feb. 1998.
[30] F. D'Agostino, F. Ferrara, C. Gennarelli, R. Guerriero, S. McBride, and M. Migliozzi, "Fast and accurate antenna pattern evaluation from near-field data acquired via planar spiral scanning," *IEEE Trans. Antennas Prop.*, vol. 64, Aug. 2016.
[31] A. D. Yaghjian, "Approximate formulas for the far field and gain of open-ended rectangular waveguide," *IEEE Trans. Antennas Prop.*, vol. AP-32, pp. 378-384, Apr. 1984.
[32] F. D'Agostino, F. Ferrara, C. Gennarelli, R. Guerriero, and M. Migliozzi, "Far-field reconstructtion from plane-polar near-field data affected by probe position errors," in *Proc. of AMTA 2015*, Long Beach, CA, pp. 308-313, Oct. 2015.

Francesco D'Agostino was born near Salerno (Italy) in 1965. He received the Laurea degree in Electronic Engineering from the University of Salerno in 1994, where in 2001 he received the Ph.D. degree in Information Engineering. From 2002 to 2005 he was Assistant Professor at the Engineering Faculty of the University of Salerno where, in October 2005, he was appointed Associate Professor of Electromagnetics and joined the Department of Industrial Engineering, where he is currently working. His research activity includes application of sampling techniques to electromagnetics and to innovative NF–FF transformations, diffraction problems radar cross section evaluations, Electromagnetic Compatibility. In this area, D'Agostino has co-authored 4 books and about 220 scientific papers, published in peer-reviewed international journals and conference proceedings. He is a regular Reviewer for several journals and conferences and has chaired some international events and conferences. D'Agostino is a Member of AMTA, EurAAP, and IEEE.

Flaminio Ferrara was born near Salerno, Italy, in 1972. He received the Laurea degree in Electronic Engineering from the University of Salerno in 1999. Since the same year, he has been with the Research Group in Applied Electromagnetics at the University of Salerno. He received the Ph.D. degree in Information Engineering at the same University, where he is presently an Assistant Professor of Electromagnetic Fields. His interests include: application of sampling techniques to the efficient reconstruction of electromagnetic fields and to NF–FF transformation techniques; monostatic radar cross section evaluations of corner reflectors. Ferrara is co-author of about 220 scientific papers, mainly in international journals and conference proceedings. He is Reviewer for several international journals and Member of the Editorial board of the International Journal of Antennas and Propagation. He is Member of the IEEE society.

Claudio Gennarelli was born in Avellino, Italy, in 1953. He received the Laurea degree (*summa cum laude*) in Electronic Engineering from the University of Naples, Italy, in 1978. From 1978 to 1983, he worked with the Research Group in Electromagnetics at the Electronic Engineering Department of the University "Federico II" of Naples. In 1983, he became Assistant Professor at the Istituto Universitario Navale (IUN), Naples. In 1987, he was appointed Associate Professor of Antennas, formerly at the Engineering Faculty of Ancona University and subsequently at the Engineering Faculty of Salerno University. In 1999, he has been appointed Full Professor at the same University. The main topics of his scientific activity are: reflector antennas analysis, antenna measurements, diffraction problems, radar cross section evaluations, scattering from surface impedances, application of sampling techniques to electromagnetics and to NF–FF transformations. Gennarelli is co-author of about 400 scientific papers, mainly in international journals and conference proceedings. In particular, he is co-author of four books on NF–FF transformation techniques. He is a Senior Member of the IEEE and Member of the Editorial board of the Open Electrical and Electronic Engineering Journal and of the International Journal of Antennas and Propagation.

Rocco Guerriero received the Laurea degree in Electronic Engineering and the Ph.D. degree in Information Engineering from the University of Salerno in 2003 and 2007, respectively. Since 2003, he has been with the Research Group in Applied Electromagnetics of University of Salerno, where he is currently an Assistant Professor of Electromagnetic Fields. His interests include: application of sampling techniques to the efficient reconstruction of electromagnetic fields and to near-field-far-field transformation techniques; antenna measurements; inversion of ill-posed electromagnetic problems; analysis of microstrip reflectarrays; diffraction problems. Guerriero is co-author of about 180 scientific papers, mainly in international journals and conference proceedings. He is Reviewer for several international journals and Member of the Editorial board of the International Journal of Antennas and Propagation. Since 2015, he is Member IEEE.

Massimo Migliozzi received the Laurea degree in Electronic Engineering from the University of Salerno, in 1999. He received the Ph.D. degree in Information Engineering at the same University, where at the present time he is a Research Fellow in Electromagnetic Fields. His scientific interests include: application of sampling techniques to the efficient reconstruction of electromagnetic fields and to NF–FF transformation techniques; antenna measurements; electromagnetic compatibility; antenna design; diffraction problems. Migliozzi is co-author of over 130 scientific papers, mainly in international journals and conference proceedings. He is Reviewer for several international journals.

High-order Staggered Finite Difference Time Domain Method for Dispersive Debye Medium

A. Guellab and W. Qun

School of Electronics and Information Engineering
Harbin Institute of Technology, Harbin, 150001, China
Ammarguellab400@hit.edu.cn, qwu@hit.edu.cn

Abstract ─ In this paper, a high order accuracy Finite Difference Time Domain method was proposed for the simulation of electromagnetic waves in the Debye dispersive medium. The proposed method was based on the use of the third order Backward Differentiation scheme for the approximation of the time derivatives and the use of the fourth order Central Finite Difference scheme for the approximation of space derivatives. The stability of the present method was analyzed by using the Root-Locus method. The accuracy of the proposed method was analyzed in the case of free space and the dispersive media, in the case of plane wave and the case of a Hertzian dipole source.

The proposed method offered high performance regarding the accuracy and the stability in comparison with the other methods.

Index Terms ─ Accuracy, backward differentiation, central finite difference, Debye model, dispersive media, finite difference time domain, stability.

I. INTRODUCTION

Since the Finite-Difference-Time-Domain (FDTD) has been proposed [1], it has been widely used for the simulation of the electromagnetic (EM) waves behavior within frequency dependent media such as saline water [2], human tissues [3-5], and plasma [6,7]. For modeling these frequency dependent media, many dispersive models have been proposed, such as the multi-pole Debye, Lorentz, and Drude model. The use of the conventional FDTD for the simulation of these models leads to a lack of accuracy and complexity of the stability analysis, especially when multiple poles are used. Therefore, the development of more accurate and stable FDTD based schemes acquire a great interest in the scientific society.

Many techniques have been proposed for the numerical implementation of the dispersive models into the FDTD method. Those methods can be grouped into three main categories: Z-transformation methods, recursive convolution methods, and the Auxiliary Differential Equation (ADE) methods.

The Z-transform (ZT) methods are based on the digital filtering theory [8,9]. The transfer function of the dielectric permittivity is converted from the frequency domain to the Z-domain, then the actual update equations in the discrete time domain are obtained. The recursive convolution (RC) methods are based on writing the dispersion equation as a convolution product in the time domain, then using the discrete recursive integrator for the actual update equations. Among these methods, we find the trapezoidal recursive convolution technique (TRC) and the Piecewise linear recursive convolution method (PLRC) [10-12]. The ADE methods are based on writing the dispersion relations under the form of differential equations. Then using the finite difference schemes to obtain the actual update equations [13-15].

Contrary to the RC and ZT methods which are in their improved versions limited to the second order of precision, the ADE methods offer more flexibility regarding the implementation of dispersive media while using a higher order of accuracy.

Therefore, seeking for improvement of the accuracy order and the stability condition, many techniques among the ADE category have been proposed. The Alternating Direction Implicit (ADI) FDTD [16,17] have been widely used to guarantee unconditional stability. Also, it saves both the memory and time consumption. However, this technique suffers from inaccuracies especially for a high Courant–Friedrichs–Levy (CFL) number. Another method based on the fact that Maxwell's equations can be written under the form of a symplectic integrator has been used to improve the accuracy of the FDTD method in many researches [18-20]. The symplectic method offers high performances in both stability and precision. However, it consists of repetitive loops inside one-time iteration. this leads to cumbersome the CPU use and then slows down the execution. Previously in the literature, Fang [21] proposed two high order FDTD methods for solving Maxwell's equations. The staggered FDTD (2,4) and FDTD (4,4) (where the first and the second index refer to the time and space accuracy order, respectively) are more accurate than the previously mentioned methods. Then, the FDTD (2,4) has been widely applied for frequency dependent media [22]. However, the FDTD

Submitted On: August 11, 2017
Accepted On: January 22, 2018

(4,4) did not get a significant focus in the simulation of the frequency dependent media, regarding its complexity.

We have proposed a high order FDTD (3,4) for the non-dispersive media [23], and in this paper, the method has been extended for the simulation of a frequency dependent media which consisted of the combination of a multi-pole Debye model with a lossy conductive model. An analysis of the accuracy and the stability proved that the proposed method offered high performance in comparison with the previously cited methods.

II. FORMULATIONS

Consider the time-dependent form of Maxwell's equations for a homogeneous Debye dispersive medium:

$$\frac{\partial \vec{D}}{\partial t} = \nabla \times \vec{H} \ , \tag{1.a}$$

$$\frac{\partial \vec{B}}{\partial t} = \frac{\partial}{\partial t}\left(\mu \vec{H}\right) = -\nabla \times \vec{E} \ . \tag{1.b}$$

Together with the dispersive permeability relationship:

$$\vec{D} = \varepsilon * \vec{E} \ , \tag{2}$$

where $\vec{E}$ and $\vec{H}$ are the electric and magnetic fields; $\vec{D}$ and $\vec{B}$ are the electric and the magnetic flux density; ε and μ are the dispersive permittivity and permeability of the medium; * denotes the convolution operator.

The permittivity of a multi-pole Debye model combined with a static conductivity factor in the frequency domain is expressed as follows:

$$\varepsilon(\omega) = \varepsilon_0\left(\varepsilon_\infty + \sum_{k=1}^{K}\frac{\Delta\varepsilon_k}{1+j\tau_k\omega} + \frac{\sigma_s}{j\omega\varepsilon_0}\right), \tag{3}$$

where $j=\sqrt{-1}$; ω is the angular frequency; ε_0 is the free space permittivity; ε_∞ is the permittivity at the infinite frequency; K is the number of Debye poles; $\Delta\varepsilon_k$ and τ_k are the k^{th} Debye pole's magnitude and the relaxation time, respectively; σ_s is the static conductivity.

The permittivity relation in Equation (3) can be expressed as a system of ADE as follows:

$$\vec{D}(t) = \varepsilon_0\varepsilon_\infty \vec{E}(t) + \sum_{k=1}^{K}\vec{P_k}(t) + \overrightarrow{P_{loss}}(t), \tag{4.a}$$

$$\vec{P_k}(t) + \tau_k \frac{\partial \vec{P}}{\partial t}(t) = \varepsilon_0 \Delta\varepsilon_k \vec{E}(t), \tag{4.b}$$

$$\frac{\partial \overrightarrow{P_{loss}}}{\partial t}(t) = \sigma_s \vec{E}(t), \tag{4.c}$$

where K is the number of the Debye poles; P_k is the polarization density of the k^{th} Debye pole; P_{loss} is the conductive loss term.

The computational domain is discretized by using the Yee's staggered grid. Δx, Δy, and Δz denote the spatial step; Δt is the time increment. For a given function F which can be one of the electric or magnetic field's component, the discrete is defined form as follows:

$$F_{i,j,k}^{n} = F(i\Delta x, j\Delta y, k\Delta z, n\Delta t). \tag{5}$$

The principle of the proposed method is based on applying the fourth order Central Finite Difference scheme for the approximation of the space derivatives in the curl equations, and the third order Backward Differentiation scheme for the approximation of the time derivatives, as shown in the following equations:

$$\left.\frac{\partial F}{\partial t}\right|_{i,j,k}^{n-\frac{1}{2}} = \frac{1}{\Delta t}\sum_{q=0}^{N} a_q F_{i,j,k}^{n-q} + O\left(\Delta t^{N+1}\right), \tag{6.a}$$

$$\left.\frac{\partial F}{\partial t}\right|_{i,j,k}^{n} = \frac{1}{\Delta t}\sum_{q=0}^{N} b_q F_{i,j,k}^{n-q} + O\left(\Delta t^{N+1}\right), \tag{6.b}$$

$$\left.\frac{\partial F}{\partial x}\right|_{i,j,k}^{n} = \frac{1}{\Delta x}\sum_{p=1}^{M/2} w_p\left(F^{n}_{i+p-\frac{1}{2},j,k} - F^{n}_{i-p+\frac{1}{2},j,k}\right) + O\left(\Delta x^{M+1}\right), \tag{6.c}$$

where N and M are the accuracy order in the time and the spatial domain, respectively. The coefficients a_q, b_q, and w_p are shown in Table 1 and Table 2. Equation (6.a) is used for the approximation of the time derivative of the electric and magnetic flux density. Equation (6.b) is used to approximate the time derivatives of the polarization density P_k and the conductive lossy term P_{loss}. Equation (6.c) is used for the approximation of the spatial derivatives

Table 1: Coefficients of the N^{th} order backward time differentiation

N	$\{a_0,a_1,\ldots,a_N\}$	$\{b_0,b_1,\ldots,b_N\}$
1	{1,-1}	{1,-1}
2	{1,-1,0}	{3, -4,1}/2
3	{23, -21, -3, 1}/24	{11, -18, 9, -2}/6
4	{22, -17, -9, 5,-1}/24	{25, -48, 36, -16, 3}/12

Table 2: Coefficients of the M^{th} order central spatial differentiation

M	$\{w_1,\ldots,w_{M/2}\}$
2	{1}
4	{27, -1}/24

After applying the backward differentiation in the time domain and the central differentiation in the space domain to Maxwell's equation and the dielectric dispersive relation Equation (6), we obtain the update equations of the high order FDTD scheme which is composed of the following steps (we show only the update steps for the X-axis components. The same procedure is applied to the Y and Z-axis components):

1. Update of the electric flux density:

$$D_{x}{}^{n}_{i+\frac{1}{2},j,k} = -\frac{1}{a_0}\sum_{q=1}^{N} a_q D_{x}{}^{n-q}_{i+\frac{1}{2},j,k} + \frac{\Delta t}{a_0}\left[\frac{1}{\Delta y}\sum_{p=1}^{M/2} w_p\left(H_{z}{}^{n-\frac{1}{2}}_{i+\frac{1}{2},j+p-\frac{1}{2},k} - H_{z}{}^{n-\frac{1}{2}}_{i+\frac{1}{2},j-p+\frac{1}{2},k}\right) - \frac{1}{\Delta z}\sum_{p=1}^{M/2} w_p\left(H_{y}{}^{n-\frac{1}{2}}_{i+\frac{1}{2},j,k+p-\frac{1}{2}} - H_{y}{}^{n-\frac{1}{2}}_{i+\frac{1}{2},j,k-p+\frac{1}{2}}\right)\right]. \tag{7}$$

2. Update of the electric field:

$$E_{\boldsymbol{x}}{}^{n}_{i+\frac{1}{2},j,k} = \frac{1}{\varepsilon_0\left(\varepsilon_\infty+\sum_{k=1}^{K}\frac{\Delta t\Delta\varepsilon_k}{\Delta t+b_0\tau_k}+\frac{\Delta t\sigma_s}{b_0\varepsilon_0}\right)}\Bigg[D_x{}^{n}_{i+\frac{1}{2},j,k} + \sum_{k=1}^{K}\tau_k\sum_{q=1}^{N}\frac{b_q}{\Delta t+b_0\tau_k}P_{\boldsymbol{k},\boldsymbol{x}}{}^{n-q}_{i+\frac{1}{2},j,k} + \sum_{q=1}^{N}\frac{b_q}{b_0}P_{\boldsymbol{s},\boldsymbol{x}}{}^{n-q}_{i+\frac{1}{2},j,k}\Bigg], \quad (8.a)$$

$$P_{k,x}{}^{n}_{i+\frac{1}{2},j,k} = \varepsilon_0\frac{\Delta t\Delta\varepsilon_k}{\Delta t+b_0\tau_k}E_x{}^{n}_{i+\frac{1}{2},j,k} - \tau_k\sum_{q=1}^{N}\frac{b_q}{\Delta t+b_0\tau_k}P_{k,x}{}^{n-q}_{i+\frac{1}{2},j,k}, \quad (8.b)$$

$$P_{loss,x}{}^{n}_{i+\frac{1}{2},j,k} = \frac{\Delta t\sigma_s}{b_0}E_x{}^{n}_{i+\frac{1}{2},j,k} - \sum_{q=1}^{N}\frac{b_q}{b_0}P_{loss,x}{}^{n-q}_{i+\frac{1}{2},j,k}. \quad (8.b)$$

3. Update of the magnetic field:

$$H_x{}^{n-\frac{1}{2}}_{i,j+\frac{1}{2},k+\frac{1}{2}} = -\frac{1}{a_0}\sum_{q=1}^{N}a_q H_x{}^{n-\frac{1}{2}-q}_{i,j+\frac{1}{2},k+\frac{1}{2}} - \frac{\Delta t}{a_0\mu}\left[\frac{1}{\Delta y}\sum_{p=1}^{M/2}w_p\left(E_z{}^{n-\frac{1}{2}}_{i,j+p,k+\frac{1}{2}} - E_z{}^{n-\frac{1}{2}}_{i,j-p+1,k+\frac{1}{2}}\right) + \frac{1}{\Delta z}\sum_{p=1}^{M/2}w_p\left(E_y{}^{n-\frac{1}{2}}_{i,j+\frac{1}{2},k+p} - E_y{}^{n-\frac{1}{2}}_{i,j+\frac{1}{2},k-p+1}\right)\right]. \quad (9)$$

III. STABILITY ANALYSIS

As stated, the Lax–Richtmyer theorem, a consistent finite difference scheme associated to a well-posed system of auxiliary differential equations is convergent to the analytical solution if and only if it is stable [24]. Therefore, the stability analysis leads also to prove the convergence of the studied scheme.

Regarding the fact that we only deal with linear equations, the Z-transformation is applicable for the update Equations (7, 8 and 9). Then by assuming a plane wave propagating in a homogeneous domain, the computed electric field can be presented as follows:

$$E_x^n(\vec{r}) = z^n E_x^0\, e^{-i\vec{k}.\vec{r}}, \quad (10)$$

where $\vec{k} = (k_x, k_y, k_z)$ is the wave vector, z is the Z-transformation variable, and $\vec{r} = (x, y, z)$ is a position vector.

By applying the Z-transformation to the update Equations (7, 8 and 9), the Z-domain wave equation is obtained:

$$\left[{\delta_t}^2(z)\mu_r(z)\varepsilon_r(z)I - z^{-1}c_0^2\tilde{C}\tilde{C}^T\right]E(z) = 0, \quad (11)$$

$$\tilde{C} = \begin{bmatrix} 0 & -\delta_z & \delta_y \\ \delta_z & 0 & -\delta_x \\ -\delta_y & \delta_x & 0 \end{bmatrix}, \quad (12)$$

where $c_0 = 1/\sqrt{\mu_0\varepsilon_0}$, $\delta_t = \frac{1}{\Delta t}\sum_{q=0}^{N}a_q z^{-q}$ is the Z-transform of the time backward differentiation, $\tilde{C}$ is the discrete form of the matrix curl-operator, $\delta_x = \frac{2j}{\Delta x}\sum_{p=1}^{M/2}w_p sin\left((p-1/2)k_x\Delta x\right)$ is the central difference operator for the plane wave, δ_y and δ_z are computed similarly to δ_x, and $\varepsilon_r(z)$ is obtained by applying the Z-transformation to Equation (8).

By computing the eigenvalues of Equation (11), it can be reduced to a scalar wave equation:

$$z{\delta_t}^2(z)\mu_r(z)\varepsilon_r(z) + {c_0}^2\left({\delta_x}^2 + {\delta_y}^2 + {\delta_z}^2\right) = 0. \quad (13)$$

By consequence, the stability analysis of the proposed method is reduced to analyzing the stability of the scalar wave Equation (13).

In the automatic control theory, one of the widely used methods for analyzing the stability of discrete control systems is the Root-Locus method [25]. The Root-Locus method is based first on, writing the studied equations under the form of a linear discrete feedback system as shown Equation (14).

$$1 + K\frac{1}{z{\delta_t}^2(z)}\frac{1}{\mu_r(z)\varepsilon_r(z)} = 0, \quad (14)$$

where

$$K = {c_0}^2\sum_{\eta=x,y,z}\left[\frac{2\Delta t}{\Delta\eta}\sum_{p=1}^{M/2}w_p sin\left((p-1/2)k_\eta\Delta\eta\right)\right]^2.$$

Then, the Root-Locus analysis plots the locations of the Equation 14 roots in the complex plane as a function of the gain *K*. The stability condition of a discrete feedback system is granted when all the roots are located within the unit circle.

The maximum value of the gain K that maintains the stability criteria is evaluated. Then, assuming the worst case by letting $sin\left((p-1/2)k_\eta\Delta\eta\right) = 1$, to compute the CFL condition in the in the case of $\Delta = \Delta x = \Delta y = \Delta z$:

$$CFL = c_0\frac{\Delta t_{max}}{\Delta}. \quad (15)$$

The above procedure is applied for studying the stability condition for the High-order FDTD implementation of a Four-pole Debye model [3], which is used for modeling human muscle, fat, and skin tissues. The special resolution is selected at 25, 50, 75, or 100 points per wavelength (PPW) $\lambda_{min} = 0.05m$.

Figure 1 shows the Root-Locus plot for the free space with the implementation of different FDTD methods. The curves represent the paths traveled by the roots of Equation 14. The critical point for which the stability limit is attained and the maximal values of the gain *K* are indicated in the figure.

Figure 2 shows the Root-Locus plot for the muscle tissue with the implementation of FDTD methods with a fixed resolution at 25 PPW. Figure 3 shows the Root-Locus plot for the muscle tissue with the implementation of the FDTD (3,4) with different resolutions (25, 50, 75, and 100 PPW). Then the CFL limit for each case is computed from the maximum values of the gain *K*. Table 3 resumes a comparison of the CFL condition between the different FDTD methods. Table 4 summarizes the maximum CFL for each tissue.

Based on the results in Table 3, in the case of the free space, the Root-Locus method fits with the Von-Neumann [26] stability condition; which is independent of the spatial grid resolution. However, in the case of

a dispersive media, the stability limit is inversely proportional to the grid resolution. Also, we can note that for the high grid resolution, the stability condition tends to retain that of a non-dispersive case where $\varepsilon_r = \varepsilon_\infty$.

From Table 4, regardless the type of the material, the FDTD with high accuracy order are less stable than those with low accuracy order. As a consequence, a tradeoff between the stability and the precision is recommended.

In order to validate the Root-Locus analysis results, a numerical stability test is carried out. A simple electromagnetic scenario is simulated using the FDTD (3,4). The computational space is filled with a dispersive Debye media (muscles tissue). An infinitesimal Hertzian dipole is inserted in the center of the computational space. Two current numbers ($c\Delta t/\Delta x$) are used, 0.1% below and above the CFL limit, respectively. Where the CFL limit of the FDTD (3,4) was found to be 1.2446 for a resolution of 25 PPW in Table 3.

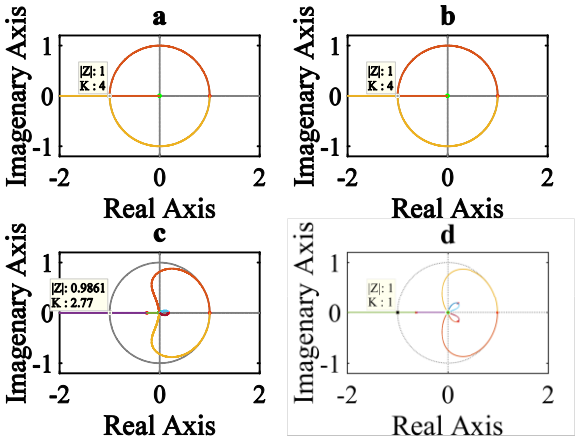

Fig. 1. Root-Locus for FDTD schemes in the free space: (a) FDTD (2,2), (b) FDTD (2,4), (c) FDTD (3,4), and (d) FDTD (4,4).

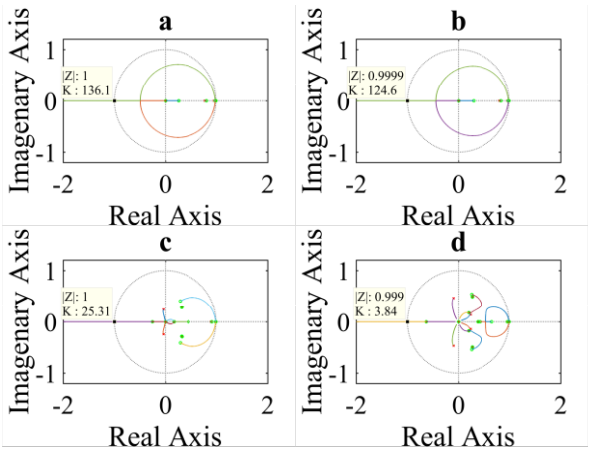

Fig. 2. Root-Locus for FDTD schemes in human muscle tissue: (a) FDTD (2,2), (b) FDTD (2,4), (c) FDTD (3,4), and (d) FDTD (4,4).

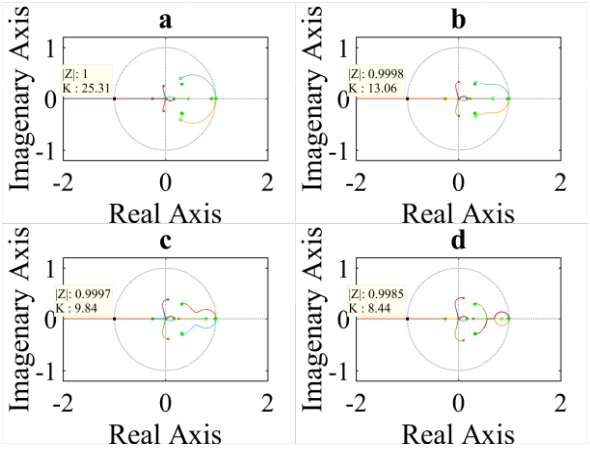

Fig. 3. Root-Locus for FDTD (3,4) schemes in human muscle tissue, for different resolutions: (a) 25 PPW, (b) 50 PPW, (c) 75 PPW, and (d) 100 PPW.

Table 3: CFL for Human muscle tissue modeled by 4-Pole Debye [3], with different PPW, with fmax = 6 GHz

Tissue	Muscle						Free Space
PPW	25	50	75	100	2000	Non-Dispersive	
FDTD(2,2)	3.3019	2.5384	2.0568	1.7565	0.8347	0.7874	0.5715
FDTD(2,4)	2.6852	2.0643	1.6726	1.4285	0.7094	0.6749	0.4899
FDTD(3,4)	1.2446	0.8942	0.7762	0.7188	0.5696	0.5621	0.4118
FDTD(4,4)	0.4849	0.4073	0.3825	0.3712	0.3384	0.3374	0.2474

Table 4: CFL for different human tissues modeled by 4-Pole Debye [3], with PPW = 25, and f_{max} = 6 GHz

Tissue	Muscle	Fate	Wet Skin	Dry Skin
FDTD(2,2)	3.3019	0.984	2.9722	2.8199
FDTD(2,4)	2.6852	0.831	2.4171	2.4171
FDTD(3,4)	1.2446	0.6328	1.3219	1.4285
FDTD(4,4)	0.4849	0.3695	0.5359	0.7493

Figure 4 (a) shows the simulation results of the first case after 20000 steps. There is no sign of instability. Figure 4 (b) shows the situation results of the second case. It is clear that the simulation, in this case, is unstable. This confirms the results obtained by the Root-Locus method.

As a conclusion of this part, the Root-Locus method offers an accurate estimation of the CFL stability condition

of the FDTD methods regardless the complexity of the implementation medium and the accuracy orders of the FDTD method.

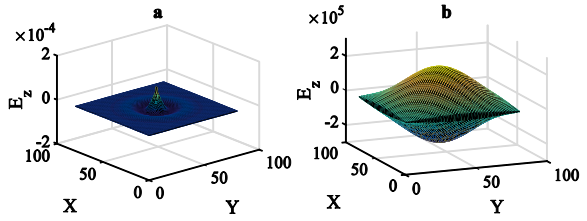

Fig. 4. Stability test in the case of muscle tissue at 25PPW: (a) $c\Delta t/\Delta x = 1.2444$, and (b) $c\Delta t/\Delta x = 1.2458$.

IV. NUMERICAL VALIDATION

In this part, the accuracy of the proposed method is compared to the original FDTD, the high order FDTD (2,4) [22], and the FDTD (4,4) [21]. The simulation of some problems for which the analytical solution is well known, to compute the numerical dispersion of electromagnetic waves traveling in the free space and the Debye dispersive media.

A. Simulation in the free space

First, we consider the scenario of a plane wave traveling in the free space in different directions. The numerical dispersion is evaluated as the relative error in the phase velocity. The multicycle sine plane wave is introduced to the computational space by using the total field scattered field (TFSF) technique [27]. The frequency of the multicycle sine pulse is a function of the PPW. The simulation runs for the necessary time for the multicycle sine wave to entirely vanish through the TFSF interface. Then, the Fourier transform is applied on the electric field to compute the phase velocity.

Figure 5 shows the phase velocity error as a function of the PPW and the propagation angle. The FDTD (4,4) [21] has the lowest phase velocity errors, then the proposed scheme comes in the second place with about 2 dB above the FDTD (4,4), but it is largely lower than both the FDTD (2,2) and FDTD (2,4).

Second, we consider the scenario of a Hertzian dipole source inserted in the center of the computational space which is 200x200x200 cells sized. The space increments are $\Delta x = \Delta y = \Delta x = 1$ mm. The CFL is 0.2. Ten cells perfectly matched layers (PML) surrounds the computational space to absorb the outgoing waves. The Hertzian dipole is fed by a wideband current pulse as shows Equation 16. The observation point is located at a distance of 20 cells from the Hertzian dipole source:

$$Src(t) = \frac{1}{s^2}(t-m)e^{-0.5\left((t-m)/s\right)^2}, \qquad (16)$$

where $s = 16\Delta t$; $m = 160\Delta t$.

The obtained results are compared with the fields computed using the analytic formula of the Hertzian dipole [28]. As shown in Fig. 6, all of the FDTD (2,4), FDTD (3,4) and FDTD (4,4) fit with the analytic solution rather than the FDTD (2,2). Figure 7 shows the error of each method which is expressed by Equation 17. The proposed scheme offers almost the same precision as the FDTD (4,4) and higher than both the original FDTD (2,2) and the FDTD (2,4):

$$Err(r) = \sqrt{\frac{\sum_t |E_z(r,t) - E_{FDTD}(r,t)|^2}{\sum_t |E_z(r,t)|^2}}, \qquad (17)$$

where $E_z(r,t)$ is the analytically computed electric field and $E_{FDTD}(r,t)$ is the electric field computed by the FDTD method.

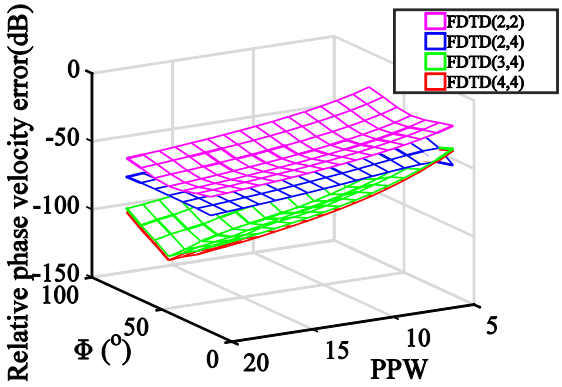

Fig. 5. Relative phase velocity errors as function of the number of points per wavelength (PPW) and the propagation angle Φ.

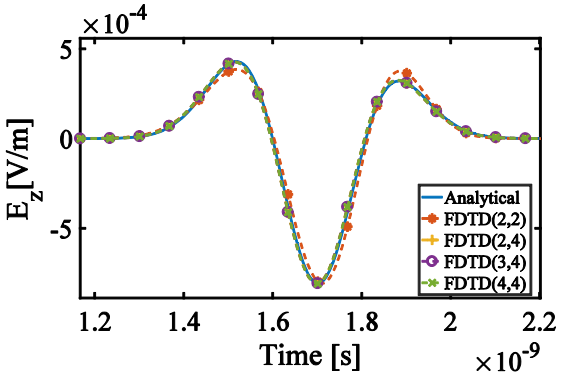

Fig. 6. Comparison of the electric field at $20\Delta x$ from the dipole source in the time domain, as computed by the FDTD methods and the theory.

From the above results, in the case of a non-dispersive media, the proposed scheme is better than the original FDTD and the FDTD (2,4), and it offers almost similar performance as the FDTD (4,4) in terms of precision. Also if we consider the low stability condition of the FDTD (4,4) discussed in Section 3, we can deduce that our scheme is more efficient regarding the stability-precision criterion.

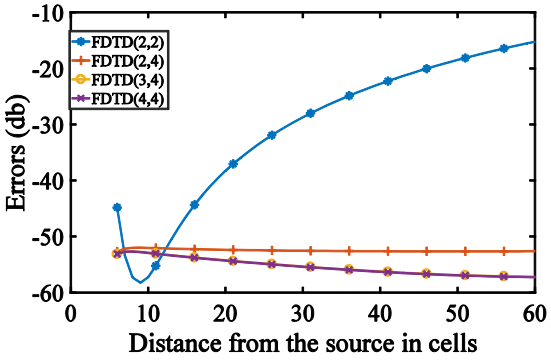

Fig. 7. Errors on the computed electric field expressed by Equation (16), as a function of the distance from the source.

B. Simulation in the Debye media

To validate the accuracy of the proposed method relating to the simulation in the dispersive media, we effectuate the following simulations using the Debye model.

The first scenario consists of the simulation of a plane wave normally incident on the interface between the free space and a homogeneous dispersive media. As an example, we take the Four-Pole Debye model of the muscles where the parameters are listed in [3]. Figure 8 shows the FDTD simulation model. The computational space is delimited by a perfect electric conductor (PEC) from z-direction boundaries, a perfect magnetic conductor (PEM) from the y-direction boundaries. At the x-direction boundaries, a polarized current source excitation surface is placed on one side, and perfectly matched layers (PML) boundary is on the other side. Figure 9 demonstrates the ability of the proposed method to model the Debye dispersive media in comparison with the others methods. It shows that at the interval above 20 PPW the reflection coefficients computed by FDTD (3,4) and FDTD (4,4) fit perfectly with the theoretical one. Figure 10 shows the errors in the computed coefficient of reflection effectuated by each scheme. The obtained results demonstrate that the errors effectuated by the proposed scheme are almost equivalent to the high order FDTD (4,4) and largely lower than those of the FDTD (2,4) and FDTD (2,2).

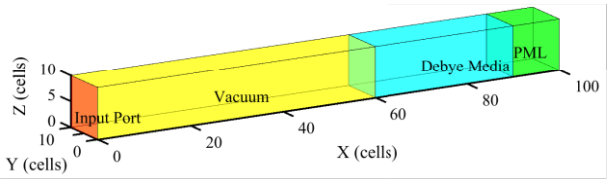

Fig. 8. Numerical FDTD model used to validate the FDTD (3,4) for modeling 4-pole Debye media.

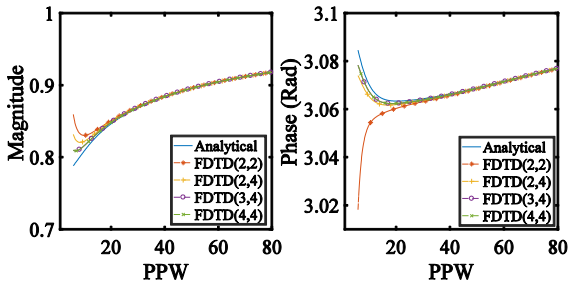

Fig. 9. Magnitude and phase of the reflection coefficient of vacuum – human muscle model interface.

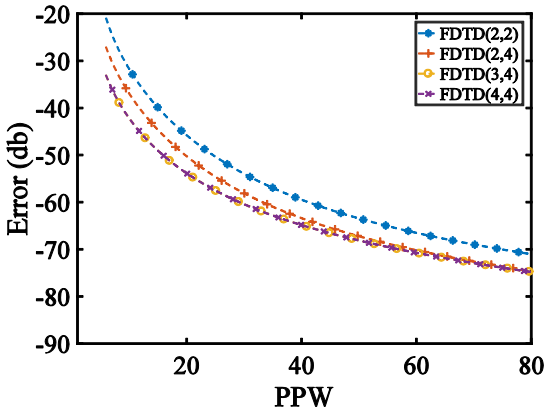

Fig. 10. Errors in the computed reflection coefficient as a function of the PPW.

Secondly, we consider a Hertzian dipole source inserted in the center of the FDTD computational space which is filled with a dispersive media. We refer to the Four-Pole Debye model of the human muscles [3]. The analytical solution is expressed in the frequency domain by including the complex dielectric conductivity and the frequency spectrum of the input source signal $S(f)$ to the general solution of the Hertzian dipole [29]. Equation 18 expresses the electric field in the frequency domain:

$$\vec{E}(r,f) = S(f)l\frac{e^{-2j\pi fr\sqrt{\mu\varepsilon_0\varepsilon_r}}}{4j\pi^2 f\varepsilon_0\varepsilon_r} \times \left(\frac{1}{r^3} + \frac{2j\pi f\sqrt{\mu\varepsilon_0\varepsilon_r}}{r^2}\right) cos(\theta)\overrightarrow{e_r} + S(f)l\frac{e^{-2j\pi fr\sqrt{\mu\varepsilon_0\varepsilon_r}}}{8j\pi^2 f\varepsilon_0\varepsilon_r} \times \left(\frac{1}{r^3} + \frac{2j\pi f\sqrt{\mu\varepsilon_0\varepsilon_r}}{r^2} - \frac{4\pi^2 f^2\mu\varepsilon_0\varepsilon_r}{r}\right) sin(\theta)\overrightarrow{e_\theta}, \quad (18)$$

where l is length of the Hertzian dipole, r is the distance of the observation point from the source, $\overrightarrow{e_r}$ is the unite vector from the source to the observation point and $\overrightarrow{e_\theta}$ is the unite vector perpendicular to $\overrightarrow{e_r}$.

The numerical dispersion of the FDTD is evaluated as follows:

$$Err(r) = \sqrt{\frac{\sum_f |E_z(r,f) - E_{FDTD}(r,f)|^2}{\sum_f |E_z(r,f)|^2}}, \quad (19)$$

where $E_z(r,f)$ is the analytically computed electric field, and $E_{FDTD}(r,f)$ is the frequency component computed by the FDTD method.

Figure 11 shows the agreement of the proposed method with the analytical solution. Also, the others methods agree with the analytical solution in varying proportion. Figure 12 shows the errors of each method as a function of the distance from the source. FDTD (3,4) and FDTD (4,4) offer almost the same precision which is higher than both the FDTD (2,4) and the original FDTD (2,2).

According to the results of the numerical experiments in both the free space and in the Debye dispersive medium, the proposed method is more accurate than both the FDTD (2,2) and the FDTD (2,4). Moreover, it offers almost the same precision as the FDTD (4,4). Hence, when considering the low stability provided by FDTD (4,4), one can conclude that the proposed method offers the best tradeoff between the accuracy and the stability.

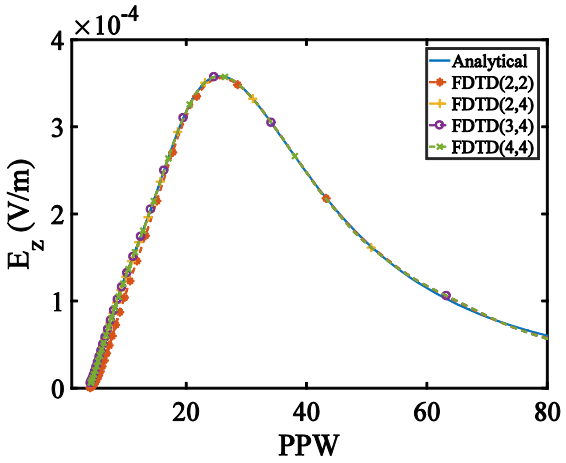

Fig. 11. Comparison of the electric field at 20Δx from the dipole source in the frequency domain, as computed by the FDTD methods and the theory as a function of the PPW.

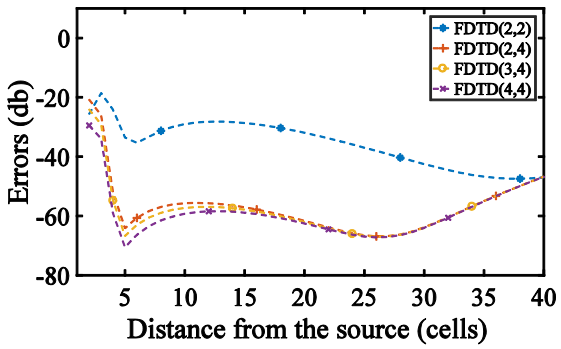

Fig. 12. Errors on the electric field expressed by Equation (18) as a function of the distance from the source.

V. CONCLUSION

A high order accuracy FDTD method for the simulation of the electromagnetic wave behavior in the dispersive media is developed. The proposed method is third order accuracy concerning the approximation of the time domain derivatives and fourth order accuracy concerning the space domain derivatives. The stability of the proposed method is analyzed by using the Root-Locus method, first in the case of the free space, then in the case of the Debye dispersive media. The proposed method comes in third place after the original FDTD method and the FDTD (2,4) which are less accurate. The numerical dispersion analysis in both cases, in the free space and the Debye dispersive media, revealed that the proposed method offered almost the same precision as the high order FDTD (4,4). However, this last has a deficient stability performance. As a tradeoff between the stability and accuracy, the proposed method offers the best performances.

ACKNOWLEDGMENT

This project is partly supported by the National Natural Science Foundation of China (Grant No. 61371044).

REFERENCES

[1] K. Yee, "Numerical solution of initial boundary value problems involving maxwell's equations in isotropic media," *IEEE Trans. Antennas Propagat.*, vol. 14, no. 3, pp. 302-307, 1966.

[2] M. Pieraccini, A. Bicci, D. Mecatti, G. Macaluso and C. Atzeni, "Propagation of large bandwidth microwave signals in water," *IEEE Trans. Antennas Propagat.*, vol. 57, no. 11, pp. 3612-3618, 2009.

[3] S. Mustafa, A. Abbosh, and P. Nguyen, "Modeling human head tissues using fourth-order Debye model in convolution-based three-dimensional finite-difference time-domain," *IEEE Trans. Antennas Propagat.*, vol. 62, no. 3, pp. 1354-1361, 2014.

[4] C. Gabriel, "Compilation of the Dielectric Properties of Body Tissues at RF and Microwave Frequencies," *Brooks Air Force, Tech. Rep. AL/OE-TR-19960037*, 1996.

[5] P. Bia, L. Mescia, and D. Caratelli, "Fractional calculus-based modeling of electromagnetic field propagation in arbitrary biological tissue," *Mathematical Problems in Engineering*, vol. 2016, pp. 1-11, 2016.

[6] J. Li, L.-X. Guo, Y.-C. Jiao, and R. Wang, "Composite scattering of a plasma-coated target above dispersive sea surface by the ADE-FDTD method," *IEEE Geoscience and Remote Sensing Letters*, vol. 10, no. 1, pp. 4-8, 2013.

[7] S. Liu, S. Liu, and S. Liu, "Finite-difference time-domain algorithm for plasma based on trapezoidal

recursive convolution technique," *Journal of Infrared, Millimeter, and Terahertz Waves*, 2010.

[8] D. Sullivan, "Nonlinear FDTD formulations using Z transforms," *IEEE Transactions on Microwave Theory and Techniques*, vol. 43, no. 3, pp. 676-682, 1995.

[9] D. B. Miron, "Z-transform frameworks for FDTD," *Antennas and Propagation Magazine IEEE*, vol. 54, pp. 131-144, 2012, ISSN 1045-9243.

[10] R. Luebbers and F. Hunsberger, "FDTD for Nth-order dispersive media," *IEEE Trans. Antennas Propagat*., vol. 40, no. 11, pp. 1297-1301, 1992.

[11] D. F. Kelley and R. J. Luebbers, "Piecewise linear recursive convolution for dispersive media using FDTD," *IEEE Trans. Antennas Propagat*., vol. 44, no. 6, pp. 792-797, June 1996.

[12] I. Giannakis and A. Giannopoulos, "A novel piecewise linear recursive convolution approach for dispersive media using the finite-difference time-domain Method," *IEEE Trans. Antennas Propagat*., vol. 62, no. 5, pp. 2669-2678, 2014.

[13] M. Okoniewaki, M. Mrozowski, and M. Stuchly, "Simple treatment of multi-term dispersion in FDTD," *IEEE Microwave and Guided Wave Letters*, vol. 7, no. 5, pp. 121-123, 1997.

[14] M. Alsunaidi and A. Al-Jabr, "A general ADE-FDTD algorithm for the simulation of dispersive structures," *IEEE Photonics Technology Letters*, vol. 21, no. 12, pp. 817-819, 2009.

[15] M. Okoniewski and E. Okoniewska, "Drude dispersion in ADE FDTD revisited," *Electronics Letters*, vol. 42, no. 9, p. 503, 2006.

[16] S. Garcia, R. Rubio, A. Bretones, and R. Martin, "Extension of the ADI-FDTD method to Debye media," *IEEE Trans. Antennas Propagat*., vol. 51, no. 11, pp. 3183-3186, 2003.

[17] H.-L. Chen, B. Chen, D.-G. Fang, and H. Liu, "Extension of the ADI-BOR-FDTD method to Debye dispersive media," *IEEE Microwave and Wireless Components Letters*, vol. 19, no. 6, pp. 344-346, 2009.

[18] T. Hirono, Wayne Lui, S. Seki, and Y. Yoshikuni, "A three-dimensional fourth-order finite-difference time-domain scheme using a symplectic integrator propagator," *IEEE Transactions on Microwave Theory and Techniques*, vol. 49, no. 9, pp. 1640-1648, 2001.

[19] W. Sha, Z. Huang, M. Chen, and X. Wu, "Survey on symplectic finite-difference time-domain schemes for Maxwell's equations," *IEEE Trans. Antennas Propagat*., vol. 56, no. 2, pp. 493-500, 2008.

[20] X. Ren, Z. Huang, X. Wu, S. Lu, H. Wang, L. Wu, and S. Li, "High-order unified symplectic FDTD scheme for the metamaterials," *Computer Physics Communications*, vol. 183, no. 6, pp. 1192-1200, 2012.

[21] J. Fang, "Time domain finite difference computation for Maxwell's equations," *Ph.D. dissertation, Univ. California*, Berkeley, CA, 1989.

[22] I. Jung, I. Oh, Y. Hong, and J. Yook, "Optimized higher order 3-D (2,4) FDTD scheme for isotropic dispersion in plasma," *in Asia-Pacific Microwave Conference Proceedings*, Seoul, South Korea, pp. 815-817, 2013.

[23] Q. Wu and A. Guellab, "Accuracy and stability analysis of a 3D high-order staggered FDTD for Maxwell's equations*," in Applied Computational Electromagnetics Society Symposium (ACES), 2017 International*, pp. 1-2, 2017.

[24] L. Trefethen, *Finite Difference and Spectral Methods for Ordinary and Partial Differential Equations*. Chap. 4: Stability, and Convergence, Ithaca, N.Y.: Cornell University-Department of Computer Science and Center for Applied Mathematics, 1996.

[25] O. Ramadan, "On the stability of the FDTD implementation of high order rational constitutive relations," *IEEE Microwave and Wireless Components Letters*, vol. 27, no. 1, pp. 4-6, 2017.

[26] X. Fei and T. Xiaohong, "Stability and numerical dispersion analysis of a fourth-order accurate FDTD method," *IEEE Trans. Antennas Propagat*., vol. 54, no. 9, pp. 2525-2530, 2006.

[27] K. Abdijalilov and J. Schneider, "Analytic field propagation TFSF boundary for FDTD problems involving planar interfaces: Lossy material and evanescent fields," *Antennas and Wireless Propagation Letters*, vol. 5, no. 1, pp. 454-458, 2006.

[28] C. A. Balanis, *Antenna Theory Analysis and Design*. 3rd ed., Chap 4: Linear Wire Antennas, Wiley-Interscience, 2005.

[29] F. Costen, J. Berenger, and A. Brown, "Comparison of FDTD hard source with FDTD soft source and accuracy assessment in Debye media," *IEEE Trans. Antennas Propagat*., vol. 57, no. 7, pp. 2014-2022, 2009.

Effective CFS-PML Formulations Based on 2-D TE_ϕ BOR-FDTD for the Drude Model

Jianxiong Li [1,2,*] and Wei Jiao [1,2]

[1] School of Electronics and Information Engineering
Tianjin Polytechnic University, Tianjin, 300387, China
lijianxiong@tjpu.edu.cn

[2] Tianjin Key Laboratory of Optoelectronic Detection Technology and Systems
Tianjin, 300387, China

Abstract ─ Effective formulations of the complex frequency-shifted perfectly matched layer (CFS-PML) based on the two-dimensional (2-D) TE_ϕ body of revolution finite-difference time-domain (BOR-FDTD), named as the BOR-CFS-PML, are proposed to truncate the Drude media. The auxiliary differential equation (ADE) method and the trapezoidal recursive convolution (TRC) method are applied to the implementation of the BOR-CFS-PML. The proposed formulations have good performance in attenuating low-frequency evanescent waves and reducing late-time reflections. A numerical test is provided to validate the effectiveness of the proposed algorithm.

Index Terms ─ Auxiliary differential equation (ADE), body of revolution (BOR), complex frequency-shifted perfectly matched layer (CFS-PML), finite-difference time-domain (FDTD), trapezoidal recursive convolution (TRC).

I. INTRODUCTION

The body of revolution finite-difference time-domain (BOR-FDTD) method [1],[2] plays an important role in simulating electromagnetic wave propagation in rotationally symmetric geometries. The BOR-FDTD has an advantage of simplifying an original three-dimensional (3-D) problem to a two-dimensional (2-D) problem, so that it saves much running time.

When the open region problems are simulated, an effective absorbing boundary condition is necessary. The perfectly matched layer (PML) was firstly introduced by Berenger in [4]. Next, the stretched coordinate PML (SC-PML) with simple implementation in the corners and edges of the PML regions was presented in [5]. However, the SC-PML had a drawback of the inefficiency in attenuating the evanescent waves [6],[7]. To overcome the shortcoming of the SC-PML, the complex frequency-shifted PML (CFS-PML) [8] was proposed to efficiently damp the low-frequency evanescent waves and late-time reflections [6].

To analyze the Drude model and other dispersive models, the recursive convolution (RC) method [9],[10], the piecewise linear RC (PLRC) method [11] and the trapezoidal RC (TRC) method [12,13] have been explored to realize the frequency-dependent FDTD method. Especially, the TRC method has the advantages of high accuracy and simplicity.

In this paper, effective formulations of the CFS-PML based on the (2-D) TE_ϕ BOR-FDTD, named here as the BOR-CFS-PML, are proposed. The formulations of the BOR-CFS-PML utilize the auxiliary differential equation (ADE) method [14] and the TRC method to truncate the Drude media. The results of the numerical example show that the BOR-CFS-PML has much better absorbing performance than the SC-PML based on the BOR-FDTD.

II. FORMULATIONS

In the cylinder coordinate, the complex spatial coordinate-stretching variables are defined as:

$$\tilde{r} = r_1 + \int_{r_1}^{r} S_r(r')dr', \tag{1}$$

$$\tilde{z} = z_1 + \int_{z_1}^{z} S_z(z')dz', \tag{2}$$

where r_1 and z_1 are the interfaces between the FDTD and the PML grids along the directions of r and z, respectively, and S_η $(\eta = r, z)$ are the CFS-PML variables given by:

$$S_\eta = \kappa_\eta + \frac{\sigma_\eta}{\alpha_\eta + j\omega\varepsilon_0}, \tag{3}$$

where σ_η and α_η are positive real and κ_η is real and ≥ 1.

In 2-D TE_ϕ case, based on the SC-PML formulations [5], the frequency-domain modified Maxwell's equations

Submitted On: March 27, 2017
Accepted On: April 21, 2018

in the Drude media can be written as:

$$j\omega D_r = -\frac{1}{S_z}\cdot\frac{\partial H_\phi}{\partial z}, \tag{4}$$

$$j\omega D_z = \frac{1}{S_r}\cdot\frac{\partial H_\phi}{\partial r} + \frac{H_\phi}{\tilde{r}}, \tag{5}$$

$$-j\omega\mu_0 H_\phi = \frac{1}{S_z}\cdot\frac{\partial E_r}{\partial z} - \frac{1}{S_r}\cdot\frac{\partial E_z}{\partial r}. \tag{6}$$

The frequency-domain electric flux density D_η $(\eta = r, z)$ are given by:

$$D_\eta = \varepsilon_0\varepsilon_r(\omega)E_\eta, \tag{7}$$

where $\varepsilon_r(\omega)$ is the complex relative permittivity of the Drude model defined as:

$$\varepsilon_r(\omega) = 1 + \frac{\omega_p^2}{-\omega^2 + j\omega\Gamma}, \tag{8}$$

where ω_p is the Drude pole frequency and Γ is the damping constant.

By using the partial fraction expansion, S_η^{-1} can be expressed as:

$$S_\eta^{-1} = \frac{1}{\kappa_\eta} - \frac{\dfrac{\sigma_\eta}{\kappa_\eta^2\varepsilon_0}}{j\omega + \dfrac{\alpha_\eta}{\varepsilon_0} + \dfrac{\sigma_\eta}{\kappa_\eta\varepsilon_0}} = \frac{1}{\kappa_\eta} - \frac{\beta_\eta}{j\omega + \varphi_\eta}, \tag{9}$$

where

$$\beta_\eta = \frac{\sigma_\eta}{\kappa_\eta^2\varepsilon_0} \text{ and } \varphi_\eta = \frac{\alpha_\eta}{\varepsilon_0} + \frac{\sigma_\eta}{\kappa_\eta\varepsilon_0}.$$

By submitting (9) into (4)-(6) and using the inverse Fourier transformation and the ADE method, ones obtains:

$$\frac{\partial D_r}{\partial t} = -\frac{1}{\kappa_z}\cdot\frac{\partial H_\phi}{\partial z} + F_{rz}, \tag{10}$$

$$\frac{\partial D_z}{\partial t} = \frac{1}{\kappa_r}\cdot\frac{\partial H_\phi}{\partial r} - G_{zr} + \frac{1}{\lambda_r}\cdot\frac{H_\phi}{r} - P_{zr}, \tag{11}$$

$$-\mu_0\frac{\partial H_\phi}{\partial t} = \frac{1}{\kappa_z}\cdot\frac{\partial E_r}{\partial z} - Q_{\phi z} - \frac{1}{\kappa_r}\cdot\frac{\partial E_z}{\partial r} + Q_{\phi r}, \tag{12}$$

where F_{rz}, G_{zr}, P_{zr}, $Q_{\phi z}$ and $Q_{\phi r}$ are the auxiliary variables expressed as follows:

$$\frac{\partial F_{rz}}{\partial t} + \varphi_z F_{rz} = \beta_z\cdot\frac{\partial H_\phi}{\partial z}, \tag{13}$$

$$\frac{\partial G_{zr}}{\partial t} + \varphi_r G_{zr} = \beta_r\cdot\frac{\partial H_\phi}{\partial r}, \tag{14}$$

$$\frac{\partial P_{zr}}{\partial t} + \left(\frac{\alpha_r}{\varepsilon_0} + \frac{\theta_r}{\varepsilon_0\lambda_r}\right)P_{zr} = \frac{\theta_r}{\varepsilon_0\lambda_r^2}\cdot\frac{H_\phi}{r}, \tag{15}$$

$$\frac{\partial Q_{\phi z}}{\partial t} + \varphi_z Q_{\phi z} = \beta_z\cdot\frac{\partial E_r}{\partial z}, \tag{16}$$

$$\frac{\partial Q_{\phi r}}{\partial t} + \varphi_r Q_{\phi r} = \beta_r\cdot\frac{\partial E_z}{\partial r}, \tag{17}$$

where

$$\lambda_r = \frac{1}{r}\cdot\left(r_1 + \int_{r_1}^{r}\kappa_r(r')dr'\right) \text{ and } \theta_r = \frac{1}{r}\cdot\int_{r_1}^{r}\sigma_r(r')dr'.$$

Using the BOR-FDTD scheme and the TRC method [12] to discretize (10)-(17), ones obtains:

$$\begin{aligned}E_r^{n+1}(i+\tfrac{1}{2},k) &= a_1E_r^n(i+\tfrac{1}{2},k) + a_2\psi_r^n(i+\tfrac{1}{2},k)\\ &-c_{z1}(k)\left[H_\phi^{n+1/2}(i+\tfrac{1}{2},k+\tfrac{1}{2}) - H_\phi^{n+1/2}(i+\tfrac{1}{2},k-\tfrac{1}{2})\right]\\ &+c_{z2}(k)F_{rz}^n(i+\tfrac{1}{2},k),\end{aligned} \tag{18}$$

$$\begin{aligned}\psi_r^{n+1}(i+\tfrac{1}{2},k) &= \frac{\Delta\chi^0}{2}\left[E_r^{n+1}(i+\tfrac{1}{2},k) + E_r^n(i+\tfrac{1}{2},k)\right]\\ &+e^{-\Gamma\Delta t}\psi_r^n(i+\tfrac{1}{2},k),\end{aligned} \tag{19}$$

$$\begin{aligned}E_z^{n+1}(i,k+\tfrac{1}{2}) &= a_1E_z^n(i,k+\tfrac{1}{2}) + a_2\psi_z^n(i,k+\tfrac{1}{2})\\ &+c_{r1}(i)\left[H_\phi^{n+1/2}(i+\tfrac{1}{2},k+\tfrac{1}{2}) - H_\phi^{n+1/2}(i-\tfrac{1}{2},k+\tfrac{1}{2})\right]\\ &+w_{r1}(i)\cdot\frac{H_\phi^{n+1/2}(i+\tfrac{1}{2},k+\tfrac{1}{2}) + H_\phi^{n+1/2}(i-\tfrac{1}{2},k+\tfrac{1}{2})}{2i}\\ &-c_{r2}(i)G_{zr}^n(i,k+\tfrac{1}{2}) - w_{r2}(i)P_{zr}^n(i,k+\tfrac{1}{2}),\end{aligned} \tag{20}$$

$$\begin{aligned}\psi_z^{n+1}(i,k+\tfrac{1}{2}) &= \frac{\Delta\chi^0}{2}\left[E_z^{n+1}(i,k+\tfrac{1}{2}) + E_z^n(i,k+\tfrac{1}{2})\right]\\ &+e^{-\Gamma\Delta t}\psi_z^n(i,k+\tfrac{1}{2}),\end{aligned} \tag{21}$$

$$\begin{aligned}H_\phi^{n+1/2}(i+\tfrac{1}{2},k+\tfrac{1}{2}) &= H_\phi^{n-1/2}(i+\tfrac{1}{2},k+\tfrac{1}{2})\\ &-d_{z1}(k+\tfrac{1}{2})\left[E_r^n(i+\tfrac{1}{2},k+1) - E_r^n(i+\tfrac{1}{2},k)\right]\\ &+d_{r1}(i+\tfrac{1}{2})\left[E_z^n(i+1,k+\tfrac{1}{2}) - E_z^n(i,k+\tfrac{1}{2})\right]\\ &+d_{z2}(k+\tfrac{1}{2})Q_{\phi z}^{n-1/2}(i+\tfrac{1}{2},k+\tfrac{1}{2})\\ &-d_{r2}(i+\tfrac{1}{2})Q_{\phi r}^{n-1/2}(i+\tfrac{1}{2},k+\tfrac{1}{2}),\end{aligned} \tag{22}$$

$$\begin{aligned}F_{rz}^{n+1}(i+\tfrac{1}{2},k) &= a_z(k)F_{rz}^n(i+\tfrac{1}{2},k)\\ &+b_z(k)\left[H_\phi^{n+1/2}(i+\tfrac{1}{2},k+\tfrac{1}{2}) - H_\phi^{n+1/2}(i+\tfrac{1}{2},k-\tfrac{1}{2})\right],\end{aligned} \tag{23}$$

$$\begin{aligned}G_{zr}^{n+1}(i,k+\tfrac{1}{2}) &= a_r(i)G_{zr}^n(i,k+\tfrac{1}{2})\\ &+b_r(i)\left[H_\phi^{n+1/2}(i+\tfrac{1}{2},k+\tfrac{1}{2}) - H_\phi^{n+1/2}(i-\tfrac{1}{2},k+\tfrac{1}{2})\right],\end{aligned} \tag{24}$$

$$\begin{aligned}P_{zr}^{n+1}(i,k+\tfrac{1}{2}) &= u_r(i)P_{zr}^n(i,k+\tfrac{1}{2})\\ &+v_r(i)\cdot\frac{H_\phi^{n+1/2}(i+\tfrac{1}{2},k+\tfrac{1}{2}) + H_\phi^{n+1/2}(i-\tfrac{1}{2},k+\tfrac{1}{2})}{2i},\end{aligned} \tag{25}$$

$$\begin{aligned}Q_{\phi z}^{n+1/2}(i+\tfrac{1}{2},k+\tfrac{1}{2}) &= a_z(k+\tfrac{1}{2})Q_{\phi z}^{n-1/2}(i+\tfrac{1}{2},k+\tfrac{1}{2})\\ &+b_z(k+\tfrac{1}{2})\left[E_r^n(i+\tfrac{1}{2},k+1) - E_r^n(i+\tfrac{1}{2},k)\right],\end{aligned} \tag{26}$$

$$\begin{aligned}Q_{\phi r}^{n+1/2}(i+\tfrac{1}{2},k+\tfrac{1}{2}) &= a_r(i+\tfrac{1}{2})Q_{\phi r}^{n-1/2}(i+\tfrac{1}{2},k+\tfrac{1}{2})\\ &+b_r(i+\tfrac{1}{2})\left[E_z^n(i+1,k+\tfrac{1}{2}) - E_z^n(i,k+\tfrac{1}{2})\right].\end{aligned} \tag{27}$$

It can be seen that (11) includes a singularity when $r = 0$ for the $1/r$ term. The proposed update equation to

solve the problem [2] is:

$$E_z^{n+1}(0,k+\tfrac{1}{2}) = a_1 E_z^n(0,k+\tfrac{1}{2}) + a_2 \psi_z^n(0,k+\tfrac{1}{2}) + \frac{a_2 \Delta t}{\varepsilon_0}\cdot\frac{4}{\Delta r}\cdot H_\phi^{n+1/2}(\tfrac{1}{2},k+\tfrac{1}{2}). \quad (28)$$

The corresponding coefficients in (18)-(28) are listed as follows:

$$a_1 = a_2\left(1-\frac{\chi^0}{2}\right),\ \ a_2 = \left(1+\frac{\chi^0}{2}\right)^{-1},$$

$$\chi^0 = \frac{\omega_p^2}{\Gamma}\Delta t - \frac{\omega_p^2}{\Gamma^2}\left(1-e^{-\Gamma\Delta t}\right),\ \Delta\chi^0 = -\frac{\omega_p^2}{\Gamma^2}\left(1-e^{-\Gamma\Delta t}\right)^2,$$

$$a_\eta = \frac{2-\varphi_\eta \Delta t}{2+\varphi_\eta \Delta t},\ b_\eta = \frac{2\beta_\eta \Delta t}{2+\varphi_\eta \Delta t}\cdot\frac{1}{\Delta\eta},$$

$$u_r = \frac{2\varepsilon_0\lambda_r - \alpha_r \Delta t\lambda_r - \theta_r \Delta t}{2\varepsilon_0\lambda_r + \alpha_r \Delta t\lambda_r + \theta_r \Delta t},$$

$$v_r = \frac{2\theta_r \Delta t}{\lambda_r\left[2\varepsilon_0\lambda_r + \alpha_r \Delta t\lambda_r + \theta_r \Delta t\right]}\cdot\frac{1}{\Delta r},$$

$$c_{\eta 1} = \frac{a_2\Delta t}{\varepsilon_0}\left(\frac{1}{\kappa_\eta \Delta\eta} - \frac{b_\eta}{2}\right),\ c_{\eta 2} = \frac{a_2\Delta t}{2\varepsilon_0}(1+a_\eta),$$

$$d_{\eta 1} = \frac{\Delta t}{\mu_0}\left(\frac{1}{\kappa_\eta \Delta\eta} - \frac{b_\eta}{2}\right),\ d_{\eta 2} = \frac{\Delta t}{2\mu_0}(1+a_\eta),$$

$$w_{r1} = \frac{a_2\Delta t}{\varepsilon_0}\left(\frac{1}{\lambda_r \Delta r} - \frac{b_{\theta r}}{2}\right),\ w_{r2} = \frac{a_2\Delta t}{2\varepsilon_0}(1+a_{\theta r}),$$

where $\Delta\eta$ ($\eta = r, z$) are the space cell size and Δt is the time step.

III. NUMERICAL RESULTS

A numerical example is provided to validate the effectiveness of the proposed BOR-CFS-PML formulations. The model structure of the numerical example is presented in Fig. 1. The BOR-CFS-PML with 10-cell-thick layers is used to truncate the FDTD computation domain filled with the Drude media with $\omega_p = 2\pi\times 28.7$ Grad/s and Γ=20 Grad/s, which occupies 60×80 cells. The space cell size is $\Delta r = \Delta z = 2\times 10^{-4}$ m and the time step is $\Delta t = 4.48\times 10^{-13}$ s. In this simulation, the excite source, which is located at (10, 50) as shown in Fig. 1, is a modulated Gaussian pulse whose center frequency is 35 GHz and maximum interesting frequency is 70 GHz. In the PML domain, σ_η and κ_η are scaled using an *m*-order polynomial scaling and α_η is a constant. To obtain the low reflection, the BOR-CFS-PML parameters $\kappa_{\eta,\max} = 10$, $\alpha_\eta = 0.6$, $\sigma_{\eta,\max} = \sigma_{\eta,ratio}(m+1)/(150\pi\Delta\eta)$, $\sigma_{\eta,ratio} = 1.4$, $m = 2$ are selected empirically. The simulation is operated for 2240 ps.

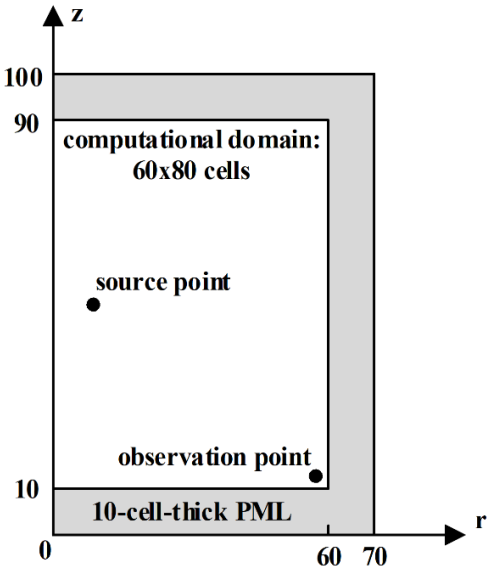

Fig. 1. The model structure of the numerical example.

The relative reflection error of the BOR-CFS-PML in the time-domain is shown in Fig. 2. The relative reflection error is calculated at an observation point located at (59, 11) as:

$$R_{\mathrm{dB}}(t) = 20\log_{10}\left|\frac{H_\phi^R(t) - H_\phi^T(t)}{\max(H_\phi^R(t))}\right|, \quad (29)$$

where $H_\phi^T(t)$ represents the value calculated in the test domain, $H_\phi^R(t)$ is the reference solution based on the extended 260x480-cell FDTD computational domain terminated by additional 128-cell-thick PML layers. For comparing, the SC-PML based on the BOR-FDTD, named here as the BOR-SC-PML, is also computed by using the same PML parameters except $\alpha_\eta = 0$. Compared with the BOR-SC-PML, the BOR-CFS-PML has better performance in reducing late-time reflection error. Specially, it has about 60 dB improvement near $t = 1500$ ps.

Figure 3 shows the reflection coefficients in the frequency-domain with the BOR-CFS-PML and the BOR-SC-PML. The reflection coefficients are calculated at the same observation point by using:

$$R_{\mathrm{dB}}(f) = 20\log_{10}\left|\frac{F[H_\phi^R(t) - H_\phi^T(t)]}{F[H_\phi^R(t)]}\right|, \quad (30)$$

where the operator $F[*]$ is the symbol of the Fourier transformation. The maximum reflection coefficient of the BOR-CFS-PML is -68 dB in the interesting frequency range. Within the low-frequency, the BOR-CFS-PML holds significant improvement compared with the BOR-SC-PML.

In conclusion, the BOR-CFS-PML holds the remarkable advantages in attenuating low-frequency evanescent waves and reducing late-time reflections over the BOR-SC-PML.

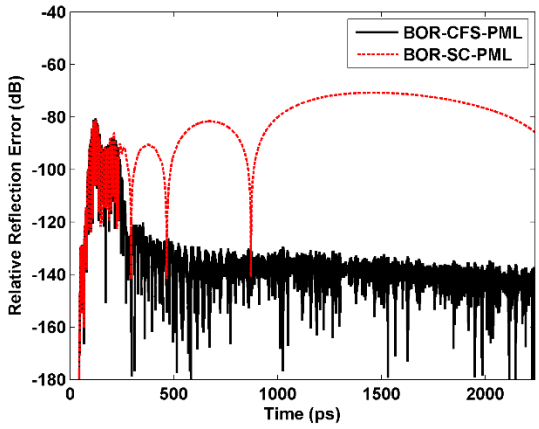

Fig. 2. Relative reflection errors versus time of the BOR-CFS-PML and the BOR-SC-PML for truncating the Drude media. (Two curves almost overlap before 237ps).

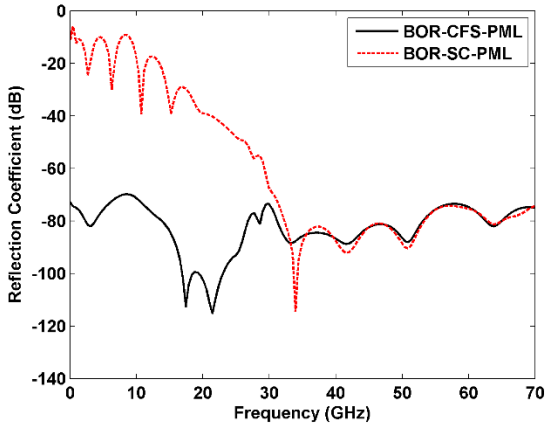

Fig. 3. Reflection coefficients versus frequency of the BOR-CFS-PML and the BOR-SC-PML for truncating the Drude media. (Two curves almost overlap after 35 GHz).

IV. CONCLUSION

An effective implementation of the BOR-CFS-PML, which takes advantage of the ADE method and the TRC method to terminate the Drude media, is presented. It is confirmed in the numerical example that the proposed BOR-CFS-PML is efficient in the absorption of the low-frequency evanescent waves and the reduction of late-time reflections.

ACKNOWLEDGMENT

This work was supported by the National Natural Science Foundation of China (Grant No. 61372011) and the Program for Innovative Research Team in University of Tianjin (Grant No. TD13-5040).

REFERENCES

[1] A. Taflove and S. C. Hagness, *Computational Electrodynamics: The Finite-Difference Time-Domain Method*. 3rd ed., Norwood, MA: Artech House, 2005.

[2] M. F. Hadi, A. Z. Elsherbeni, M. J. Piket-May, and S. F. Mahmoud, "Radial waves based dispersion analysis of the body-of-revolution FDTD method," *IEEE Trans. Antennas & Propagation*, vol. 65, no. 2, pp. 721-729, Feb. 2017.

[3] Y. Chen, R. Mittra, and P. Harms, "Finite-difference time-domain algorithm for solving Maxwell's equations in rotationally symmetric geometries," *IEEE Trans. Microw. Theory Tech.*, vol. 44, no. 6, pp. 832-839, June 1996.

[4] J. P. Berenger, "A perfectly matched layer for the absorption of electromagnetic waves," *J. Comp. Phys.*, vol. 114, no. 2, pp. 185-200, Oct. 1994.

[5] W. C. Chew and W. H. Weedon, "A 3D perfectly matched medium from modified Maxwell's equations with stretched coordinates," *Microw. Opt. Technol. Lett.*, vol. 7, no. 13, pp. 599-604, Sep. 1994.

[6] J. P. Berenger, "Numerical reflection from FDTD-PMLS: A comparison of the split PML with the unsplit and CFS PMLs," *IEEE Trans. Antennas Propag.*, vol. 50, no. 3, pp. 258-265, Mar. 2002.

[7] J. P. Berenger, "Evanescent waves in PML's: Origin of the numerical reflection in wave-structure interaction problems," *IEEE Trans. Antennas Propag.*, vol. 47, no. 10, pp. 1497-1503, Oct. 1999.

[8] M. Kuzuoglu and R. Mittra, "Frequency dependence of the constitutive parameters of causal perfectly matched anisotropic absorbers," *IEEE Microw. Guided Wave Lett.*, vol. 6, no. 12, pp. 447-449, Dec. 1996.

[9] R. Luebbers, F. P. Hunsberger, K. S. Kunz, R. B. Standler, and M. Schneider, "A frequency-dependent finite-difference time-domain formulation for dispersive materials," *IEEE Trans. Electromag. Compat.*, vol. 32, no. 3, pp. 222-227, Aug. 1990.

[10] R. J. Luebbers, F. Hunsberger, and K. S. Kunz, "A frequency-dependent finite-difference time-domain formulation for transient propagation in plasma," *IEEE Trans. Antennas Propag.*, vol. 39, no. 1, pp. 29-34, Jan. 1991.

[11] D. F. Kelley and R. J. Luebbers, "Piecewise linear recursive convolution for dispersive media using FDTD," *IEEE Trans. Antennas Propag.*, vol. 44, no. 6, pp. 792-797, June 1996.

[12] R. Siushansian and J. LoVetri, "A comparison of numerical techniques for modeling electromag-

netic dispersive media," *IEEE Microw. Guided Wave Lett.*, vol. 5, no. 12, pp. 426-428, Dec. 1995.
[13] R. Siushansian and J. LoVetri, "Efficient evaluation of convolution integrals arising in FDTD formulations of electromagnetic dispersive media," *J. Electromag. Waves Applicat.*, vol. 11, pp. 101-117, 1997.
[14] O. Ramadan, "Auxiliary differential equation formulation: An efficient implementation of the perfectly matched layer," *IEEE Microw. Wireless Compon. Lett.*, vol. 13, no. 2, pp. 69-71, Feb. 2003.

Jianxiong Li received the B.Sc. and M.Sc. degrees in Physics in 1991 and 1994, respectively, and obtained the Ph.D. degree in Communication and Information System in 2007, from Tianjin University, Tianjin, China. His main research interests are in computational electromagnetics, wireless communication and antenna.

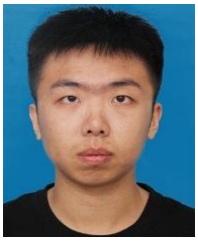

Wei Jiao received the B.Sc. degree in Communication Engineering in 2015 from Tianjin Polytechnic University, Tianjin, China. He is currently pursuing the M.Sc. degree in the same university. His main research interests are in computational electromagnetics.

Complex-Envelope ADE-LOD-FDTD for Band Gap Analysis of Plasma Photonic Crystals

Tu-Lu Liang, Wei Shao, and Sheng-Bing Shi

School of Physics
University of Electronic Science and Technology of China, Chengdu, 610054, China
liangtul@163.com, weishao@uestc.edu.cn, shengbing77@163.com

Abstract ─ In this paper, a complex-envelope (CE) scheme is introduced into the locally one-dimensional finite-difference time-domain (LOD-FDTD) method for the band-gap analysis of the plasma photonic crystal (PPC). The un-magnetized plasma, characterized by a complex frequency-dependent permittivity, is expressed by the Drude model and solved with a generalized auxiliary differential equation (ADE) technique. The CE scheme is also applied to the perfectly matched layer. Numerical examples show that the proposed CE-ADE-LOD-FDTD method provides much more accurate results than the traditional ADE-LOD-FDTD with the same CFL number. The reflection and transmission coefficients of the PPC are calculated and their dependence on the relative permittivity of dielectric, the plasma frequency, the collision frequency and the plasma layer thickness is studied. The results show that the photonic band gaps of the PPC could be tuned by adjusting the parameters.

Index Terms ─ Band-gaps, complex envelope (CE), locally one-dimensional finite-difference time-domain (LOD-FDTD) method, plasma photonic crystal (PPC).

I. INTRODUCTION

Much attention has been paid to the photonic crystal due to its unique characteristics since the conception was put forward by Yablonovitch [1] and John [2] in the 1980s. The plasma photonic crystal (PPC) is an important branch of the photonic crystal. A PPC structure is an artificially periodic one composed of the alternating thin un-magnetized (or magnetized) plasmas and dielectric materials (or vacuum). In recent years, scholars have devoted much of the energy to the research of PPCs. At the same time, a number of related literatures continue to emerge. The natures of the PPC include photonic band gap properties of photonic localization and optical properties [3], [4]. For the analysis of the PPC, the frequency-dependent finite-difference time-domain (FDTD) method has been widely used. Because surface plasmon polaritons (SPPs) are highly localized along the plasma-dielectric interface, fine spatial grids are required to attain sufficient accuracy. Thus, an extremely small time step constrained by the Courant-Friedrich-Levy (CFL) stability condition results in a long computation time [5].

Some unconditionally stable FDTD methods have been presented to eliminate the CFL condition and to improve the computational efficiency. Several unconditionally stable time-marching methods only need to deal with the tri-diagonal matrix equation with low computational complexity, such as the locally one-dimensional (LOD) FDTD method [6], [7], the alternating-direction implicit (ADI) FDTD method [8], [9] and the split-step (SS) FDTD method [10]-[12]. The unconditionally stable Crank-Nicolson (CN) FDTD method is another time-marching method, in which the full time step size in one marching step is used to solve the discretized Maxwell's equations [13], [14]. Although the above time-marching methods are unconditionally stable, their time steps are restricted by the dispersion errors [15]-[17]. The order-marching weighted Laguerre polynomial (WLP) FDTD method, in which the spatial and the temporal variables are separated, does not have to deal with the time step [18], [19]. Both CN-FDTD and WLP-FDTD have to solve a large banded-spare matrix equation at the beginning of the calculation.

In order to reduce the numerical dispersion for large time-step sizes in ADI-FDTD, a technique called the complex-envelope (CE) has been proposed in [20]. It was claimed that CE-ADI-FDTD is more accurate than ADI-FDTD with the same time step. By using the CE technique, the carrier frequency term is absorbed into the Maxwell's equations as a known quantity. Consequently, only the signal envelopes become the variants to be sampled and computed. Generally, LOD-FDTD requires fewer arithmetic operations than ADI-FDTD [21]. [22] introduced a CE-LOD-FDTD method for the analysis of the optical waveguide. The CE-LOD-FDTD method was also used to analyze ionospheric propagation in a simple one-dimensional space without absorbing boundary conditions [23].

With the auxiliary differential equation (ADE) technique [24], [25], the CE-LOD-FDTD method is employed for the analysis of PPCs in this work. The

Submitted On: July 28, 2017
Accepted On: April 21, 2018

dispersion of the plasma expressed by the Drude model, is solved with the ADE technique to establish the relationship between the electric field intensity and conductive electric current in the PPC. Furthermore, the CE technique is integrated with the Berenger's perfectly matched layer (PML) to truncate the computational domain effectively. With the proposed CE-ADE-LOD-FDTD method, the reflection and transmission coefficients through the PPC are calculated, and their dependence on the dielectric permittivity, the plasma frequency, the collision frequency and the plasma layer thickness is studied. The numerical examples verify accuracy and effectiveness of the proposed method.

II. NUMERICAL FORMULATION

A. CE-ADE-LOD-FDTD method

The time dependence of $e^{-i\omega t}$ is assumed. According to the Drude model, the relative permittivity (in frequency domain) of the un-magnetized plasma is given by:

$$\varepsilon_{\mathrm{m}}(\omega)=1-\frac{\omega_{\mathrm{p}}^2}{\omega^2+\mathrm{i}\gamma\omega}, \tag{1}$$

where ω is the angular frequency of the impinging light, ω_{p} is the plasma frequency, and γ is the collision frequency of the plasma.

For simplicity, a 2-D TM wave including E_x, E_z and H_y components is considered. The 2-D Maxwell's equations and auxiliary differential equations in a dispersive material can be written as [26]:

$$\frac{\partial E_x}{\partial t}=-\frac{1}{\varepsilon}\frac{\partial H_y}{\partial z}-\frac{1}{\varepsilon}J_x, \tag{2a}$$

$$\frac{\partial E_z}{\partial t}=\frac{1}{\varepsilon}\frac{\partial H_y}{\partial x}-\frac{1}{\varepsilon}J_z, \tag{2b}$$

$$\frac{\partial H_y}{\partial t}=\frac{1}{\mu_0}\frac{\partial E_z}{\partial x}-\frac{1}{\mu_0}\frac{\partial E_x}{\partial z}, \tag{2c}$$

$$\frac{\partial J_x}{\partial t}=-\gamma J_x+\varepsilon_0\omega_{\mathrm{p}}^2E_x, \tag{2d}$$

$$\frac{\partial J_z}{\partial t}=-\gamma J_z+\varepsilon_0\omega_{\mathrm{p}}^2E_z, \tag{2e}$$

where ε and ε_0 are the electric permittivity of the medium and free space, respectively, and μ_0 is the magnetic permeability.

The fields can be represented as:

$$(E,H,J)=\mathrm{Re}\left\{\left(\hat{E},\hat{H},\hat{J}\right)e^{\mathrm{i}\omega_{\mathrm{c}}t}\right\}, \tag{3}$$

where $\mathrm{Re}\{\cdot\}$ denotes the operation that takes the real part of a complex number, ω_{c} is the center carrier angular frequency, and $\hat{E}$, $\hat{H}$ and $\hat{J}$ represent the associated complex-envelope fields and electric current.

Substituting (3) into (2a)-(2e), we get:

$$\frac{\partial \hat{E}_x}{\partial t}+\mathrm{i}\omega_{\mathrm{c}}\hat{E}_x=-\frac{1}{\varepsilon}\frac{\partial \hat{H}_y}{\partial z}-\frac{1}{\varepsilon}\hat{J}_x, \tag{4a}$$

$$\frac{\partial \hat{E}_z}{\partial t}+\mathrm{i}\omega_{\mathrm{c}}\hat{E}_z=\frac{1}{\varepsilon}\frac{\partial \hat{H}_y}{\partial x}-\frac{1}{\varepsilon}\hat{J}_z, \tag{4b}$$

$$\frac{\partial \hat{H}_y}{\partial t}+\mathrm{i}\omega_{\mathrm{c}}\hat{H}_y=\frac{1}{\mu_0}\frac{\partial \hat{E}_z}{\partial x}-\frac{1}{\mu_0}\frac{\partial \hat{E}_x}{\partial z}, \tag{4c}$$

$$\frac{\partial \hat{J}_x}{\partial t}+\mathrm{i}\omega_{\mathrm{c}}\hat{J}_x=-\gamma\hat{J}_x+\varepsilon_0\omega_{\mathrm{p}}^2\hat{E}_x, \tag{4d}$$

$$\frac{\partial \hat{J}_z}{\partial t}+\mathrm{i}\omega_{\mathrm{c}}\hat{J}_z=-\gamma\hat{J}_z+\varepsilon_0\omega_{\mathrm{p}}^2\hat{E}_z. \tag{4e}$$

With the LOD scheme [6], we obtain the CE-ADE-LOD-FDTD formalism. In the first step (n+1/2), we have:

$$\hat{E}_x^{n+1/2}=\frac{4-\mathrm{i}\omega_{\mathrm{c}}\Delta t}{4+\mathrm{i}\omega_{\mathrm{c}}\Delta t}\hat{E}_x^n, \tag{5a}$$

$$\hat{E}_z^{n+1/2}=\frac{4-\mathrm{i}\omega_{\mathrm{c}}\Delta t}{4+\mathrm{i}\omega_{\mathrm{c}}\Delta t}\hat{E}_z^n+\frac{2\Delta t}{4\varepsilon+\mathrm{i}\omega_{\mathrm{c}}\varepsilon\Delta t}\left(\frac{\partial \hat{H}_y^{n+1/2}}{\partial x}+\frac{\partial \hat{H}_y^{n}}{\partial x}-\hat{J}_z^{n+1/2}-\hat{J}_z^{n}\right), \tag{5b}$$

$$\hat{H}_y^{n+1/2}=\frac{4-\mathrm{i}\omega_{\mathrm{c}}\Delta t}{4+\mathrm{i}\omega_{\mathrm{c}}\Delta t}\hat{H}_y^n+\frac{2\Delta t}{4\mu_0+\mathrm{i}\omega_{\mathrm{c}}\mu_0\Delta t}\left(\frac{\partial \hat{E}_z^{n+1/2}}{\partial x}+\frac{\partial \hat{E}_z^{n}}{\partial x}\right), \tag{5c}$$

$$\hat{J}_x^{n+1/2}=\frac{4-\mathrm{i}\omega_{\mathrm{c}}\Delta t-2\gamma\Delta t}{4+\mathrm{i}\omega_{\mathrm{c}}\Delta t+2\gamma\Delta t}\hat{J}_x^n+\frac{2\varepsilon_0\omega_{\mathrm{p}}^2\Delta t}{4+\mathrm{i}\omega_{\mathrm{c}}\Delta t+2\gamma\Delta t}\left(\hat{E}_x^{n+1/2}+\hat{E}_x^{n}\right), \tag{5d}$$

$$\hat{J}_z^{n+1/2}=\frac{4-\mathrm{i}\omega_{\mathrm{c}}\Delta t}{4+\mathrm{i}\omega_{\mathrm{c}}\Delta t}\hat{J}_z^n. \tag{5e}$$

In the second step (n+1), we have:

$$\hat{E}_x^{n+1}=\frac{4-\mathrm{i}\omega_{\mathrm{c}}\Delta t}{4+\mathrm{i}\omega_{\mathrm{c}}\Delta t}\hat{E}_x^{n+1/2}-\frac{2\Delta t}{4\varepsilon+\mathrm{i}\omega_{\mathrm{c}}\varepsilon\Delta t}\left(\frac{\partial \hat{H}_y^{n+1}}{\partial z}+\frac{\partial \hat{H}_y^{n+1/2}}{\partial z}+\hat{J}_x^{n+1}+\hat{J}_x^{n+1/2}\right), \tag{6a}$$

$$\hat{E}_z^{n+1}=\frac{4-\mathrm{i}\omega_{\mathrm{c}}\Delta t}{4+\mathrm{i}\omega_{\mathrm{c}}\Delta t}\hat{E}_z^{n+1/2}, \tag{6b}$$

$$\hat{H}_y^{n+1}=\frac{4-\mathrm{i}\omega_{\mathrm{c}}\Delta t}{4+\mathrm{i}\omega_{\mathrm{c}}\Delta t}\hat{H}_y^{n+1/2}-\frac{2\Delta t}{4\mu_0+\mathrm{i}\omega_{\mathrm{c}}\mu_0\Delta t}\left(\frac{\partial \hat{E}_x^{n+1}}{\partial z}+\frac{\partial \hat{E}_x^{n+1/2}}{\partial z}\right), \tag{6c}$$

$$\hat{J}_x^{n+1}=\frac{4-\mathrm{i}\omega_{\mathrm{c}}\Delta t}{4+\mathrm{i}\omega_{\mathrm{c}}\Delta t}\hat{J}_x^{n+1/2}, \tag{6d}$$

$$\hat{J}_z^{n+1}=\frac{4-\mathrm{i}\omega_{\mathrm{c}}\Delta t-2\gamma\Delta t}{4+\mathrm{i}\omega_{\mathrm{c}}\Delta t+2\gamma\Delta t}\hat{J}_z^{n+1/2}+\frac{2\varepsilon_0\omega_{\mathrm{p}}^2\Delta t}{4+\mathrm{i}\omega_{\mathrm{c}}\Delta t+2\gamma\Delta t}\left(\hat{E}_z^{n+1}+\hat{E}_z^{n+1/2}\right). \tag{6e}$$

Since (5b) includes the unknown term $\hat{H}_y^{n+1/2}$, taking the first step for example, we substitute (5c) into (5b) to eliminate $\hat{H}_y^{n+1/2}$ and then get a tri-diagonal matrix equation in term of $\hat{E}_z^{n+1/2}$ which can be solved with Thomas algorithm. The rest of the equations can be calculated in an explicit way. It is clear that the equations of the CE-ADE-LOD-FDTD method degrade into those of the ADE-LOD-FDTD method for $\omega_c = 0$.

B. CE-PML in CE-ADE-LOD-FDTD

In a Berenger's PML medium, the magnetic field component $\hat{H}_y$ is divided into $\hat{H}_{yx}$ and $\hat{H}_{yz}$. With the LOD scheme [6], we obtain the CE-PML difference formalism in the first step (n+1/2):

$$\hat{E}_x^{n+1/2}\Big|_{i+1/2,k} = A\hat{E}_x^{n}\Big|_{i+1/2,k}, \tag{7a}$$

$$\begin{aligned}\hat{E}_z^{n+1/2}\Big|_{i,k+1/2} &= C_1\Big|_{i,k+1/2}\hat{E}_z^{n}\Big|_{i,k+1/2} \\ &+ C_2\Big|_{i,k+1/2}\left(\hat{H}_{yx}^{n+1/2}\Big|_{i+1/2,k+1/2} - \hat{H}_{yx}^{n+1/2}\Big|_{i-1/2,k+1/2}\right) \\ &+ C_2\Big|_{i,k+1/2}\left(\hat{H}_{yx}^{n}\Big|_{i+1/2,k+1/2} - \hat{H}_{yx}^{n}\Big|_{i-1/2,k+1/2}\right) \\ &+ C_2\Big|_{i,k+1/2}\begin{pmatrix}\hat{H}_{yz}^{n+1/2}\Big|_{i+1/2,k+1/2} - \hat{H}_{yz}^{n+1/2}\Big|_{i-1/2,k+1/2} \\ +\hat{H}_{yz}^{n}\Big|_{i+1/2,k+1/2} - \hat{H}_{yz}^{n}\Big|_{i-1/2,k+1/2}\end{pmatrix}, \\ &- \frac{\Delta x_i + \Delta x_{i-1}}{2}\cdot C_2\Big|_{i,k+1/2}\left(\hat{J}_z^{n+1/2}\Big|_{i,k+1/2} + \hat{J}_z^{n}\Big|_{i,k+1/2}\right)\end{aligned} \tag{7b}$$

$$\begin{aligned}\hat{H}_{yx}^{n+1/2}\Big|_{i+1/2,k+1/2} &= C_3\Big|_{i+1/2}\hat{H}_{yx}^{n}\Big|_{i+1/2,k+1/2} \\ &+ C_4\Big|_{i+1/2}\begin{pmatrix}\hat{E}_z^{n+1/2}\Big|_{i+1,k+1/2} - \hat{E}_z^{n+1/2}\Big|_{i,k+1/2} \\ +\hat{E}_z^{n}\Big|_{i+1,k+1/2} - \hat{E}_z^{n}\Big|_{i,k+1/2}\end{pmatrix},\end{aligned} \tag{7c}$$

$$\hat{H}_{yz}^{n+1/2}\Big|_{i+1/2,k+1/2} = A\hat{H}_{yz}^{n}\Big|_{i+1/2,k+1/2}, \tag{7d}$$

$$\begin{aligned}\hat{J}_x^{n+1/2}\Big|_{i+1/2,k} &= \frac{2-\mathrm{i}\omega_c\Delta t/2-\Delta t\gamma\big|_{i+1/2,k}}{2+\mathrm{i}\omega_c\Delta t/2+\Delta t\gamma\big|_{i+1/2,k}}\hat{J}_x^{n}\Big|_{i+1/2,k} \\ &+ \frac{\varepsilon_0\Delta t\omega_p^2\big|_{i+1/2,k}}{2+\mathrm{i}\omega_c\Delta t/2+\Delta t\gamma\big|_{i+1/2,k}}\left(\hat{E}_x^{n+1/2}\Big|_{i+1/2,k} + \hat{E}_x^{n}\Big|_{i+1/2,k}\right),\end{aligned} \tag{7e}$$

$$\hat{J}_z^{n+1/2}\Big|_{i,k+1/2} = A\hat{J}_z^{n}\Big|_{i,k+1/2}. \tag{7f}$$

The coefficients of (7a)–(7f) are expressed as:

$$A = \frac{4-\mathrm{i}\omega_c\Delta t}{4+\mathrm{i}\omega_c\Delta t}, \tag{8a}$$

$$C_1\Big|_{i,k+1/2} = \frac{2\varepsilon\big|_{i,k+1/2} - \mathrm{i}\omega_c\varepsilon_0\Delta t/2 - \Delta t\sigma_x\big|_i}{2\varepsilon\big|_{i,k+1/2} + \mathrm{i}\omega_c\varepsilon_0\Delta t/2 + \Delta t\sigma_x\big|_i}, \tag{8b}$$

$$C_2\Big|_{i,k+1/2} = \frac{2\Delta t}{\left(2\varepsilon\big|_{i,k+1/2} + \mathrm{i}\omega_c\varepsilon_0\Delta t/2 + \Delta t\sigma_x\big|_i\right)\left(\Delta x_i + \Delta x_{i-1}\right)}, \tag{8c}$$

$$C_3\Big|_{i+1/2} = \frac{2\mu_0 - \mathrm{i}\omega_c\mu_0\Delta t/2 - \Delta t\rho_x\big|_{i+1/2}}{2\mu_0 + \mathrm{i}\omega_c\mu_0\Delta t/2 + \Delta t\rho_x\big|_{i+1/2}}, \tag{8d}$$

$$C_4\Big|_{i+1/2} = \frac{\Delta t}{\left(2\mu_0 + \mathrm{i}\omega_c\mu_0\Delta t/2 + \Delta t\rho_x\big|_{i+1/2}\right)\Delta x_i}, \tag{8e}$$

where Δt is the time step, Δx_i is the discretization step along the x-direction, σ_x and ρ_x are the conductivity and reluctivity, respectively. The equations of the second step can be obtained in a similar way.

III. NUMERICAL RESULTS AND DISCUSSION

With the proposed CE-ADE-LOD-FDTD method, the reflection and transmission coefficients through the PPC are calculated and their dependence on the relative permittivity of dielectric medium, the plasma frequency, the plasma collision frequency and the plasma layer thickness is studied in this section.

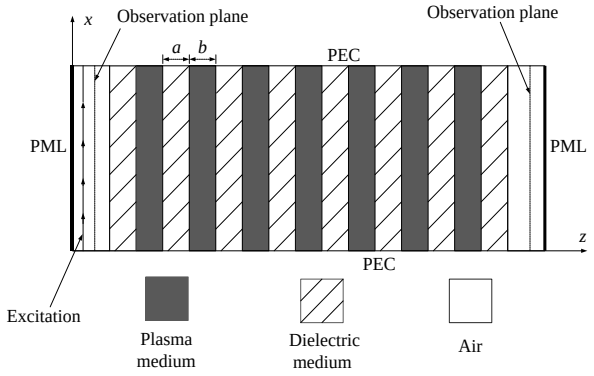

Fig. 1. Schematic model of a plasma photonic crystal.

A normally incident TM-polarized plane wave illuminates a PPC from the left side, as shown in Fig. 1. The eight dielectric layers and seven plasma layers are set in the PPC model, where $a = b = 15$ μm. The computational region is truncated by the Berenger's PML on the left and right sides. The top and bottom boundaries are treated by the perfect electric conductors (PECs).

A Gaussian pulse is used as the source excitation, which can be written as:

$$F(t) = e^{-\frac{(t-t_0)^2}{\tau^2}}, \tag{9}$$

where the maximum frequency f_{max} = 10 THz, $\tau = 1/(2f_{max})$ and $t_0 = 3\tau$. The frequency characteristics of the transmission are calculated with the discrete Fourier transform (DFT) of time-domain responses in the observation plane.

Here, the graded cells are used to attain sufficient accuracy. The center carrier angular frequency $\omega_c = 2\pi \times 5 \times 10^{12}$ rad/s, the spatial step along the x-direction is 1.5 μm, and the minimum and maximum spatial steps

along the *z*-direction are Δ_{min} = 0.05 μm and Δ_{max} = 2 μm, respectively. The total cell number in the computational domain is 40 × 355.

A. Accuracy verification of CE-ADE-LOD-FDTD

First, the accuracy and effectiveness of the proposed CE-ADE-LOD-FDTD method are verified. We choose the plasma frequency $\omega_p = 2\pi \times 2 \times 10^{12}$ rad/s, the plasma collision frequency γ = 40 THz, and the relative permittivity of dielectric ε_r = 4 in the simulation.

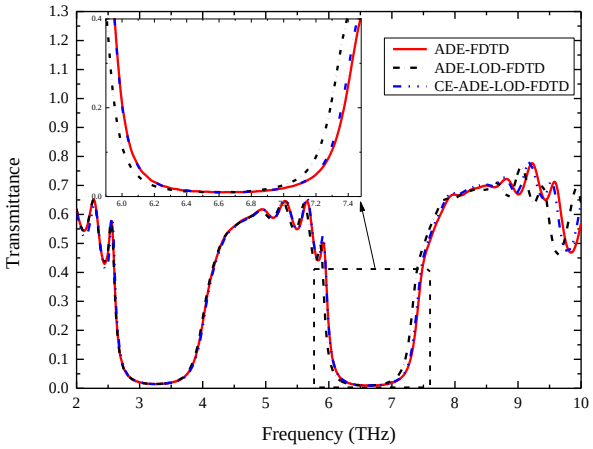

Fig. 2. Results of transmittance of the PPC from ADE-FDTD, ADE-LOD-FDTD and CE-ADE-LOD-FDTD.

Table 1: Comparison of the computational efforts for the three methods

Method	CFLN	Marching Steps	CPU Time (s)	Memory (Mb)
FDTD	1	200000	45017	8.99
ADE-LOD-FDTD	100	2000	251	11.35
CE-ADE-LOD-FDTD	100	2000	529	16.06

Figure 2 shows the transmission coefficients calculated by ADE-FDTD, ADE-LOD-FDTD [26], and the proposed CE-ADE-LOD-FDTD method, where $\Delta t_{FDTD} = \Delta_{min}/2/c$ (c is the velocity of light in the vacuum) is chosen for the explicit ADE-FDTD according to the CFL constraint, $\Delta t_{LOD} = 100\Delta t_{FDTD}$ (CFLN = Δt_{LOD} /Δt_{FDTD} = 100) is chosen for ADE-LOD-FDTD, and $\Delta t_{CE\text{-}LOD} = 100\Delta t_{FDTD}$ (CFLN = 100) is chosen for CE-ADE-LOD-FDTD. It is clear from Fig. 2 that the results from CE-ADE-LOD-FDTD and ADE-FDTD are in good agreement. The results from ADE-LOD-FDTD are worse than those from the other two methods because its dispersion deteriorates with the large time step.

Table 1 shows the comparison of computational efforts of the three methods. Because of the storage of the sparse matrix, the memory requirement of CE-ADE-LOD-FDTD is larger than ADE-FDTD. With the much larger time step beyond the CFL constraint, the CPU time of CE-ADE-LOD-FDTD can be much less than that of ADE-FDTD. Although CE-ADE-LOD-FDTD costs more CPU time than ADE-LOD-FDTD, it gets much more accuracy results. All calculations in this paper are performed on an AMD Athlon (tm) II X4 3.00 GHz computer with 6 GB RAM.

B. Effects of the relative permittivity of dielectric

First, we discuss the effects of the relative permittivity of dielectric on the band gap of the PPC. We choose the plasma frequency $\omega_p = 2\pi \times 2 \times 10^{12}$ rad/s and the plasma collision frequency γ = 40 THz in the simulation. With the proposed CE-ADE-LOD-FDTD method, the reflection and transmission coefficients for the PPC with different relative permittivities of dielectric are depicted in Figs. 3, 4 and 5. Here, we choose CFLN = 100 in the CE-ADE-LOD-FDTD method.

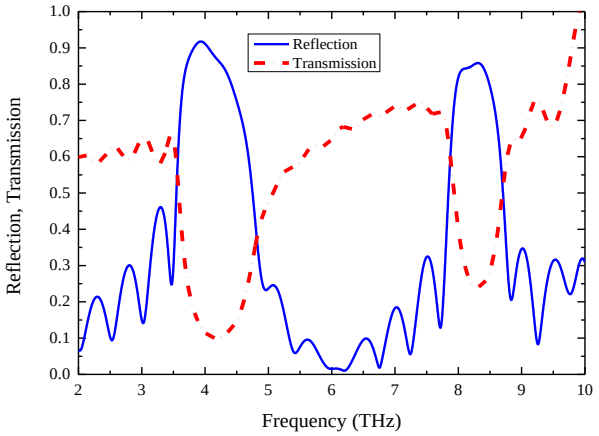

Fig. 3. Electromagnetic band-gap characteristics with the relative dielectric permittivity ε_r = 2.

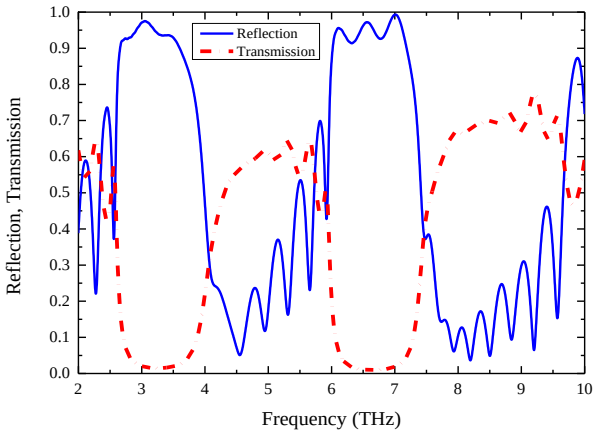

Fig. 4. Electromagnetic band-gap characteristics with the relative dielectric permittivity ε_r = 4.

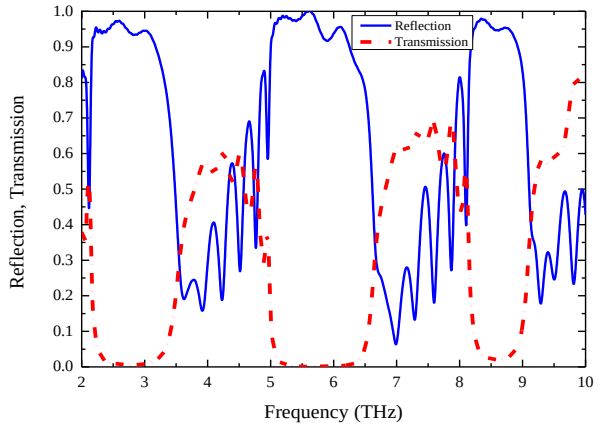

Fig. 5. Electromagnetic band-gap characteristics with the relative dielectric permittivity $\varepsilon_r = 6$.

It is difficult to form the band gap when the relative permittivity of the dielectric medium equals to 1 because the dielectric constant of the plasma is close to 1. That means that the PPC structure tends to a single medium when the relative permittivity of the dielectric medium is close to that of the background medium. The double band gap appears near $f = 4.2$ THz and 8.4 THz when the relative permittivity of the dielectric medium equals to 2. With the increase of the relative permittivity value of the dielectric medium, the depth and number of the band gap increase. Therefore, the band gap can be well controlled by changing the relative permittivity value of the dielectric medium.

C. Effects of the plasma frequency

Next, we study the effects of the plasma frequency on the band gap of the PPC. Here we choose the relative permittivity of the dielectric medium $\varepsilon_r = 5$, and the plasma collision frequency $\gamma = 40$ THz in the simulation. Figure 6 depicts the transmission coefficients for the plasma frequency from $\omega_p = 2\pi \times 2 \times 10^{12}$ rad/s to $2\pi \times 10 \times 10^{12}$ rad/s.

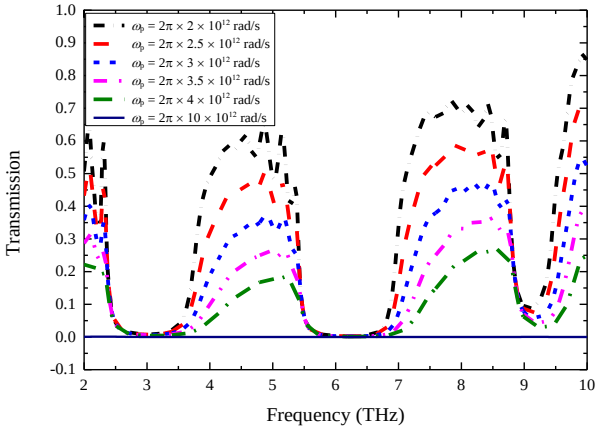

Fig. 6. Transmittance of different plasma frequencies.

With the increase of the plasma frequency, from Fig. 6, the periodicity of photonic band gaps gets unobvious, but the band gap range is a little extended. The transmission coefficient of the PPC will be reduced to zero when the plasma frequency increases to a certain value. This is mainly because when the frequency of the incident electromagnetic wave is close to the maximum plasma frequency, the attenuation of the electromagnetic wave becomes very large, i.e., the resonance attenuation [27].

D. Effects of the Plasma Collision Frequency

Then, we discuss the effects of the plasma collision frequency on the band gap of the PPC. Here we choose the relative permittivity of the dielectric medium $\varepsilon_r = 5$ and the plasma frequency $\omega_p = 2\pi \times 2 \times 10^{12}$ rad/s in the simulation. Figure 7 depicts the transmission coefficients for the plasma collision frequency from $\gamma = 20$ THz to 80 THz. From Fig. 7, the plasma collision frequency has little effect on the periodicity of the band gap.

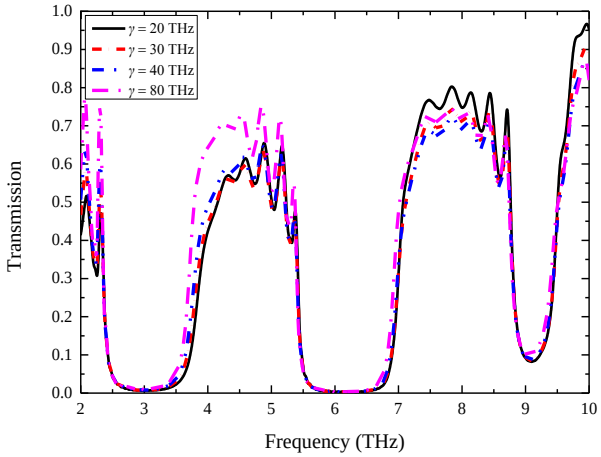

Fig. 7. Transmittance of different plasma collision frequencies.

E. Effects of the plasma layer thickness

Finally, we study the effects of the variation of the plasma layer thickness on the band gap of the PPC. Here we choose the relative permittivity of the dielectric medium $\varepsilon_r = 4$, the plasma frequency $\omega_p = 2\pi \times 2 \times 10^{12}$ rad/s, and the plasma collision frequency $\gamma = 40$ THz in the simulation. Figure 8 depicts the transmission coefficients for the plasma layer thickness from $b = 15$ μm to 49 μm. From Fig. 8, with the increase of the plasma layer thickness, the periodicity of the band gap deteriorates. The absorption performance of the plasma enhances with the increase of plasma layer thickness, and then the attenuation of the incident wave gets large. The periodic band gaps can be generated when the frequency of the incident wave is high and the plasma layer thickness is small.

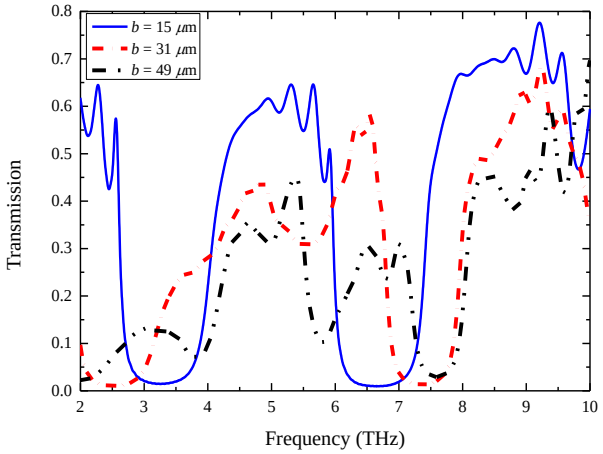

Fig. 8. Transmittance of different plasma layer thicknesses.

IV. CONCLUSION

In this paper, an effective time-domain method with Berenger's PML has been developed for the analysis of the band-gap characteristics in the PPC. With the introduction of the CE technique, the ADE-LOD-FDTD method can provide much more accurate results than the traditional ADE-LOD-FDTD in the numerical examples. The numerical examples verify accuracy and effectiveness of the proposed method, and the results show that the photonic band gaps of the PPC could be tuned by changing the value of the relative permittivity of the dielectric medium, the plasma frequency or the plasma layer thickness.

ACKNOWLEDGMENT

This work was supported by the National Natural Science Foundation of China (61471105 and 61331007) and 973 Project (No. 613273).

REFERENCES

[1] E. Yablonovitch, "Inhibited spontaneous emission in solid-state physics and electronics," *Phys. Rev. Lett.*, vol. 58, no. 20, pp. 2059-2062, May 1987.

[2] S. John, "Strong localization of photons in certain disordered dielectric superlattices," *Phys. Rev. Lett.*, vol. 58, no. 23, pp. 2486-2489, June 1987.

[3] J. G. Fleming and S. Y. Lin, "Three-dimensional photonic crystal with a stop band from 1.35 to 1.95 μm," *Opt. Lett.*, vol. 24, no. 1, pp. 49-51, Jan. 1999.

[4] S. Noda, K. Tomoda, N. Yamanoto, and A. Chutinan, "Full three-dimensional photonic band gap crystals at near-infrared wavelengths," *Science*, vol. no. 5479, pp. 604-606, July 2000.

[5] A. Taflove and S. C. Hagness, *Computational Electro-dynamics: The Finite-Difference Time-Domain Method*. Norwood, MA: Artech House, 2000.

[6] J. Shibayama, M. Muraki, J. Yamauchi, and H. Nakano, "Efficient implicit FDTD algorithm based on locally one-dimensional scheme," *Electron. Lett.*, vol. 41, no. 19, pp. 1046-1047, Sep. 2005.

[7] V. E. D. Nascimento, B.-H. V. Borges, and F. L. Teixeira, "Split-field PML implementations for the unconditionally stable LOD-FDTD method," *IEEE Microw. Wireless Compon. Lett.*, vol. 16, no. 7, pp. 398-400, July 2006.

[8] T. Namiki, "A new FDTD algorithm based on alternating-direction implicit method," *IEEE Trans. Microw. Theory Tech.*, vol. 47, no. 10, pp. 2003-2007, Oct. 1999.

[9] F. H. Zheng, Z. Z. Chen, and J. Z. Zhang, "A finite-difference time-domain method without the Courant stability conditions," *IEEE Microw. Guided Wave Lett.*, vol. 9, no. 11, pp. 441-443, Nov. 1999.

[10] J. Lee and B. Fornberg, "A split step approach for the 3-D maxwell's equations," *J. Comput. Appl. Math.*, vol. 158, no. 5, pp. 485-505, Sep. 2003.

[11] J. Lee and B. Fornberg, "Some unconditionally stable time stepping methods for the 3-D Maxwell's equations," *J. Comput. Appl. Math.*, vol. 166, no. 2, pp. 497-523, Apr. 2004.

[12] L. Gao, B. Zhang, and D. Liang, "The splitting finite difference time-domain methods for Maxwell's equations in two dimensions," *J. Comput. Appl. Math.*, vol. 205, no. 1, pp. 207-230, Aug. 2007.

[13] G. Sun and C. W. Trueman, "Approximate Crank-Nicolson schemes for the 2-D finite-difference time-domain method for TE_z waves," *IEEE Trans. Antennas Propag.*, vol. 52, no. 11, pp. 2963-2972, Nov. 2004.

[14] G. Sun and C. W. Truneman, "Efficient implementations of the Crank-Nicolson scheme for the finite-difference time-domain method," *IEEE Trans. Microw. Theory Tech.*, vol. 54, no. 5, pp. 2275-2284, May 2006.

[15] J. Lee and B. Fornberg, "A split step approach for the 3-D maxwell's equations," *J. Comput. Appl. Math.*, vol. 158, no. 5, pp. 485-505, Sep. 2003.

[16] F. Zheng and Z. Chen, "Numerical dispersion analysis of the unconditionally stable 3-D ADI-FDTD method," *IEEE Trans. Microw. Theory Tech.*, vol. 49, no. 5, pp. 1006-1009, May 2001.

[17] I. Ahmed, E. K. Chun, and E. P. Li, "Numerical dispersion analysis of the unconditionally stable three-dimensional LOD-FDTD method," *IEEE Trans. Antennas Propag.*, vol. 58, no. 12, pp. 3983-3989, Dec. 2010.

[18] Y. S. Chung, T. K. Sarkar, B. H. Jung, and M. Salazar-Palma, "An unconditionally stable scheme for the finite-difference time-domain method," *IEEE Trans. Microw. Theory Tech.*, vol. 51, no. 3,

pp. 697-704, Mar. 2003.
[19] M. Ha, K. Srinivasan, and M. Swaminathan, "Transient chip-package co-simulation using the Laguerre-FDTD scheme," *IEEE Trans. Adv. Packag.*, vol. 32, no. 4, pp. 816-830, Nov. 2009.
[20] H. Rao, R. Scarmozzino, and R. M. Osgood, "An improved ADI-FDTD method and its application to photonic simulations," *IEEE Photon. Technol. Lett.*, vol. 14, no. 4, pp. 477-479, Apr. 2002.
[21] I. Ahmed, E. K. Chua, E. P. Li, and Z. Z. Chen, "Development of the three-dimensional unconditionally stable LOD-FDTD method," *IEEE Trans. Antennas Propag*., vol. 56, no. 11, pp. 3596-3600, Nov. 2008.
[22] J. Shibayama, M. Muraki, R. Takahashi, J. Yamauchi, and H. Nakano, "Performance evaluation of several implicit FDTD methods for optical waveguide analyses," *J. Lightw. Technol.*, vol. 24, no. 6, pp. 2465-2472, June 2006.
[23] D. Y. Heh and E. L. Tan, "Complex-envelope LOD-FDTD method for ionospheric propagation," in *IEEE International Symposium on Antennas and Propagation (APSURSI)*, Fajardo, pp. 2027-2028, 2016.
[24] S. K. Gray and T. Kupka, "Propagation of light in metallic nanowire arrays: Finite-difference time-domain studies of silver cylinders," *Physical Review B.*, vol. 68, no. 4, pp. 045415, July 2003.
[25] J. Shibayama, R. Takahashi, J. Yamauchi, and H. Nakano, "Frequency-dependent LOD-FDTD implementtations for dispersive media," *Electron. Lett.*, vol. 42, no. 19, pp. 1084-1086, Sep. 2006.
[26] T. L. Liang, W. Shao, S. B. Shi, and H. Ou, "Analysis of extraordinary optical transmission with periodic metallic gratings using ADE-LOD-FDTD method," *IEEE Photon. J.*, vol. 8, no. 5, pp. 7804710, Oct. 2016.
[27] N. C. Panoiu, R. M. Osgood, S. Zhang, and S. R. J. Brueck, "Zero-*n* bandgap in photonic crystal superlattices," *J. Opt. Soc. Am. B.*, vol. 23, no. 3, pp. 506-513, Mar. 2006.

Tu-Lu Liang was born in Jiangxi, China, in 1991. He received the B.S. degree in Physics from the GanNan Normal University, Ganzhou, China, in 2014. Currently, he is working toward the Ph.D. degree in Radio Physics at the University of Electronic Science and Technology of China (UESTC), Chengdu, China.

His research interest is computational electromagnetic.

Wei Shao received the B.E. degree in Electrical Engineering, and the M.Sc. and Ph.D. degrees in Radio Physics from the University of Electronic Science and Technology of China (UESTC), Chengdu, in 1998, 2004, and 2006, respectively. He joined the UESTC in 2007. From 2010 to 2011, he was a Visiting Scholar with the Electromagnetic Communication Laboratory, Pennsylvania State University, State College, PA, USA. He is currently a Professor with UESTC.

His current research interests include computational electromagnetics and antenna design.

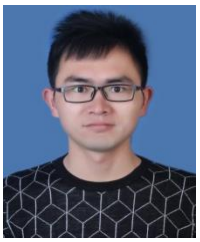

Sheng-Bing Shi was born in Hubei, China, in 1990. He received the B.S. degree in Physics from the Yangtze University, Jingzhou, China, in 2013. In 2015, he received the M.S. degree in Radio Physics at University of Electronic Science and Technology of China (UESTC). Currently, he is working toward the Ph.D. degree in Radio Physics at UESTC.

His research interest is computational electromagnetic.

FPGA Based Fast Bartlett DoA Estimator for ULA Antenna Using Parallel Computing

Fahri M. Unlersen [1], Ercan Yaldiz [2], and Sehabeddin T. Imeci [3]

[1] Department of Electrical and Electronics Engineering
Necmettin Erbakan University, Konya, 42090, Turkey
mfunlersen@konya.edu.tr

[2] Department of Electrical and Electronics Engineering
Selcuk University, Konya, 42031, Turkey
eyaldiz@selcuk.edu.tr

[3] Department of Electrical and Electronics Engineering
International University of Sarajevo, Ilıdza, 71210, Bosnia and Herzegovina
simeci@ius.edu.ba

Abstract ─ This paper presents a design and implementation of a structure which uses Bartlett Direction of Arrival (DoA) algorithm and a receiver system on Altera Cyclone IV and Cyclone III FPGAs. First of all, a software defined radio (SDR) that has 4 simultaneous inputs, is designed. All data used in this study are obtained by using this radio system. Then one of the FPGA is configured as antenna simulator and the other one is used for implementing Bartlett DoA estimation algorithm. Bartlett DoA estimation algorithm is developed completely in parallel and compared with a previous study which is performed sequentially on an FPGA using NIOS processor. The designs are tested by using 4-element Uniform Linear Array (ULA) antenna. Implemented hardware is compared in terms of DoA calculation speed and the sources that occupy on the FPGA. Furthermore, the paper has significant improvement in calculation duration thereby achieving lower response latency compared with previously published similar works.

Index Terms ─ Bartlett algorithm, direction of arrival estimation, FPGA, parallel computing.

I. INTRODUCTION

An antenna array is a system consisted of singular antenna elements that are designed to behave like a single antenna used to receive and/or radiate the electromagnetic waves. These antenna arrays are also known as smart antennas have the ability to estimate Direction of Arrival (DoA) as well as high directivity, high gain, formable radiation pattern features. In addition, having the features to prevent co-channel fading and to create low side lobe level (SLL) abilities, interference is reduced by antenna arrays. With the help of these features, the use of antenna arrays on systems such as surveillance radar, ground penetrating radar, sonar, ultrasonic imaging, seismic data processing and medical imaging offers significant advantages [1-5].

Detection of the direction of an incident signal received by an antenna array is called DoA estimation. This bases on process actualized with processing the relative phase difference between incident signals onto antenna elements. DoA estimation is widely used in such applications like mobile communication, radar, and sonar etc. [6]. There are three principles of DoA estimation methods named conventional spectral-based, subspace spectral-based, and statistical methods. The most popular conventional spectral-based methods are Bartlett, Capon, First Order Forward Prediction, Maximum Entropy [7], Deterministic and Stochastic Maximum Likelihood (DML, SML) [8]. The popular subspace spectral-based methods are Multiple Signal Classifying (MUSIC), Min-Norm and Weighted Subspace Fitting (WSF). And the statistical methods are Estimation of Signal Parameters via Rotational Invariance Techniques (ESPRIT), Root-MUSIC and Root-WSF [8-11]. These methods have really long calculation processes. Since operations are performed one after the other in the sequential calculation, the DoA estimation calculations like eigenvalue decomposition in subspace-based methods and covariance calculation operation which is the most common operation in all of the methods, cost huge calculation duration [12]. Because of having the ability of parallel calculation, an FPGA could be employed to solve these DoA Estimation problems much faster than a classical microprocessor.

Submitted On: July 31, 2017
Accepted On: April 8, 2018

Table 1: Comparison of the studies in literature in terms of calculation duration and utilized logic elements

Ref.	Structure / Method	Number of Antenna	Calculation Duration (μs)	Utilized Logic Elements
[13]	Sequential / New EVD Structure-based MUSIC DoA Estimation	4 ULA	27.64	14609
[14]	Sequential / ROM Based Unitary MUSIC processor with spatial smoothing	4 ULA	30.59	12007
[14]	Sequential / ROM Based Unitary MUSIC processor without spatial smoothing	4 ULA	57.11	12995
[14]	Sequential / ROM Based Unitary MUSIC processor without spatial smoothing	8 ULA	373.99	29472
[15]	Sequential / ARM-Cortex Core microprocessor based MUSIC DoA Estimator	8 ULA	2560	-
[16]	Parallel-Sequential / Butterfly FFT Core based on DSP48E microprocessor	8 ULA	-	33961
[17]	Sequential / A coordinate rotation digital computer (CORDIC) based Sum&Delay DoA Estimator	16 ULA	768	-
[18]	Sequential / MicroBlaze soft processor based Bartlett DoA Estimator	8 UCA	684	2349
[18]	Parallel-Sequential / Bartlett DoA Estimator	8 UCA	312.13	165
[18]	Parallel-Sequential / FFT DoA Estimator	8 UCA	104.8×10^3	7434

In literature, due to the aim of the application (like improve calculation speed, reduce complexity or optimal hardware consumption), the results could be various. The most attractive studies about DoA estimation based on an FPGA with Uniform Linear Array (ULA) and Uniform Circular Array (UCA) are presented in Table 1.

In this study, working with data taken from the real environment is aimed. For this purpose, a data collection hardware is designed. The collected dataset is stored on a PC. Then with the next hardware implementation, a DoA estimation is done by using the dataset which was collected from antenna array in a real environment. The proposed system is a highly parallel calculating method. For each angle, the values in the pseudo spectrum are calculated fully parallel but the calculation of whole pseudo spectrum needs 181 sequences.

In the second section, the design of the systems is presented. In the third section, the proposed DoA estimation method, Bartlett, is introduced. In the fourth section, the architecture in the FPGA is presented, in the next section, the performance comparison is done. In the last section, the conclusions are presented.

II. SYSTEM DESIGN

Usage of the FPGAs in a system does not guarantee that this system is going to be faster. The most important point of an FPGA usage is the ability of parallel computing. So, for a significant improvement in process duration, it is an obligation to use of parallel calculation ability of the FPGAs. Furthermore, to make an existing algorithm possible to run parallel, it has to be investigated and optimized deeply.

The established system to estimate DoA calculation has two stages. The first stage is for data collecting from the real environment. That hardware collects data from 4 quarter wave antenna and saved into a PC. These recordings are done in an open area to avoid reflections. In this stage, the FPGA evaluation board is employed as 4 channel shift register and serial communicator.

In the second stage, Bartlett DoA estimation is done by using the recorded data. In this stage, two FPGA evaluation board are used. The first FPGA evaluation board is employed to simulate an antenna array output by using the data collected in the first stage. The dataset comprises the environmental noise, the mutual coupling effects of the antennas in the array. So, it is possible to examine the DoA estimation algorithms in the laboratory environment as if they are done in the real world. The setups used in these stages are presented in Fig. 1.

In the first stage, an RF Front-End and data collector structure has been designed. The signals received from 4 monopole antenna elements are amplified by a preamplifier (PA). This amplifier has 4 channels that have equal and fixed gain about 10 dB. The amplified received signal is applied to a mixer IC. Each channel has own mixer ICs, but all of the local oscillator (LO) inputs of mixers are fed from same crystal oscillator with the same length of a path. The obtained intermediate frequency (IF) signal at the output of mixer IC is filtered by a crystal resonator filter (CRF). The IF signal with

the frequency of 2MHz, has been amplified by IF amplificator (IF). ADA daughter board (ADA-GPIO) by Altera Company is used as the analog-digital converter. The IF signals received from 4 channels are converted into 8-bit digital data in 40 MSPS speed using two ADA-GPIOs. The ADA-GPIOs are connected to Altera DE0 Board. For the rest of the operations, Altera DE0 Board is used.

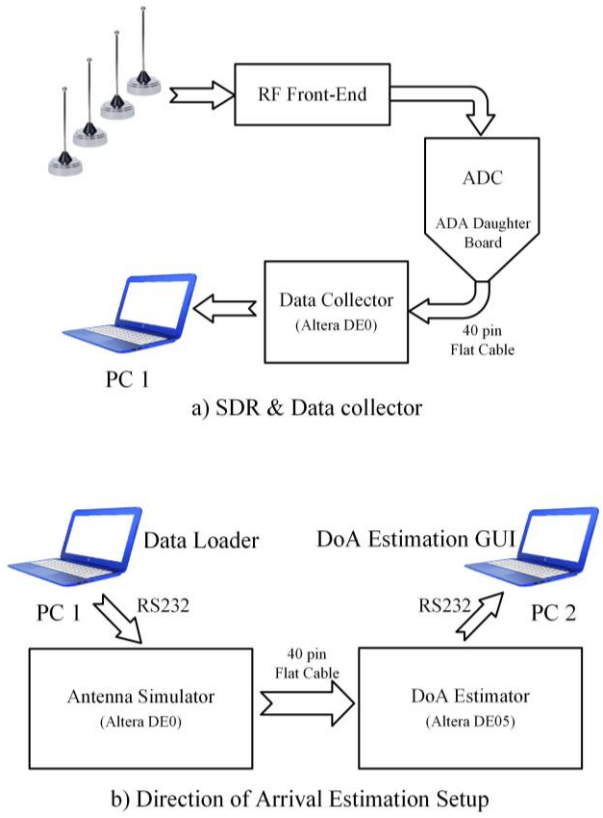

Fig. 1. (a) The first stage: Data acquisition setup. (b) The second stage: DoA estimation setup.

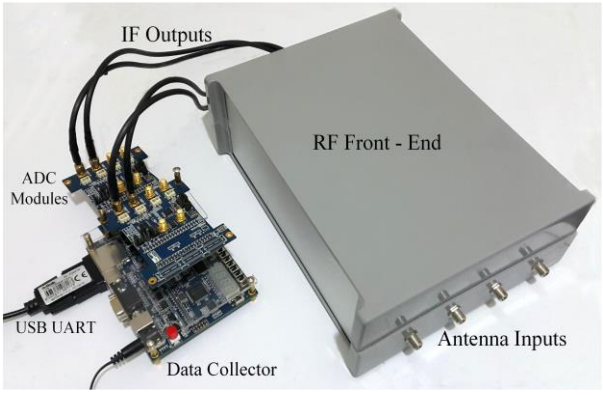

Fig. 2. Software defined radio & data collecting.

The measurements are done in an open area to avoid reflections. They are performed while two unmodulated narrowband transmitters are at different angles and results are recorded. The measurement set-up whose flow chart is presented in Fig. 1 (a) is shown in Fig. 2. The block diagram of data collection hardware whose picture is seen in Fig. 2 is presented in Fig. 3.

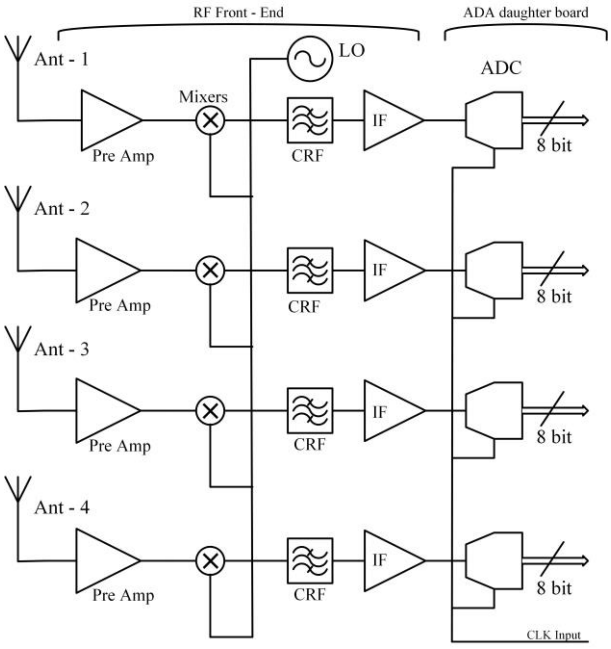

Fig. 3. The block diagram of RF Front-End & data collecting setup.

After the ADA-GPIOs the IF signal is digitized and taken into the FPGA. Each of these digitized samples has taken into shift registers from each channel simultaneously. Totally 480 samples are transferred to a PC via Universal Synchronous/Asynchronous Receiver/ Transmitter (USART) when 120 samples are collected from all of the inputs. To avoid mistakes, a header consists of 5 bytes to the beginning of the stream and a checksum byte at the end of the stream is added. So, each transfer sequence consists of 486 bytes. The block diagram of the shift register used for data collection operations and implemented by VHDL codes for FPGA DE0 board is presented in Fig. 4.

When the user asks from the software in the PC to take a capture, the software looks for a header, then collects 480 bytes of data after the header, and after receiving the checksum, compares it with the calculated one. If the checksum byte comparison is confirmed the collected data is stored on the hard disk with date, time and an explanatory text. Else, whole instructions mentioned above are repeated.

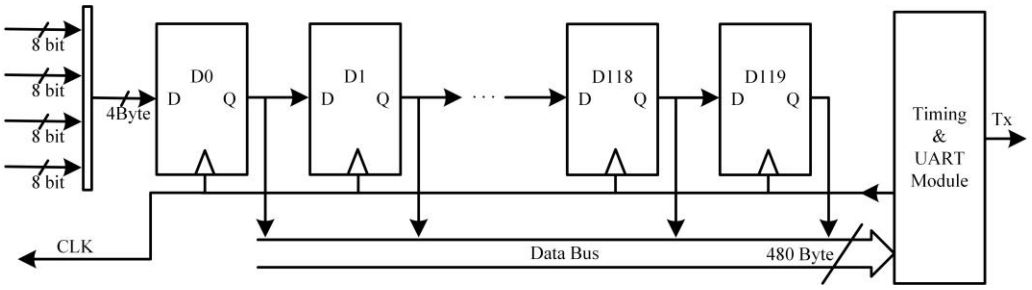

Fig. 4. The block diagram of data collector implemented on the FPGA.

Since there is a filtration operation during the IF signal amplification, the IF signal almost consists of a single frequency at 2MHz. So, the digital IF signal recorded on the hard disk is subject to the mathematical models given in Equation (1):

$$U[n] = A\cos\left(2\pi f_0 \frac{n}{f_s} + \varphi\right), \quad (1)$$

where A represents signal amplitude, n represents the sample index changing between 1 and 120, f_0 represents the operating frequency (2MHz), f_s represents the sampling frequency (40MHz).

All measurements are done in open area due to avoid unwanted reflections. A signal generator connected to a monopole antenna is used as the signal source. In measurements, two unmodulated signal sources are settled up to various angles and 120 samples of 4 IF signals are recorded. Totally 480 records are taken for each setup and stored on a PC to use in DoA estimation stage.

In the second stage, the recorded data in the first stage is embedded into DE0 board which simulates an antenna array or an RF front-end outputs. The data is sequentially driven to the outputs through Circular Shift Register (CSR). The antenna simulator whose flowchart is presented in Fig. 1 (b) is demonstrated as a block diagram in Fig. 5.

DoA estimation is done on DE2-115 development and education board of Altera Company. The DoA estimation is achieved by using Bartlett algorithm on DE2-115 board. Results are transferred to a PC via a UART protocol. They are observed and saved by a GUI software on a PC. The inner connection between DE0 and DE2-115 is done by using 40 pin Integrated Drive Electronics (IDE) cable. But to avoid interferences into the data signals in IDE cable, it is screened with a grounded aluminum foil. The measurement set-up is presented in Fig. 6.

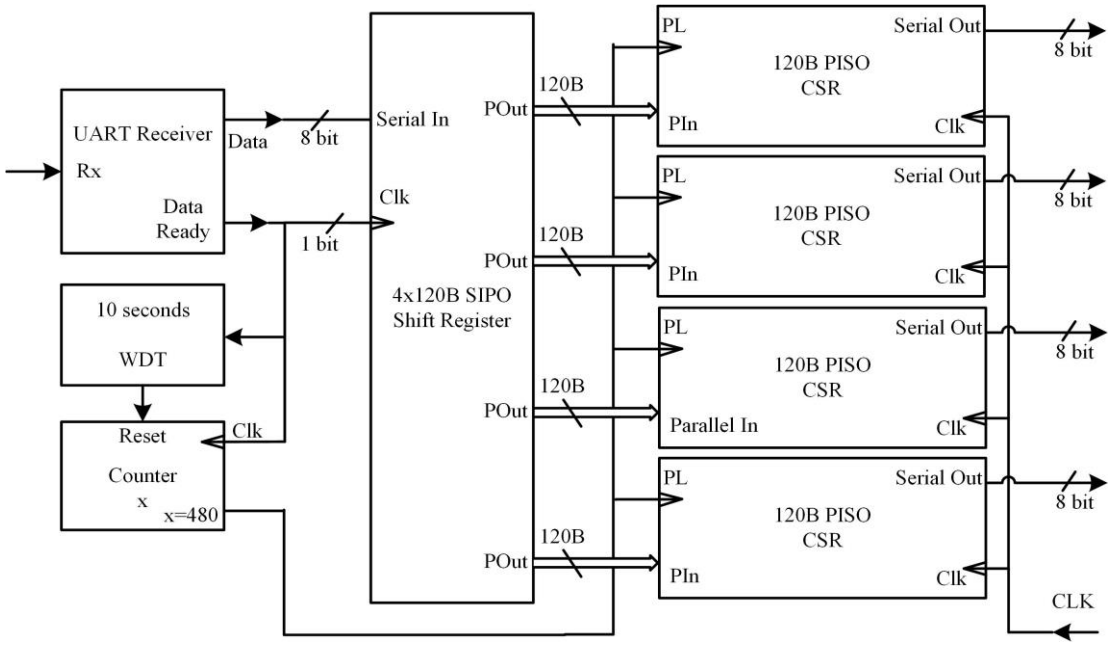

Fig. 5. The block diagram of the antenna simulator implemented on the FPGA.

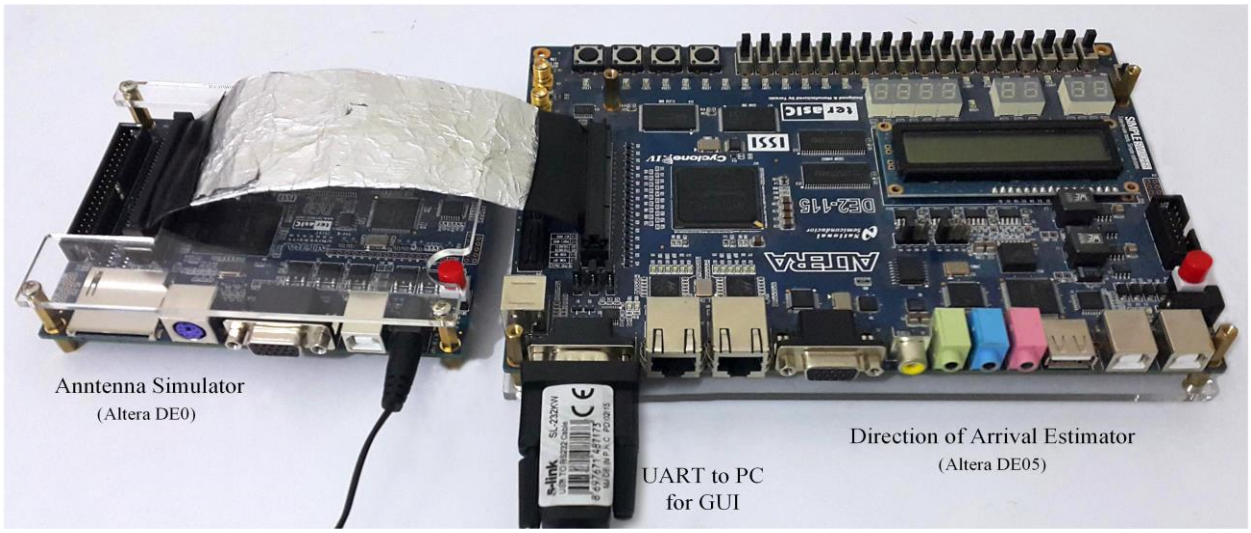

Fig. 6. DoA estimation set-up.

III. BARTLETT DoA ESTIMATION

In the Bartlett spectral estimation method, the power maintained from the antenna array is calculated as the function of θ, and a spatial spectrum is obtained. Local maximums are determined in this spatial spectrum. The result is the power coming through $P_B(\theta)$. This value is obtained by Equation (2) [9]:

$$P_B(\theta) = \frac{S_\theta^H \times R \times S_\theta}{N^2}, \tag{2}$$

where S_θ represents steering vector for θ, N represents the number of antenna elements forming ULA antenna and R represents covariance matrix of the array. $(\ )^H$ represents Hermitian conjugate of a vector. S_θ and Hermitian conjugate of S_θ are given by Equation (3) [9]:

$$\begin{aligned} S_\theta[n] &= e^{\ jnkd\sin(\theta)} \\ S_\theta^H[n] &= e^{-jnkd\sin(\theta)} \end{aligned} \qquad n = 0 \to N-1. \tag{3}$$

In Equation (3) the k represents the wave number which is equal to $2\pi/\lambda$. And the d represents distances between antenna elements in the ULA. This value is chosen as $\lambda/2$. The N parameter which represents the number of antenna elements in ULA antenna is 4 in this study.

To make Equation (2) suitable for parallel computing, following simplifications are done:

$$\begin{aligned} P_B(\theta) &= \frac{1}{N^2}\sum_{n=1}^{4}\sum_{m=1}^{4} S_\theta[n].R[n,m].S_\theta^H[m], \\ P_B(\theta) &= \frac{1}{N^2}\sum_{n=1}^{N}\sum_{m=1}^{N} e^{jn\pi\sin(\theta)}.e^{-jm\pi\sin(\theta)}.R[n,m], \\ P_B(\theta) &= \frac{1}{N^2}\sum_{n=1}^{N}\sum_{m=1}^{N} e^{j(n-m)\pi\sin(\theta)}.R[n,m]. \end{aligned} \tag{4}$$

In Equation (4), it is possible to observe that the minimum and maximum value of n-m is 1-N and N-1 respectively. So if a W vector is defined as in Equation (5), the Bartlett DoA estimation formula in Equation (4) can be presented as in Equation (6):

$$W_\theta[p] = e^{\ jp\pi\sin(\theta)} \quad p = 1-N \to N-1. \tag{5}$$

$$P_B(\theta) = \frac{1}{N^2}\sum_{n=1}^{N}\sum_{m=1}^{N} W[n-m].R[n,m]. \tag{6}$$

The new vector W_θ is calculated in this study by the Equation (7):

$$\begin{aligned} W_\theta &= \begin{bmatrix} e^{-j3\pi\sin(\theta)}, e^{-j2\pi\sin(\theta)}, e^{-j\pi\sin(\theta)}, \\ 1,\ e^{j\pi\sin(\theta)}, e^{j2\pi\sin(\theta)}, e^{j3\pi\sin(\theta)} \end{bmatrix}, \\ W_{\theta r} &= \begin{bmatrix} \cos(-3\pi\sin(\theta)), \cos(-2\pi\sin(\theta)), \cdots \\ \cdots, \cos(2\pi\sin(\theta)), \cos(3\pi\sin(\theta)) \end{bmatrix}, \\ W_{\theta i} &= \begin{bmatrix} \sin(-3\pi\sin(\theta)), \sin(-2\pi\sin(\theta)), \cdots \\ \cdots, \sin(2\pi\sin(\theta)), \sin(3\pi\sin(\theta)) \end{bmatrix}. \end{aligned} \tag{7}$$

This process conducted on Bartlett DoA estimation algorithm resembles the calculation of the power radiated from the antenna array towards each angle physically. However, the obtained value from a certain direction not only contains the signal sources in the direction, but also the signal sources from side lobes slightly [19].

IV. HARDWARE IMPLEMENTATION

The signals obtained in the physical environment have real values. However, DoA estimation algorithms need also imaginary parts of the signals as input [20]. Since the IF is a narrow band signal, the polar expression of IF signal can be expressed as in Equation (8):

$$\begin{aligned} U[n] &= Ae^{\ j\left(\frac{2\pi f_0}{f_s}n+\varphi\right)}, \\ U[n] &= A\left(\cos\left(\frac{2\pi f_0}{f_s}n+\varphi\right) + j\sin\left(\frac{2\pi f_0}{f_s}n+\varphi\right)\right). \end{aligned} \tag{8}$$

The collected data is the real part of the value in Equation (8). In order to derive imaginary part needed in Bartlett algorithm, several methods could be employed. For example, the imaginary part is equal to $(A^2 - R^2)^{1/2}$ where A is the envelope of signal and R is the real values. But both "envelope determination" and "square root operation" cause extra calculation duration.

In this study, some trigonometric manipulations are done to obtain the imaginary part of the signal by using just basic four operations. The well-known sum and subtraction formulas of cosine presented in Equation (9) form the basis of the manipulations:

$$\begin{aligned}\cos x+\cos y &= 2\cos\left(\frac{(x+y)}{2}\right).\cos\left(\frac{(x-y)}{2}\right),\\ \cos x-\cos y &= -2\sin\left(\frac{(x+y)}{2}\right).\sin\left(\frac{(x-y)}{2}\right).\end{aligned} \tag{9}$$

Since the f_s and f_0 are chosen as 40MHz and 2MHz respectively, two sequential samples ((n-1)th and nth) can be expressed as in Equation (10):

$$\begin{aligned}U[n] &= A\cos\left(\frac{2\pi f_0}{f_s}n+\varphi\right)=A\cos\left(\frac{\pi}{10}n+\varphi\right),\\ U[n-1] &= A\cos\left(\frac{2\pi f_0}{f_s}(n-1)+\varphi\right)=A\cos\left(\frac{\pi}{10}(n-1)+\varphi\right).\end{aligned} \tag{10}$$

In order to obtain an expression contains sinus function, it is clear that subtraction formulas should be used:

$$\begin{aligned}DeltaU &= U[n-1]-U[n],\\ DeltaU &= A\left(\cos\left(\frac{\pi}{10}(n-1)+\varphi\right)-\cos\left(\frac{\pi}{10}n+\varphi\right)\right),\\ DeltaU &= -A\times 2\times\sin\left(\frac{\pi}{10}\left(n-\tfrac{1}{2}\right)+\varphi\right)\times\sin\left(-\frac{\pi}{20}\right),\end{aligned} \tag{11}$$

Hence sinus expression can be written as in Equation (12) [21]:

$$\begin{aligned}A\sin\left(\frac{2\pi f_0}{f_s}\left(n-\tfrac{1}{2}\right)+\varphi\right) &= \frac{DeltaU}{2\times\sin\left(\frac{\pi}{20}\right)}=\frac{(U[n-1]-U[n])}{0.3129},\\ A\sin\left(\frac{2\pi f_0}{f_s}\left(n-\tfrac{1}{2}\right)+\varphi\right) &\simeq \frac{25}{8}\times(U[n-1]-U[n]).\end{aligned} \tag{12}$$

It can be seen that the sample index of the obtained imaginary part (sinus expression) is (n-0.5). To make real part concurrently with the imaginary part, some manipulations need on real part. In order to obtain a cosine expression with (n-0.5) sample index, the sum of two sequential samples in Equation (10) can be calculated:

$$\begin{aligned}SumU &= U[n-1]+U[n],\\ SumU &= A\left(\cos\left(\frac{\pi}{10}(n-1)+\varphi\right)+\cos\left(\frac{\pi}{10}n+\varphi\right)\right),\\ SumU &= A\times 2\times\cos\left(\frac{\pi}{10}\left(n-\tfrac{1}{2}\right)+\varphi\right)\times\cos\left(-\frac{\pi}{20}\right),\end{aligned} \tag{13}$$

The cosine expression can be written as in Equation (14):

$$\begin{aligned}A\cos\left(\frac{2\pi f_0}{f_s}\left(n-\tfrac{1}{2}\right)+\varphi\right) &= \frac{U[n-1]+U[n]}{2\times\cos\left(-\frac{\pi}{20}\right)}=\frac{U[n-1]+U[n]}{1.9754},\\ A\cos\left(\frac{2\pi f_0}{f_s}\left(n-\tfrac{1}{2}\right)+\varphi\right) &\simeq \frac{1}{2}\times(U[n-1]+U[n]).\end{aligned} \tag{14}$$

As a result of manipulations seen above, the real and imaginary values can be expressed as in Equation (15) [21]:

$$\begin{aligned}U_r[n-0.5] &= \frac{1}{2}(U[n-1]+U[n]),\\ U_i[n-0.5] &= \frac{25}{8}(U[n-1]-U[n]).\end{aligned} \tag{15}$$

First, the *U[n]* data is taken from ADC into the FPGA. Then the real and imaginary parts of this data are calculated by the help of the Equation (15). And two shift registers are added to record U_r and U_i on each clock cycle. The calculation method of imaginary and real parts of the data on the FPGA is presented as a block diagram in Fig. 7.

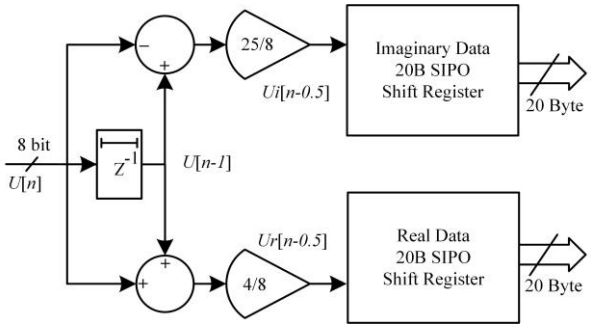

Fig. 7. The extraction of imaginary - real values and shift registers on the FPGA.

Next step is the calculation of the covariance matrix. The input matrix of covariance calculation consists of 20 samples obtained from each antenna outputs. Since there are 4 sensors in the ULA antenna, the dimension of input matrix is 4×20.

The covariance of X_a and X_b vectors are calculated as in Equation (16) [22]:

$$Cov(X_a,X_b)=E\left[\left(X_a-E(X_a)\right)^H\times\left(X_b-E(X_b)\right)\right]. \tag{16}$$

Here, E operator shows the average of the related vector. $(\ )^H$ symbol indicates the Hermitian conjugate of the concerned vector. The E operator executes the operations in Equation (17):

$$E(U)=\frac{1}{N}\sum_{n=1}^{N}U[n]=\frac{1}{N}\sum_{n=1}^{N}\cos\left(\frac{2\pi f_0}{f_s}n+\varphi\right). \tag{17}$$

A practical identity about the sum of cosine series is presented in Equation (18) [23]:

$$\sum_{n=1}^{N}\cos(xn+\varphi)=\frac{\cos\left(\frac{N+1}{2}x+\varphi\right)\sin\left(\frac{N}{2}x\right)}{\sin\left(\frac{x}{2}\right)}. \tag{18}$$

If the transformation in Equation (18) is performed in the Equation (17), the Equation (19) is obtained:

$$E(U)=\frac{1}{N}\sum_{n=1}^{N}\cos\left(\frac{2\pi f_0}{f_s}n+\varphi\right)$$

$$E(U)=\frac{\cos\left((N+1)\frac{\pi f_0}{f_s}+\varphi\right)\sin\left(\frac{N\pi f_0}{f_s}\right)}{N\sin\left(\frac{\pi f_0}{f_s}\right)}. \quad (19)$$

In order to make the mean value of U presented in Equation (19) zero, $\sin(N\pi f_0/f_s)$ has to be equal to zero. Therefore $N\pi f_0/f_s$ needs to be equal to πk which makes sinus zero:

$$\text{if}\quad \frac{N\pi f_0}{f_s}=\pi k \quad \text{then } E(U)=0 \quad \text{for } k=0,1,2...$$
$$N=\frac{f_s}{f_0}k=\frac{40}{2}k=20k. \quad (20)$$

The sampling frequency is chosen as a multiple of the signal frequency. Additionally, the number of samples taken into shift registers is chosen as 20 which is a multiple of the ratio between the sampling frequency and the signal frequency. These predilections make the average of the related vector zero as presented in Equation (20).

That circumstance eliminates the average calculations in the covariance calculation. So, the Equation (16) could be reconstructed as in Equation (21):

$$Cov(X_a,X_b)=E\left[(X_a)^H\times(X_b)\right]. \quad (21)$$

This provides a reduction in the FPGA source consumption and calculation duration. As the number of sensors in the ULA antenna is 4, the covariance matrix has to be 4×4 size as shown in Equation (22):

$$R=\begin{bmatrix} R[1,1] & R[1,2] & R[1,3] & R[1,4] \\ R[2,1] & R[2,2] & R[2,3] & R[2,4] \\ R[3,1] & R[3,2] & R[3,3] & R[3,4] \\ R[4,1] & R[4,2] & R[4,3] & R[4,4] \end{bmatrix}. \quad (22)$$

The covariance matrix is diagonally symmetric [22]. In order to get calculations simple, $R[2,1]$, $R[3,1]$, $R[4,1]$, $R[3,2]$, $R[4,2]$ and $R[4,3]$ are not calculated, only the conjugant value of related element is assigned. The real and imaginary parts of R matrix are calculated as shown in Equation (23) [21]:

$$R[a,b]=R_r[a,b]+j\times R_i[a,b],$$
$$R_r[a,b]=\frac{1}{20}\sum_{n=1}^{20}\begin{pmatrix}U_r[a,n]\times U_r[b,n]\\ +U_i[a,n]\times U_i[b,n]\end{pmatrix}, \quad (23)$$
$$R_i[a,b]=\frac{1}{20}\sum_{n=1}^{20}\begin{pmatrix}U_r[a,n]\times U_i[b,n]\\ -U_i[a,n]\times U_r[b,n]\end{pmatrix},$$

where $U[a,n]$ is n^{th} sample taken from the a^{th} antenna:

$$P_B(\theta)=\frac{1}{N^2}\sum_{n=1}^{N}\sum_{m=1}^{N}W[n-m].R[n,m],$$
$$P_{B\,real}(\theta)=\frac{1}{16}\sum_{n=1}^{4}\sum_{m=1}^{4}\left(W_r[n-m].R_r[n,m]-W_i[n-m].R_i[n,m]\right), \quad (24)$$
$$P_{B\,imag}(\theta)=\frac{1}{16}\sum_{n=1}^{4}\sum_{m=1}^{4}\left(W_r[n-m].R_i[n,m]+W_i[n-m].R_r[n,m]\right),$$

with the covariance matrix R, DoA strength estimation for any angle θ is calculated by using Equation (6).

In order to reduce calculation process, the W vector is obtained from a pre-calculated table. Integer is used as the class in all process. The whole block diagram of the Bartlett DoA system is shown in Fig. 8 [21].

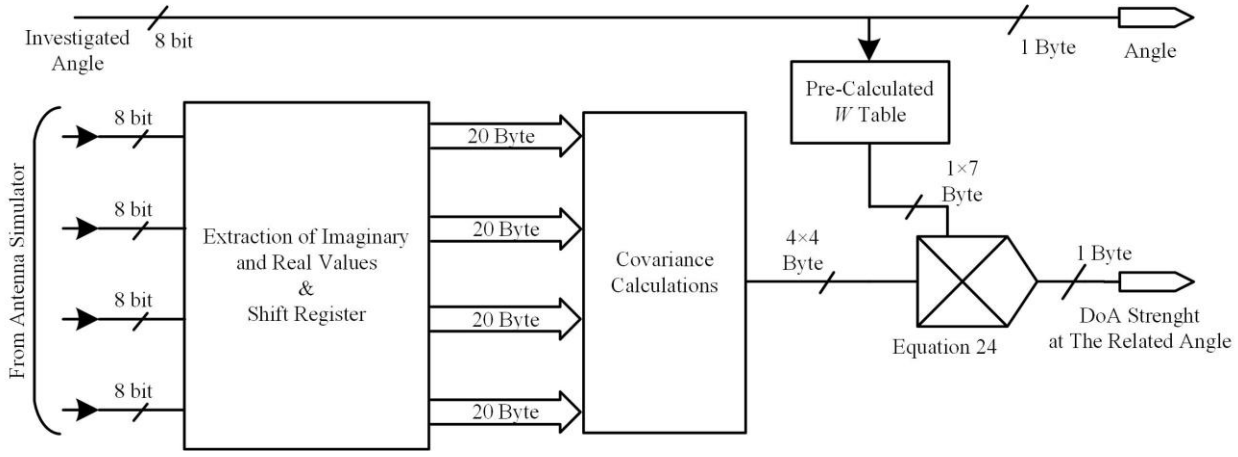

Fig. 8. Block diagram of the Bartlett DoA algorithm on the FPGA.

The data obtained from this system is kept by a sphift register and transferred to a PC via serial port. The DoA estimation results are observed by a GUI on a PC. Figure 9 shows a screenshot of GUI taken from a PC [21].

The most important disadvantage of this method is

the data transfer process. The process of transferring data from the FPGA to a PC is slower compared to the DoA estimation calculations. Designing a system that creates control outputs according to the DoA results on the same device, (means a fully embedded system) would provide significant benefits in real-time applications.

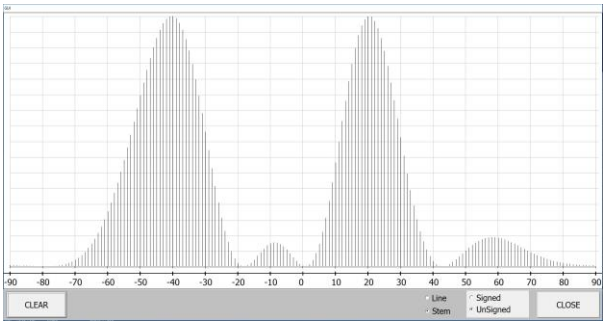

Fig. 9. Screenshot of the GUI shows DoA estimation results on pseudo-spectrum.

V. PERFORMANCE COMPARISON

In this algorithm, DoA estimation is done for 181° pseudo-spectrum between -90° and 90°. By means of 1° increase in each clock pulse, the incoming signal existence from the related angle is calculated. Thereby, for the DoA estimation of the whole pseudo-spectrum, 181 clock pulse is needed. Since the working frequency is 225MHz, the DoA estimation duration for the whole pseudo-spectrum calculations is about 804.44 ns.

In the study [18], the Bartlett DoA Estimation algorithm had done using MicroBlaze soft processor on an FPGA as presented in Table 2 Structure No. 1. When the scripts in the study [17] are considered, it is seen that the DoA estimation of the whole pseudo-spectrum is calculated with 118193 clock pulse.

Besides, the custom VHDL in the study [18] is designed in two types, as Parallel-Sequential Bartlett DoA Estimator and Parallel-Sequential FFT DoA Estimator; presented in Table 2 with Structure No. 2 and 3 respectively. The DoA estimation durations on FPGA are presented as 312.13 µs and 104825 µs respectively. Clock cycle, calculation duration, utilized logic elements for the study [17] and the proposed method are given in Table 2.

VI. CONCLUSION

This paper presents design and implementation of a fast parallel Bartlett DoA estimation hardware on an FPGA. Since the signals in the study are collected from the real world, the data involves all the effects such as noise, reflections, and interferences between antennas. Moreover, its comparison with Bartlett DoA estimation algorithm, which is created by using MicroBlaze soft processor and custom design VHDL codes, was done.

Table 2: Comparison of the proposed method and the study [17] in calculation duration

Structure No.	Structure / Method / Reference	Clock Cycle	Calculation duration (µs)	Utilized Logic Elements
1	Seq. MicroBlaze soft processor based Bartlett DoA estimator [18]	118193	684	2349
2	Parallel-Seq. Bartlett DoA estimator [18]	53929 (Estimate)	312.1	165
3	Parallel-Seq. FFT DoA estimator [18]	18.19×10^6 (Estimate)	104.8×10^3	7434
4	Parallel Presented in this paper	181	0.804	8467

Besides the improvements in the FPGA technology, the optimization process on the algorithm has an important role on the duration reduction of calculation. It can be seen that DoA estimation which is performed by using parallel calculation, provides a considerable increase in calculation speed. This provides a significant improvement over the similar studies found in literature. By making modifications to covariance matrix calculation and steering vector usage, it has become possible to scan the whole pseudo-spectrum in just 181 clock pulses. The DoA estimation hardware developed in this study is presented as Structure 4 in Table 2. By comparing based on calculation duration, the Structure 4 produces results in 0.034% of calculation duration of Structure 1 (2920 times faster than Structure 1), 0.49% of calculation duration of Structure 2 (205 times faster than Structure 2) and 0.01% of calculation duration of Structure 3 (9241 times faster than Structure 3). Although calculation durations could give an impression, this information has a close relation between working frequency, it has also a relation between improvements in the technology. In order to obtain more objective results, the clock cycle count need to be compared. If a comparison is done based on clock counts, it could be seen clearly that Structure 4 is 653 times faster than Structure 1. This radical decrease in the calculation is occurred because of the algorithm optimizations and adaptation of sequential algorithm into parallel. In this study, arrangements on Bartlett algorithm and imaginary part obtaining method is performed. These are the major effects on achieving the low latency. The results are promising for future works about a standalone fast DoA estimator system on an FPGA.

REFERENCES

[1] M. Viberg and T. Svantesson, *Direction-of-Arrival Estimation in Mobile Communication Environments, in Handbook of Antennas in Wireless Communication*. CRC Press, Boca Raton, London, New York, Washington D.C., 2002.

[2] M. H. Rahmani and A. Pirhadi, "Optimum design of conformal array antenna with a shaped radiation pattern and wideband feeding network," *ACES Journal*, vol. 29, no. 1, pp. 37-46, Jan. 2014.

[3] C. A. Balanis, *Antenna Theory: Analysis and Design*. John Wiley & Sons, New Jersey, 2005.

[4] H. L. Sneha, H. Singh, and R. M. Jha, "Analytical estimation of radar cross section of arbitrary compact dipole array," *ACES Journal*, vol. 29, no. 9, pp. 726-734, Sep. 2014.

[5] C. Furse, "A survey of phased arrays for medical applications," *ACES Journal*, vol. 21, no. 3, pp. 365-379, Nov. 2006.

[6] G. Buttazzoni and R. Vescovo, "Far-field synthesis of sparse arrays with cross-polar pattern reduction," *ACES Express Journal*, vol. 1, no. 2, pp. 44-47, Jan. 2016.

[7] Y. Khmou, S. Safi, and M. Frikel, "Comparative study between several direction of arrival estimation methods," *Journal of Telecommunications and Information Technology*, vol. 1, no. 41-48, Jan. 2014.

[8] H. Krim and M. Viberg, "Two decades of array signal processing research: The parametric approach," *IEEE Signal Processing Magazine*, vol. 13, no. 4, pp. 67-94, July 1996.

[9] L. C. Godara, "Application of antenna arrays to mobile communications II. Beam-forming and direction-of-arrival considerations," *Proceedings of the IEEE*, vol. 85, no. 8, pp. 1195-1245, Aug. 1997.

[10] E. M. Al-Ardi, R. M. Shubair, and M. E. Al-Mualla, "Direction of arrival estimation in a multipath environment: An overview and a new contribution," *ACES Journal*, vol. 21, no. 3, pp. 14, Nov. 2006.

[11] S. J. Ovaska and O. Vainio, "Recursive linear smoothed newton predictors for polynomial extrapolation," *IEEE Transactions on Instrumentation and Measurement*, vol. 41, no. 4, pp. 510-516, Aug. 1992.

[12] B. J. Fasenfest, F. Capolino, and D. R. Wilton, "Preconditioned gifft: A fast mom solver for large arrays of printed antennas," *ACES Journal*, vol. 21, no. 3, pp. 276-283, Nov. 2006.

[13] K. Minseok, I. Koichi, and A. Hiroyuki, "Implementation of FPGA based fast DoA estimator using unitary MUSIC algorithm [cellular wireless base station applications]," *2003 IEEE 58th Vehicular Technology Conference*, vol. 1, pp. 213-217, 6-9 Oct. 2003.

[14] M. Kim, K. Ichige, and H. Arai. "Real-time smart antenna system incorporating FPGA-based fast DoA estimator," *2003 IEEE 58th Vehicular Technology Conference*, vol. 1, pp. 26-29, Sep. 2004.

[15] M. Devendra and K. Manjunathachari, "Direction of arrival estimation using MUSIC algorithm in FPGA: Hardware software co-design," *International Journal of Applied Engineering Research*, vol. 11, no. 5, pp. 3112-3116, 2016.

[16] M. Jamali, J. Downey, N. Wilikins, C. R. Rehm, and J. Tipping, "Development of a FPGA-based high speed FFT processor for wideband direction of arrival applications," *2009 IEEE Radar Conference*, pp. 1-4, 4-8 May 2009.

[17] Y. Yang and A. E. Fathy, "Development and implementation of a real-time see-through-wall radar system based on FPGA," *IEEE Transactions on Geoscience and Remote Sensing*, vol. 47, no. 5, pp. 1270-1280, 24 Mar. 2009.

[18] M. Abusultan, S. Harkness, B. J. LaMeres, and Y. Huang, "FPGA implementation of a Bartlett direction of arrival algorithm for a 5.8 ghz circular antenna array," *2010 IEEE Aerospace Conference*, pp. 1-10, 6-13 Mar. 2010.

[19] P. Hyberg, "Antenna array mapping for DoA estimation in radio signal reconnaissance," *Ph.D. Dissertation, Sensors and Systems Royal Institute of Technology*, Sweden, p. 266, 2005.

[20] R. L. Haupt, "Phased array beam steering through serial control of the phase shifters," *ACES Express Journal*, vol. 1, no. 1, pp. 12-15, Jan. 2016.

[21] M. F. Unlersen, "FPGA kullanilarak dizi anten performansinin iyilestirilmesi - Improving array antenna performance using FPGA," *Ph.D. Dissertation, Selcuk University*, Konya - Turkey, p. 132, 29 Oct. 2015.

[22] J. I. Marden, *Multivariate Statistics: Old School: Mathematical and Methodological Introduction to Multivariate Statistical Analytics, Including Linear Models, Principal Components, Covariance Structures, Classification, and Clustering, Providing Background for Machine Learning and Big Data Study, With r*. Create Space Independent Publishing Platform, 2015.

[23] L. B. W. Jolley, *Summation of Series*. Dover Publications Inc., New York, 1961.

Muhammed Fahri Unlersen received B.Sc, MSEE and Ph.D. degrees in Electrical and Electronics Engineering from Selçuk University, Konya, Turkey in 2004, 2007 and 2015, respectively. He was a Lecturer in Doganhisar Vocational School at Selcuk University from 2005 to 2016, and Assistant Professor from 2016 in the Department of Electrical and Electronics Engineering at Necmettin Erbakan University. His current research interests are the array antennas, electromagnetic theory, field programable gate arrays and optimization techniques.

Ercan Yaldiz received B.Sc., MSEE and Ph.D. degrees in Electrical and Electronics Engineering from Selçuk University, Konya, Turkey in 1991, 1995 and 2002, respectively. He was a Teaching Assistant from 1992 to 2003, Assistant Professor from 2003 to 2013, and Associate Professor from 2013 to 2018 in the Department of Electrical and Electronics Engineering at Selçuk University. He is already Professor at Selçuk University. His current research interests are in the areas of the electromagnetic radiation, scattering, and numerical techniques.

Şehabeddin Taha İmeci received the B.Sc. degree in Electronics and Communications Engineering from Yildiz Technical University, Istanbul, Turkey in 1993, and M.S.E.E. and Ph.D. degrees from Syracuse University, Syracuse, NY in 2001 and 2007 respectively. He was with Anaren Microwave Inc., East Syracuse, NY from 2000 to 2002, and Herley Farmingdale, New York from 2002 to 2003, and PPC, Syracuse, NY from 2003 to 2005, and Sonnet Software Inc., Liverpool, NY from 2006 to 2007. He was a Teaching Assistant in the Department of Electrical Engineering and Computer Science at Syracuse University from 2005 to 2006. He received the Assistant Professorship and Associate Professorship degrees at Istanbul Commerce University, Istanbul Turkey in 2011 and 2014, respectively. İmeci joined International University of Sarajevo (IUS) as full Professor in 2017. His current research areas are microwave antennas and electromagnetic theory. İmeci authored two books and more than 100 scientific papers.